

**Structural, Electron Transfer and Spectroscopic
Studies of Transition Metal Complexes with
Redox-Active Non-Innocent Ligands**

Atanu Kumar Das

Structural, Electron Transfer and Spectroscopic Studies of Transition Metal Complexes with Redox- Active Non-Innocent Ligands

Von der Fakultät Chemie der Universität Stuttgart
Zur Erlangung der Würde eines
Doktors der Naturwissenschaften
(Dr. rer. nat.)
genehmigte Abhandlung

vorgelegt von
Atanu Kumar Das
aus Midnapore (Indien)

Hauptberichter:

Prof. Dr. W. Kaim

Mitberichter:

Prof. Dr. Th. Schleid

Tag der mündlichen Prüfung:

08.06.2009

Institut für Anorganische Chemie der Universität Stuttgart

2009

To My Family

***“Knowledge can only be got in one way, the way of
experience; there is no other way to know.”***

Swami Vivekananda

Acknowledgements

This work was completed from September 2005 to December 2008 at the institute of Inorganic Chemistry, University of Stuttgart.

I am grateful to many for the support and encouragement they provided me through the course of this study, without them it would have never been possible. I would specially like to acknowledge the following:

First I would like to thank Prof. W. Kaim for providing me with the opportunity to work within his research group, for all the ideas, the scientific guidance and enormous encouragement. I am greatly indebted for him.

Next I would like to take the opportunity to thank all the people who had helped me through out this doctoral work

Prof. G. K. Lahiri from IIT-Bombay, India for his helpful suggestions, continuous encouragements and many fruitful scientific discussions and Prof. M. Ravikanth from IIT-Bombay, India for helping me with the early synthetic exposure,

Dr. Biprajit Sarkar for his motivated words, continuous inspirations and suggestions on synthetic difficulties which helped me a lot to approach in the right direction at some crucial points, at the same time he helped me measuring the EPR, correcting the thesis initially and explaining the basics of different spectroscopic techniques,

Mr. Jan Fiedler for spectroelectrochemical measurements and Dr. S. Zálíš for DFT calculations from the Heyrovský Institute of Physical Chemistry in Prague, Czech Republic,

Dr. Monika Sieger solving the crystallographic related problems,

Ms. B. Förtsch for elemental analysis, Ms. K. Török for NMR measurements, Dr. F. Lissner, Dr. M. Niemeyer, Dr. I. Hartenbach and Dr. S. Strobel for crystallographic data collections and solving the crystal structures.

Dr. C. Duboc from the Grenoble High Field Laboratory for her with the high field EPR measurements,

Dr. J. Optiz, Mr. J. Trinker and Ms. K. Wohlbold for the mass spectroscopic measurements,

Mr. Ralph Hübner for the German translation of the part of the summary of this thesis,

Ms. A. Winkelmen and Dr. B. Schwederski helping me in the administrative works,

Mr. Negelein, Mr. Wesch, Mr. Lenz and Mr. Münch for their help related to chemicals, glasswares and solving the electronic problems,

Mr. M. Leboschka and Mr. O. Sarper for solving computer problems,

My research student A. Paretzki and T. Sube for doing part of the synthetic work,

Mr. Sayak Roy (Stuttgart, Germany), Mr. Somnath Maji (IIT-Bombay, India) and Mr. Nabarun Roy (Mülheim an der Ruhr, Germany) to be there always as good friends.

I would also like to thank,

All the past and present members of the group of Prof. Kaim for creating a nice environment to work,

All the members of the group of Dr. Sarkar for making much easier and enjoyable stay in the university,

Dr. Amarendranath Maity (Department of Physics, Taiwan) for helping me during my early days in Stuttgart,

Orkan, Cüneyt, Ralph, Johannes, Markus, Rajkumar and Hari for making my life much easier in Stuttgart with friendly support.

I am indebted to my parents, for their love, affection, blessings and inspiration.

Final words of gratitude to Swati, for her love, affection, faith and her aspiring words.

I am also grateful to Deutsche Forschungsgemeinschaft (Bonn, Germany) and Institute für Anorganische Chemie, Universität Stuttgart for the financial support.

CONTENTS

| | |
|--|-----------|
| 1. Introduction | 1 |
| 2. Redox Properties of Ruthenium Nitrosyl Octaethylporphyrin Complexes with Different axial ligation: Spectroscopic and Theoretical studies | 10 |
| 2.1. Introduction | 10 |
| 2.2. Syntheses and characterization | 11 |
| 2.3. Electrochemistry | 12 |
| 2.4. IR spectroelectrochemistry | 14 |
| 2.5. EPR spectroscopy | 17 |
| 2.5.1. Theory | 17 |
| 2.5.2. Results | 19 |
| 2.6. UV-Vis spectroelectrochemistry | 21 |
| 2.7. DFT calculations | 23 |
| 2.8. Conclusion | 27 |
| 3. An Oxo-Bridged Dirhenium Dinitrosyl Complex with Cyanide as Co-ligands | 28 |
| 3.1. Introduction | 28 |
| 3.2. Synthesis and characterization | 29 |
| 3.3. Crystal structure | 29 |
| 3.4. Electrochemistry | 31 |
| 3.5. IR spectroelectrochemistry | 32 |
| 3.6. EPR spectroscopy | 33 |
| 3.7. Conclusion and outlook | 33 |
| 4. Ruthenium Complexes with a Non-Innocent <i>o</i>-Iminobenzoquinone Ligand | 35 |
| 4.1. Introduction | 35 |
| 4.2. Syntheses and characterization | 37 |
| 4.2.1. The chloro complexes | 37 |
| 4.2.2. The nitro complexes | 40 |

| | |
|--|-----------|
| 4.3. Crystal structures | 41 |
| 4.4. Electrochemistry | 45 |
| 4.4.1. The chloro complexes | 45 |
| 4.4.2. The nitro complexes | 47 |
| 4.5. EPR spectroscopy | 49 |
| 4.5.1. The chloro complexes | 49 |
| 4.5.2. The nitro complexes | 52 |
| 4.6. UV-Vis-NIR spectroelectrochemistry | 55 |
| 4.6.1. The chloro complexes | 55 |
| 4.6.2. The nitro complexes | 60 |
| 4.7. Conclusion | 61 |
| | |
| 5. Paramagnetic Ruthenium Complexes with Two Different Non- Innocent Ligands: Nitrosyl and an <i>o</i>-Iminobenzoquinone | 63 |
| 5.1. Introduction | 63 |
| 5.2. Syntheses and characterization | 64 |
| 5.2.1. The complex [Ru(NO)(Q)(terpy)](PF ₆) ₂ | 64 |
| 5.2.2. The complex [Ru(NO)(Q)(tppz)](PF ₆) ₂ | 65 |
| 5.3. Crystal structure | 66 |
| 5.4. Electrochemistry | 68 |
| 5.5. IR spectroelectrochemistry | 70 |
| 5.5.1. The complex [Ru(NO)(Q)(terpy)](PF ₆) ₂ | 70 |
| 5.5.2. The complex [Ru(NO)(Q)(tppz)](PF ₆) ₂ | 72 |
| 5.6. EPR spectroscopy | 73 |
| 5.6.1. The complex [Ru(NO)(Q)(terpy)](PF ₆) ₂ | 73 |
| 5.6.2. The complex [Ru(NO)(Q)(tppz)](PF ₆) ₂ | 74 |
| 5.7. DFT calculations | 75 |
| 5.8. Conclusion | 78 |
| | |
| 6. A Dinuclear Ruthenium Complex with tppz as a Bridging Ligand and Non- innocent <i>o</i>-Iminobenzoquinone Terminal Ligands | 79 |
| 6.1. Introduction | 79 |

| | |
|---|------------|
| 6.2. Synthesis and characterization | 80 |
| 6.3. Crystal structure | 81 |
| 6.4. Electrochemistry | 83 |
| 6.5. EPR spectroscopy | 86 |
| 6.6. UV-Vis-NIR spectroelectrochemistry | 89 |
| 6.7. DFT calculations | 93 |
| 6.8. Conclusion | 98 |
| 7. Spectroelectrochemical (UV-Vis-NIR and EPR) and Theoretical Studies of the Redox Series $[M(Q_O)_3]^n$ ($Q_O = 3,5$-Di-<i>tert</i>-butyl-<i>o</i>-benzoquinone $M = Ru$ and Os) and $[M(Q)_3]^n$ ($Q = 4,6$-Di-<i>tert</i>-butyl-<i>N</i>-phenyl-<i>o</i>-iminobenzoquinone, $M = Ru$), $n = +2$ to -2 | 99 |
| 7.1. Introduction | 99 |
| 7.2. Syntheses and characterization | 100 |
| 7.3. Electrochemistry | 102 |
| 7.4. EPR spectroscopy | 104 |
| 7.4.1. The complexes $[Ru(Q_O)_3]$ and $[Os(Q_O)_3]$ | 104 |
| 7.4.2. The complex $[Ru(Q)_3]$ | 107 |
| 7.5. UV-Vis-NIR spectroelectrochemistry | 111 |
| 7.6. DFT calculations | 119 |
| 7.6.1. The complexes $[Ru(Q_O)_3]$ and $[Os(Q_O)_3]$ | 119 |
| 7.6.1. The complex $[Ru(Q)_3]$ | 122 |
| 7.7. Conclusion | 125 |
| 8. Rhenium and Platinum Complexes of the Diphosphine Chelate Ligand <i>R,R</i>-QuinoxP | 127 |
| 8.1. Introduction | 127 |
| 8.2. Syntheses and characterization | 128 |
| 8.3. Crystal structures | 132 |
| 8.4. Electrochemistry | 135 |
| 8.5. IR spectroelectrochemistry | 137 |
| 8.6. EPR spectroscopy | 138 |

| | |
|---|------------|
| 8.7. UV-Vis spectroelectrochemistry | 141 |
| 8.8. Conclusion and outlook | 142 |
| 9. Experimental | 143 |
| 9.1. Instrumentation | 143 |
| 9.2. Solvents and working conditions | 144 |
| 9.3. DFT calculations | 144 |
| 9.4. Syntheses | 148 |
| 9.4.1. Commercially available compounds | 148 |
| 9.4.2. Syntheses of reported compounds | 148 |
| 9.4.3. Synthesis of $(PPh_4)_4[(CN)_4(NO)Re(\mu-O)Re(NO)(CN)_4]$ | 149 |
| 9.4.4. Synthesis of complexes with $[Ru(terpy)(Cl)_3]$ | 149 |
| 9.4.5. Synthesis of mononuclear complexes with $[Cl_3Ru(\mu-tppz)RuCl_3]$ | 152 |
| 9.4.6. Synthesis of dinuclear complex with $[Cl_3Ru(\mu-tppz)RuCl_3]$ | 154 |
| 9.4.7. Synthesis of $[Ru(Q)_3]$ | 155 |
| 9.4.8 Syntheses of complexes with <i>R,R</i> -QuinoxP ligand | 156 |
| 9.5. Crystallography | 158 |
| 9.5.1. $(PPh_4)_4[(CN)_4(NO)Re(\mu-O)Re(NO)(CN)_4]$ | 158 |
| 9.5.2. $[(terpy)Ru(Q)Cl](ClO_4)$ | 159 |
| 9.5.3. $[(terpy)Ru(Q)(NO_2)](ClO_4)$ | 160 |
| 9.5.4. $[(terpy)Ru(Q)(NO)](PF_6)_2$ | 161 |
| 9.5.5. $[(tppz)Ru(Q)Cl](PF_6)$ | 163 |
| 9.5.6. $[(tppz)Ru(Q)(NO_2)](PF_6)$ | 164 |
| 9.5.7. $[(Q)ClRu(\mu-tppz)RuCl(Q)](PF_6)_2$ | 165 |
| 9.5.8. $[(R,R\text{-QuinoxP})PtCl_2]$ | 166 |
| 9.5.9. $[(R,R\text{-QuinoxP})Re(CO)_3Cl]$ | 167 |
| 10. Summary | 169 |
| 11. Zusammenfassung | 177 |
| Appendix | |
| Bibliography | |
| Abbreviations | |
| Curriculum Vitae | |

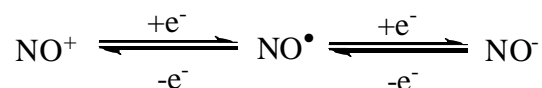
CHAPTER 1

Introduction

As Jørgensen pointed out in 1966 (*Coord. Chem. Rev.* **1966**, *1*, 164), a ligand is to be regarded as ‘innocent’ if it allows the oxidation state of a metal in a complex to be defined.¹ When a ligand binds to a metal, there is some charge transfer between the ligand and the metal. Often, this charge transfer is sufficiently small that oxidation states can still be easily determined. A non-innocent ligand² such as nitrosyl,³⁻⁵ 1,2-dithiolene⁶ or 1,2-dioxolene⁷⁻⁹ is a ligand that, when attached to a metal, exhibits so much charge transfer that the oxidation state of the metal is no longer clear. In terms of MO theory, there is a strong mixing between ligand and metal frontier orbitals, such that assignments of oxidation states to individual metal and ligand components are difficult. It is difficult to assign the correct oxidation state because the redox active ligand can bind to the metal in different redox forms.²

1.1. Nitrosyl: a monodentate non-innocent ligand

The NO ligand which can be bound to the metal ion either as NO⁺ (nitrosonium cation)⁵ or NO[•] (nitric oxide, neutral)⁶ or NO⁻ (nitroxide anion)⁴ (Scheme 1.1.1), is considered as a ‘non-innocent’ ligand.



Scheme 1.1.1. Different redox forms of nitrosyl.

The bonding of NO mostly involves attachment of the N atom to the metal, and in a molecular orbital approach, it is considered to be made up of two components.³ The first involves donation of electron density from a σ -type orbital of NO onto the metal ion while the second includes back donation from the filled metal d orbitals to the π^* orbitals of NO. Presence of NO always creates ambiguity of oxidation state assignments,⁵ because of the possibility to bind in different oxidation states⁵⁻⁷ and the covalent nature of M–N–O interaction.⁹ Enemark and Feltham proposed a formalism to describe metal nitrosyl complexes which treated the metal nitrosyl as a single entity.⁴ This was represented as $\{\text{M}(\text{NO})_x\}^n$, in which n is the total number of electrons associated with the metal d and π^* (NO) orbitals. The number of d electron is determined by the formal oxidation state of the metal atom, assuming no charge on the NO group. A clear difference in M–N–O bond angle³ is observed (Figure 1.1.1) in the

series $\{MNO\}^6 \rightarrow \{MNO\}^7 \rightarrow \{MNO\}^8$. The M–N–O moiety is essentially linear for configuration $\{MNO\}^6$ describing nitrosyl bound as NO^+ . In contrast, the bond angles for $\{MNO\}^7$ and $\{MNO\}^8$ have been estimated to be $145 \pm 10^\circ$ and $125 \pm 10^\circ$, respectively. A difference in N–O bond length³ is also observed for these three different configurations, reflected also in the ν_{NO} stretching frequency.

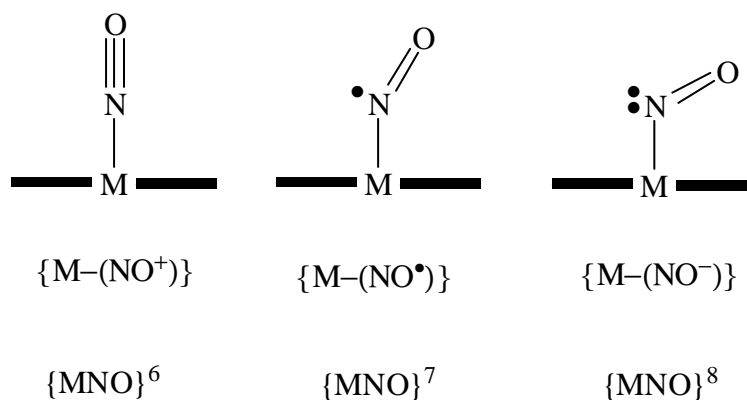


Figure 1.1.1. The M–N–O bond angles in mononitrosyl complexes.

In addition to its interesting non-innocent behavior, nitric oxide is involved in several important biological events,¹⁰⁻¹¹ including neurotransmission, vasodilation and blood clotting.¹¹ Nitric oxide is biosynthesized by a class of enzymes called nitric oxide synthases (NOSs),^{11a} which contain heme as a prosthetic group. Soluble guanylate cyclase is one of the other heme-containing enzymes that act as biological receptors for NO .^{11e}

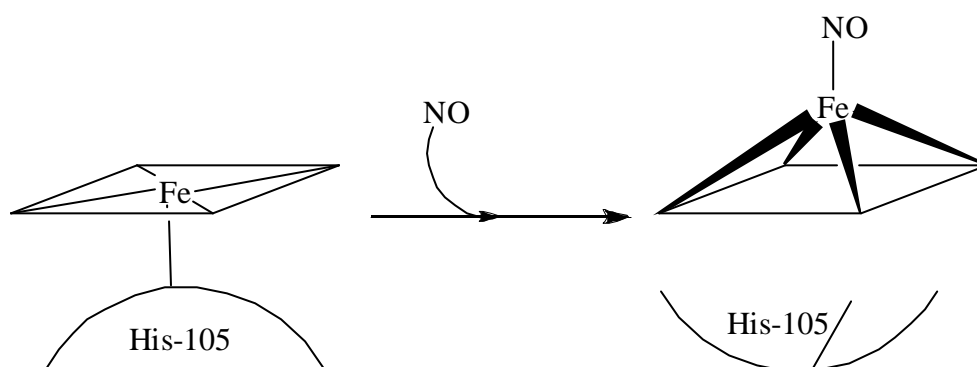


Figure 1.1.2. Proposed mechanism of heme–NO interaction during the activation of soluble guanylate cyclase.^{11e}

In many physiological processes the interaction of nitric oxide with heme proteins plays a very important role. Because of the general importance of the heme–NO interaction (Figure

1.1.2), a large amount of research has been carried out towards the synthesis of corresponding model systems. Many investigations on iron nitrosyl porphyrins have included variations of the axial ligand in the trans position to NO, ranging from N donors¹² such as pyridine, imidazole or piperidine to S donors such as thiolates¹³, in order to understand the role of axial ligands on the properties of coordinated NO. The heavier analogues, ruthenium nitrosyl porphyrins, have also been anticipated to be promising models in the study of the interactions of NO with heme because of their enhanced stability relative to iron nitrosyl complexes. However, in contrast to several reports on the syntheses^{14,15} and structure¹⁶ of ruthenium nitrosyl porphyrins, there have been far fewer investigations on the electrochemistry¹⁷ and spectroelectrochemistry^{18,19} of ruthenium nitrosyl porphyrin despite the fact that these would be essential in understanding electron-transfer processes.

The first part of my thesis highlights the synthetic aspects as well as the structural, spectroscopic and electronic properties of transition metal (Ru and Re) nitrosyl complexes. A Ru-octaethylporphyrin-NO complex was studied as model to understand the interaction of NO with heme. The actual form of coordinated NO^m ($m = +/0/-$) was established based on the experimental results (IR, UV-Vis-NIR, EPR spectroelectrochemistry) which are elucidated by calculations.

Chapter 2 describes the experimental and theoretical studies of ruthenium-nitrosyl-octaethylporphyrin (OEP) complexes linked to different axial ligands (X) such as water, pyridine, 4-cyanopyridine, 4-*N,N*-dimethylaminopyridine (Figure 1.1.3). The oxidation state of NO in $[(\text{OEP})\text{Ru}(\text{NO})(\text{H}_2\text{O})]^+$ and the redox properties of $[(\text{OEP})\text{Ru}(\text{NO})(\text{X})]^+$ where X = different pyridine have been investigated by means of electrochemical and various spectroelectrochemical methods, including EPR.

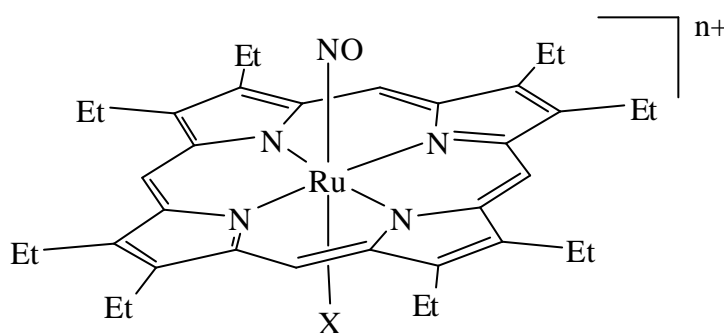


Figure 1.1.3. Molecular formula of $[(\text{OEP}^{2-})\text{Ru}(\text{NO})(\text{X})]^{n+}$ where X = H_2O ($n = 1, 2, 3$) or pyridine, 4-cyanopyridine or 4-*N,N*-dimethylaminopyridine ($n = 1, 0$).

Chapter 3 deals with an oxo-bridged rhenium-dinitrosyl complex (Figure 1.1.4) with cyanide as coligand. The complex was characterized by single-crystal X-ray crystallography. The oxidation state of NO^m has been formulated using the crystal data and IR vibrational spectroscopic results. The electron transfer behavior has been investigated by cyclic voltammetry and the oxidation has been probed by IR spectroelectrochemistry.

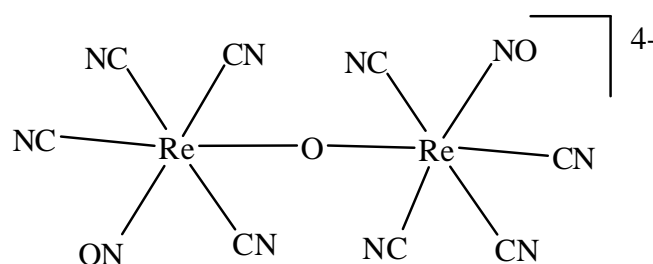
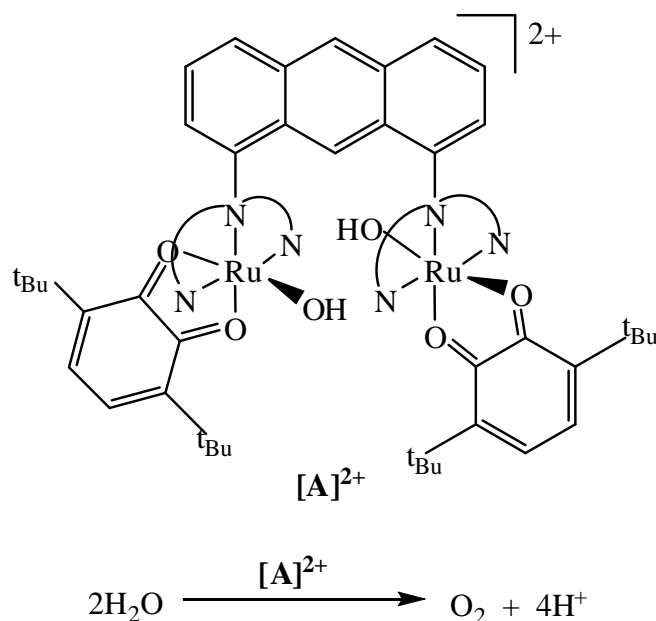


Figure 1.1.4. Molecular formula of $[(\text{CN})_4(\text{NO})\text{Re}(\mu\text{-O})\text{Re}(\text{NO})(\text{CN})_4]^{4-}$.

1.2. 4,6-Di-*tert*-butyl-*N*-phenyl-*o*-iminobenzoquinone (Q): A bidentate non-innocent ligand

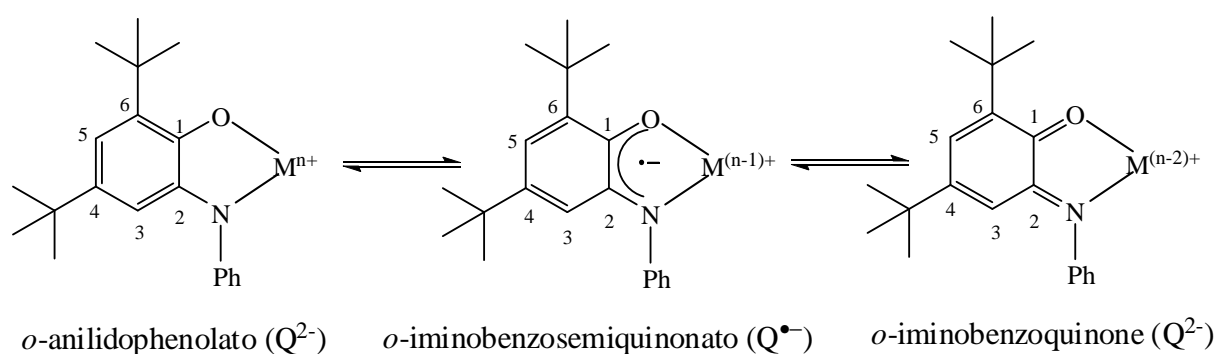
The well known non-innocent 1,2-dioxolene⁷⁻⁹ ligands can exist in the three redox forms of *o*-quinone (L_Q^0), *o*-semiquinone ($\text{L}_\text{Q}^{\cdot-}$) and catecholate (L_Q^{2-}), and it has been established by X-ray crystallography^{8,20} that the geometries of these ligands differ in a systematic fashion, depending on the respective oxidation level. Many studies^{20,21} have been aimed at studying the interaction between redox-active transition metals and *o*-quinonoid π systems. Such interactions may even have biochemical implications, e.g., in biocopper or bioiron chemistry^{21b-22}. Partial or complete substitution of the O donor atoms by S, NH or NR and other modifications were used to broaden the scope of this remarkable coordination chemistry.

The combination between ruthenium and quinone-type ligands has received much attention because of exceptional metal-to-ligand charge-transfer interaction (back donation)^{8f,g,24} and the ambiguity of oxidation state assignments,²³⁻²⁸ because of the stability and EPR accessibility of ruthenium(II)-semiquinone complexes²⁵⁻²⁶ and the non-trivial electronic structure,²⁷ because of the antiferromagnetic coupling between Ru^{III} and semiquinone radicals,²⁸ because of the possible stabilization of coordinated radicals²⁹⁻³⁰ and due to the potential use of dinuclear such systems in water oxidation catalysis (Figure 1.2.1).³¹



Scheme 1.2.1. Oxidation of water catalyzed by the dinuclear Ru-quinone complex $[\text{A}]^{2+}$.³¹

In this doctoral work, mostly a *N*-phenyl substituted *o*-iminoquinone 4,6-di-*tert*-butyl-*N*-phenyl-*o*-iminobenzoquinone (Q),³² has been employed with different co-ligands to obtain mainly ruthenium complexes, displaying non-innocent behavior. All complexes were characterized and studied by using different spectroscopic and electrochemical techniques. DFT calculations have been performed if necessary, to rationalize the experimental results and establish the electronic structure. Scheme 1.2.2 shows different oxidation levels of ligand in combination with different metal oxidation states. Small but significant structural differences in the coordinated ligands ($\text{Q}^{2-}/\text{Q}^{\bullet-}/\text{Q}^0$) are clearly detectable and C1–N, C2–O and intra ring C–C bond lengths supply evidence of these different oxidation levels.³³⁻³⁵



Scheme 1.2.2. Different redox forms of 4,6-di-*tert*-butyl-*N*-phenyl-*o*-iminobenzoquinone.

Chapter 4 presents the results obtained from four ruthenium 4,6-di-*tert*-butyl-*N*-phenyl-*o*-iminobenzoquinone-Cl⁻ and NO₂⁻ complexes (Figure 1.2.1) with two different meridional tridentate ligands terpy = 2,2':6,2''-terpyridine or tppz = 2,3,5,6-tetrakis(2-pyridyl)pyrazine as ancillary ligands. The four complexes [(terpy)Ru(Q)Cl]ⁿ⁺, [(terpy)Ru(Q)(NO₂)]ⁿ⁺, [(tppz)Ru(Q)Cl]ⁿ⁺ and [(tppz)Ru(Q)(NO₂)]ⁿ⁺ displaying non-innocent behavior have been isolated in the monocationic form and all of these were crystallographically characterized. The C–O, C–N and the intra-ring bond distances obtained from the single crystal X-ray data have been employed to formulate the valence state distribution in the isolated form. Electrochemical and spectroelectrochemical (UV-Vis-NIR, X-band and high-field EPR) studies have been performed, when possible, to evaluate the appropriate oxidation state in accessible redox states.

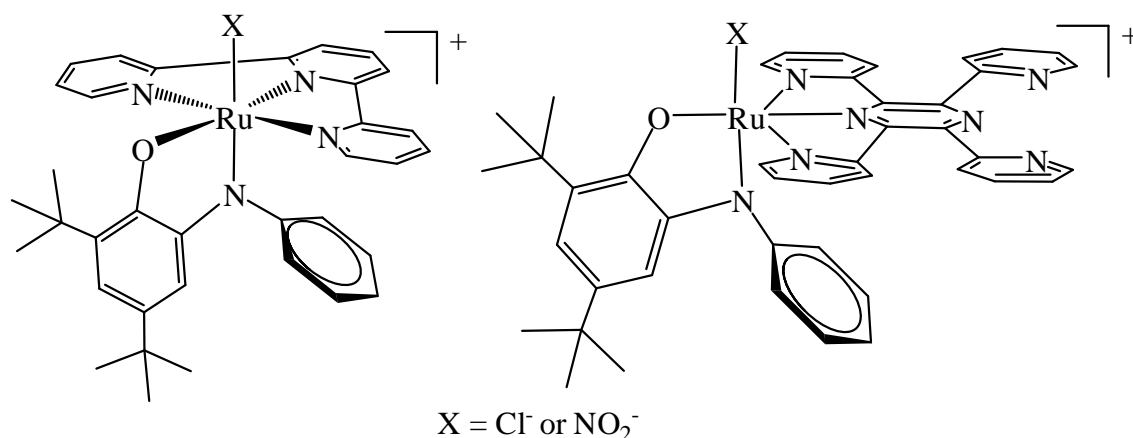


Figure 1.2.1. Molecular formulae of the complexes [(terpy)Ru(Q)(X)]⁺ (left) and [(tppz)Ru(Q)(X)]⁺ (right) where X = Cl⁻ or NO₂⁻.

Chapter 5 deals with two complexes (Figure 1.2.2) obtained combining two mentioned non-innocent ligand nitrosyl (NO) and 4,6-di-*tert*-butyl-*N*-phenyl-*o*-iminobenzoquinone (Q). A detailed study of complex [Ru(NO)(Q)(terpy)](PF₆)₂ including DFT has been presented illustrating “how the art of establishing oxidation states”³³ can be applied successfully to such unique systems. The most stable positional isomer of [Ru(NO)(Q)(terpy)](PF₆)₂ with NO trans to the O donor atom of Q was isolated and characterized by single crystal X-ray analysis. The energy minima for different possible isomers (positional isomers with the rotamers, spin and valence isomers) of [Ru(NO)(Q)(terpy)](PF₆)₂ have been calculated using

DFT calculations. Additionally, the synthesis, characterization and redox properties of $[\text{Ru}(\text{NO})(\text{Q})(\text{tppz})](\text{PF}_6)_2$ are presented.

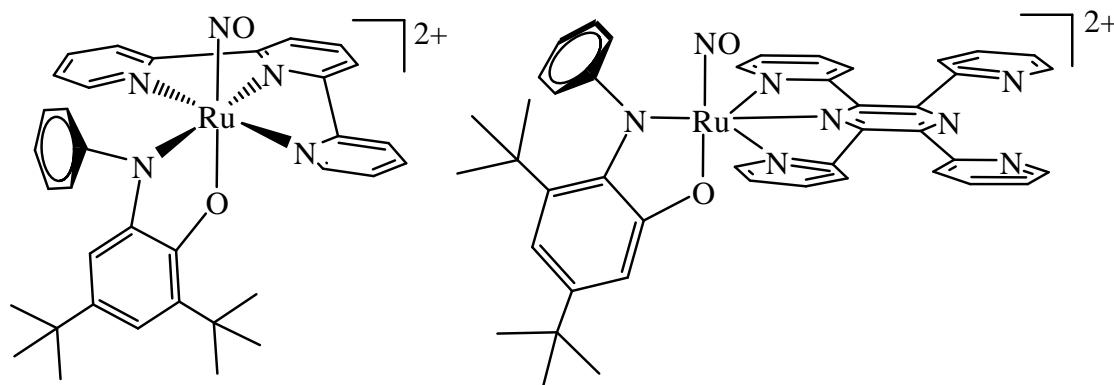


Figure 1.2.2. Molecular formulae of the complexes $[(\text{terpy})\text{Ru}(\text{Q})(\text{NO})]^{2+}$ (left) and $[(\text{tppz})\text{Ru}(\text{Q})(\text{NO})]^{2+}$ (right).

Chapter 6 deals with a dinuclear ruthenium complex (Figure 1.2.3) with π accepting bis-tridentate 2,3,5,6-tetrakis(2-pyridyl)pyrazine (tppz) as a bridging ligand and 4,6-di-*tert*-butyl-*N*-phenyl-*o*-iminobenzoquinone (Q) as terminal ligands. The complex $[\text{Cl}(\text{Q})\text{Ru}(\mu\text{-tppz})\text{Ru}(\text{Q})\text{Cl}](\text{PF}_6)_2$, containing the five-component redox system $[\text{Q}^{\text{n}}\text{-Ru}^{\text{m}}\text{-}(\mu\text{-tppz})^{\text{x}}\text{-Ru}^{\text{m}'}\text{-Q}^{\text{n}}]$ has been structurally characterized and the accessible redox processes (two oxidations and four reductions) were monitored by EPR and UV-Vis-NIR spectroelectrochemistry in order to assign the appropriate oxidation states to all five redox-active components.

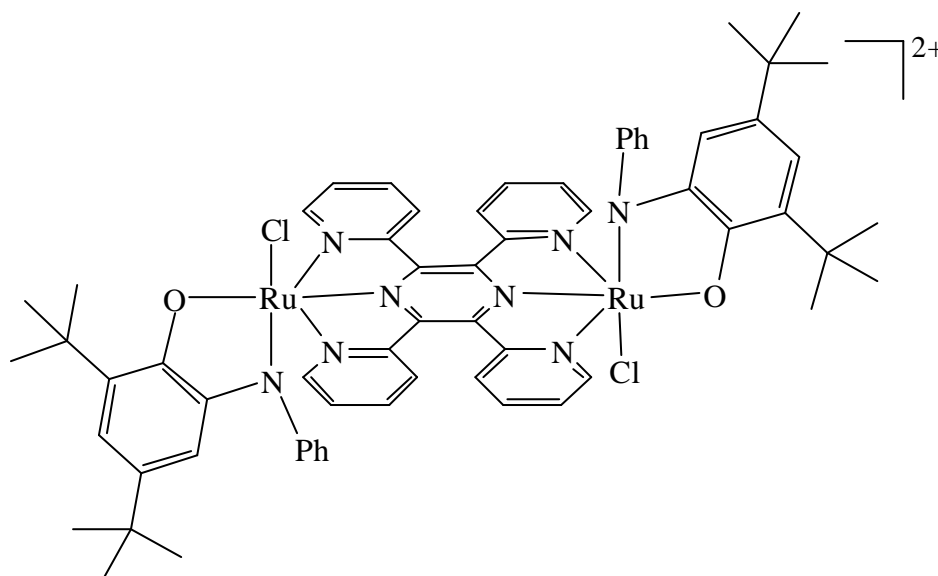


Figure 1.2.3. Molecular formula of the complex $[\text{Cl}(\text{Q})\text{Ru}(\mu\text{-tppz})\text{Ru}(\text{Q})\text{Cl}](\text{PF}_6)_2$.

Structure-based DFT and TD-DFT calculations confirm the experimental results. The mediated coupling of two substituted monoimino-*o*-benzoquinonato-ruthenium moieties Q^nRu^m with variable oxidation states of both the metal *and* of the (non-innocent) quinonoid ligand are described.

Chapter 7 deals with tris(3,5-di-*tert*-butyl-*o*-benoquinone) complexes of Ru and Os and with the tris(4,6-di-*tert*-butyl-*N*-phenyl-*o*-iminobenzoquinone) complex of Ru. The complexes initially characterized as the neutral species while their oxidized and reduced forms were studied by EPR and UV-Vis-NIR spectroelectrochemistry. The complexes were subjected to DFT and TD-DFT calculations to interpret the experimental data and establish the electronic structure.

1.3. 2,3-Bis(*tert*-butylmethylphosphino)quinoxaline (QuinoxP) : A redox active P-chiral phosphine ligand

Chiral 1,4-diphosphine³⁶ ligands capable of forming five or six-membered metal chelate rings have long been established as essential components of successful enantioselective catalysis systems, involving especially hydrogenation and C–C bond forming reactions.³³

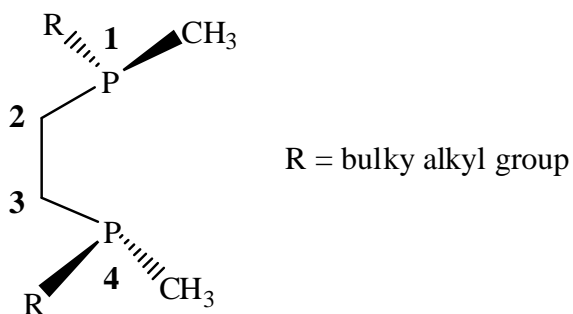


Figure 1.3.1. Molecular formula of 1,2-bis(alkylmethylphosphino)ethane, a chiral 1,4-diphosphine ligand.³⁶

However, these ligands are extremely air sensitive. Enormous efforts have been put in to overcome this inconvenience and simultaneously preserve or even improve the catalytic activity and selectivity. Imamoto and co-workers have recently developed a new class of P-chiral diphosphine ligands which fulfill these requirements, using the rigid and π electron-deficient quinoxaline heterocycle as a platform to which the dialkylphosphinosubstituents could be attached in 2,3 position.^{37,38} The resulting molecules such as 2,3-bis(*tert*-

butylmethylphosphino)quinoxaline (QuinoxP)³⁷ and related diphosphines³⁸ were employed in connection with rhodium and palladium components for asymmetric hydrogenation and carbon–carbon bond formation. Considering the tendency of quinoxalines,³⁹ specially metal coordinated ones,⁴⁰ to undergo reversible electron uptake to form persistent, EPR-detectable radical anion species, the *R,R* isomer L of QuinoxP has been used in order to obtain the relevant metal complexes.

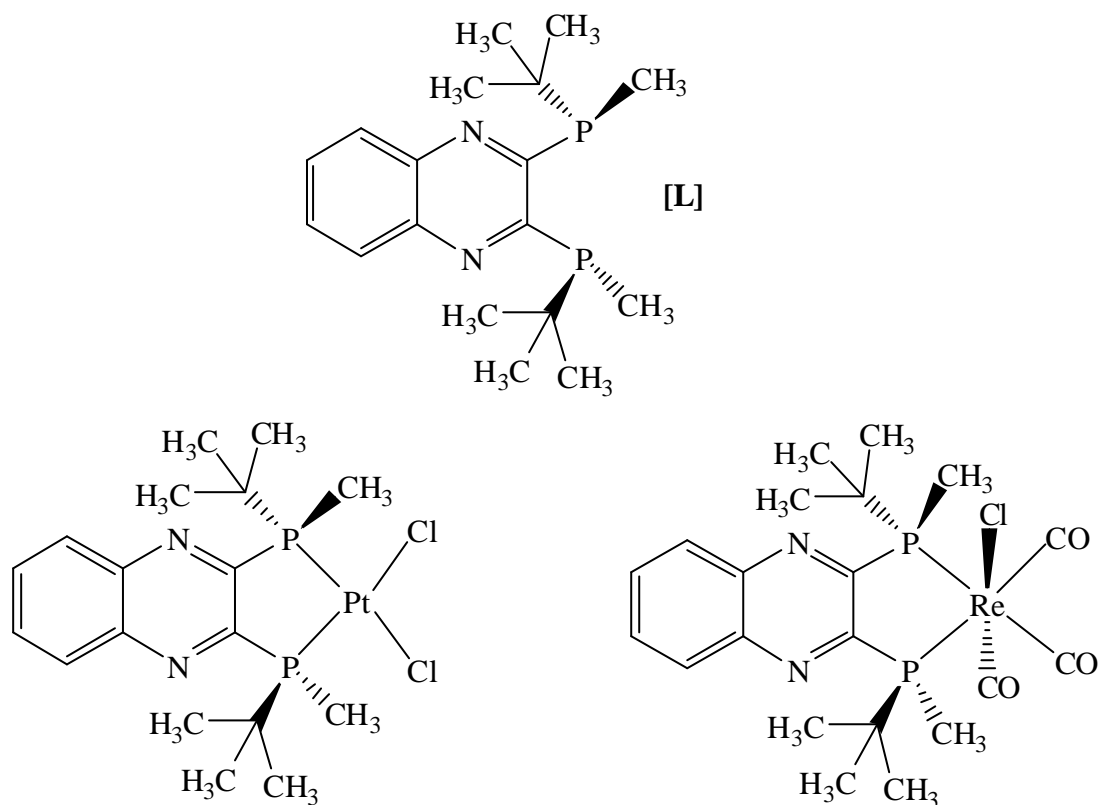


Figure 1.3.2. Molecular formulae of the ligand QuinoxP (**L**) (top), complexes (QuinoxP)PtCl₂ (bottom left) and (QuinoxP)Re(CO)₃Cl (bottom right).

Chapter 8 describes the reactions of metal precursors Pt(dmsO)₂Cl₂ and Re(CO)₅Cl with the *R,R* isomer L of QuinoxP resulting in two air stable neutral mononuclear complexes (Figure 1.3.5) with the formulations (L)PtCl₂ and (L)Re(CO)₃Cl, including their single crystal X-ray structures. The electron transfer behaviour of these complexes has been investigated by cyclic voltammetry and by EPR, UV-Vis and IR spectroelectrochemistry.

CHAPTER 2

Redox Properties of Ruthenium Nitrosyl Octaethylporphyrin Complexes with Different Axial Ligation: Spectroscopic and Theoretical Studies

2.1. Introduction

The interaction of nitric oxide with heme proteins is of tremendous physiological importance and plays a key role in many processes^{10,11} like nerve-signal transduction, vasodilation, blood clotting and immune response¹¹. Nitric oxide is biosynthesized by a class of enzymes called nitric oxide synthases (NOSs),^{2a} which contain heme as a prosthetic group. Soluble guanylate cyclase (sCG) is one of the other heme-containing enzymes that act as biological receptors for NO. In addition to its significance in physiology, the interaction of NO with heme is also important in the nitrogen cycle.^{11b} Because of the general importance of the heme–NO interaction, a large amount of research has been carried out toward the synthesis of corresponding model systems. These investigations employ synthetic porphyrins such as tetraphenyl (TPP) or the more electron-rich octaethylporphyrin (OEP), and iron nitrosyl complexes of these synthetic porphyrins have been extensively studied.⁴¹ Many investigations on iron nitrosyl porphyrins have included variations of the axial ligand in the trans position to NO, ranging from N donors,¹² such as pyridine, imidazole, or piperidine, to S donors, such as thiolates,¹³ in order to understand the role of axial ligands in the properties of coordinated NO.

The heavier analogues of iron, ruthenium nitrosyl porphyrins, have also been anticipated to be promising models in the study of the interactions of NO with heme because of their enhanced stability relative to iron nitrosyl complexes.⁴² However, in contrast to the several reports on the syntheses^{42b,43} and structural studies¹⁶ of ruthenium nitrosyl porphyrins, there have been far fewer investigations on the electrochemistry¹⁷ and spectroelectrochemistry^{18,19} of ruthenium nitrosyl porphyrin despite the fact these would be essential in understanding electron-transfer processes. In addition, the unambiguous assignment of the NO oxidation state^{3,4} for NO-coordinated ruthenium porphyrin complexes [(por)Ru(NO)(X)] with different porphyrins (Por) and various axial ligands (X) can be useful in understanding the electron transfer processes. All three components, the porphyrinato ligands (Pro^{-2-/3-}), the metal (Ru^{2+/3+}), and the NO system (NO^{+/0/-}) are redox-active in the central

redox potential region so that the determination of individual oxidation state combination is not trivial.

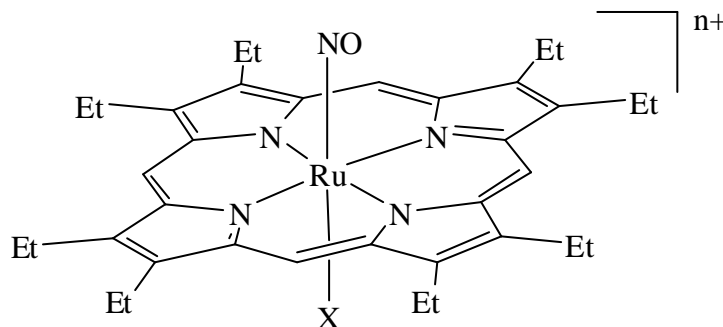


Figure 2.1.1 Molecular formula of $[(\text{por})\text{Ru}(\text{NO})(\text{X})]^{n+}$ (where Por^{2-} = octaethylporphyrin dianion (OEP^{2-}) and $\text{X} = \text{H}_2\text{O}$ ($n = 1, 2, 3$) or pyridine, 4-cyanopyridine, 4-*N,N*-dimethylaminopyridine ($n = 1, 0$)).

The present chapter deals with the experimental and theoretical studies of ruthenium-nitrosyl-octaethylporphyrin (OEP) complexes linked to different axial ligands (X) such as water; pyridine, 4-cynopyridine, 4-*N,N*-dimethylaminopyridine (Figure 2.1.1). The effect of axial ligands on the redox properties of ruthenium nitrosyl octaethylporphyrin complexes has been investigated by means of electrochemical and various spectroelectrochemical methods including EPR.

2.2. Syntheses and characterization

The complex $[(\text{OEP})\text{Ru}(\text{NO})(\text{H}_2\text{O})]\text{BF}_4$, (OEP^{2-} = octaethylporphyrin dianion) was prepared according to the literature reported procedure⁴⁵ as shown in Figure 2.2.1 and characterised by $^1\text{H-NMR}$, elemental analysis and IR spectroscopy. The complex $[(\text{OEP})\text{Ru}(\text{NO})(\text{H}_2\text{O})]\text{BF}_4$

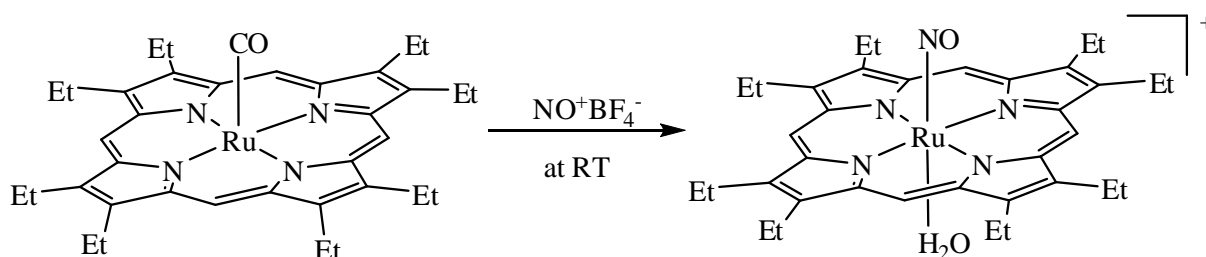


Figure 2.2.1. Synthesis of $[(\text{OEP})\text{Ru}(\text{NO})(\text{H}_2\text{O})]\text{BF}_4$.

shows the $\nu(\text{NO})$ at 1853 cm^{-1} in KBr and at 1877 cm^{-1} in dichloromethane. Intense solet band at 410 nm and Q band at 558 nm are observed in the optical spectrum (see section 2.5) in dichloromethane. The reduction studies on $[(\text{OEP})\text{Ru}(\text{NO})(\text{X})]\text{BF}_4$ where X = pyridine, 4-cyanopyridine, 4-*N,N*-dimethylaminopyridine were performed after electrocatalysed exchange in the solution of the aqua complex and excess (ca. tenfold) of the respective pyridine (Figure 2.2.2).¹⁷

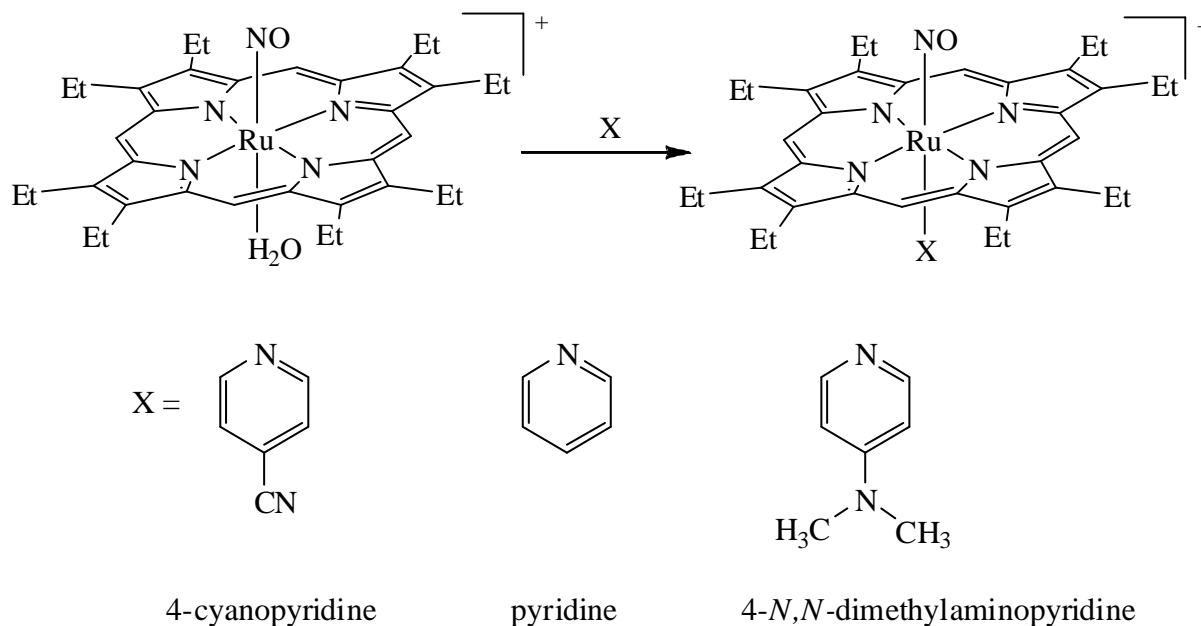


Figure 2.2.2. Electrocatalysed formation of $[(\text{OEP})\text{Ru}(\text{NO})(\text{X})]\text{BF}_4$ on addition of X to $[(\text{OEP})\text{Ru}(\text{NO})(\text{H}_2\text{O})]\text{BF}_4$.

2.3. Electrochemistry

Cyclic voltammetry has been performed on the precursor compound $[(\text{OEP})\text{Ru}(\text{NO})(\text{H}_2\text{O})]\text{BF}_4$ and the analogues containing pyridines instead of H_2O in the trans position to NO. A cyclic voltammogram for the oxidation of $[(\text{OEP})\text{Ru}(\text{NO})(\text{H}_2\text{O})]\text{BF}_4$ in $\text{CH}_2\text{Cl}_2/0.1\text{ M } n\text{-Bu}_4\text{NClO}_4$ is shown figure 2.3.1. The compound undergoes two one-electron reversible oxidation processes at $E_{1/2}(\text{ox1}) = +0.71\text{ V}$ and $E_{1/2}(\text{ox2}) = +1.13\text{ V}$ versus $\text{Fc}^{+/0}$. In contrast to the oxidations, even the first reduction is irreversible⁷ and thus it was not investigated further. However, as reported earlier,¹⁷ $[(\text{TPP})\text{Ru}(\text{NO})(\text{H}_2\text{O})]^+$ can be reduced reversibly in presence of pyridine. A similar trend was observed for the reduction of $[(\text{OEP})\text{Ru}(\text{NO})(\text{py})]^+$ with different pyridine bases. The compound $[(\text{OEP})\text{Ru}(\text{NO})(\text{py})]^+$ shows a reversible first reduction (Figure 2.3.2) followed by a quasi reversible reduction

process. The reduction potentials are sensitive to the electronic nature of the pyridines. A better electron acceptor than pyridine, 4-cyanopyridine shifts the potential for the first reduction of $[(\text{OEP})\text{Ru}(\text{NO})(\text{X})]^+$ to a less negative value (-0.68 V versus $\text{Fc}^{+/0}$), whereas 4-*N,N*-dimethylaminopyridine, a better electron donor but poorer π -electron acceptor than unsubstituted pyridine, shifts the potential to more negative values, (-1.00 V versus $\text{Fc}^{+/0}$, Table 2.3.1). The sites of the reversible electron-transfer processes, the two oxidations and the reduction of $[(\text{OEP})\text{Ru}(\text{NO})(\text{H}_2\text{O})]^+$ by different spectroelectrochemical measurements.

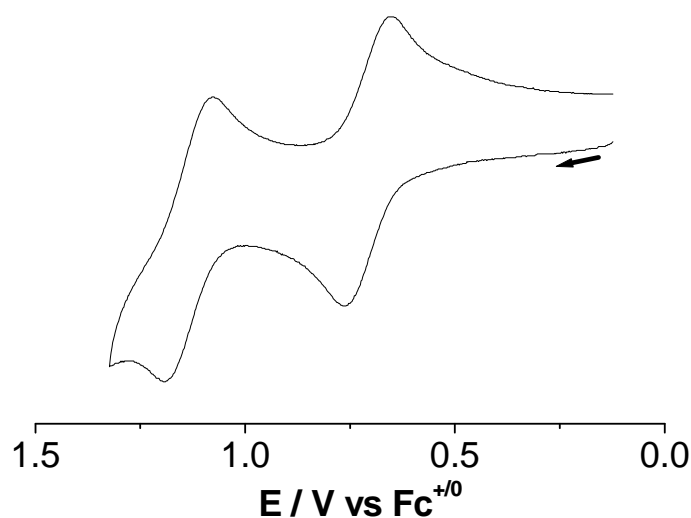


Figure 2.3.1. Cyclic voltammogram of $[(\text{OEP})\text{Ru}(\text{NO})(\text{H}_2\text{O})]\text{BF}_4$ in $\text{CH}_2\text{Cl}_2/0.1$ M *n*- Bu_4ClO_4 at 25 °C (oxidation); scan rate = 200 mV/s.

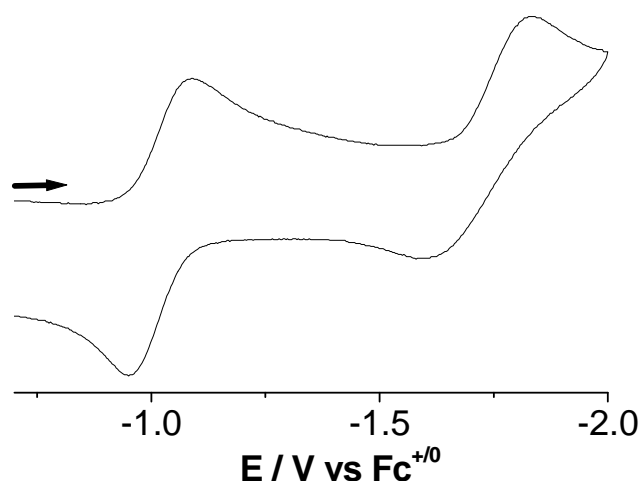


Figure 2.3.2. Cyclic voltammogram of $[(\text{OEP})\text{Ru}(\text{NO})(\text{py})]\text{BF}_4$ in $\text{CH}_2\text{Cl}_2/0.1$ M *n*- Bu_4ClO_4 at 25 °C (reduction); scan rate = 100 mV/s.

Table 2.3.1 Redox potentials of complexes^a.

| Complex | $E_{1/2}(\text{ox1})$ | $E_{1/2}(\text{ox2})$ | $E_{1/2}(\text{red1})$ |
|---|-----------------------|-----------------------|------------------------|
| $[(\text{OEP})\text{Ru}(\text{NO})(\text{H}_2\text{O})]\text{BF}_4$ | 0.71 | 1.13 ^c | b |
| $[(\text{OEP})\text{Ru}(\text{NO})(\text{py})]\text{BF}_4$ | b | n.o. | -0.95 |
| $[(\text{OEP})\text{Ru}(\text{NO})(4\text{-CN-py})]\text{BF}_4$ | b | n.o. | -0.67 |
| $[(\text{OEP})\text{Ru}(\text{NO})(4\text{-N,N-Me}_2\text{N-py})]\text{BF}_4$ | b | n.o. | -1.00 |

^aPotentials in volts versus $\text{Fc}^{+/0}$ from cyclic voltammetry at 100 mV/s in $\text{CH}_2\text{Cl}_2/0.1 \text{ M } n\text{-Bu}_4\text{NClO}_4$ solutions. ^b peak potential for irreversible process. ^cquasi reversible.

2.4. IR spectroelectrochemistry

IR spectroelectrochemistry has been applied to investigate the location of the accessible redox process, oxidation of $[(\text{OEP})\text{Ru}(\text{NO})(\text{H}_2\text{O})]^+$ and reduction of $[(\text{OEP})\text{Ru}(\text{NO})(\text{py})]^+$. Table 2.4.1 summarizes the data on the vibrational frequency of NO in different oxidation states together with DFT calculated values.

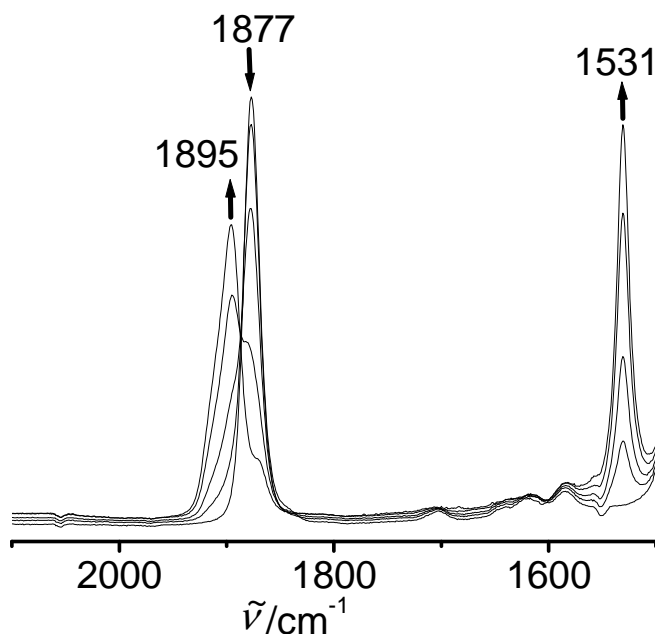


Figure 2.4.1. IR spectroelectrochemical of the conversion $[(\text{OEP})\text{Ru}(\text{NO})(\text{H}_2\text{O})]^{(+)\rightarrow(2+)}$ in $\text{CH}_2\text{Cl}_2/0.1 \text{ M } n\text{-Bu}_4\text{NClO}_4$.

The first oxidation of the aqua complex causes a comparatively small positive shift of the NO stretching frequency ($\Delta\nu(\text{NO}) = 18 \text{ cm}^{-1}$, Figure 2.4.1), suggesting that the oxidation occurs

neither on NO nor Ru but on the porphyrin ring. DFT calculations give a ca 20 cm^{-1} positive shift of the NO stretching frequency, which is in good agreement with the experimental data. The appearance of the porphyrin radical anion (“radical cation”)⁴⁶ diagnostic ring vibrational band at 1531 cm^{-1} after the spectroelectrochemical oxidation of the aqua complex also confirms that the porphyrin ring is the target of the oxidation process.⁴⁷ DFT calculations found intense, almost-degenerate pairs of ring vibration bands at 1548 and 1549 cm^{-1} for the oxidized OMP complex. The second oxidation causes a positive shift of $\Delta\nu(\text{NO}) = 55\text{ cm}^{-1}$ for $[(\text{OEP})\text{Ru}(\text{NO})(\text{H}_2\text{O})]^+$ in $\text{CH}_2\text{Cl}_2/0.1\text{ M } n\text{-Bu}_4\text{NClO}_4$ (Figure 2.4.2). A high energy shift of 64 cm^{-1} is also observed for the 1531 cm^{-1} ring vibrational band. $\Delta\nu(\text{NO}) = 55\text{ cm}^{-1}$ may be compared to $\Delta\nu(\text{NO}) = 79\text{ cm}^{-1}$ observed for the $\text{Ru}^{\text{II}} \rightarrow \text{Ru}^{\text{III}}$ transition in $[\text{Ru}(\text{NO})\text{Cl}_5]^{(2-)\rightarrow(-)}$,^{5d} suggesting the relevance of a presumably spin-paired $[(\text{OEP}^{\bullet-})\text{Ru}^{\text{III}}(\text{NO}^+)(\text{H}_2\text{O})]^{3+}$ configuration as an alternative $[(\text{OEP}^0)\text{Ru}^{\text{II}}(\text{NO}^+)(\text{H}_2\text{O})]^{3+}$. The combination of mono-oxidized porphyrin ligands with oxidized metal centers is of general interest with respect to active intermediates of heme enzymes (e.g., peroxidases).⁴⁸ Metal/porphyrin π overlap and thus partial covalency would result in shifts of both $\nu(\text{NO})$ and of porphyrin ring vibrational band

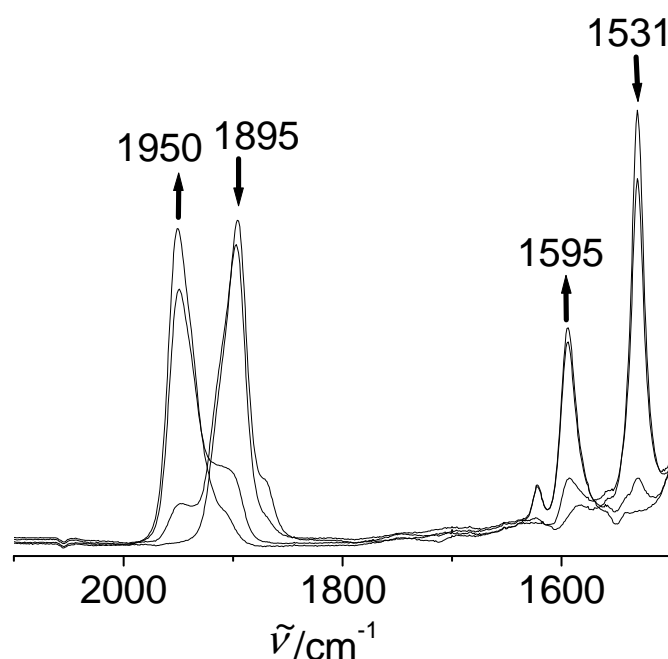


Figure 2.4.2 IR spectroelectrochemical of the conversion $[(\text{OEP})\text{Ru}(\text{NO})(\text{H}_2\text{O})]^{(2+)\rightarrow(3+)}$ in $\text{CH}_2\text{Cl}_2/0.1\text{ M } n\text{-Bu}_4\text{NClO}_4$.

The vibrational stretching band of NO shifts to lower values by a much larger amount (ca. -300 cm^{-1} for $[(\text{OEP})\text{Ru}(\text{NO})(\text{py})]^+$ during the reduction. Such large negative shifts in the

vibrational frequency of NO are typical⁵ for the reduction involving mainly electron uptake by nitrosyl based orbitals (Figure 2.4.2, Table 2.4.1). The DFT calculations indicate the formation of the typical bent Ru–N–O structure (Ru–N–O angle of 140.5° for octamethyl(OEP) complex) during the reduction accompanied by negative shifts of the calculated NO-stretching frequency by about 240 cm⁻¹.

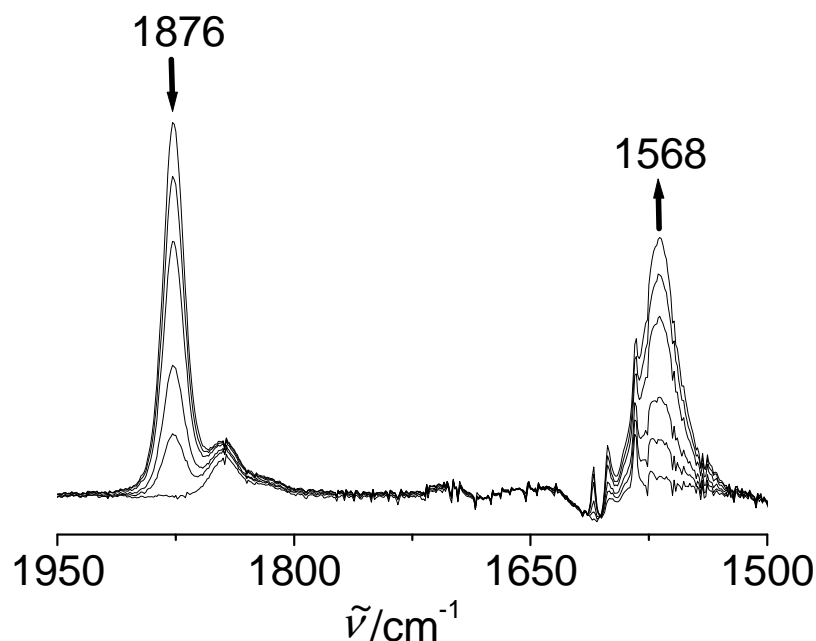


Figure 2.4.2. IR spectroelectrochemical of the conversion $[(\text{OEP})\text{Ru}(\text{NO})(\text{H}_2\text{O})]^{(+)\rightarrow(0)}$ in $\text{CH}_2\text{Cl}_2/0.1 \text{ M } n\text{-Bu}_4\text{NClO}_4$.

Table 2.4.1. Experimental and G03/BPW91-calculated NO stretching frequencies for $[(\text{OEP})\text{Ru}(\text{NO})(\text{X})]^{n+}$.

| Complexes | $n = 2$ | | $n = 1$ | | $n = 0$ | |
|---|------------------------------|------------------------------|------------------------------|------------------------------|------------------------------|------------------------------|
| | calcd. v/cm ⁻¹ | exptl. v/cm ⁻¹ | calcd. v/cm ⁻¹ | exptl. v/cm ⁻¹ | calcd. v/cm ⁻¹ | exptl. v/cm ⁻¹ |
| $[(\text{OEP})\text{Ru}(\text{NO})(\text{H}_2\text{O})]^{n+}$ | 1921 | 1895 | 1901 | 1877 | | n.o. |
| $[(\text{OEP})\text{Ru}(\text{NO})(\text{py})]^{n+}$ | | n.o. | 1901 | 1876 | 1664 | 1568 |

2.5. EPR spectroscopy

2.5.1. Theory

Electron Paramagnetic Resonance (EPR) is the ideal spectroscopic method for identification and characterization of radicals and metal-centred spin. In the present case the paramagnetic species are radical complexes where an anion radical ligand is bound to diamagnetic transition metals (Ru^{II} or Pt^{II} or Re^{I}) or metal-based paramagnetic complex with one unpaired spin. EPR gives three sources of information.

The isotropic g value: Deviations of g from the free electron value g_e can be attributed to the contribution of other excited states with non-zero angular momentum to the radical ground state. They arise from spin-orbit interactions which are proportional to the spin-orbit coupling constants of the involved atoms which increase with the atomic number as Z . The sign of the deviation is indicative of the frontier orbital situation according to Stone's approximation (Eq. 3.5.1.1.).

$$g = g_e - \frac{2}{3} \sum_i \sum_n \sum_{kj} \frac{\langle \Psi_0 | \xi_k L_{ik} \delta_k | \Psi_n \rangle \langle \Psi_n | L_{ij} \delta_j | \Psi_0 \rangle}{E_n - E_0} = g_e + \Delta g_s$$

$$g_e = 2.0023$$

Ψ_0 : MO of the unpaired electron in the ground state

Ψ_n : all other MOs

ξ_k : spin-orbit coupling constant

$L_{ik/ij}$: angular momentum operator for AO at nucleus k, j

$L_{ik} \delta_k = 0$ except at atom k

E_0 : energy of a singly occupied molecular orbital (SOMO)

E_n : energies of empty or doubly occupied molecular orbitals (LUMO or HOMO)

Considering the denominator of the equation, only the neighboring levels have a significant contribution to Δg . This means that heavy atoms which are bound near the radical center have a large effect on the g value. However, two cases are possible:

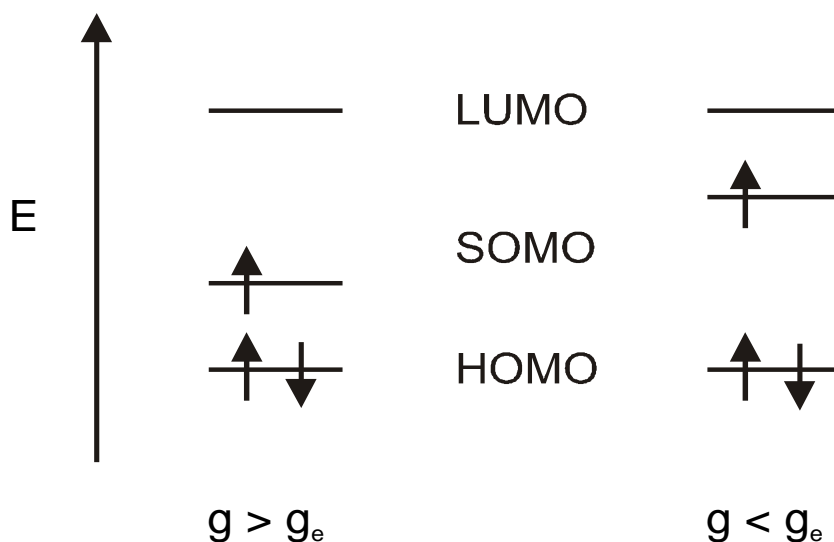


Fig. 2.5.1.1. Energy level diagram.

If $E_0 > E_n$, a deviation to higher values than g_e is to be expected. This means that the SOMO lies closer to the HOMO than to the LUMO.

If $E_0 < E_n$, the SOMO lies closer to LUMO than to the HOMO.

Even though anion radical complexes of transition metal fragments usually display rather small deviations of g_{iso} from g_e ($\Delta g_s \leq \pm 0.02$) because the spin is mainly delocalized over the light atoms from the ligand with small spin-orbit coupling constants, the characteristic changes on going from the ligand anion radical to the complexes can provide valuable information on the orbital ordering.

The g anisotropy ($\Delta g = g_1 - g_3$) from measurements of powders or glassy frozen solutions is largely a result of contributions from elements with high spin-orbit coupling constants. In the EPR spectra of transition metal complexes where the spin is predominantly on the metal centre, the g -anisotropy is usually quite large. However, in the case of transition metal complexes with anion radical ligands the g anisotropy is generally small, even in species which contain 5d metal centers like osmium or rhenium. Moreover, the broadness of the lines, sometimes in adjunction with insufficiently resolved metal hyperfine splitting, can preclude the determination of the expected g anisotropy for complexes with heavy transition metal elements at conventional EPR frequencies (X band). Thus, it is often necessary to go to high fields / high frequencies (≥ 95 GHz) to resolve it.

The hyperfine coupling between the unpaired electron and the various nuclei of the radical species is another most informative source of insight from EPR. Ideally, all nuclei with non-zero nuclear spins should couple to a certain extent with the unpaired electron and thus reveal the nature of the SOMO. Unfortunately, it is not always possible to obtain such information from conventional EPR experiments: the intrinsic line-width may be too large for the resolution of the hyperfine structure, the dominant metal hyperfine splitting can obscure the hyperfine splitting from the spin-bearing ligand atoms, and the low natural abundance and / or low nuclear magnetic moment of isotopes can lead to undetectable hyperfine coupling.

2.5.2. Results

The reversibly-obtained oxidized form $[(\text{OEP})\text{Ru}(\text{NO})(\text{H}_2\text{O})]^{2+}$ shows signal at $g_{\text{iso}} = 2.0017$ and line widths of about 25 G (Figure 2.5.2.1). Such EPR signal with $g_{\text{iso}} \approx 2.00$ and without noticeable g anisotropy in the frozen state at X-band frequency (9.5 GHz) is typical for organic radicals and here for paramagnetic species containing the spin almost exclusively in the conjugated π system of the porphyrin ring.⁴⁷ Metal based oxidation should result in rather large g anisotropy that is well detectable at X-band frequency and $g_{\text{iso}} > 2$ for a $4d^5$ (Ru^{III}) configuration because of the high SO coupling constant of Ru.¹⁵ Thus, the formation of ruthenium(III) during the first oxidation process can be excluded. No EPR signal was observed during the further oxidation to the (3^+) ion, which would be compatible with a singlet or rapidly-relaxing triplet species.

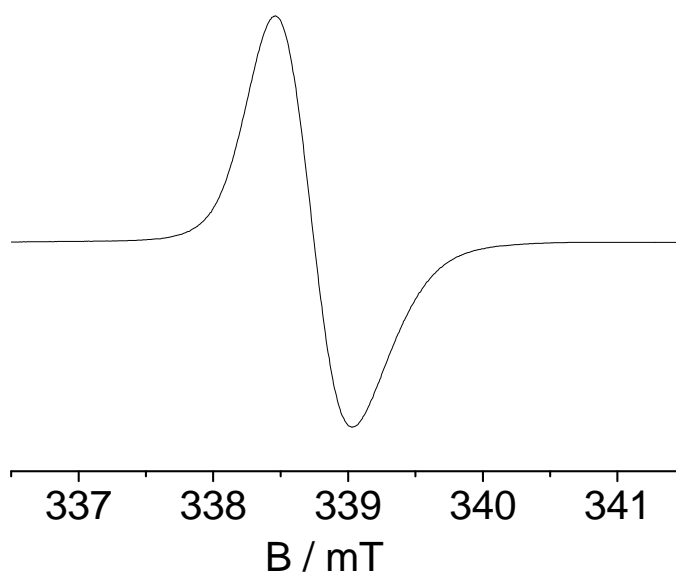


Figure 2.5.2.1. EPR spectrum of electrochemically generated $[(\text{OEP})\text{Ru}(\text{NO})(\text{H}_2\text{O})]^{2+}$ at 298 K in $\text{CH}_2\text{Cl}_2/0.1 \text{ M } n\text{-Bu}_4\text{ClO}_4$

The EPR spectrum of the obtained reduced species $[(\text{OEP})\text{Ru}(\text{NO})(\text{py})]^0$ (Figure 2.5.2.2; Table 2.5.2.1) show typically invariant EPR characteristics ($g_1 > 2$, $g_2 \approx 2.0$, $g_3 < 2$; $A_2(^{14}\text{N}) \approx 3.4$ mT) of $\{\text{RuNO}\}^7$ species that have been preciously observed for a large number of very different complexes containing RuNO where the spin densities resides mainly (ca. 70%) on the NO ligand.

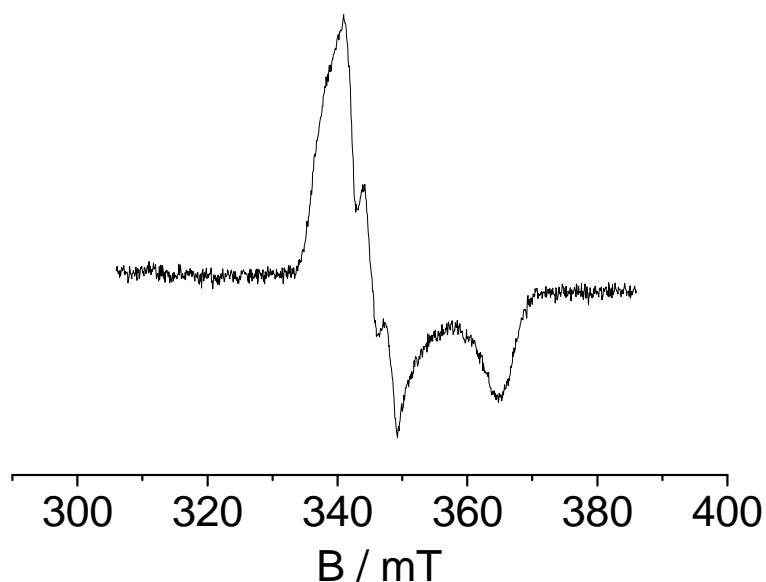


Figure 2.5.2.2. EPR spectrum of electrochemically generated $[(\text{OEP})\text{Ru}(\text{NO})(\text{py})]^0$ at 110 K in $\text{CH}_2\text{Cl}_2/0.1$ M $n\text{-Bu}_4\text{ClO}_4$.

Table 2.5.2.1. Experimental and calculated EPR parameters for $[(\text{OEP})\text{Ru}(\text{NO})(\text{X})]^0$

| ^a Axial ligand (X) | g_1 | g_2 | g_3 | $A_2(^{14}\text{N})/\text{mT}$ |
|-------------------------------|-----------------------------|-----------------------------|-----------------------------|--------------------------------|
| 4-cyanopyridine | 2.009 | 1.986 | 1.881 | 3.2 |
| pyridine | 2.007 2.028 ^b | 1.984 1.984 ^b | 1.877 1.916 ^b | 3.2 3.18 ^b |
| 4-N,N-dimethylaminopyridine | 2.017 | 1.985 | 1.872 | 3.2 |

^aIn $\text{CH}_2\text{Cl}_2/0.1$ M $n\text{-Bu}_4\text{ClO}_4$ at 110 K.

^bCalculated values for octamethylporphyrin.

2.6. UV-Vis spectroelectrochemistry

The UV-Vis absorption spectra of ruthenium nitrosyl porphyrins show blue-shifted Q band and a very sharp Soret band (Table 2.6.1), as known from a great amount of work on porphyrins and their metal complexes.^{43,49} As illustrated in Figure 2.6.1, the spectrum of oxidized $[(\text{OEP})\text{Ru}(\text{NO})(\text{H}_2\text{O})]^{(+)\rightarrow(2+)}$ displays a decrease in intensity of both the Soret and the Q band. Whereas the Soret band is only partially diminished, the Q bands at 478 nm and 573 nm decrease at the cost of new broad bands at 595 nm and 642 nm. Such changes in the absorption spectra is typical⁴⁹ for the formation of porphyrin π -radical complexes. During the second oxidation, there is a noticeable splitting of the Soret band in the UV region and the transition in the visible are diminished (Figure 2.6.2).

The observed splitting of the Soret band presumably arises from perturbed orbital degeneracy when the ligand arrangement induces a lower-than- D_{4h} symmetry (e.g., through different axial ligands); such Soret and Q-band splitting has been observed before.⁵⁰

In contrast, the UV-vis spectroelectrochemical reduction experiments for $[(\text{OEP})\text{Ru}(\text{NO})(\text{py})]^+$ (Figure 2.6.3) shows a nitrosyl-based reduction⁵ accompanied by the appearance of new bands in the visible region (Table 2.6.1), these could be due to metal-to-ligand charge transfer (MLCT) transitions $d(\text{Ru}) \rightarrow \pi^*$ and to ligand-to-ligand charge transfer process $\pi^*(\text{NO}^\bullet) \rightarrow \pi^*(\text{Por})$.

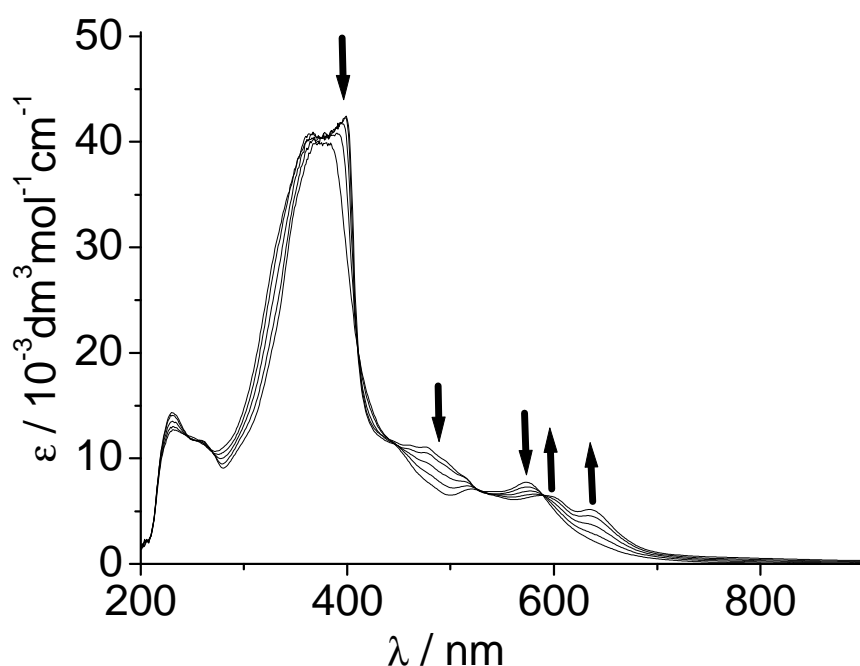


Figure 2.6.1. UV-Vis spectroelectrochemical of the conversion $[(\text{OEP})\text{Ru}(\text{NO})(\text{H}_2\text{O})]^{(+)\rightarrow(2+)}$ in $\text{CH}_2\text{Cl}_2/0.1 \text{ M } n\text{-Bu}_4\text{NClO}_4$.

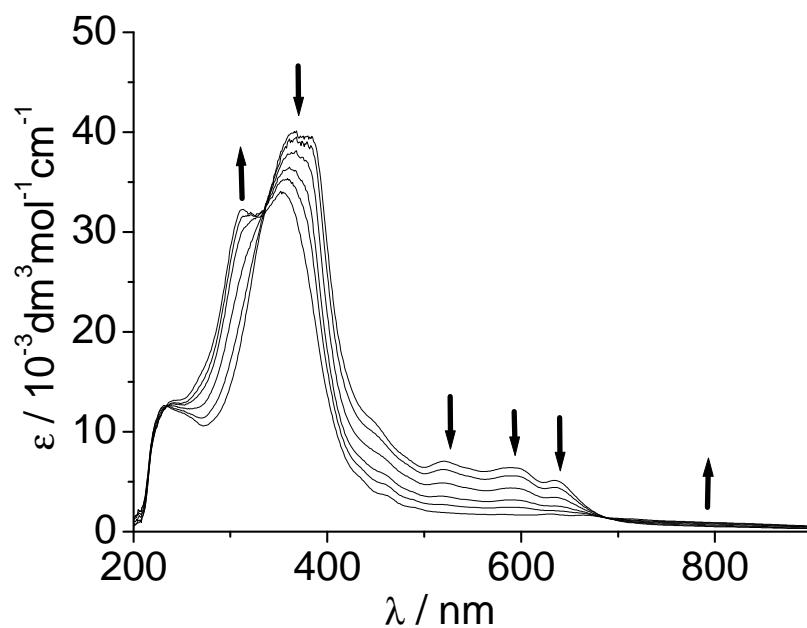


Figure 2.6.2. UV-Vis spectroelectrochemistry of the conversion $[(\text{OEP})\text{Ru}(\text{NO})(\text{H}_2\text{O})]^{(2+) \rightarrow (3+)}$ in $\text{CH}_2\text{Cl}_2/0.1 \text{ M } n\text{-Bu}_4\text{NClO}_4$

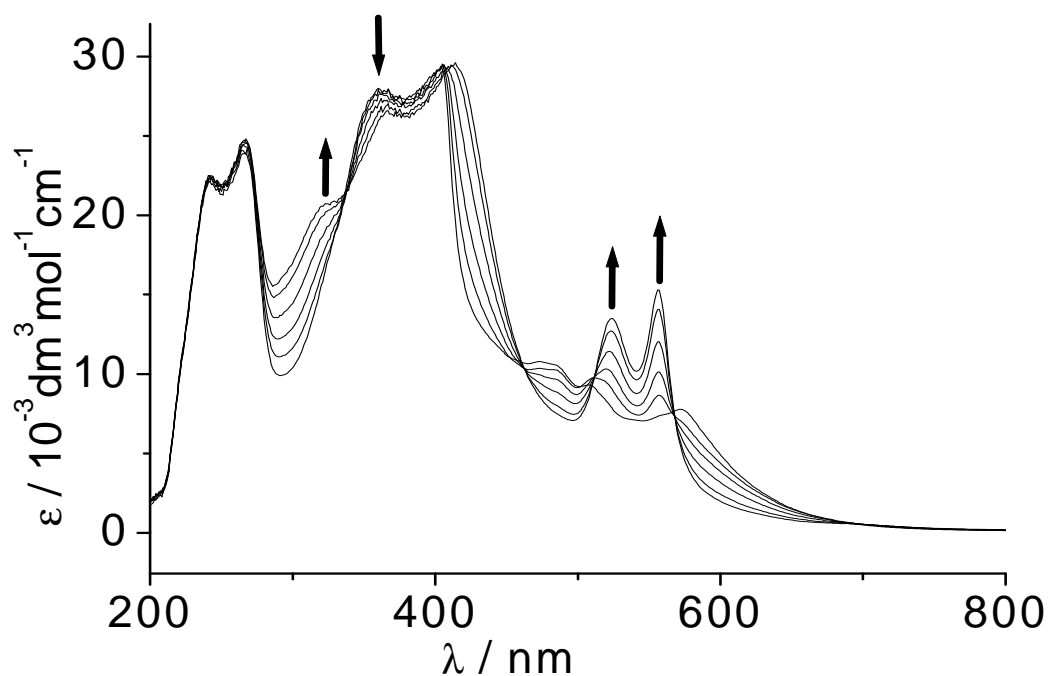


Figure 2.6.3. UV-Vis spectroelectrochemistry of the conversion $[(\text{OEP})\text{Ru}(\text{NO})(\text{py})]^{(+)\rightarrow(0)}$ in $\text{CH}_2\text{Cl}_2/0.1 \text{ M } n\text{-Bu}_4\text{NClO}_4$.

Table 2.6.1 Absorption data for [(OEP)Ru(NO)(X)]ⁿ⁺ (X = H₂O, py; n = 0,1,2).

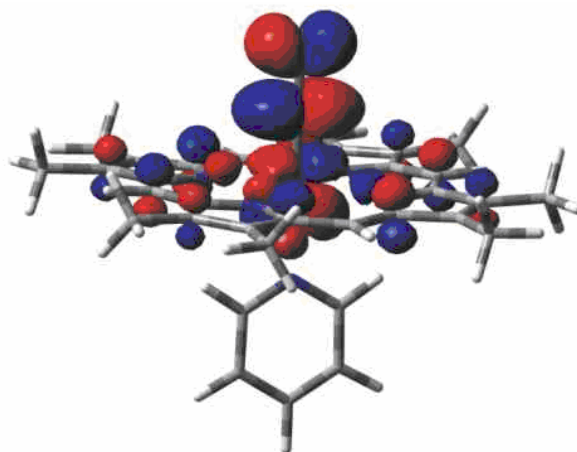
| ^a Compounds | λ/nm ($\text{dm}^3 \text{mol}^{-1} \text{cm}^{-1}$) |
|---|--|
| [(OEP)Ru(NO)(H ₂ O)] ⁺ | 370 (406000), 397 (42400), 478 (11000) |
| [(OEP)Ru(NO)(H ₂ O)] ²⁺ | 448 (11500), 574 (89800), 642 (62400) |
| [(OEP)Ru(NO)(py)] ⁺ | 266 (24000), 359 (27900), 484 (10700), 507 (9300), 573 (7800) |
| [(OEP)Ru(NO)(py)] ⁰ | 319 (20700), 362 (26400), 404 (28600)524 (13500), 557 (15400) |

^aFrom spectroelectrochemistry CH₂Cl₂/0.1 M *n*-Bu₄NClO₄.

2.7. DFT calculations

The compositions of the DFT-calculated frontier orbitals of [(OEP)Ru(NO)(H₂O)]⁺ and [(OEP)Ru(NO)(py)]⁺ complexes are listed in Tables 2.7.1 and 2.7.2. Spin density representation is shown in Figure 2.7.1.

Predominantly NO-centered reduction was observed by the large change of the NO-stretching frequency (about 300 cm⁻¹) to lower frequencies in IR-spectroelectrochemistry and from the resolved nitrogen hyperfine coupling for only one ¹⁴N nucleus in EPR spectroscopy measured in dichloromethane 0.1M Bu₄NClO₄ at 110K. DFT calculations are in good agreement with the experimental data. The set of two almost-degenerate lowest-unoccupied molecular orbitals (LUMO and LUMO+1) (Figure 2.7.2) is mainly formed by π^* orbitals of NO ligand with contributing 4d (Ru) orbitals which is supportive to the experimental results. Pyridine and H₂O do not contribute substantially to the frontier orbitals; the most significant of such an effect concerns the LUMO of [(OEP)Ru(NO)(py)]⁺ with a 5% contribution from pyridine. Accordingly, the stabilization of the reduced forms has been achieved with pyridine axial ligands.

**Figure 2.7.1.** Representation of spin densities of [(OEP)Ru(NO)(py)].

Two close lying highest-occupied orbitals (HOMO and HOMO-1) are mainly composed of π (porphyrin) orbitals. Appearance of the diagnostic porphyrin radical cation band at 1531 cm^{-1} and the very small shift of the NO stretching frequency (by about 18 cm^{-1}) after the 1st oxidation indicates that this process is porphyrin centered which is confirmed by an unresolved isotropic EPR signal ($g = 2.0017$) in dichloromethane Bu_4NClO_4 at 110K. DFT calculations found intense, almost-degenerate pairs of ring vibration bands at 1548 and 1549 cm^{-1} . The DFT-calculated EPR parameters, listed in Table 2.5.1 agree satisfactorily with the experimental data; the calculations confirm either porphyrin or NO-centered process in the course of the first oxidation or reduction, respectively (Tables 2.7.1 and 2.7.2).

DFT-calculated frontier orbital spin densities of $[(\text{OEP})\text{Ru}(\text{NO})(\text{H}_2\text{O})]^{3+}$ are presented in Figure 2.7.3. Two almost degenerate orbital HOMO and HOMO-1 orbitals are mainly composed by 4d (Ru) orbitals.

Table 2.7.1. DFT G03/PBE0-calculated one-electron energies and compositions of selected highest-occupied and lowest-unoccupied molecular orbitals of the $[(\text{OEP})\text{Ru}(\text{NO})(\text{H}_2\text{O})]^+$

| MO | E (eV) | Prevailing character | Ru | NO | porph | H ₂ O |
|------------|--------|----------------------|----|----|-------|------------------|
| Unoccupied | - | | | | | |
| LUMO+3 | -4.95 | π^* porph + Ru | 10 | 13 | 77 | 0 |
| LUMO+2 | -4.96 | π^* porph + Ru | 10 | 12 | 78 | 0 |
| LUMO+1 | -5.47 | π^* NO + Ru | 19 | 54 | 27 | 0 |
| LUMO | -5.49 | π^* NO + Ru | 19 | 55 | 26 | 0 |
| Occupied | | | | | | |
| HOMO | -8.26 | π porph | 0 | 0 | 100 | 0 |
| HOMO-1 | -8.52 | π porph | 1 | 0 | 98 | 1 |
| HOMO-2 | -9.26 | π porph | 4 | 6 | 90 | 0 |
| HOMO-3 | -9.26 | π porph | 4 | 6 | 90 | 0 |

Table 2.7.2. DFT G03/PBE0-calculated one-electron energies and compositions of selected highest-occupied and lowest-unoccupied molecular orbitals of the $[(\text{OEP})\text{Ru}(\text{NO})(\text{py})]^+$.

| MO | E (eV) | Prevailing character | Ru | NO | porph | Py |
|------------|--------|----------------------|----|----|-------|----|
| Unoccupied | - | | | | | |
| LUMO+3 | -4.75 | π^* porph + Ru | 7 | 7 | 85 | 1 |
| LUMO+2 | -4.75 | π^* porph + Ru | 9 | 10 | 81 | 0 |
| LUMO+1 | -5.33 | π^* NO + Ru | 20 | 58 | 22 | 0 |
| LUMO | -5.36 | π^* NO + Ru | 19 | 57 | 18 | 5 |
| Occupied | | | | | | |
| HOMO | -8.05 | π porph | 0 | 0 | 100 | 0 |
| HOMO-1 | -8.27 | π porph | 1 | 0 | 98 | 1 |
| HOMO-2 | -9.01 | π porph | 5 | 6 | 89 | 0 |
| HOMO-3 | -9.01 | π porph | 5 | 7 | 88 | 0 |

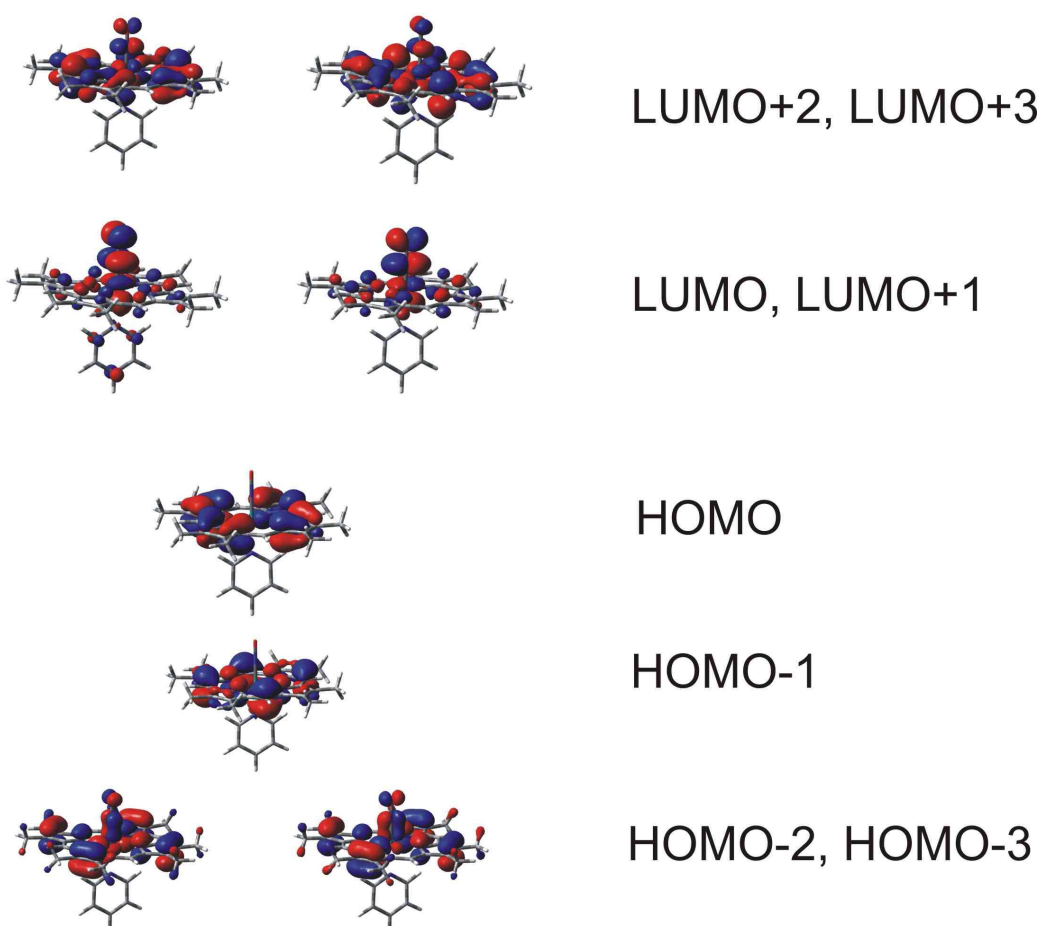


Figure 2.7.2. The representation of frontier molecular orbitals of $[(\text{OMP})\text{Ru}(\text{NO})(\text{py})]^+$ complex..

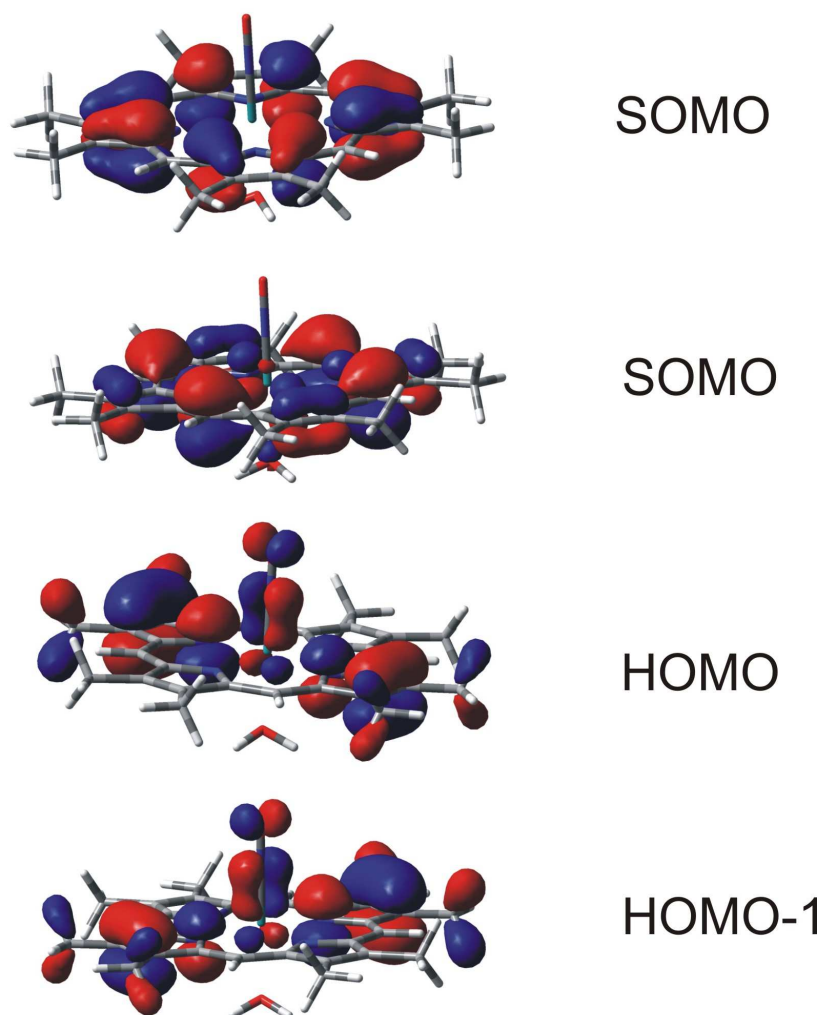


Fig. 2.7.3. Frontier orbitals of $[(\text{OMP})\text{Ru}(\text{NO})(\text{H}_2\text{O})]^{3+}$ from UKS G03/BPW91 calculations. Only the α parts of the UKS MOs are depicted, the shapes of the β orbitals are qualitatively the same.

2.8. Conclusion

Experimental and computational results for $[(\text{OEP})\text{Ru}(\text{NO})(\text{X})]^{n+}$ ($n = 1, 0, -1$, OEP = octaethylporphyrinatodianion) with varying ligands X (H_2O , pyridine, 4-Cyanopyridine, 4-*N,N*-dimethylaminopyridine) are studied with respect to their electron-transfer behavior. For that different spectroscopic techniques such as IR and UV-Vis spectroelectrochemistry and EPR spectroscopy have been imposed and finally, the electronic structure has been rationalized through DFT calculations. Except for the redox potentials, the differences among complexes involving different pyridine ligands have been small. The complex containing X as a neutral O-donor aqua ligand show a two step oxidation and those X as neutral N-donor pyridine ligand show a reversible reduction. Predominantly NO-centered reduction was observed by the large change of the NO-stretching frequency (about 300 cm^{-1}) to lower frequencies in IR-spectroelectrochemistry and from the resolved nitrogen hyperfine coupling for only one ^{14}N nucleus in EPR spectroscopy measured in dichloromethane $0.1\text{M } n\text{-Bu}_4\text{NClO}_4$ at 110K . The EPR response of NO^\bullet complexes was essentially unaffected by the variation in the substituent pyridine. Spectroelectrochemical measurements indicate that the first oxidation occurs on the porphyrin ring, as evident from the appearance from the diagnostic porphyrin radical cation band at 1531 cm^{-1} , the very small shift of the NO stretching frequency (by about 20 cm^{-1}) and from the EPR signal at $g_{\text{iso}} \approx 2.00$. This is then followed by a metal involving second oxidation according to the observed $\Delta\nu(\text{NO})$ shift of about 55 cm^{-1} . DFT calculations support the interpretation of the experimental results because the HOMO of $[(\text{OEP})\text{Ru}(\text{NO})(\text{H}_2\text{O})]^+$, where X = H_2O or pyridines, was calculated to be centered at the porphyrin π system, whereas the LUMO of $[(\text{OEP})\text{Ru}(\text{NO})(\text{X})]^+$ has about 50% $\pi^*(\text{NO})$ character. This confirms that the (first) oxidation of $[(\text{OEP})\text{Ru}(\text{NO})(\text{H}_2\text{O})]^+$ occurs on the porphyrin ring whereas the reduction of $[(\text{OEP})\text{Ru}(\text{NO})(\text{X})]^+$ is largely NO centered with the metal remaining in the low-spin ruthenium(II) state throughout.

CHAPTER 3

An Oxo-Bridged Dirhenium Dinitrosyl Complex with Cyanide as Co-ligands

3.1. Introduction

The chemistry of transition metal–NO complexes has gained on added significance³ in recent years because of the important role that nitric oxide has been found to play in several physiological processes.¹¹ A variety of metal-nitrosyl complexes has also been explored in recent years as possible agent.^{51,52} The oldest such therapeutic compounds have been salts of the nitroprusside dianion $[(\text{CN})_5\text{Fe}(\text{NO})]^{2-}$ which serve as directly active hypotensive agents.³ Nitric oxide NO ,^{4,5} is known as a typical non-innocent ligand ($\text{NO}^+/\text{NO}^\bullet/\text{NO}^-$)⁸ and the stability of particular redox states in a complex is essentially depending on the electronic nature of the coligands associated with the metal nitrosyl fragment.

In this Chapter a newly synthesized oxo-bridged dirhenium dinitrosyl complex (Figure 3.1.1) with cyanide as co-ligands is presented. Among the cyanonitrosyl complexes of transition metal ions, the rhenium derivatives are controversial.⁵³ There were considerable differences in opinions reported about their correct oxidation state formulation. The newly synthesized complex was crystallized for X-ray diffraction analysis and the redox property has also been studied by cyclic voltammetry, IR spectroelectrochemistry and EPR spectroscopy.

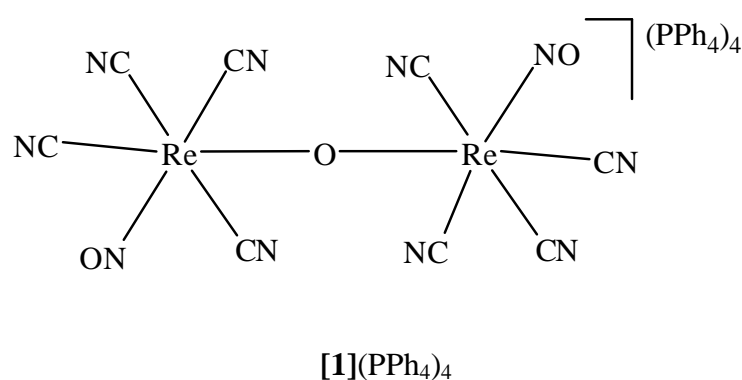
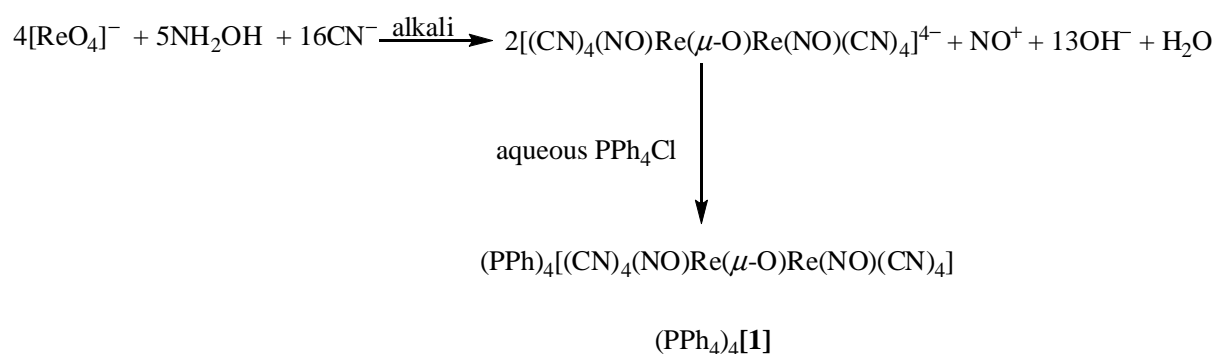


Figure 3.1.1. Molecular formula of $(\text{PPh}_4)_4[(\text{CN})_4(\text{NO})\text{Re}(\mu\text{-O})\text{Re}(\text{NO})(\text{CN})_4]$.

3.2. Synthesis and characterization

Complex $(\text{PPh}_4)_4[\mathbf{1}]$ was synthesized by the reaction of KReO_4 with excess CN^- and NH_2OH in the presence of excess KOH as a base in hot water (*ca.* 90 °C). The $[\text{ReO}_4]^-$ was reductively nitrosylated to generate the $\{\text{Re}(\text{NO})\}^{3+}$ moiety. A cation exchange has been performed, adding a saturated aqueous solution of Ph_4PCl into an aqueous solution of $\text{K}_4[(\text{CN})_4(\text{NO})\text{Re}(\mu\text{-O})\text{Re}(\text{NO})(\text{CN})_4]$. A deep purple solid material corresponding to the $(\text{PPh}_4)_4[\mathbf{1}]$ was separated and recrystallized from acetonitrile/diethylether solution which yielded analytically pure $(\text{PPh}_4)_4[\mathbf{1}]$ in 5% yield.



Scheme 3.2.1. Reaction scheme for the synthesis of $(\text{PPh}_4)_4[\mathbf{1}]$.

3.3. Crystal structure

Single crystals of $(\text{PPh}_4)_4[\mathbf{1}] \cdot 4(\text{CH}_2\text{Cl}_2)$ were obtained by slow diffusion of n-hexane into a dichloromethane solution of $(\text{PPh}_4)_4[\mathbf{1}]$ at room temperature. Crystallographic data are summarized in chapter 9.5.1. The molecular structure of the complex is shown in Figure 3.3.1. Selected bond lengths and angles are listed in Table 3.3.1.

The geometry around each rhenium center can be described as distorted octahedral with the NO and O ligands in *cis* position. The oxo atom holds an inversion center. Both the Re atoms are displaced from the $(3\text{CN},\text{O})$ plane towards the nitrosyl N atom by 0.173 Å. The Re–C bond lengths [2.098(8)–2.162(8)] are comparable with the corresponding values reported for related rhenium-nitrosyl complexes.⁵⁵ The bond angle of the Re–N–O moiety is 175.9(6)°, and the N–O and Re–N(O) bond lengths are 1.189(8) and 1.810(7) respectively. The values confirm a the linear coordination of the nitrosyl ligands and they are comparable with values previously found for $[\text{Re}(\text{NO})(\text{CN})]^{2-}$.⁵⁵ Thus a oxidation state assignment $[(\text{CN})_4(\text{NO}^+)\text{Re}^{\text{II}}(\mu\text{-O})\text{Re}^{\text{II}}(\text{NO}^+)(\text{CN})_4]^{4-}$ can be made, based on these structural parameters. The result suggests a $\{\text{Re}(\text{NO})\}^5$ moiety according to the Enemark-Feltham notation.⁴ The

metal–cyano bond length (Re–C4) *trans* to the nitrosyl is significantly longer [2.162(8)] than the average rhenium–cyano bond length [2.098(8)] *cis* to the nitrosyl group.

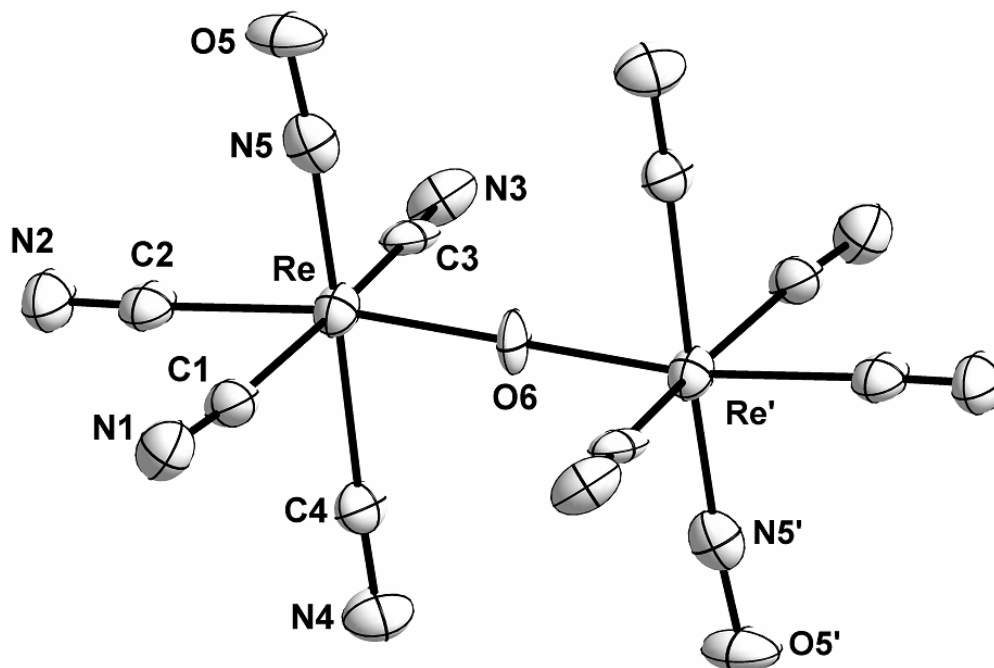


Figure 3.3.1. Molecular structure of $[1]^{4-}$ in the crystal of $[PPh_4]_4[1] \cdot 4(CH_2Cl_2)$.

Table 3.3.1. Selected bond lengths (Å) and angles (°) for the complex $[PPh_4]_4[1] \cdot 4(CH_2Cl_2)$

| | | | |
|---------|-----------|--------------|-----------|
| C1 – N1 | 1.156(10) | Re – C4 – N4 | 177.2(79) |
| C2 – N2 | 1.149(10) | C2 – Re – O6 | 168.0(2) |
| C3 – N3 | 1.143(9) | C1 – Re – C3 | 1687.8(3) |
| C4 – N4 | 1.154(9) | Re – C4 – N4 | 177.2(7) |
| N5 – O5 | 1.189(8) | N5 – Re – C1 | 92.3(3) |
| Re – C1 | 2.115(8) | Re – O – Re | 180.0 |
| Re – C2 | 2.129(8) | N5 – Re – C2 | 92.4(3) |
| Re – C3 | 2.098(8) | C4 – Re – O6 | 83.4(2) |
| Re – C4 | 2.162(8) | C4 – Re – C1 | 88.1(3) |
| Re – N5 | 1.810(7) | C4 – Re – C2 | 85.4(3) |

| | | | |
|--------------|-----------|--------------|----------|
| Re–O6 | 1.8915(4) | C4 – Re – C3 | 85.2(3) |
| Re – N5 – O5 | 175.9(6) | Re – C2 – N2 | 176.4(8) |
| Re – C1 – N1 | 174.7(4) | Re – C3 – N3 | 176.0(7) |

3.4. Electrochemistry

The redox behaviour of $(\text{PPh}_4)_4[\mathbf{1}]$ has been investigated by cyclic voltammetry in acetonitrile containing 0.1 M Bu_4NPF_6 as the supporting electrolyte. The results are summarized in Table 3.4.1.

Within the potential limit of the CH_3CN solvent the complex $(\text{PPh}_4)_4[\mathbf{1}]$ displays an irreversible reduction and one reversible one-electron oxidation followed by an irreversible oxidation. The potentials are $E_{\text{pc}} = -1.92$ V, $E_{1/2} = +0.05$ V and $E_{\text{pa}} = +0.51$ V vs $\text{Fc}^{+/0}$, respectively, as shown in Figure 3.4.1. The site of reversible oxidation has been probed by IR spectroelectrochemistry and EPR spectroscopy. The negative values for the reduction of $(\text{PPh}_4)_4[\mathbf{1}]$ compared with the mononuclear complex⁵⁵ $[(\text{CN})_5\text{Re}(\text{NO})]^{2-}$ ($E_{1/2} = -0.79$ V vs $\text{Fc}^{+/0}$) is consistent with the greater electron density in the oxo-bridged compound. The reduction process is probably followed by a chemical decomposition, making it irreversible. A similar pattern of reduction has been reported for oxo-bridged ruthenium complexes such as $\{(\mu\text{-O})[\text{RuX}(\text{bpy})_2]_2\}^{2+}$.⁵⁷

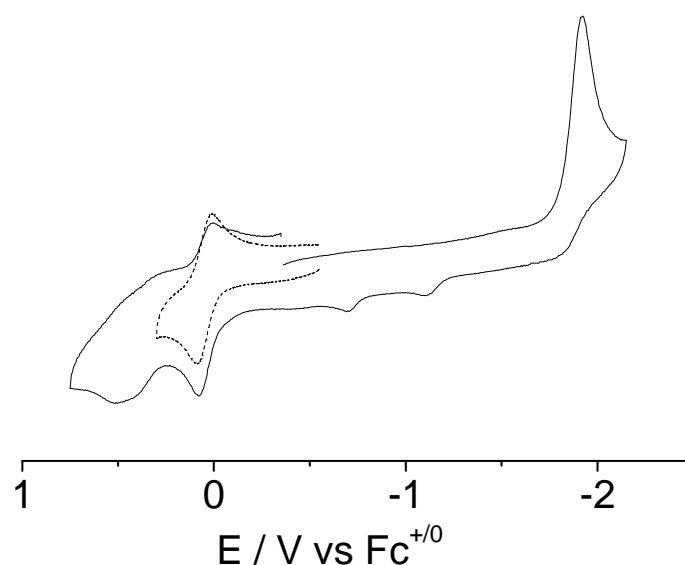


Figure 3.4.1. Cyclic voltammograms of $(\text{PPh}_4)_4[\mathbf{1}]$ in $\text{CH}_3\text{CN}/0.1$ M Bu_4NPF_6 at 100 mV/s scan rate.

3.5. IR spectroelectrochemistry

With *cis* oxo and nitrosyl vs four cyanide ligands there seems to be an approximate C_{2v} spectroscopic symmetry and it would be expected four cyanide stretching bands. The IR spectrum of $(PPh_4)_4[1]$ exhibits two cyanide bands at 2118 and 2129 cm^{-1} , with two bands overlapped. The complex shows two $\nu(\text{NO})$ vibrational bands at 1710 and 1670 cm^{-1} . The $\nu(\text{NO})$ frequency at 1710 cm^{-1} is comparable with that of the mono-nitrosyl $[\text{Re}(\text{NO})(\text{CN})_5]^{2-}$ (1700 cm^{-1})⁵⁵ and to those of other formally reported $[\text{Re}(\text{NO})\text{Cl}_5]^{2-}$ (1718 cm^{-1}) and $[\text{Re}(\text{NO})\text{Br}_5]^{2-}$ (1734 cm^{-1}) complexes.⁵⁸ The $\nu(\text{NO})$ of $(PPh_4)_4[1]$ is considerably lower in comparison with $[\text{M}(\text{NO})(\text{CN})_5]^{2-}$ ($\text{M} = \text{Fe}, \text{Ru}, \text{Os}$).⁵⁹ This indicates a large contribution of electronic back-donation from the Re atom to the $\pi^*_{(\text{NO})}$ orbitals.

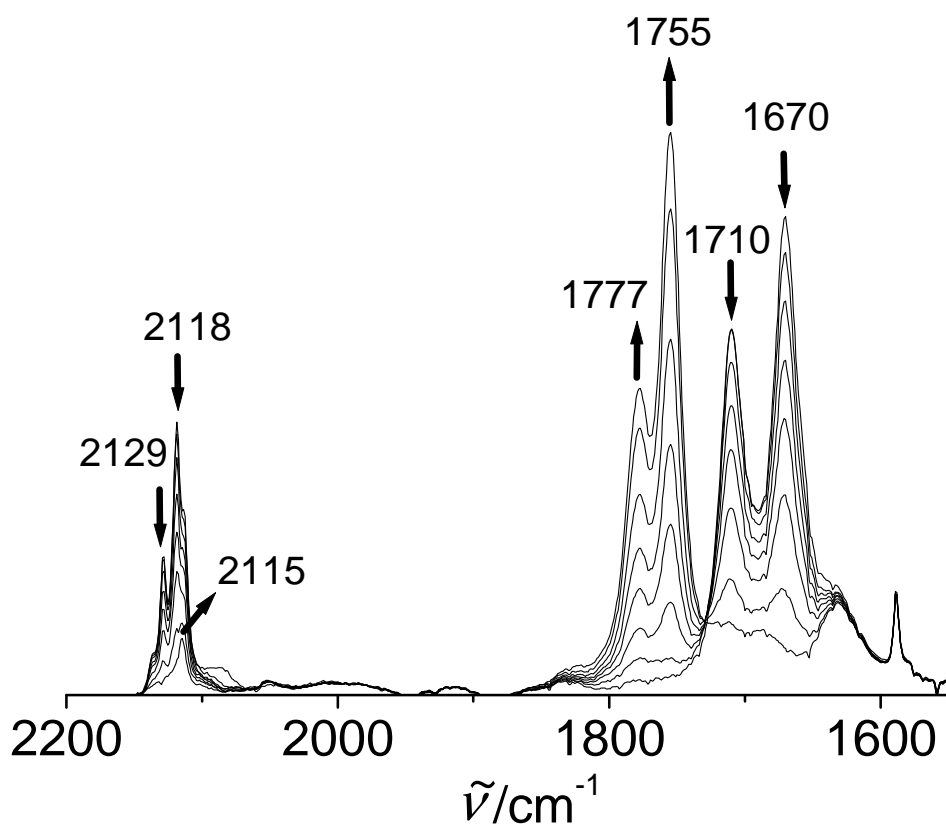


Figure 3.5.1. IR spectroelectrochemistry of the conversion $[1]^{(4-)} \rightarrow (3-)$ in $\text{CH}_3\text{CN}/0.1 \text{ M Bu}_4\text{NPF}_6$.

IR spectroelectrochemistry using an OTTLE cell⁶⁶ was applied to investigate the location of reversible oxidation. The nitrosyl stretching bands of the complex $(PPh_4)_4[1]$ were monitored. The obtained spectra are shown in Figure 3.5.1 and data are summarized in Table 3.5.1. The oxidation of the complex causes comparatively small positive shifts of $\nu(\text{NO})$ from 1710 cm^{-1}

to 1777 cm^{-1} and 1670 cm^{-1} to 1755 cm^{-1} , suggesting that the oxidation does not occur on NO but on the Re(II) center.

3.6. EPR spectroscopy

The reversible oxidation process is monitored by generating odd electron species in situ electrolysis for EPR spectroscopy. The EPR spectrum of $[\mathbf{1}]^{3-}$ in $\text{CH}_3\text{CN}/0.1\text{ M Bu}_4\text{NPF}_6$ at 100 K is shown in Figure 3.6.1. A complex pattern is observed that is indicative of hyperfine coupling to the ^{185}Re and ^{187}Re ($I = 5/2$) nuclei. The spectrum is centered at 312 mT. Given the complexity of the spectrum, exact g_{\perp} and g_{\parallel} values were not able to be determined.

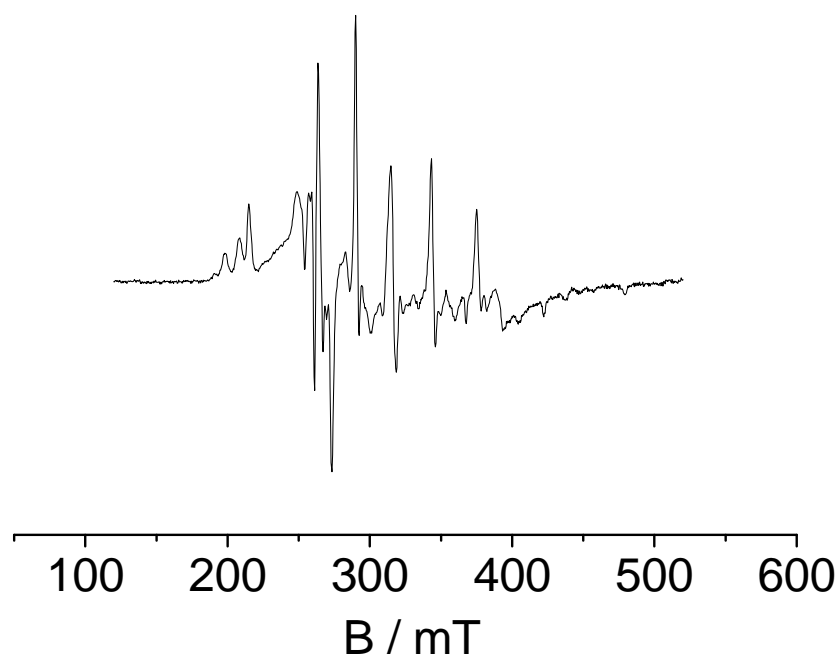


Figure 3.6.1. EPR spectrum of electrogenerated $[\mathbf{1}]^{3-}$ at 110 K in $\text{CH}_3\text{CN}/0.1\text{ M Bu}_4\text{NPF}_6$.

3.7. Conclusion and outlook

Oxo-bridged rhenium nitrosyl complex with cyanide as a co-ligand is synthesized by reductive nitrosylation of ReO_4^- in aqueous alkaline medium by $\text{NH}_2\text{OH}\cdot\text{HCl}$. The complex has been structurally and spectroscopically characterized. The complex exhibits two sharp $\nu(\text{NO})$ at 1710 and 1670 cm^{-1} and two sharp $\nu(\text{CN})$ band at 2118 and 2129 cm^{-1} in CH_3CN . Crystal structure analysis confirms the linear coordination of both the nitrosyl group. The Re–N and N–O bond lengths and $\nu(\text{NO})$ indicate a strong back-donation of electron density from the filled rhenium d orbitals into the π^* antibonding orbital of the NO group. A oxidation state

assignment $[(\text{CN})_4(\text{NO}^+)\text{Re}^{\text{II}}(\mu\text{-O})\text{Re}^{\text{II}}(\text{NO}^+)(\text{CN})_4]^{4-}$ can be made based on the obtained structural data which are comparable with values previously found.⁵⁶ Cyclic voltammetry exhibits one irreversible reduction and one reversible oxidation followed by an irreversible process. Marginal positive shifts of $\nu(\text{NO})$ 1710 cm^{-1} to 1777 cm^{-1} and 1670 cm^{-1} to 1755 cm^{-1} suggests that the oxidation does not occur on NO but on the Re(II) center. Detailed EPR investigation and DFT studies would be helpful to understand the exact spin location of this system. The interaction between two Re(II) center can be examined by studying the magnetic susceptibility measurements. The work can be further extended by changing the bridge to sulfur.

CHAPTER 4

Ruthenium Complexes with a Non-Innocent *o*-Iminobenzoquinone Ligand

4.1. Introduction

It is well established that *O,N*-coordinating *o*-aminophenolate ligands^{32,35,60} are non-innocent in the sense that they can be bound to a transition metal ion either as an *o*-aminophenolate monoanion (HQ^-) or *o*-iminophenolate dianion (Q^{2-}), as one-electron oxidized *o*-iminobenzosemiquinonate π radical mono-anion ($Q^{\bullet-}$) or as two-electron oxidized benzoquinone (Q^0) (Figure 4.1.1). The radical mono-anion ($Q^{\bullet-}$) is a redox form found in many cases.³²

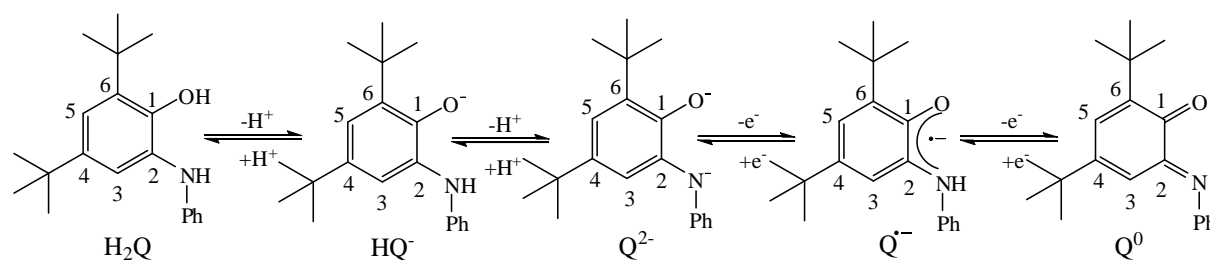


Figure 4.1.1. Different redox forms of 4,6-di-*tert*-butyl-*N*-phenyl-*o*-iminobenzoquinone Q^n .

Table 4.1.1. Average bond lengths for redox forms of 4,6-di-*tert*-butyl-*N*-phenyl-*o*-iminobenzoquinone Q^n .^{35,61}

| Bond lengths (Å) | | | | | | |
|------------------|------|------|-------|-------|-------|-------|
| | C–O | C–N | C1–C2 | C2–C3 | C3–C4 | C4–C5 |
| Q^0 | 1.24 | 1.30 | 1.52 | 1.44 | 1.36 | 1.46 |
| $Q^{\bullet-}$ | 1.30 | 1.35 | 1.46 | 1.43 | 1.37 | 1.43 |
| Q^{2-} | 1.35 | 1.37 | 1.42 | 1.40 | 1.40 | 1.41 |

Clear differences in the C–O, C–N, and ring C–C bond lengths³⁵ are diagnostic of the individual redox forms (Table 4.1.1). The proper determination of the electronic structure of transition metal complexes with non-innocent ligands requires structural identification and an array of spectroscopic techniques³⁵⁻³⁵. In contrast to most 1,2-dioxolene and *o*-iminoquinone complexes of the first row transition metals, the 4d element ruthenium was early shown to

exhibit less unambiguous oxidation state situations, in agreement with the notion of mixed ligand π /metal d orbitals.^{60,62}

This Chapter presents the results obtained from four ruthenium *o*-iminobenzoquinone-Cl⁻ / NO₂⁻ complexes with two different meridional tridentate ligands terpy = 2,2':6,2''-terpyridine or tppz = 2,3,5,6-tetrakis(2-pyridyl)pyrazine as the ancillary ligands. The four complexes [(terpy)Ru(Q)Cl]ⁿ⁺, [(terpy)Ru(Q)(NO₂)]ⁿ⁺, [(tppz)Ru(Q)Cl]ⁿ⁺ and [(tppz)Ru(Q)(NO₂)]ⁿ⁺ were isolated in the monocationic form and all of these were crystallographically characterized.

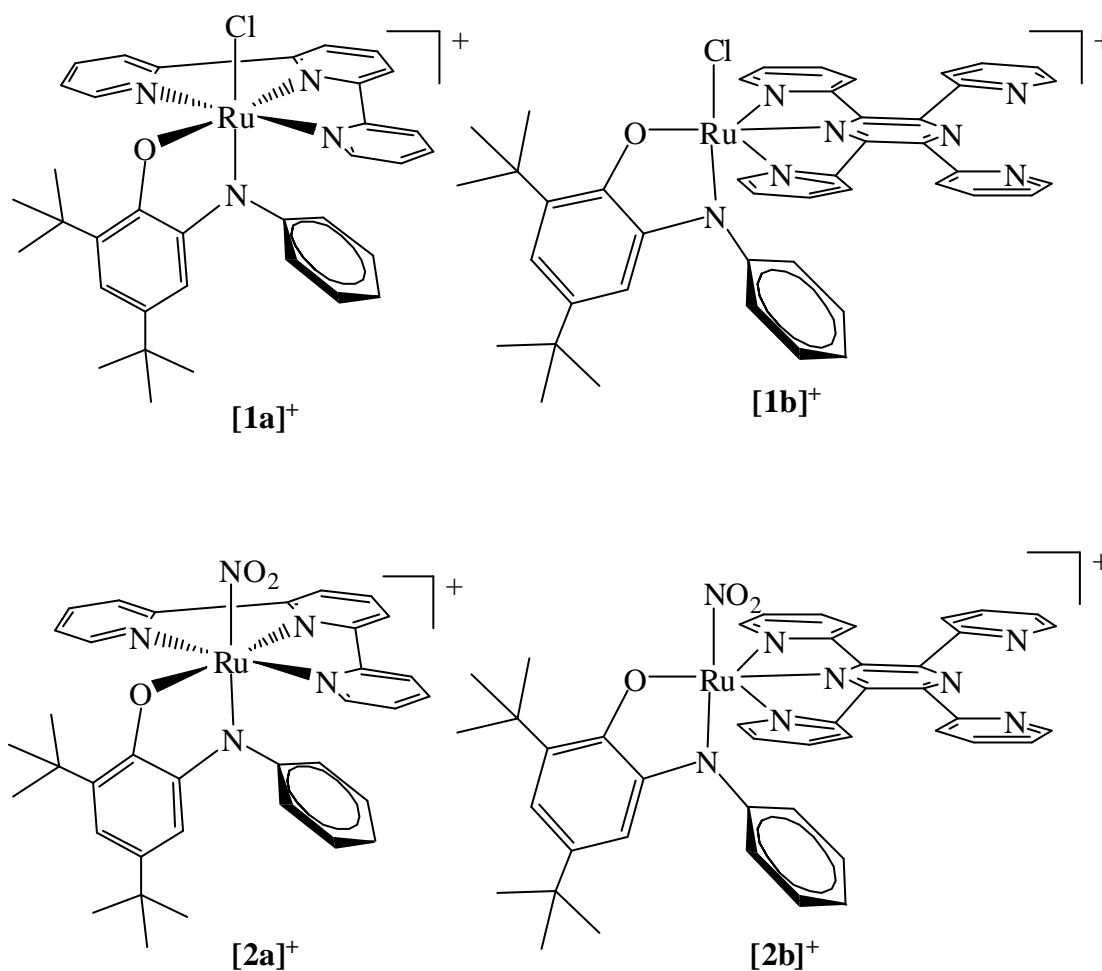


Figure 4.1.2. Molecular formulae of the complexes.

In all four complexes the C–O, C–N and intra-ring C–C bond distances obtained from the single crystal X-ray data have been imposed to formulate the valence state distribution in the isolated form. Table 4.1.1 has shown the bond distances expected for different oxidation levels. Electrochemical and spectroelectrochemical (UV-Vis-NIR and EPR) studies of the

redox systems $[(\text{terpy})\text{Ru}(\text{Q})(\text{Cl})]^{n+}$, $[(\text{tppz})\text{Ru}(\text{Q})(\text{Cl})]^{n+}$, $n = -1, 0, +1, +2$ and $[(\text{terpy})\text{Ru}(\text{Q})(\text{NO}_2)]^{n+}$, $[(\text{tppz})\text{Ru}(\text{Q})(\text{NO}_2)]^{n+}$, $n = -1, 0, +1$ have been performed to establish the appropriate oxidation state formulation.

4.2. Syntheses and characterization

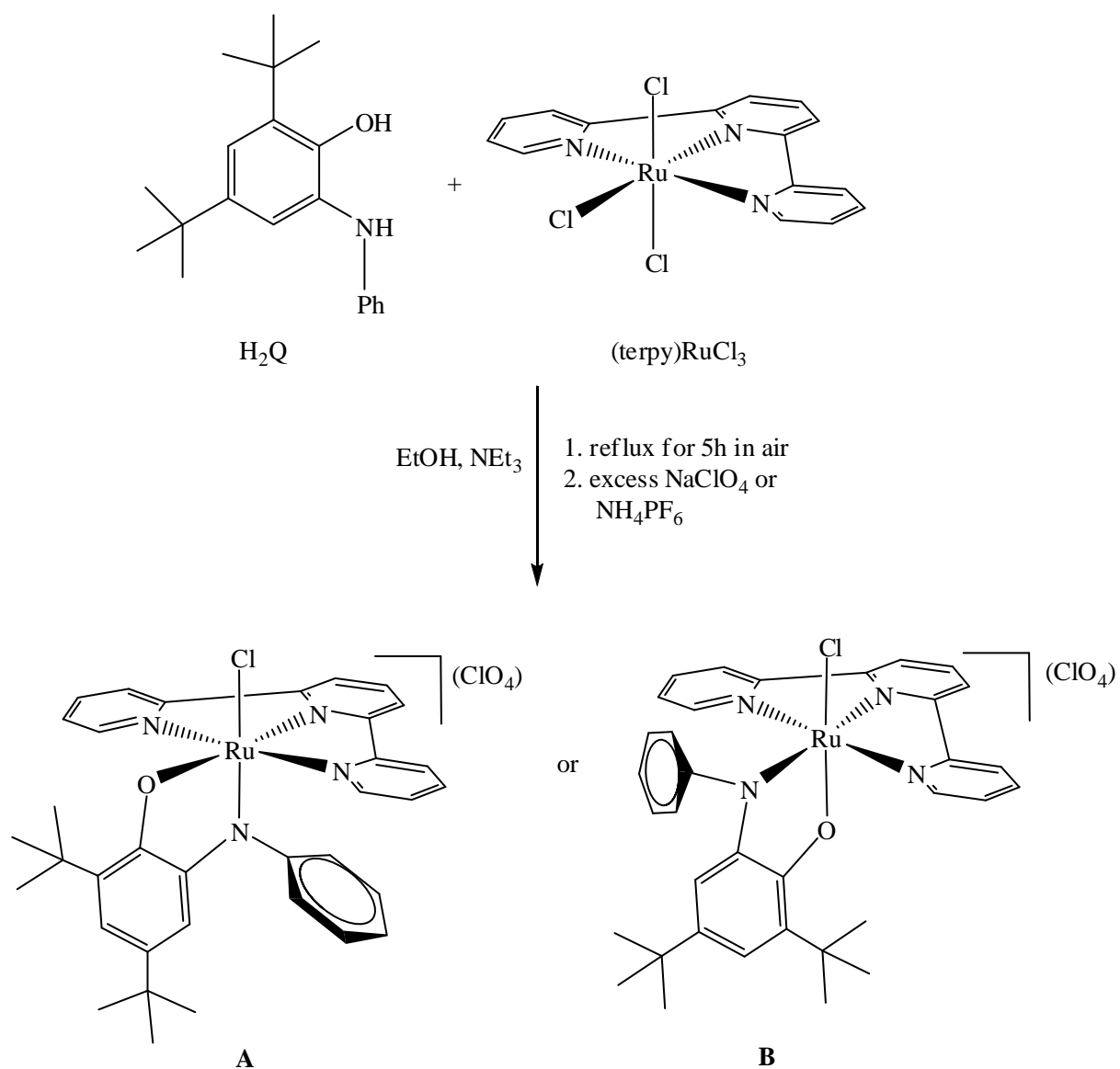
The protonated form, 2-anilino-4,6-di-*tert*-butylphenol³³ (H_2Q) of ligand, is readily available in good yield from the reaction of 3,5-di-*tert*-butylcatechol and aniline in *n*-heptane in the presence of air and the base triethylamine.

4.2.1. The chloro complexes $[\mathbf{1a}](\text{ClO}_4)$ and $[\mathbf{1b}](\text{PF}_6)$

The diamagnetic chloro complexes $[(\text{terpy})\text{Ru}(\text{Q})(\text{Cl})](\text{ClO}_4)$ $[\mathbf{1a}](\text{ClO}_4)$ was prepared by the reaction of $[(\text{terpy})\text{RuCl}_3]^{73}$ with H_2Q (Scheme 4.2.1), in the presence of NEt_3 as a base in refluxing ethanol in air, followed by chromatographic purification on a neutral alumina column.

Reaction of $[\text{Cl}_3\text{Ru}(\mu\text{-tppz})\text{RuCl}_3]$ with H_2Q , in the presence of excess LiCl and CH_3COONa as a base in refluxing ethanol under atmospheric condition even in a molar ratio (1:1) or a short reaction time, resulted a mixture of mononuclear and dinuclear complex. Mononuclear complex $[(\text{tppz})\text{Ru}(\text{Q})(\text{Cl})](\text{PF}_6)$ $[\mathbf{1b}](\text{PF}_6)$ was purified by column chromatography using a neutral alumina column. It could be the reason that, partial dissociation on the column or incomplete conversion has produced the mononuclear complex.

The complexes were characterized by $^1\text{H-NMR}$, electrospray mass spectroscopy and elemental analysis. Figure 4.2.1 shows the $^1\text{H-NMR}$ spectrum of $[\mathbf{1a}](\text{ClO}_4)$. The unsymmetrical ligand Q in combination with meridional configuration of terpy in $[\mathbf{1a}]^+$ is expected to give rise to an isomeric mixture of A and B (Scheme 4.2.1). Only one set of signals, one doublet $[(\delta = 5.87, \text{d}, J = 7.32 \text{ Hz}, 2\text{H})]$ and two triplets $[(\delta = 7.16, \text{t}, J = 7.5 \text{ Hz}, 1\text{H})]$ and $[(\delta = 6.97, \text{t}, J = 7.42 \text{ Hz}, 2\text{H})]$ from N-Ph component in the $^1\text{H NMR}$ spectrum clearly indicates exclusive formation of only one isomer. It is difficult to assign either the A or B configuration, based on $^1\text{H NMR}$ data. However preferential crystallization of isomer A was confirmed by its crystal structure analysis (Figure 4.3.1). Similar $^1\text{H-NMR}$ spectral features of $[\mathbf{1b}](\text{PF}_6)$, $[\mathbf{2a}](\text{ClO}_4)$ (Figure 4.2.2) and $[\mathbf{2b}](\text{PF}_6)$ indicate exclusive formation of one isomer which is further confirmed by crystal structures analysis showing the isomer A (Figure 4.3.1-4).



Scheme 4.2.1. Reaction scheme for the synthesis of $[(\text{L})\text{Ru}(\text{Q})(\text{Cl})]^+$, shown here by example of $\text{L} = \text{terpy}$ as a meridional tridentate ligand.

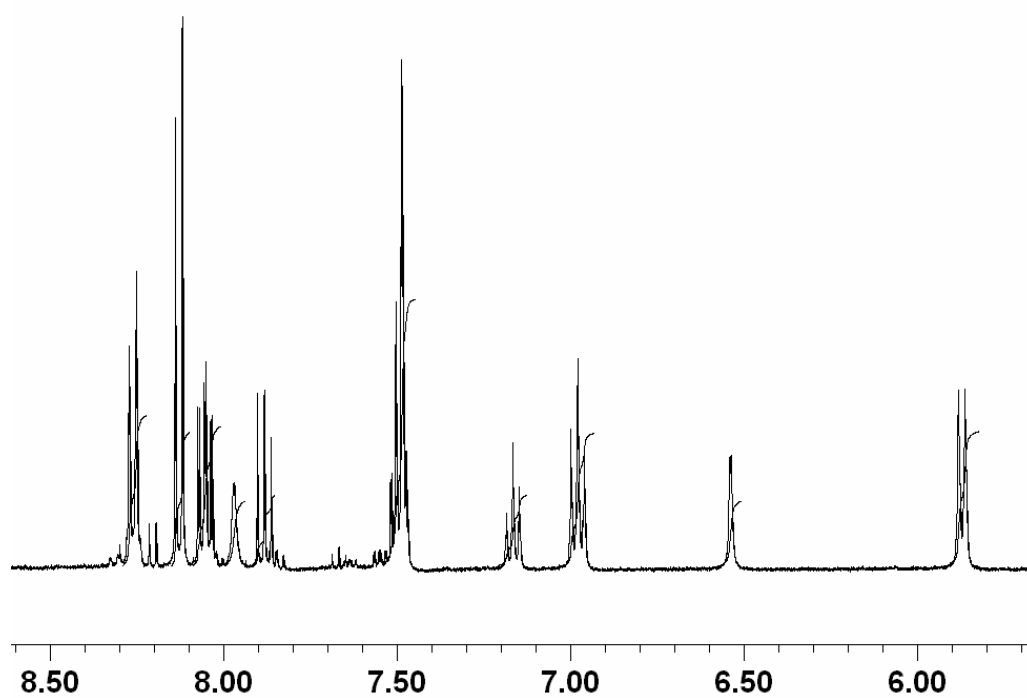


Figure 4.2.1. $^1\text{H-NMR}$ spectrum (only aromatic region) of the complex **[1a]**(ClO_4) in CD_3CN at 400 MHz.

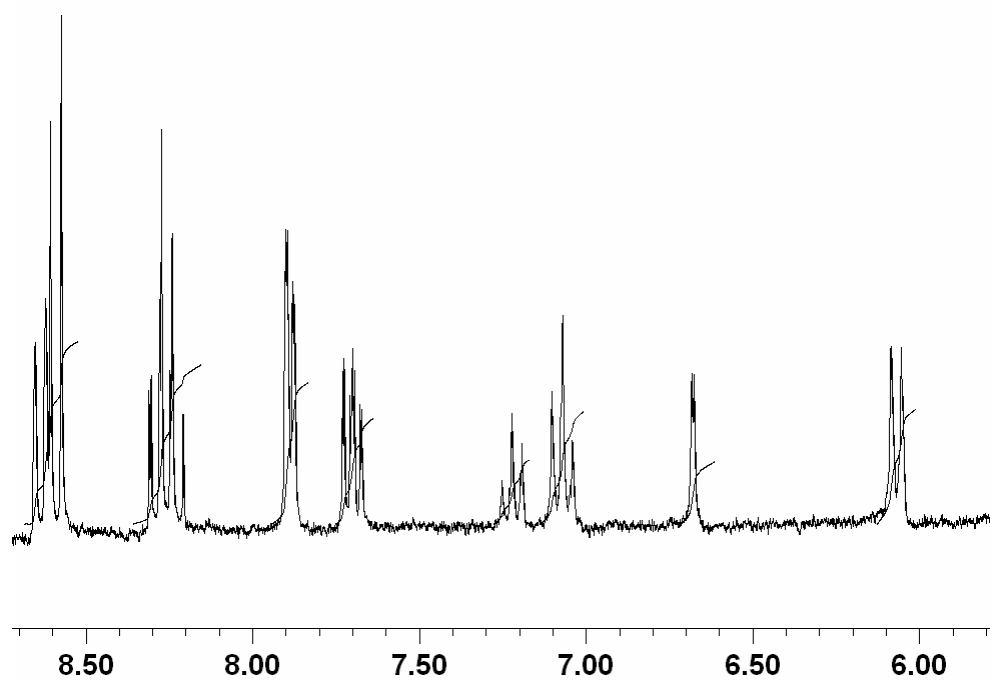
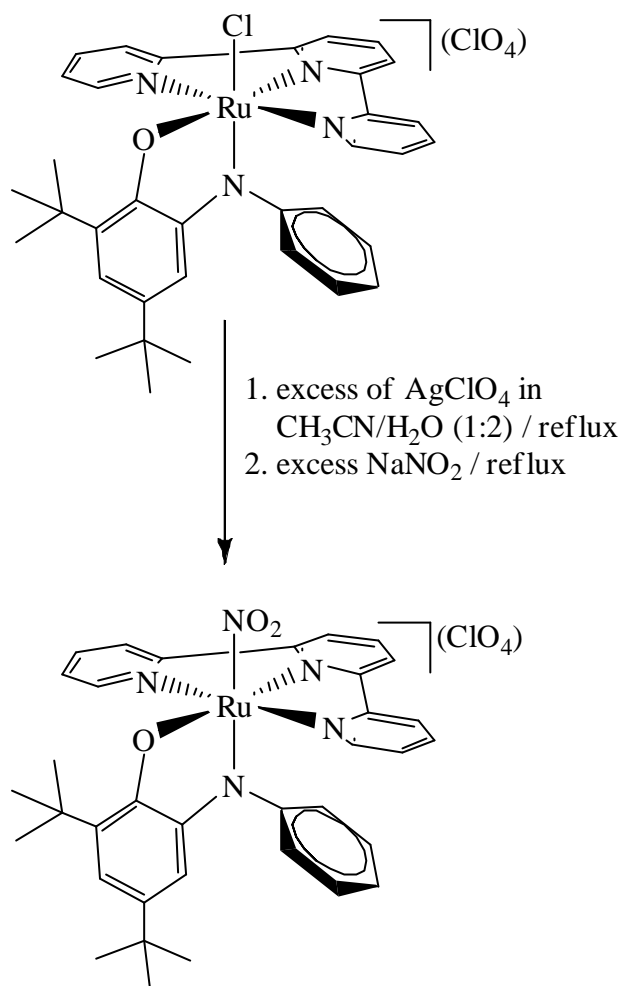


Figure 4.2.2. $^1\text{H-NMR}$ spectrum (only aromatic region) of the complex **[2a]**(ClO_4) in CD_3CN at 250 MHz.



Scheme 4.2.2. Reaction scheme for the synthesis of $[\mathbf{2a}](\text{ClO}_4)$.

4.2.2. The nitro complexes $[\mathbf{2a}](\text{ClO}_4)$ and $[\mathbf{2b}](\text{PF}_6)$

The nitro complexes $[\mathbf{2a}](\text{ClO}_4)$ and $[\mathbf{2b}](\text{PF}_6)$ were prepared from $[\mathbf{1a}](\text{ClO}_4)$ and $[\mathbf{1b}](\text{PF}_6)$ through $\text{Ag}^+/\text{NO}_2^-$ treatment as shown in Scheme 4.2.2 for $[\mathbf{2a}](\text{ClO}_4)$ complex. A corresponding synthetic procedure was applied to obtain $[\mathbf{2b}](\text{PF}_6)$.

The complexes were characterized by electrospray mass spectroscopy, elemental analysis and $^1\text{H-NMR}$ spectroscopy. Single crystal x-ray structures of both complexes $[\mathbf{2a}](\text{ClO}_4)$ (Figure 4.3.3) and $[\mathbf{2b}](\text{PF}_6)$ (Figure 4.3.4) show no isomeric change in the conversion of the chloro to the nitro complexes.

4.3. Crystal structures

Single crystals could be obtained by slow diffusion of diethylether into an acetonitrile solution of **[1a]**(ClO₄) or by slow diffusion of n-hexane into a dichloromethane solution of **[2a]**(ClO₄) at room temperature (295 K). Single crystals of the tppz complexes **[1b]**(PF₆) and **[2b]**(PF₆) were grown from dichloromethane/hexane solution (diffusion method). The molecular structures of the complexes are shown in Figure 4.3.1–4.3.4. Crystallographic data are summarized in Chapter 9.5.2–3 and 9.5.5–6. Selected bond lengths and angles are listed in Table 4.3.1.

¹H NMR spectroscopy of all four complexes shows the exclusive formation of only one positional isomer (Scheme 4.2.1). By X-ray crystallography it is possible to establish the configuration of these complexes showing that the chloride and nitrite ligands are preferentially *trans* to N1–Ph in all the four cases.

The bond distances for different oxidation levels of Qⁿ have been listed in Table 4.1.1. The bond distances obtained from the present single crystal X-ray data have been imposed to formulate the valence state distribution in the isolated forms. Comparison of the corresponding data from all four complexes (Table 4.3.1) with the listed values in Table 4.1.1, suggest that the coordinated ligand binds in the iminosemiquinone (Q^{•-}) form, leaving the +III oxidation state for the metal. The observed diamagnetism with unshifted narrow ¹H-NMR lines is thus attributed to strong antiferromagnetic coupling.

The terpy ligand in the complexes is coordinated to the six-coordinate ruthenium ion in the expected meridional fashion. Both terpy complexes **[1a]**(ClO₄) and **[2a]**(ClO₄) crystallise in the space group of $P\bar{1}$. The C1–O1, N1–C2, C3–C4 and C5–C6 bond lengths in **[1a]**⁺ indicate the Q ligand binds to the metal in iminosemiquinone (Q^{•-}) form. Similarly in the case of complex **[2a]**⁺ the oxidation level of the non-innocent ligand remains in the iminosemiquinone (Q^{•-}) form.

The tppz complexes **[1b]**(PF₆) and **[2b]**(PF₆) are crystallize in space group $P\bar{1}$. The C1–O1, N1–C2, C3–C4 and C5–C6 bond lengths (Table 4.3.1) of both complexes clearly suggest Q binding to the metal in the iminosemiquinone form.

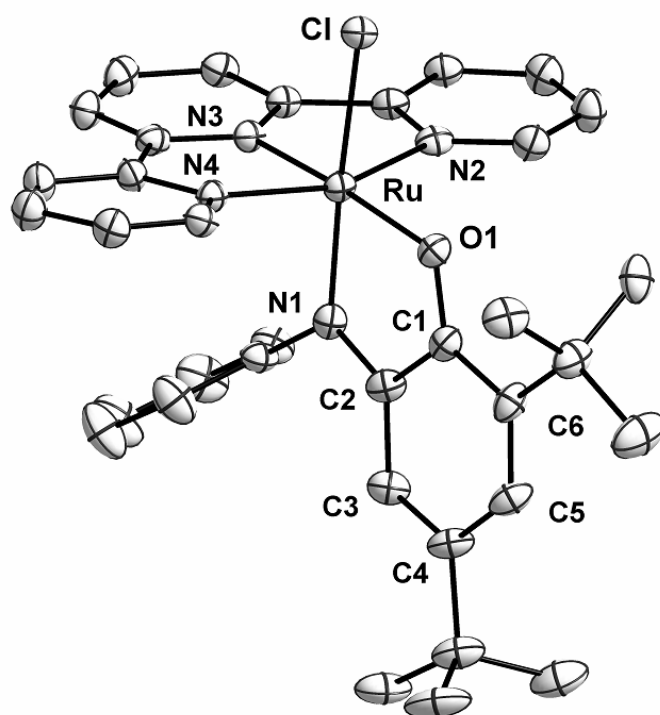


Figure 4.3.1. Molecular structure of $[1a]^+$ in the crystal of $[1a](ClO_4)$.

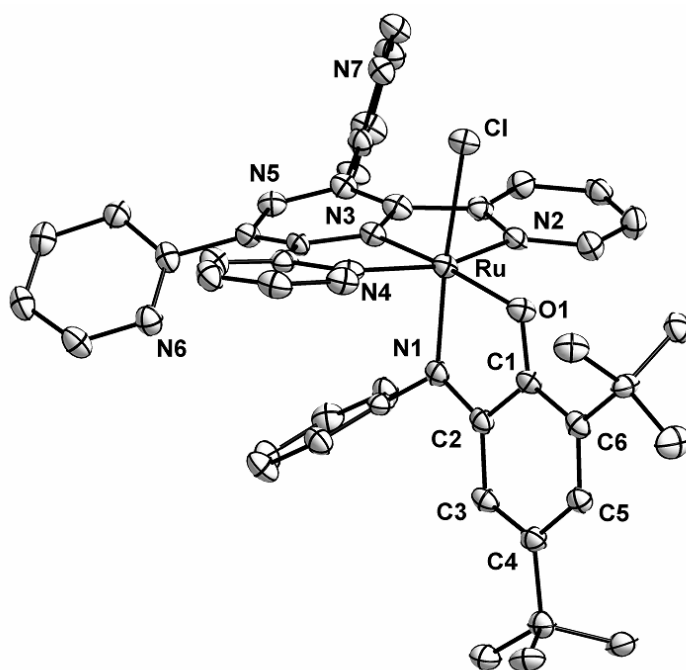


Figure 4.3.2. Molecular structure of $[1b]^+$ in the crystal of $[1b](PF_6) \cdot (CH_2Cl_2)$.

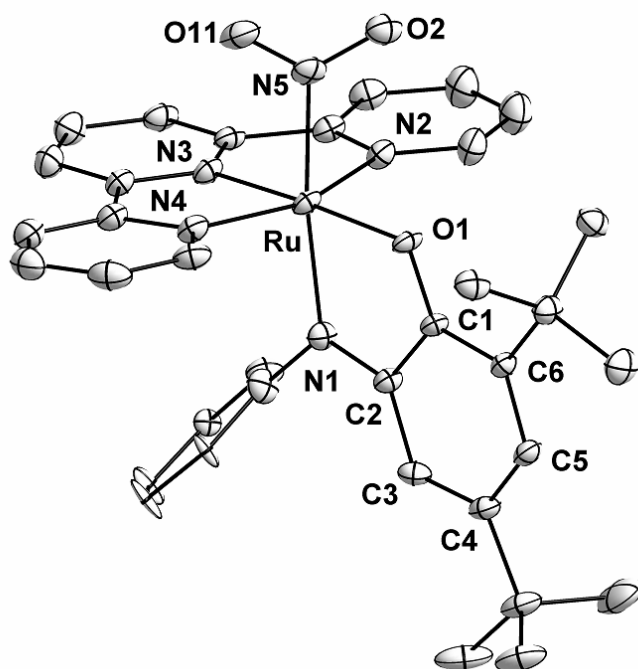


Figure 4.3.3. Molecular structure of $[2a]^+$ in the crystal of $[2a](ClO_4)$.

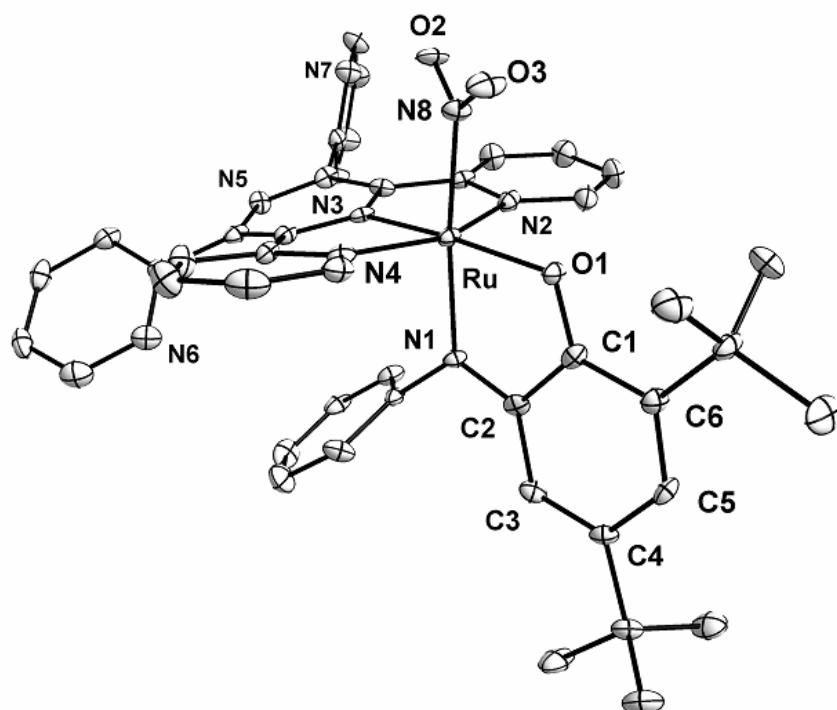


Figure 4.3.4. Molecular structure of $[2b]^+$ in the crystal of $[2b](PF_6) \cdot (CH_2Cl_2)$.

Table 4.3.1. Selected bond lengths (Å).

| Bond lengths | 1a⁺ | 1b⁺ | 2a⁺ | 2b⁺ |
|--------------|-----------------------|-----------------------|-----------------------|-----------------------|
| C1–C2 | 1.437(6) | 1.451(6) | 1.453(5) | 1.450(5) |
| C2–C3 | 1.434(6) | 1.422(6) | 1.425(5) | 1.427(5) |
| C3–C4 | 1.363(6) | 1.351(7) | 1.352(5) | 1.352(5) |
| C4–C5 | 1.435(7) | 1.453(6) | 1.445(5) | 1.449(5) |
| C5–C6 | 1.369(6) | 1.366(7) | 1.363(5) | 1.368(5) |
| C6–C1 | 1.429(6) | 1.424(7) | 1.435(5) | 1.441(4) |
| O1–C1 | 1.304(5) | 1.294(6) | 1.281(4) | 1.288(4) |
| N1–C2 | 1.351(6) | 1.349(6) | 1.333(5) | 1.339(4) |
| Ru–O1 | 2.035(3) | 2.044(4) | 2.026(2) | 2.033(2) |
| N5–O1 | ----- | ----- | 1.250(5) | ----- |
| N5–O11 | ----- | ----- | 1.217(5) | ----- |
| Ru–N8 | ----- | ----- | ----- | 2.046(3) |
| N8–O3 | ----- | ----- | ----- | 1.235(4) |
| N8–O2 | ----- | ----- | ----- | 1.229(4) |

Table 4.3.2. Selected bond angles (°).

| Bond lengths | 1a ⁺ | 1b ⁺ | 2a ⁺ | 2b ⁺ |
|--------------|------------------------|------------------------|------------------------|------------------------|
| Ru–O1–C1 | 115.3(3) | 115.2(3) | 116.4(2) | 116.1(2) |
| Ru–N1–C2 | 117.1(3) | 118.1(3) | 116.2(2) | 116.9(2) |
| N1–C2–C1 | 113.7(4) | 112.3(4) | 113.2(3) | 112.7(3) |
| C2–C1–O1 | 115.0(4) | 115.9(4) | 116.1(3) | 116.3(3) |
| N2–Ru–N4 | 157.7(1) | 154.7(2) | 157.8(1) | 157.9(1) |
| N3–Ru–O1 | 174.6(1) | 174.3(2) | 177.0(1) | 175.1(1) |
| N1–Ru–O1 | 78.9(1) | 78.4(2) | 78.0(1) | 77.9(1) |
| N4–Ru–O1 | 101.9(1) | 101.6(2) | 92.2(1) | 102.4(1) |
| O1–Ru–N2 | 99.8(1) | 99.4(1) | 101.9(1) | 99.4(1) |

4.4. Electrochemistry

The redox behaviour of the chloro complexes **[1a]**(ClO₄), **[1b]**(PF₆) and of the nitro complexes **[1a]**(ClO₄), **[2b]**(PF₆) are described separately.

4.4.1. The chloro complexes **[1a]**(ClO₄) and **[1b]**(PF₆)

Both chloro complexes **[1a]**(ClO₄) and **[1b]**(PF₆) show two successive one-electron reversible reductions and one reversible one-electron oxidation; terpy-centered reduction process cannot be observed (Figure 4.4.1) for the complex **[1a]**(ClO₄) before the negative potential limit of the CH₂Cl₂ solvent, whereas two tppz-centered reductions⁶³ (red3 and red4) [tppz] → [tppz]⁻ and [tppz] → [tppz]²⁻ can be observed (Figure 4.4.2) for **[1b]**(PF₆) within the negative potential limit of the CH₃CN solvent. The potentials are listed in Table 4.4.1. The more pi-acidic nature of the tppz ligand in **[2a]**⁺ makes the reduction easier (red1 and red2) and the oxidation process (oxd1) more difficult, compared to the terpy complex **[1a]**⁺. The large separations in potentials between the first oxidation (ox1) and reduction (red1), ΔE = 1.47 and 1.45 V for **[1a]**⁺ and **[2a]**⁺ converts into comproportionation constants (*K_c*), of 10^{24.9} and 10^{24.5}, in agreement with the high stability of the isolated mono-cationic forms. The sites of

accessible reversible electron-transfer process, two successive reductions and one oxidation were investigated by different spectroscopic techniques (EPR and UV-Vis-NIR spectroelectrochemistry).

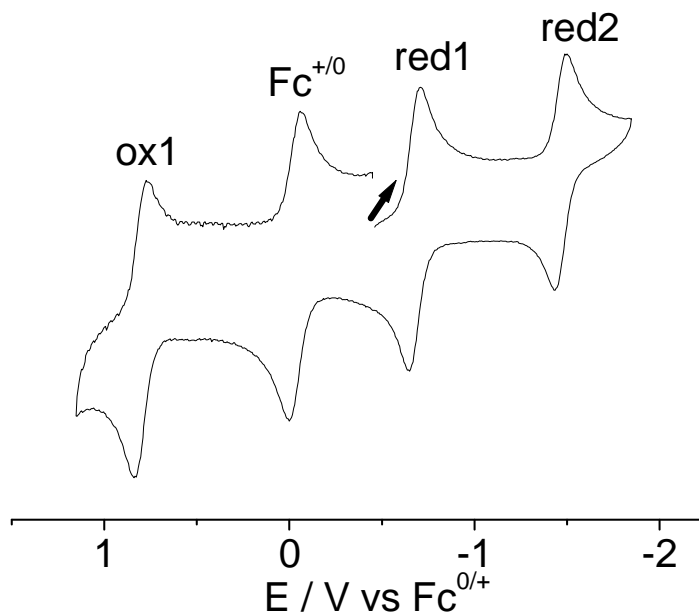


Figure 4.4.1. Cyclic voltammogram of **[1a]**(ClO₄) in CH₂Cl₂ /0.1M Bu₄NPF₆ at 100 mV/s. scan rate.

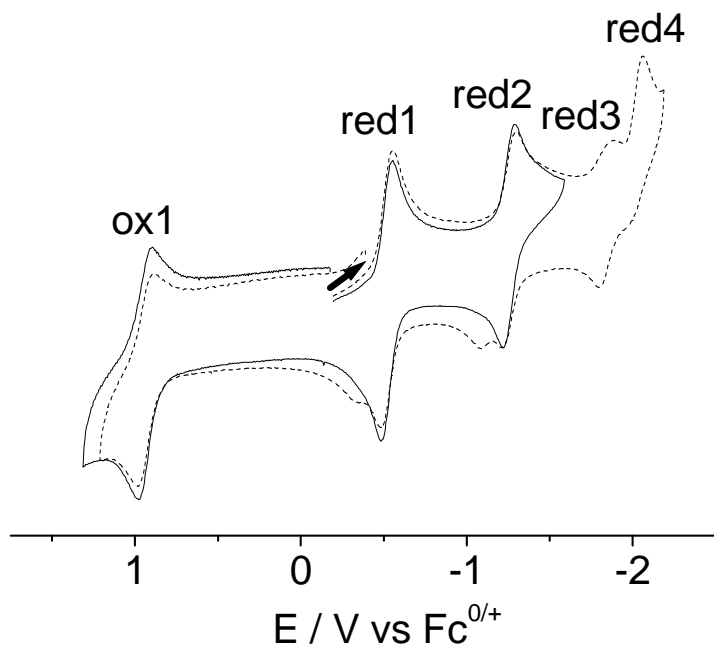


Figure 4.4.2. Cyclic voltammogram of **[1b]**(PF₆) in CH₃CN /0.1M Bu₄NPF₆ at 100 mV/s. scan rate.

4.4.2. The nitro complexes [2a](ClO₄) and [2b](PF₆)

The nitro complex [2a](ClO₄) shows two reversible one-electron reductions steps and one irreversible oxidation step (Figure 4.4.3). However, the cyclic voltammogram (Figure 4.4.4) of [2b](PF₆) shows three reduction waves, a one-electron reversible reduction, followed by an apparently irreversible wave and one tppz centered one-electron reduction. Oxidation was found irreversible at room temperature in both the cases while reversibility increased on going from lower to higher scan rate (100 to 1000 mV/s) at -30 °C (Figure 4.4.5).

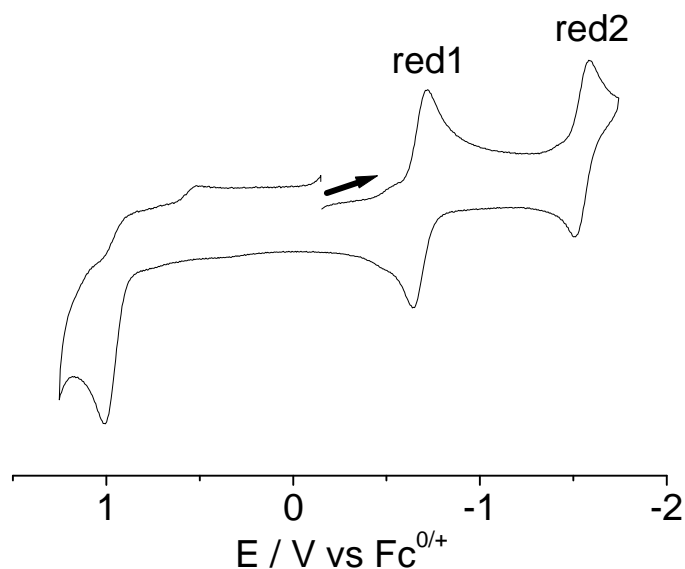


Figure 4.4.3. Cyclic voltammogram of [2a](ClO₄) in CH₂Cl₂/0.1M Bu₄NPF₆ at 100 mV/s scan rate at room temp.

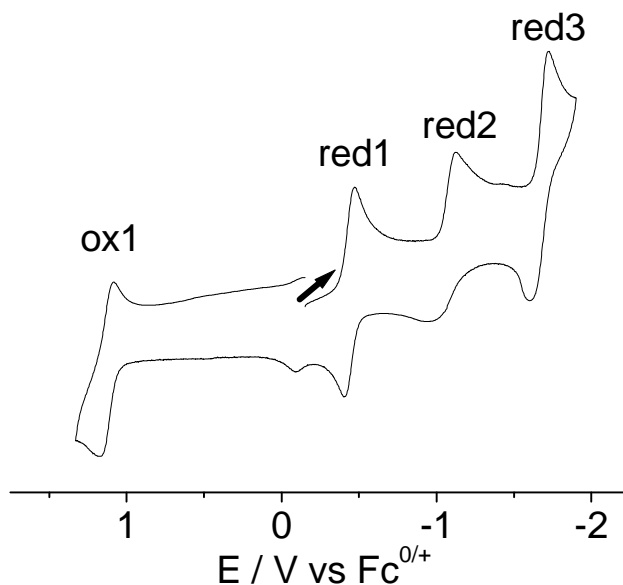


Figure 4.4.4. Cyclic voltammogram of [2b](PF₆) in CH₃CN/0.1M Bu₄NPF₆ at 1000 mV/s scan rate at -30 °C.

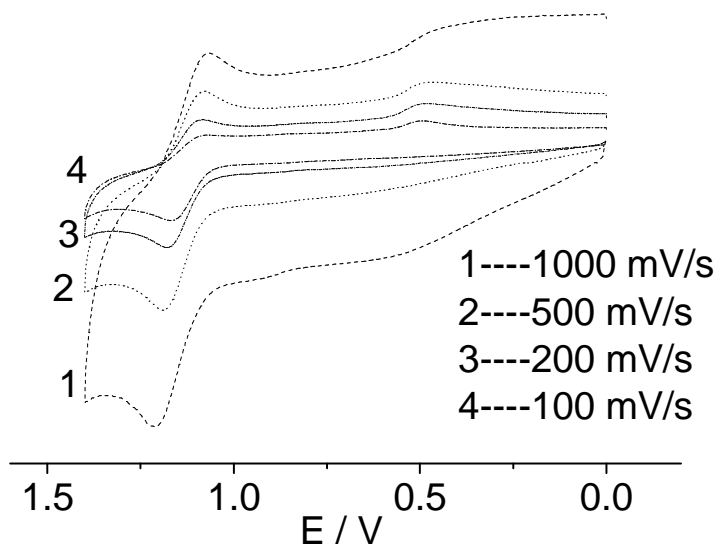


Figure 4.4.5. Cyclic voltammogram of $[2a](ClO_4)$ in $CH_2Cl_2/0.1M Bu_4NPF_6$ at different scan rates at $-30\text{ }^\circ C$ (oxidation part only).

Table 4.4.1. Redox potentials of the complexes.

| Complex | ox1 | red1 | red2 | red3 | red4 |
|------------------|--|---------------------|---------------------|---------------------|--------------------|
| $[1a]^+{}^{a,d}$ | +0.80 ($E_{1/2}$) | -0.67 ($E_{1/2}$) | -1.47 ($E_{1/2}$) | n.o. | n.o. |
| $[1b]^+{}^{b,d}$ | + 0.94 ($E_{1/2}$) | -0.51 ($E_{1/2}$) | -1.26 ($E_{1/2}$) | -1.83 ($E_{1/2}$) | -2.07 (E_{pc}) |
| $[2a]^+{}^{a,d}$ | +1.01 (E_{pa}) +1.00 ($E_{1/2}$) ^c | -0.68 ($E_{1/2}$) | -1.55 ($E_{1/2}$) | n.o. | n.o. |
| $[2b]^+{}^{b,d}$ | +1.20 (E_{pa}) +1.13 ($E_{1/2}$) ^c | -0.44 ($E_{1/2}$) | -1.13 (E_{pc}) | -1.71 ($E_{1/2}$) | n.o |

^a measurements in $CH_2Cl_2/0.1 M Bu_4NPF_6$ at 100 mV/s scan rate at room temperature.

^b measurements in $CH_3CN/0.1 M Bu_4NPF_6$ at 100 mV/s scan rate at room temperature.

^c at $-30\text{ }^\circ C$ with 1000 mV/s.

^d potentials are given in V vs $Fc^{0/+}$, with half-wave ($E_{1/2}$) or peak potentials (E_{pc} , E_{pa}) for irreversible process.

4.5. EPR spectroscopy

The EPR results are discussed for the chloro complexes **[1a]**(ClO₄) and **[1b]**(PF₆) and one of the nitro complexes in separate sections.

4.5.1. The chloro complexes **[1a]**(ClO₄) and **[1b]**(PF₆)

Because of the reversibility the odd electron species could be generated by in situ electrolysis for EPR spectroscopy on first one-electron reduction and oxidation process for the chloro complexes **[1a]**(ClO₄) and **[1b]**(PF₆). The one-electron reduced species **[1a]**⁰ (Figure 4.5.1) and **[1b]**⁰ (Figure 4.5.2) show strong EPR signals at room temp. This is a first evidence for a predominantly ligand centered spin.⁶⁴ Significant metal centered spin would be expected to lead to rapid relaxation and to large *g* anisotropy with concomitant line broadening^{23a,65}.

The X-band EPR experiments at room temperature of **[1a]**⁰ (Figure 4.5.1) and **[1b]**⁰ (Figure 4.5.2) give spectra with *g*_{iso} = 2.0045 and 2.0003, respectively, typical values for semiquinone radical complexes; indicating the formulation [Ru^{II}(Q^{•-})]. Fortunately, the spectrum is sufficiently resolved to determine the ¹⁴N and ^{99,101}Ru hyperfine couplings. The nitrogen coupling constants as obtained from the computer simulation at *a*(¹⁴N) = 0.78 mT for **[1a]**⁰ and 0.83 mT for **[1b]**⁰ are typical for iminosemiquinone based radicals. Remarkably, the metal hyperfine coupling is large enough to be clearly detectable²⁶ at the wings of the main signals in both cases. The values are *a*(^{99,101}Ru) = 1.42 mT and 1.28 mT for the complexes **[1a]**⁰ and **[1b]**⁰ respectively. These appreciable metal hyperfine coupling constants indicate efficient spin transfer from the *o*-iminosemiquinones ligands to the metal.

X-band EPR spectroscopy of glassy frozen solutions or, if necessary, high-field EPR spectroscopy of these paramagnetic species are suitable to evaluate the amount of spin on the heavy metal center because this will be reflected through spin-orbit coupling (i) by the anisotropy of *g* tensor as quantified by $\Delta g = g_1 - g_3$ and (ii) by the deviation of the isotropic *g* factor $\langle g \rangle$ from the value 2.0023 for the free electron or from the typical values of about 2.005 for free semiquinone anion radicals. The value $\Delta g = 0.0510$ as obtained from the 9.5 GHz (X-band) EPR at 110 K in dichloromethane for **[1b]**⁰ and 0.0210 as obtained from 285 GHz (high-field) EPR for **[1a]**⁰ at 4 K are so small as to allow for its formulation as [Ru^{II}(Q^{•-})] for the electronic configuration after the reduction which justifies preferential metal based reduction according to $[\text{Ru}^{\text{III}}(\text{Q}^{\bullet-})] + e^- \rightarrow [\text{Ru}^{\text{II}}(\text{Q}^{\bullet-})]$.

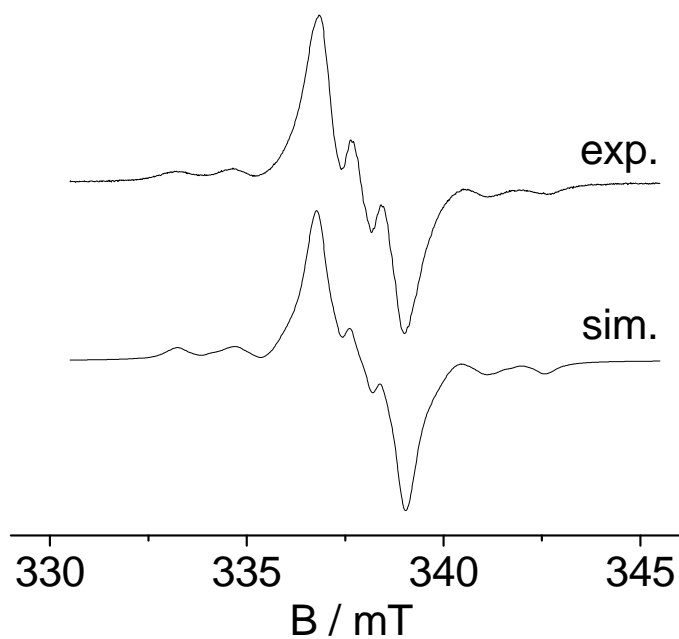


Figure 4.5.1. X-band EPR spectrum of electrochemically generated $[1\mathbf{a}]^0$ at 295 K in $\text{CH}_2\text{Cl}_2/$ 0.1 M Bu_4NPF_6 (top) with simulation (bottom).

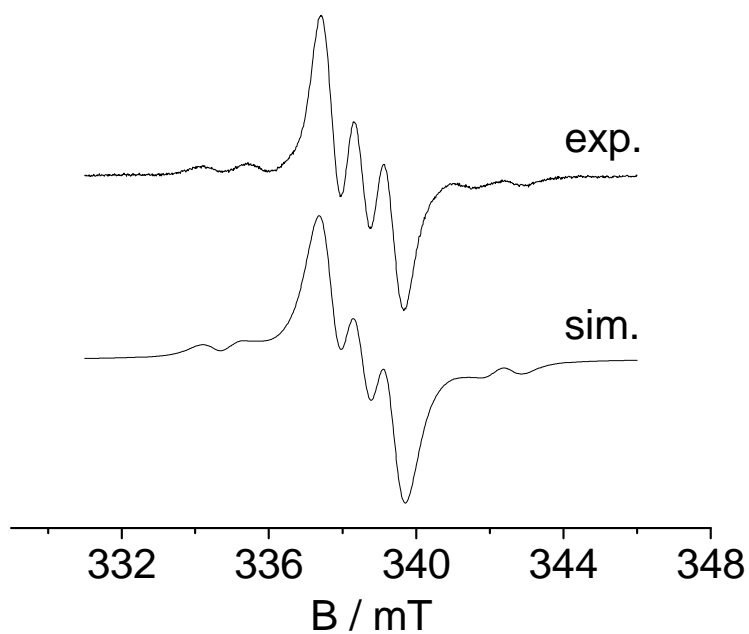


Figure 4.5.2. X band EPR spectrum of electrochemically generated $[1\mathbf{b}]^0$ at 295 K in $\text{CH}_3\text{CN}/$ 0.1 M Bu_4NPF_6 (top) with simulation (bottom).

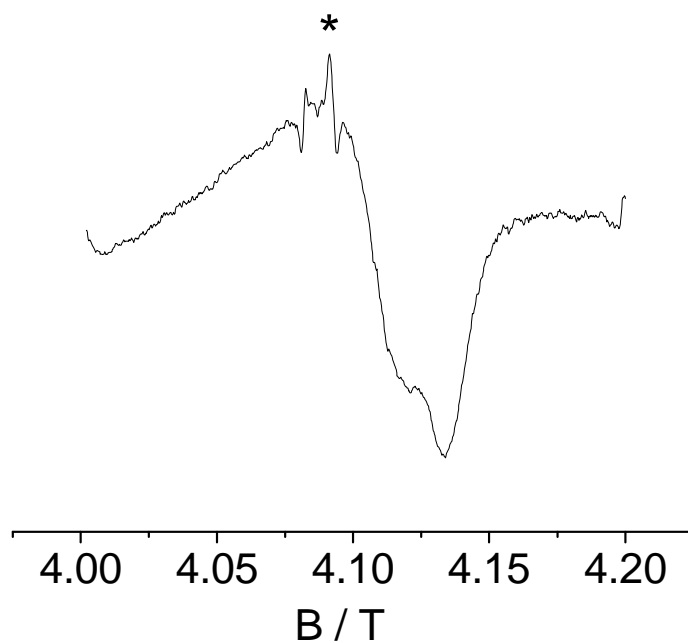


Figure 4.5.3. 285 GHz EPR spectrum of $[1a]^0$ at 5 K in dichloromethane/toluene (4/1). (* indicates a signal from field fluctuation).

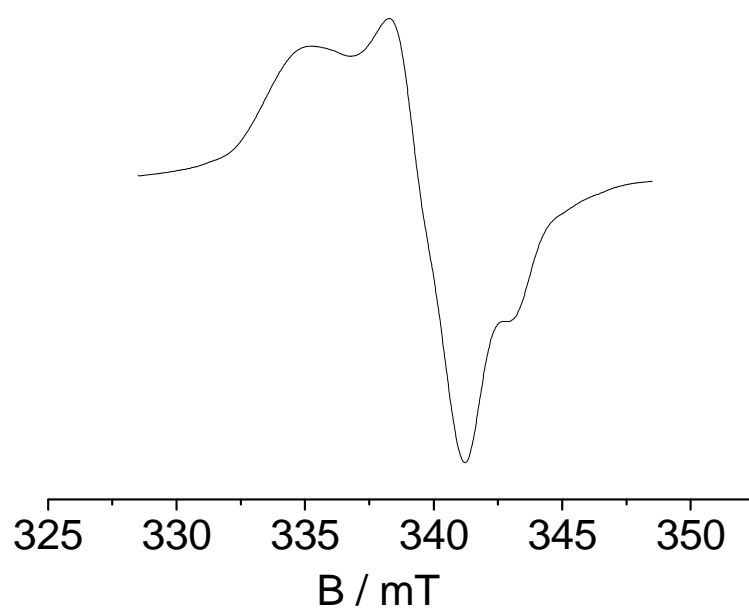


Figure 4.5.4. X-band EPR spectrum of electrochemically generated $[1b]^0$ at 110 K in $CH_3CN/0.1 M Bu_4NPF_6$.

Oxidation of $[\mathbf{1b}]^+$ results in the appearance of a rhombic EPR signal ($g_1 = 2.780$, $g_2 = 2.143$, $g_3 = 1.748$) at 110 K in acetonitrile/0.1 M Bu_4NPF_6 as is typical for distorted ruthenium(III) in its low-spin d^5 configuration. The oxidation of the semiquinone center ($\text{Q}^{\cdot-}$) from the initial configuration $[\text{Ru}^{\text{III}}(\text{Q}^{\cdot-})]^+$ leads the configuration $[\text{Ru}^{\text{III}}(\text{Q}^0)]$ which reflected by the Ru(III) signal in the EPR spectrum.

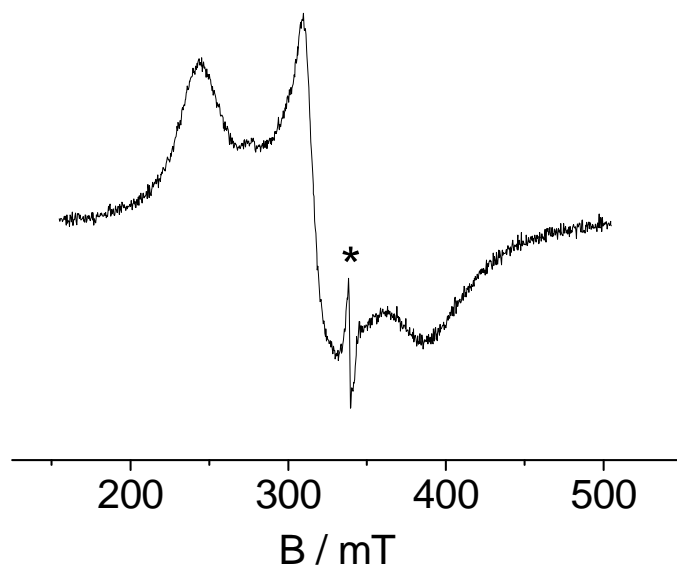


Figure 4.5.5. X-band EPR spectrum of electrochemically generated $[\mathbf{1b}]^{2+}$ at 110 K in $\text{CH}_3\text{CN}/0.1 \text{ M Bu}_4\text{NPF}_6$. (* organic radical side product yet to be assigned).

4.5.2. The nitro complexes $[\mathbf{2a}](\text{ClO}_4)$

The first one-electron reduction of nitro complexes could be investigated by X-band and high-field EPR spectroscopy. Spectra are shown in Figure 4.5.6 and Figure 4.5.7. The X-band EPR experiment at room temperature of electrochemically reduced $[\mathbf{2a}]^0$ exhibits (Figure 4.5.6) a signal at $g_{\text{iso}} = 1.9980$, a relatively small value compare to that of the chloro complex ($g = 2.0045$). It also exhibits lower g anisotropy (Figure 4.5.7), $\Delta g = g_1 - g_3$ (0.0110) than the chloro species (see Table 4.5.1). These two results indicate that the metal participation at the SOMO is lower for nitro complex as compare to the chloro complexes.

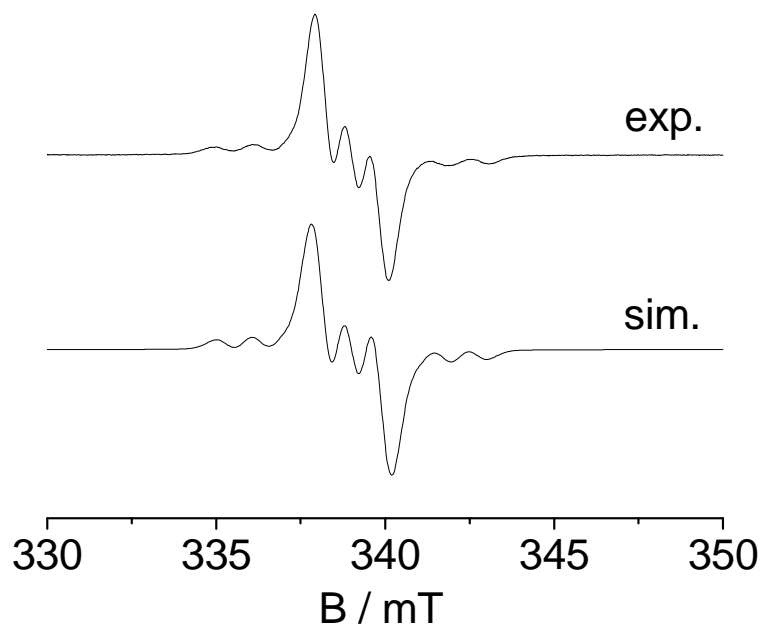


Figure 4.5.6. X-band EPR spectrum of electrochemically generated $[2a]^0$ at 295 K in $\text{CH}_2\text{Cl}_2/0.1 \text{ M Bu}_4\text{NPF}_6$ (top) with simulation (bottom).

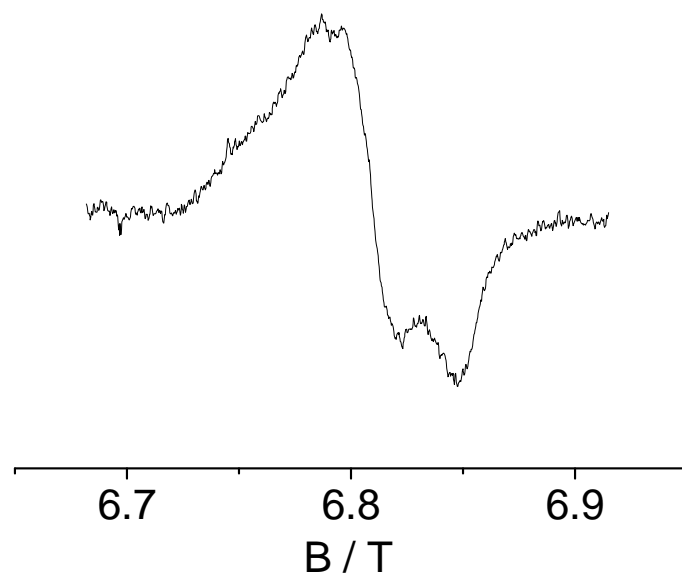


Figure 4.5.7. 285 GHz EPR spectrum of $[2a]^0$ at 5 K in dichloromethane/toluene (4/1).

Table 4.5.1. EPR data of complexes $[1a]^n$, $[1b]^n$ ($n = 0, 2+$) and $[2a]^0$.

| Complex | ^c g_{iso} | g_1 | g_2 | g_3 | g_{av}^g | Δg^h |
|--------------------------|------------------------|---------------------|---------------------|---------------------|------------|--------------|
| $[1a]^0$ | 2.0045 ^a | 2.0090 ^f | 2.0000 ^f | 1.9880 ^f | 1.9990 | 0.0210 |
| $[1a]^{2+}$ | 2.0032 ^a | 2.0610 ^b | 2.0210 ^b | 1.9850 ^b | 2.0226 | 0.0760 |
| ^b $[1b]^0$ | 2.0003 ^c | 2.0250 ^d | 1.9950 ^d | 1.9740 ^d | 1.9981 | 0.0510 |
| ^a $[1b]^{2+}$ | n.o. | 2.780 ^d | 2.1430 ^d | 1.7480 ^d | 2.2639 | 1.0320 |
| $[2a]^0$ | 1.9980 ^a | 1.9940 ^f | 1.9940 ^f | 1.9830 ^f | 1.9917 | 0.0110 |

^a In $CH_2Cl_2/0.1$ M Bu_4NPF_6 at 295 K.

^b In $CH_2Cl_2/0.1$ M Bu_4NPF_6 at 110 K

^c In $CH_3CN/0.1$ M Bu_4NPF_6 295 K.

^d In $CH_3CN/0.1$ M Bu_4NPF_6 110 K.

^e g_{iso} : isotropic g value obtained from X band experiment at 295 K.

^f from high field experiments.

^g from 285 GHz EPR at 5 K in dichloromethane/toluene (4/1).

^h $g_{av} = [(g_1^2 + g_2^2 + g_3^2)/3]^{1/2}$.

ⁱ $\Delta g = g_1 - g_3$.

Table 4.5.2. Hyperfine coupling constants obtained from X-band experiments at 298 K.

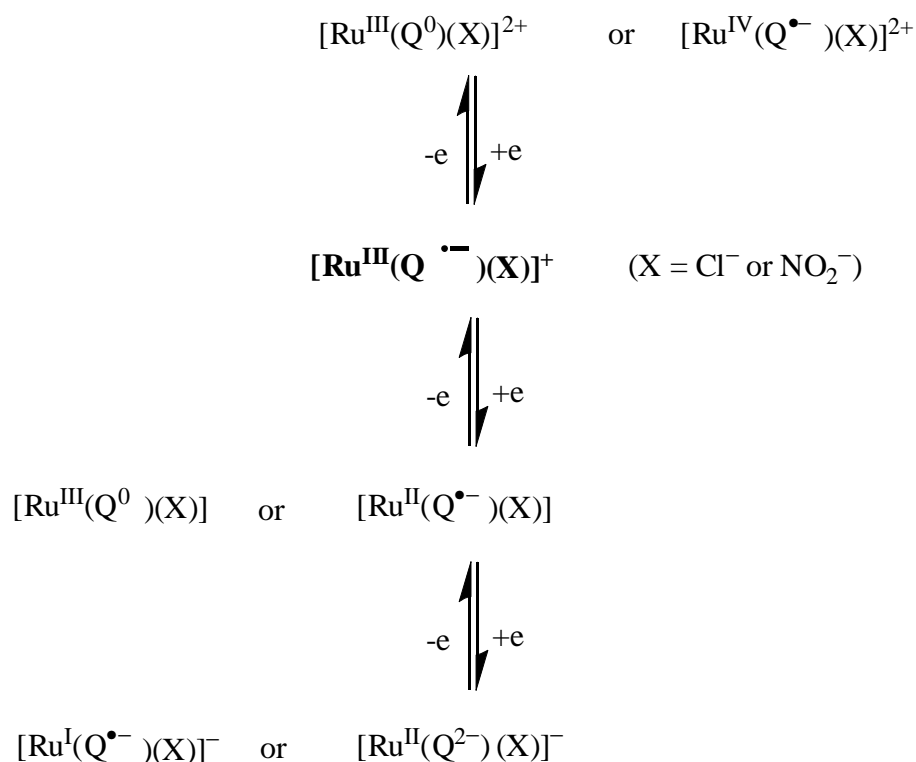
| Complex | $a(^{101}Ru, ^{99}Ru)$ | $a(^{14}N)$ |
|----------|------------------------|--------------|
| $[1a]^0$ | 1.42 mT (1Ru) | 0.77 mT (1N) |
| $[1b]^0$ | 1.28 mT (1Ru) | 0.83 mT (1N) |
| $[2a]^0$ | 1.12 mT (1Ru) | 0.85 mT (1N) |

4.6. UV-Vis-NIR spectroelectrochemistry

The spectroelectrochemistry results of chloro complexes **[1a]**(ClO₄) and **[1b]**(PF₆) and the nitro complex **[2a]**(ClO₄) will be discussed in separate sections.

4.6.1 The chloro complexes **[1a]**(ClO₄) and **[1b]**(PF₆)

The sites of two successive one-electron reductions and one one-electron oxidation of chloro complexes **[1a]**ⁿ⁺, **[1b]**ⁿ⁺ (n = -1,0,1,2) can be investigated by means of UV-Vis-NIR spectroelectrochemical experiments using an OTTLE cell.⁶⁶ The complexes exhibit partially similar behavior as shown in Figure 4.6.1 and Figure 4.6.2. The data are listed in Table 4.6.1.



Scheme 4.6.1. Possible oxidation state distribution in the isolated native form and in the first oxidized and reduced states for a Ru-quinonoid system.

The bands at about 570 nm and 315 nm (Figure 4.6.1) for **[1a]**⁺ and 582 nm and 328 nm (Figure 4.6.2) for **[2a]**⁺ can be assigned^{60b} to semiquinone and terpy/tppz-targeted MLCT transitions respectively as reported for the similar kind of system [Ru(bpy)₂(Q)]²⁺ (λ_{max} = 595 nm and 411 nm).²⁶ The first reduction could either be associated with the ruthenium(III) or Q^{•-} center as both are susceptible to one-electron reduction and the resultant reduced species

would then be formulated as $[\text{Ru}^{\text{III}}(\text{Q}^{2-})]$ or $[\text{Ru}^{\text{II}}(\text{Q}^{\bullet-})]$ (Scheme 4.6.1). The semiquinone and terpy-targeted MLCT bands at about 714 nm and 384 nm (Figure 4.6.1) for $[\mathbf{1a}]^0$ and semiquinone and tppz-targeted^{63c} MLCT bands of about 695 nm and 501 nm (Figure 4.6.2) for $[\mathbf{1b}]^0$ suggest a preferential metal-based first reduction process to form $[\text{Ru}^{\text{II}}(\text{Q}^{\bullet-})]$. The semiquinone-based free radical EPR signal ($g = 2.0045$) at room temp also support these formulations (see section 4.5). Upon second reduction the MLCT bands at 714 nm for $[\mathbf{1a}]^0$ (Figure 4.5.3) and 695 nm for $[\mathbf{1b}]^0$ (Figure 4.6.4) exhibit the high-energy shift and intensity reduction and two new broad bands appear at about 697 and 548 nm for $[\mathbf{1a}]^0$ and 576 and 473 nm for $[\mathbf{1b}]^0$ which could be assigned ligand-to-ligand charge transfer (LLCT; $\text{Q}^{2-} \rightarrow$ terpy/tppz) and $\pi^*(\text{trpy}/\text{tppz})$ -targeted metal-to-metal charge transfer (MLCT). Thus the second reduction take place on $\text{Q}^{\bullet-}$ center; leads the configuration after the second reduction $[\text{Ru}^{\text{II}}(\text{Q}^{2-})]$.

Spectroelectrochemical one electron oxidation of $[\mathbf{1a}]^+$ (Figure 4.6.5) and $[\mathbf{1b}]^+$ (Figure 4.6.6) display substantial red shift of the lowest energy charge transfer band with a slight decrease in intensity. The bands at about 570 nm for the complex $[\mathbf{1a}]^+$ shift to 504 nm and 428 nm and 582 nm for the complex $[\mathbf{1b}]^+$ shift to 492 nm which are tentatively assigned to intraquinone ligand transitions.

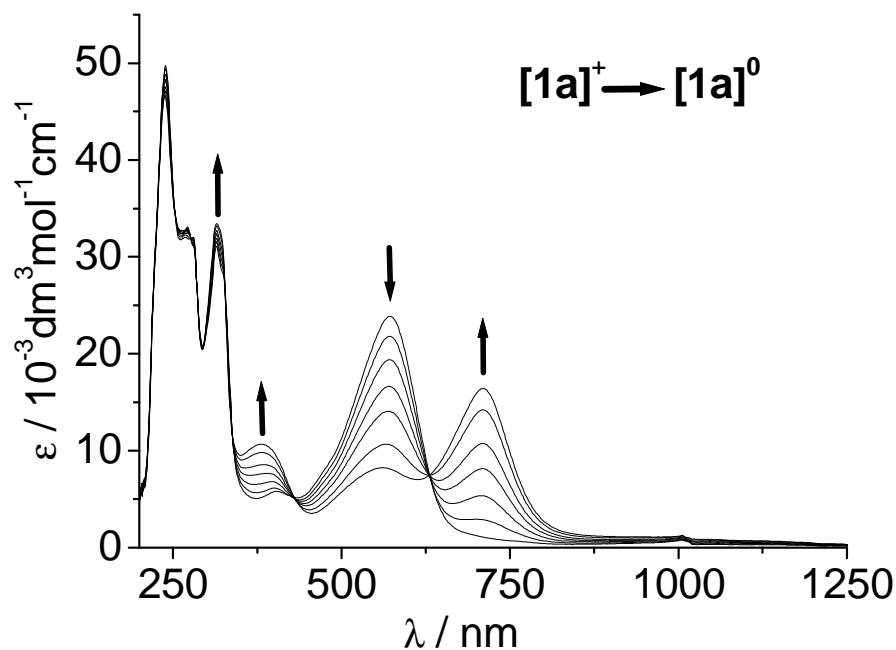


Figure 4.6.1. UV-Vis-NIR spectroelectrochemistry of the conversion $[1a]^{(1+) \rightarrow (0)}$ in $\text{CH}_2\text{Cl}_2/0.1 \text{ M Bu}_4\text{NPF}_6$.

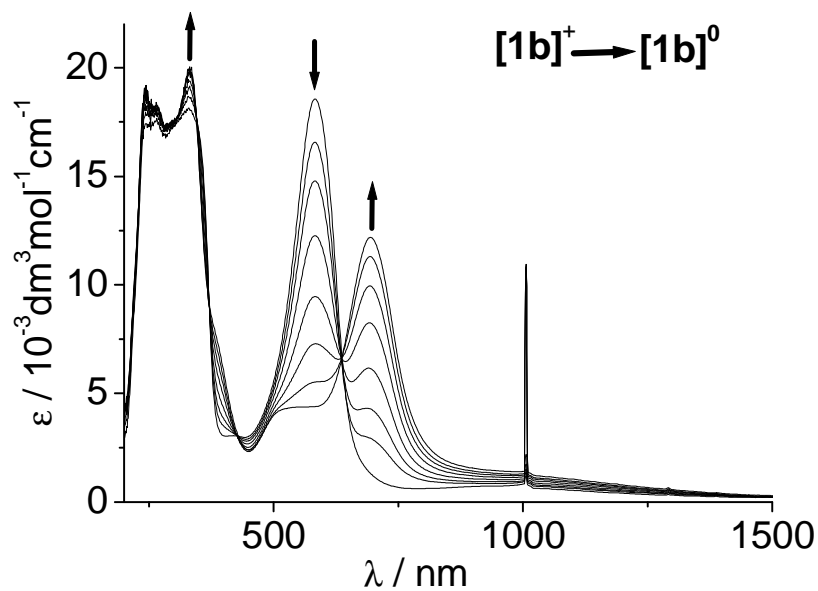


Figure 4.6.2. UV-Vis-NIR spectroelectrochemistry of the conversion $[1b]^{(1+) \rightarrow (0)}$ in $\text{CH}_3\text{CN}/0.1 \text{ M Bu}_4\text{NPF}_6$.

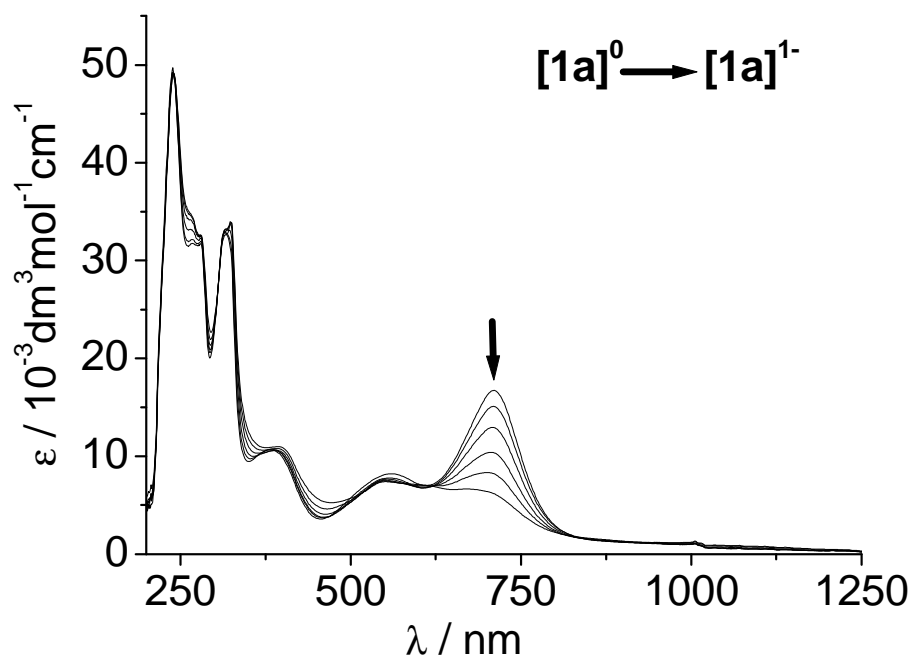


Figure 4.6.3. UV-Vis-NIR spectroelectrochemistry of the conversion $[1a]^{(0) \rightarrow (1-)}$ in $\text{CH}_2\text{Cl}_2/0.1 \text{ M Bu}_4\text{NPF}_6$.

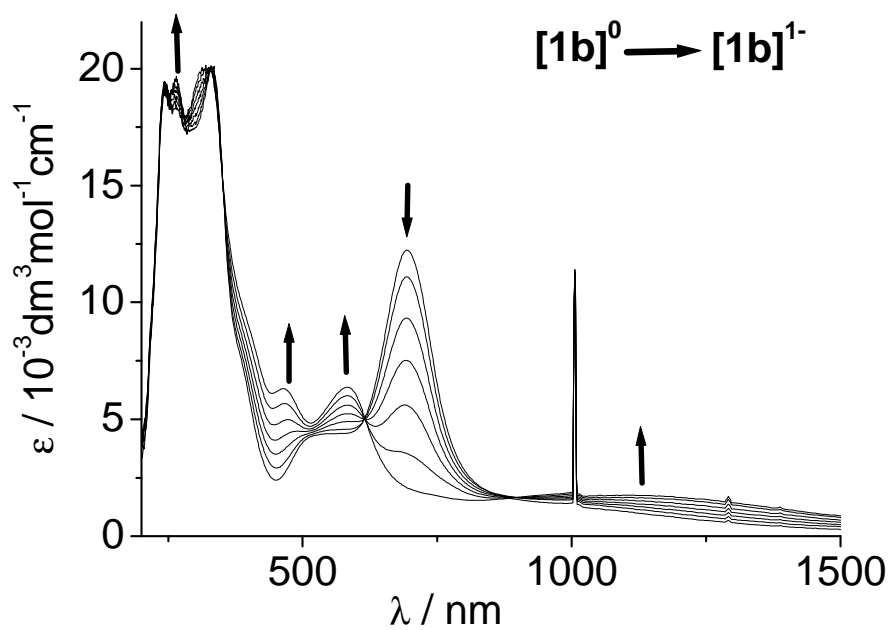


Figure 4.6.4. UV-Vis-NIR spectroelectrochemistry of the conversion $[1b]^{(0) \rightarrow (1-)}$ in $\text{CH}_3\text{CN}/0.1 \text{ M Bu}_4\text{NPF}_6$.

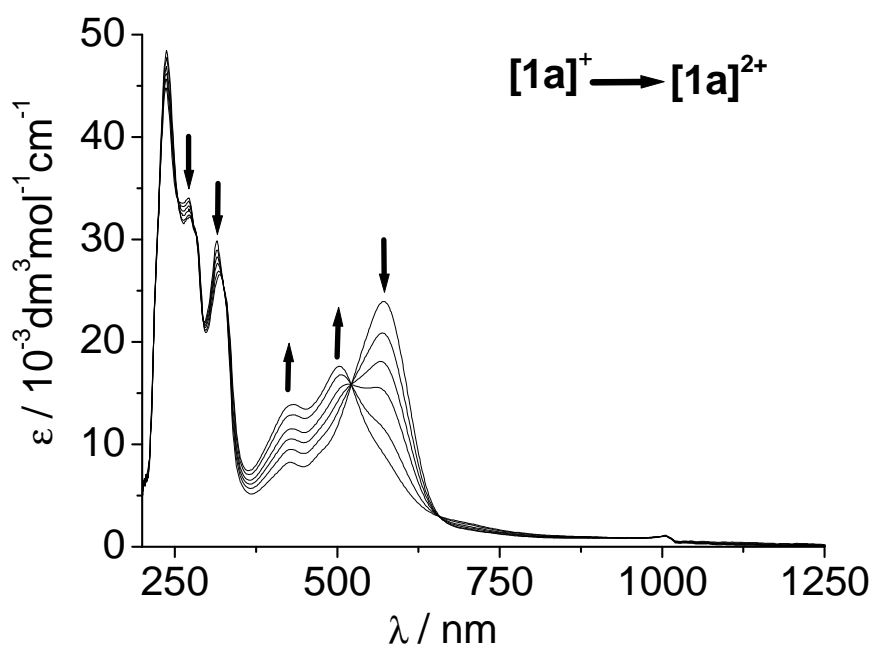


Figure 4.6.5. UV-Vis-NIR spectroelectrochemistry of the conversion $[1a]^{(+)\rightarrow(2+)}$ in $\text{CH}_2\text{Cl}_2/0.1 \text{ M Bu}_4\text{NPF}_6$.

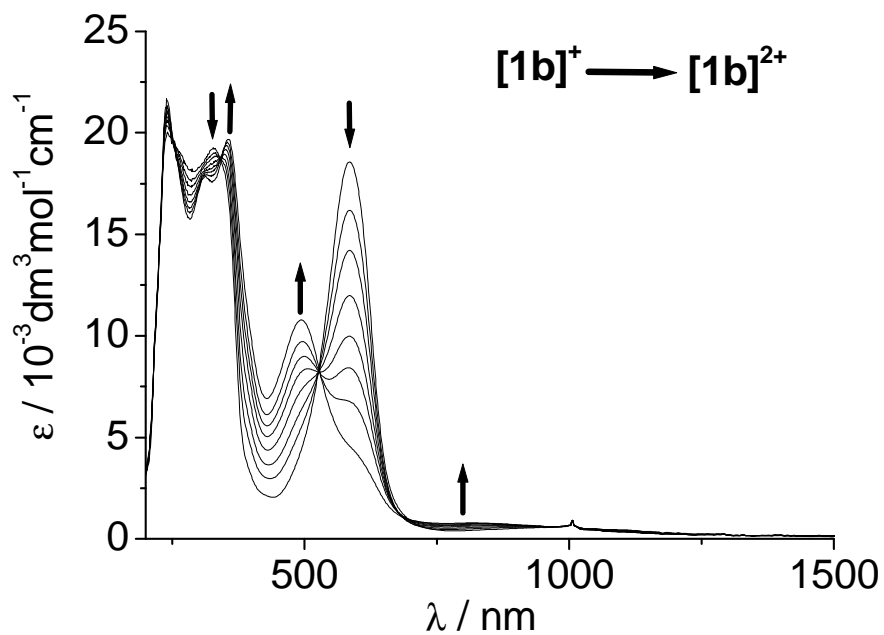


Figure 4.6.6. UV-Vis-NIR spectroelectrochemistry of the conversion $[1b]^{(+)\rightarrow(2+)}$ in $\text{CH}_3\text{CN}/0.1 \text{ M Bu}_4\text{NPF}_6$.

4.6.2. The nitro complex [2a](ClO₄)

UV-Vis spectroelectrochemical changes of the complex [2a]ⁿ⁺ (n = -1, 0, 1) are shown in Figure 4.5.7 and Figure 4.5.8. The nitro complex [2a]⁺ exhibits similar changes in the spectral patterns the chloro complexes [1a]⁺ and [1b]⁺.

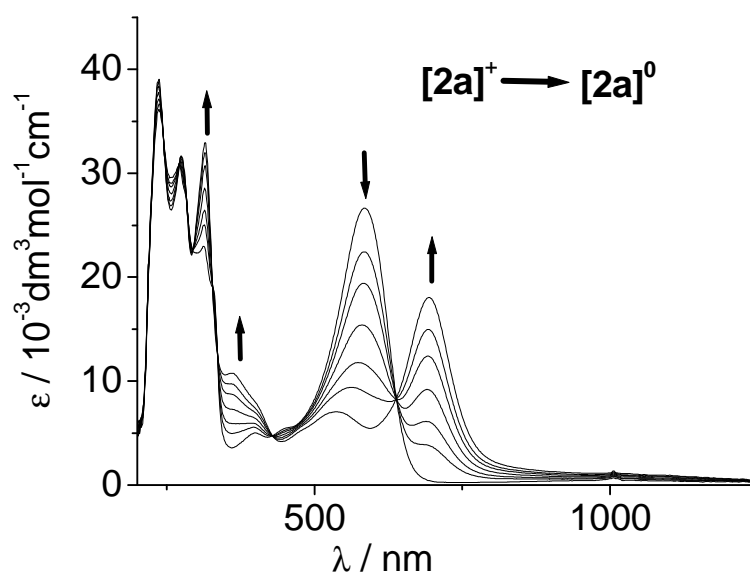


Figure 4.6.7. UV-Vis-NIR spectroelectrochemistry of the conversion [2a]^{(1+)→(0)} in CH₂Cl₂/0.1 M Bu₄NPF₆.

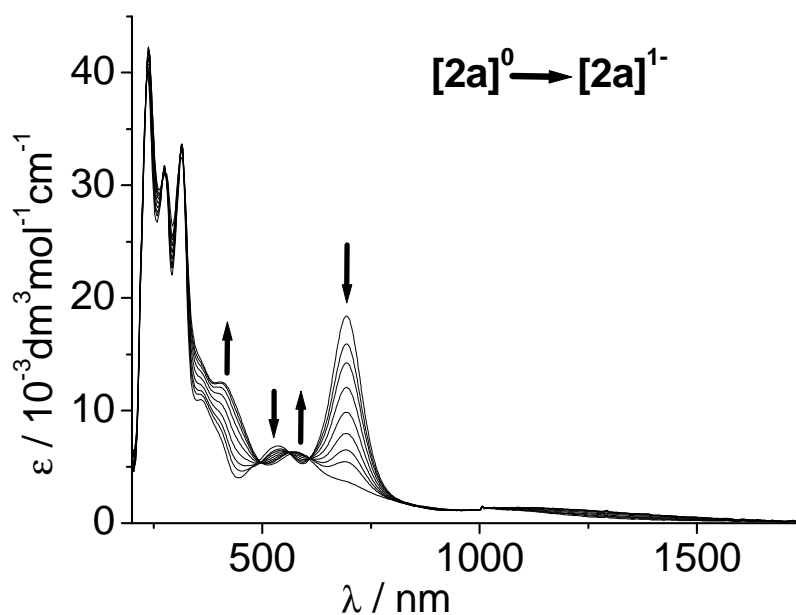


Figure 4.6.8. UV-Vis-NIR spectroelectrochemistry of the conversion [2a]^{(0)→(1-)} in CH₂Cl₂/0.1 M Bu₄NPF₆.

Table 4.6.1. Absorption data from spectroelectrochemistry.

| ^a Complex | $\lambda(\text{nm}) (\text{M}^{-1}\text{cm}^{-1})$ |
|---------------------------------|---|
| ^b [1a] ²⁺ | 504 (17800), 428 (14000), 318 (26600), 271 (32300), 237 (48700) |
| ^b [1a] ¹⁺ | 570 (24100), 315 (29900), 270 (34100), 237 (44200) |
| ^b [1a] ⁰ | 710 (16800), 555 (sh), 384 (10800), 315 (33100), 237 (49900) |
| ^b [1a] ¹⁻ | 609 (sh), 556 (sh), 399 (sh), 316(33300), 239 (49600) |
| ^c [1b] ²⁺ | 602 (sh), 492 (10800), 356 (19700), 310 (17900) |
| ^c [1b] ¹⁺ | 582 (18600), 328 (18100), 261 (17600) |
| ^c [1b] ⁰ | 695 (12200), 501 (sh), 333 (20000), 242 (19100) |
| ^c [1b] ¹⁻ | 576 (6400), 473 (6300), 327 (20100), 261 (19600) |
| ^b [2a] ¹⁺ | 585 (27300), 364 (11000), 312 (23400), 276 (32300), 234 (36800) |
| ^b [2a] ⁰ | 694 (18400), 535 (sh), 317 (33500), 276 (600), 237 (40200) |
| ^b [2a] ¹⁻ | 540 (sh), 415 (sh), 317 (33000), 274 (32000), 237 (41200) |

^a from spectroelectrochemistry experiment.

^b in CH₂Cl₂/0.1 M Bu₄NPF₆.

^c in CH₃CN/0.1 M Bu₄NPF₆.

4.7. Conclusion

Four newly synthesized complexes [1a](ClO₄), [1b](PF₆), [2a](ClO₄) and [2b](PF₆) have been characterized by ¹H-NMR and elemental analysis and the molecular structures have been determined by single crystal X-ray analysis. The bond lengths C1–O1, C2–N1 and the C–C intra-ring distances suggest that Q binds to the metal center in iminosemiquinone (Q^{•-}) oxidation state. Therefore the isolated state electronic formulation is [Ru^{III}(Q^{•-})] in all four cases. The other two possible electronic configurations (Scheme 4.5.1) [Ru^{II}(Q⁰)] and [Ru^{IV}(Q²⁻)] are not dominant. EPR and UV-Vis-NIR spectroelectrochemistry suggest a metal-based spin for the oxidized [1a]²⁺ and [1b]²⁺ complexes, leading to the [Ru^{III}(Q⁰)] electronic configuration as a result of ligand oxidation. Preferential metal-centered reduction occurred

for the first reduction in all four cases, leaving the unpaired spin preferentially on the $Q^{\bullet-}$ in the $[Ru^{II}(Q^{\bullet-})]$ electronic configuration. However the g anisotropy values as determined from X-band EPR at 110 K and high-field EPR as well as metal hyperfine data suggest a non-negligible participation of the metal at the singly participation MO (SOMO). The second reduction takes place on $Q^{\bullet-}$ center for **[1a]**(ClO₄), **[1b]**(PF₆) and **[2a]**(ClO₄) complexes, resulting in a $[Ru^{II}(Q^{2-})]$ configuration deduced from UV-Vis-NIR spectroelectrochemistry (for details see section 4.6).

CHAPTER 5

Paramagnetic Ruthenium Complexes with Two Different Non-Innocent Ligands: Nitrosyl and an *o*-Iminobenzoquinone

5.1. Introduction

Coordination compounds with redox-active transition metals, M, are most suitable for investigating intramolecular electron transfer phenomena because of the typically well-defined structural framework and the variability of metal and redox-active “non-innocent” ligands, L. Apart from the standard two-component case M-L, there has been some attention given to symmetrical three-component alternatives such as M-L-M, involving e.g. bridged mixed-valent species,⁶⁷ or L-M-L, including e.g. metal-bridged chelate ligands of the quinone-type.^{33,67} Fewer information is available for cases such as L1-M-L2 which would involve two different and thus potentially reacting non-innocent ligands in the coordination sphere of a redox-active transition metal.⁶⁹ Two such non-innocent ligands are nitrosyl ($\text{NO}^{0/+/-}$) and substituted *o*-iminobenzoquinone ($\text{Q}^{0/-/2-}$). These two ligands can exist to the complex in different redox forms depending on the metal oxidation state (Scheme 5.4.1).

Combining three prototypical components, two complexes $[\text{Ru}(\text{NO})(\text{Q})(\text{terpy})](\text{PF}_6)_2$ and $[\text{Ru}(\text{NO})(\text{Q})(\text{tppz})](\text{PF}_6)_2$ have been synthesized (terpy = 2,2':6',2''-terpyridine and tppz = 2,3,5,6-tetrakis(2-pyridyl)pyrazine), and a detailed study of $[\text{Ru}(\text{NO})(\text{Q})(\text{terpy})](\text{PF}_6)_2$ including DFT is presented illustrating “how the art of establishing oxidation states”³³ can be applied successfully to even intricate such systems. The components are:

- (i) $[\text{Ru}(\text{terpy})]^k$ and $[\text{Ru}(\text{tppz})]^k$, $k = 2+$ or $3+$, with meridionally coordinating and configuration determining tridentate ligands (terpy and tppz) (although potentially non-innocent⁷⁰, terpy is redox-invariant in the present case due to its negative reduction potential⁷¹). The more pi-acidic nature of tppz makes electron uptake easier but still it remains with a much more negative reduction potential than that of nitrosyl and substituted *o*-iminobenzoquinone.
- (ii) The NO^m redox couple ($m = 0$ or $+$) which has received much attention in connection with biochemically relevant group 8 metal complexes^{3,72}, and
- (iii) The well-used^{26,33,34} most recently reviewed³² 4,6-di-*tert*-butyl-*N*-phenyl-*o*-iminobenzoquinone, Q^n , in the structurally distinguishable^{33,34} quinone ($n = 0$), semiquinone ($n = 1-$) and “catecholate” (2-anilidophenolato) forms ($n = 2-$).

In all three instances (i) – (iii) the redox equilibria involve one paramagnetic ($S = 1/2$) state, viz., ruthenium (III) with low-spin $4d^5$ electronic configuration, the nitrosyl radical (NO^\bullet), or the *o*-semiquinoneimine form (Q^\bullet), each with a very characteristic EPR signature.^{24,26}

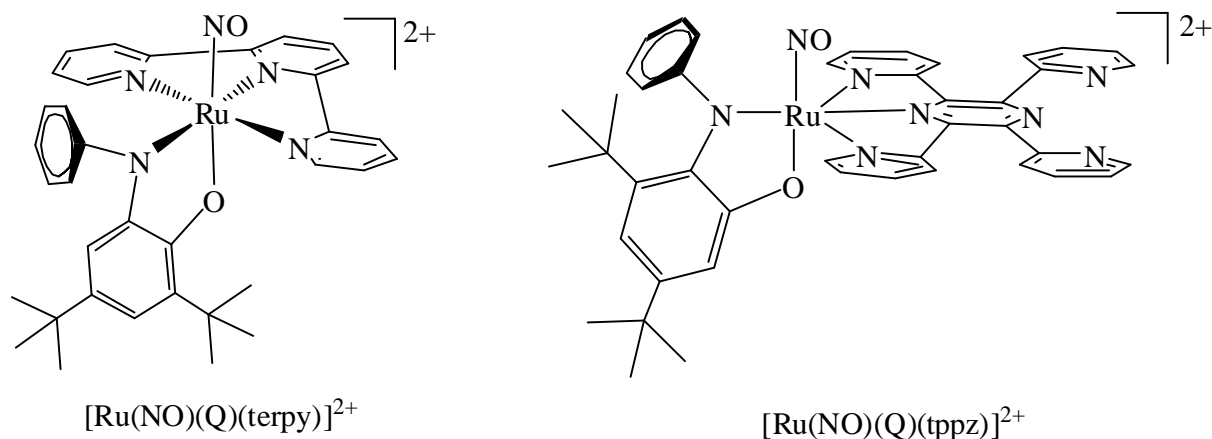
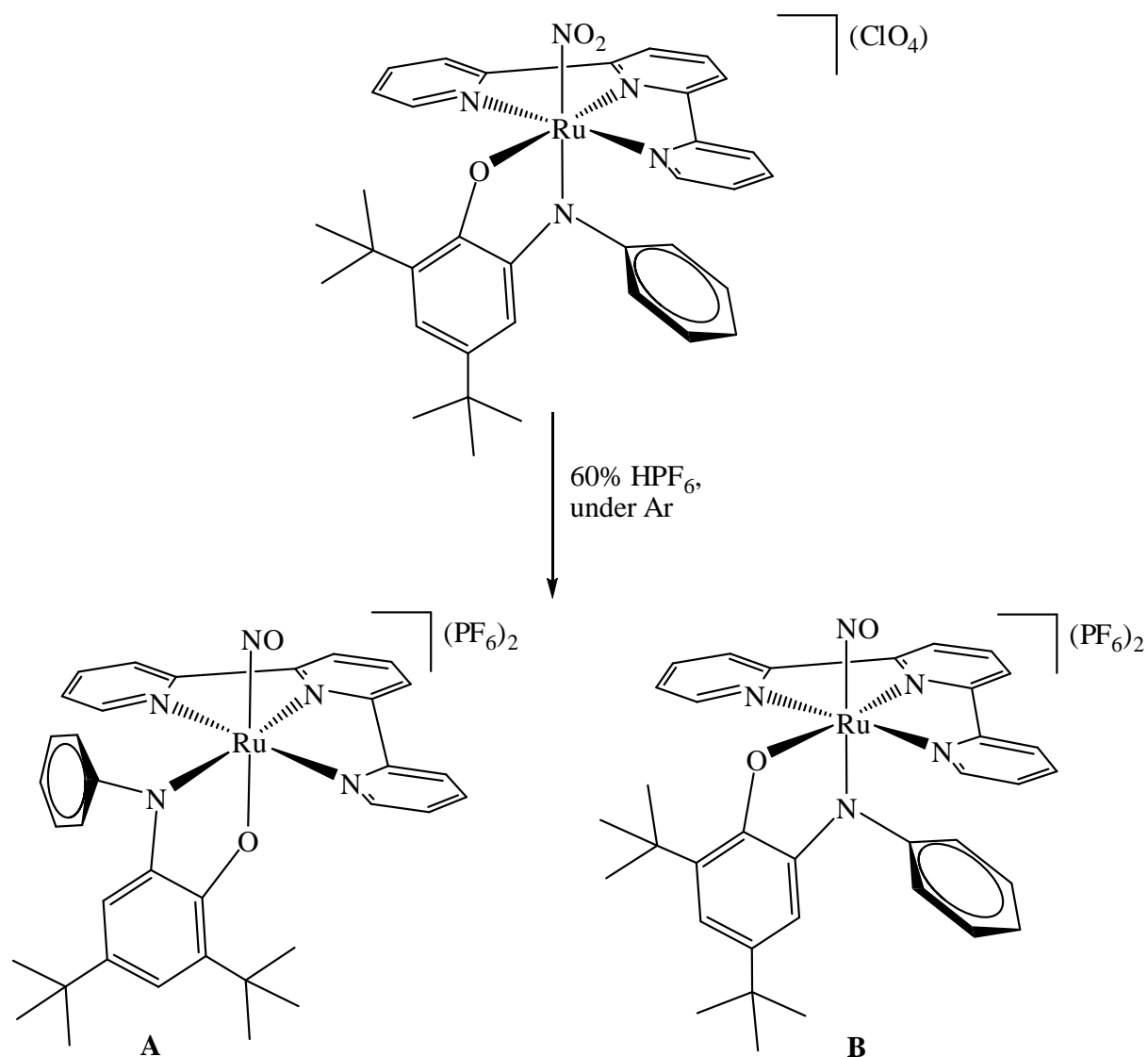


Figure 5.1.1. Molecular formulae of the complexes.

5.2. Syntheses and characterization

5.2.1 The complex $[\text{Ru}(\text{NO})(\text{Q})(\text{terpy})](\text{PF}_6)_2$

2-Anilino-4,6-di-*tert*-butylphenol³³ (H_2Q) and $\text{Ru}(\text{terpy})\text{Cl}_3$ ⁷³ were reacted to yield the chloro precursor compound $[\text{Ru}(\text{Cl})(\text{Q})(\text{terpy})](\text{ClO}_4)$ and, through $\text{Ag}^+/\text{NO}_2^-$ treatment, the nitro complex $[\text{Ru}(\text{NO}_2)(\text{Q})(\text{terpy})](\text{ClO}_4)$. The detailed synthetic procedure with full characterization of these precursor complexes is presented in Chapter 4. Crystal structure shows the ligands Cl or NO_2 in *trans* position to the N donor atom of Q.⁷⁴ The paramagnetic complex $[\text{Ru}(\text{NO})(\text{Q})(\text{terpy})](\text{PF}_6)_2$ was prepared by the treatment of the nitro complex with HPF_6 under argon at room temperature; and it was isolated in the isomer form A (Scheme 5.2.1) with the NO ligand *trans* to the oxygen atom of Q (Figure 5.3.1).



Scheme 5.2.1. Reaction scheme for the synthesis of $[\text{Ru}(\text{NO})(\text{Q})(\text{terpy})](\text{PF}_6)_2$.

5.2.2. The complex $[\text{Ru}(\text{NO})(\text{Q})(\text{tppz})](\text{PF}_6)_2$

Reaction of $[\text{Cl}_3\text{Ru}(\mu\text{-tppz})\text{RuCl}_3]$ ⁷⁷ with 2-anilino-4,6-di-*tert*-butylphenol³³ (H_2Q) produced the mononuclear chloro complex $[(\text{tppz})\text{Ru}(\text{Q})(\text{Cl})](\text{PF}_6)$ along with dinuclear complex $[\text{Cl}(\text{Q})\text{Ru}(\mu\text{-tppz})\text{Ru}(\text{Q})\text{Cl}](\text{PF}_6)_2$; the mixture was separated using a neutral alumina column and mononuclear complex was eluted with 5:1 $\text{CH}_2\text{Cl}_2/\text{CH}_3\text{CN}$ mixture. The mononuclear complex $[(\text{tppz})\text{Ru}(\text{Q})(\text{Cl})](\text{PF}_6)$ was treated as above to obtain the nitro complex $[\text{Ru}(\text{NO}_2)(\text{Q})(\text{tppz})](\text{PF}_6)$ which was treated with HPF_6 under argon at room temperature resulting the complex $[\text{Ru}(\text{NO})(\text{Q})(\text{tppz})](\text{PF}_6)_2$.

5.3. Crystal structure

Single crystals of $[\text{Ru}(\text{NO})(\text{Q})(\text{terpy})](\text{PF}_6)_2$ were grown by slow diffusion of diethyl ether into an acetonitrile solution. The complex crystallized in the space group $P2_1/c$. Crystallographic data are summarized in Table 9.5.4. The molecular structure is shown in Figure 5.3.1. The selected bond lengths and bond angles obtained from the crystal structure along with DFT calculated data are summarized in Table 5.3.1-2.

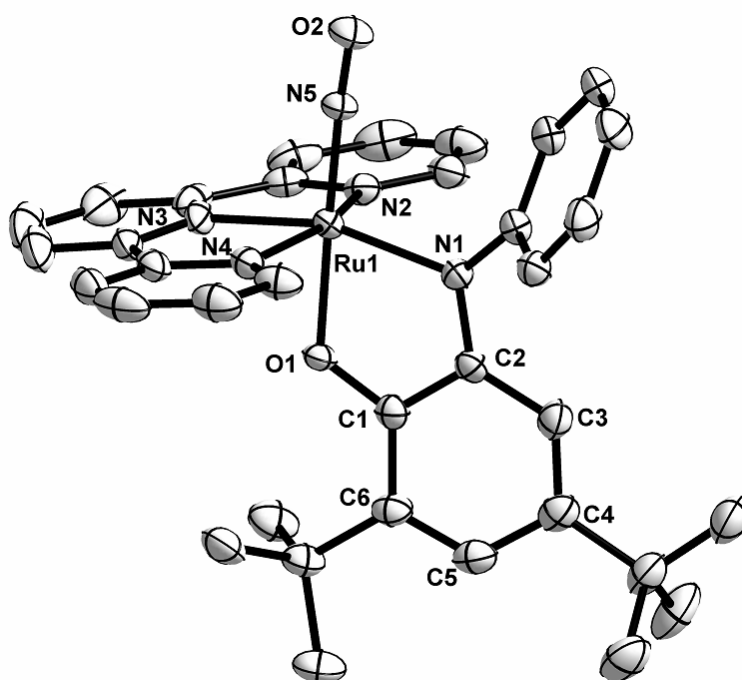


Figure 5.3.1. Molecular structure of the dication of $[\text{Ru}(\text{NO})(\text{Q})(\text{terpy})](\text{PF}_6)_2$ in the crystal.

The geometrical features of the RuNO moiety confirm the $\{\text{RuNO}\}^6$ configuration⁴ via the nearly linear Ru–N5–O2 ($175.2(3)^\circ$) RuNO arrangement (Figure 5.3.1, Table 5.3.1-2) and the typical Ru–N5 ($1.766(3)$ Å) and N5–O2 distances ($1.135(4)$ Å). The metrical parameters in the quinonoid ligand,^{35,61} mainly the C1–O1, C2–N1, C3–C4 and C5–C6 distances (Figure 5.3.1, Table 5.3.1) of $1.324(4)$, $1.349(4)$, $1.361(5)$ and $1.387(5)$ Å, respectively, suggest an iminosemiquinone complex formation. This experimental result is examined by DFT calculations (see section 5.5). It was not possible to obtain single crystals of $[\text{Ru}(\text{NO})(\text{Q})(\text{tppz})](\text{PF}_6)_2$.

Table 5.3.1. Selected bond lengths (Å) of [Ru(NO)(Q)(terpy)](PF₆)₂ with G03/PBE0 calculation results.

| | Experimental | Calculated |
|-------|---------------------|-------------------|
| Ru–N5 | 1.766(3) | 1.764 |
| Ru–N1 | 2.078(3) | 2.088 |
| Ru–N2 | 2.084(3) | 2.102 |
| Ru–N3 | 1.992(3) | 2.006 |
| Ru–N4 | 2.077(3) | 2.102 |
| Ru–O1 | 1.965(2) | 1.972 |
| N5–O2 | 1.135(4) | 1.142 |
| O1–C1 | 1.324(4) | 1.321 |
| N1–C2 | 1.349(4) | 1.354 |
| C1–C2 | 1.441(5) | 1.436 |
| C2–C3 | 1.422(5) | 1.408 |
| C3–C4 | 1.361(5) | 1.384 |
| C4–C5 | 1.434(6) | 1.428 |
| C5–C6 | 1.387(5) | 1.376 |
| C6–C1 | 1.401(5) | 1.420 |

Table 5.3.2. Selected bond angles ($^{\circ}$) of $[\text{Ru}(\text{NO})(\text{Q})(\text{terpy})](\text{PF}_6)_2$ with G03/PBE0 calculation results.

| | Experimental | Calculated |
|----------|--------------|------------|
| O1–Ru–N3 | 82.6(1) | 83.9 |
| N5–Ru–N4 | 92.8(1) | 95.2 |
| O1–Ru–N4 | 86.1(1) | 85.7 |
| N3–Ru–N4 | 79.9(1) | 79.6 |
| N5–Ru–N1 | 98.3(1) | 98.0 |
| O1–Ru–N1 | 79.5(1) | 79.5 |
| N3–Ru–N1 | 162.0(1) | 163.4 |
| N4–Ru–N1 | 97.3(1) | 99.4 |
| N5–Ru–N2 | 93.4(1) | 92.8 |
| O1–Ru–N2 | 88.4(1) | 87.1 |
| N3–Ru–N2 | 80.0(1) | 79.5 |
| N4–Ru–N2 | 159.7(1) | 158.5 |
| N1–Ru–N2 | 100.9(1) | 99.1 |
| O2–N5–Ru | 175.2(3) | 176.3 |

5.4. Electrochemistry

The radical complex ion $[\text{Ru}(\text{NO})(\text{Q})(\text{terpy})]^{2+}$ undergoes facile one-electron oxidation and reduction (Figure 5.4.1). The difference of redox potentials (0.38 V) – (–0.40 V) vs $\text{Fc}^{+/0}$ in $\text{CH}_2\text{Cl}_2/0.1\text{M Bu}_4\text{NPF}_6$) translates to a comproportionation constant K_c of $10^{13.4}$. The electron transfer site alternatives from Scheme 1 have been probed using IR-spectroelectrochemistry. The other radical complex $[\text{Ru}(\text{NO})(\text{Q})(\text{tppz})](\text{PF}_6)_2$ undergoes a quasi-reversible reduction (–0.21 V) and a irreversible oxidation (0.65 V) (Figure 5.4.2). The site of electron uptake has been probed using IR-spectroelectrochemistry.

5.5. IR spectroelectrochemistry

5.5.1. The complex $[\text{Ru}(\text{NO})(\text{Q})(\text{terpy})](\text{PF}_6)_2$

The locations of the oxidation and reduction processes have been investigated by IR-spectroelectrochemistry. The measurements were carried out in CH_3CN solution using the OTTLE cell.⁶⁶ The changes of spectra are shown in Figure 5.5.1.1 and Figure 5.5.1.2.

The complex exhibits an NO band at 1900 cm^{-1} in CH_3CN , a value⁷⁵ which reflects the mixed donor/acceptor of the iminosemiquinonato co-ligand. The results (Table 5.5.1), especially the moderate shifts of 52 cm^{-1} (oxidation) and 70 cm^{-1} (reduction) of the NO stretching frequency, suggest that neither the NO ligand nor the metal are involved to a major extent in the oxidative or reductive electron transfer but that the iminoquinone ligand is the main redox component of this system.

Spectroelectrochemical oxidation of $[\text{Ru}(\text{NO})(\text{Q})(\text{terpy})]^{2+}$ leads to disappearance of the original single $\nu(\text{NO})$ band at 1900 cm^{-1} and formation of two bands at 1919 and 1952 cm^{-1} (Figure 5.5.1.1) which can be tentatively ascribed to two positional isomers A, B (see Figure 5.7.2). Despite of a lower stability of the oxidized form and partial decomposition during the electrolysis time, the process is mostly reversible and on re-reduction the single NO band of the original stable dicationic form is restored. Reduction of the complex reveals an even more complicated behavior (Figure 5.5.1.2). In the early stages of the electrolysis a broad band at 1786 cm^{-1} is growing and subsequently a second sharper band maximum appears at 1830 cm^{-1} . Although only one reduction peak can be distinguished in cyclic voltammetry (Figure 5.4.1), the spectroelectrochemical behavior indicates slightly different potentials corresponding to different (positional) isomers formation. The broadening of NO stretching bands can result from overlapping of the bands of several isomers (see possibilities described in Section 5.7); a limited rotation of the NO group in the species with a markedly bent M-N-O bond, which gives rise to an equilibrium of several rotamers in the solution, is possibly the reason of larger broadening of the band at lower frequency (maximum 1786 cm^{-1}). Reoxidation of the solution obviously containing a mixture of reduced forms (isomers) leads reversibly back to the original single NO-band spectrum of the dicationic form.

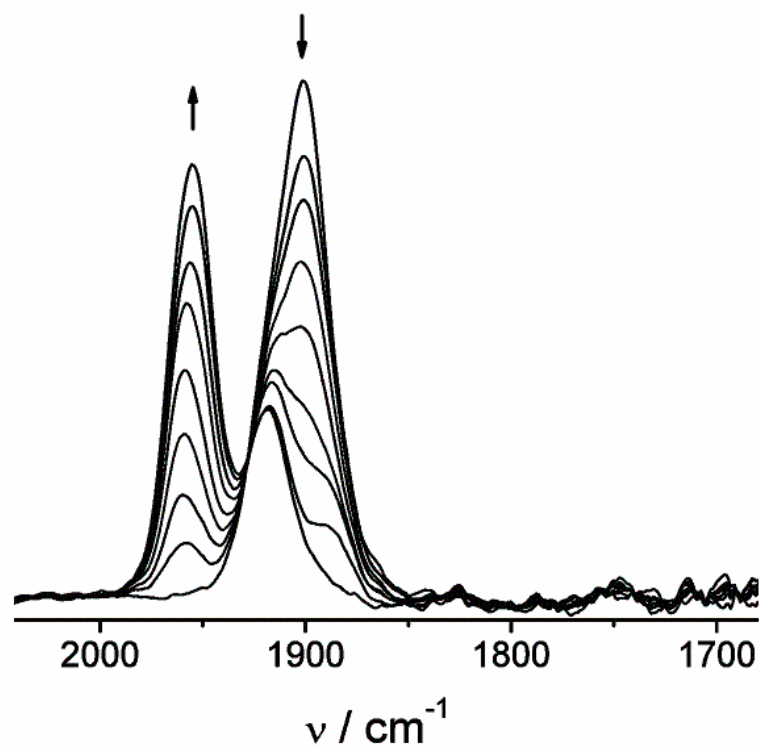


Figure 5.5.1.1. IR spectroelectrochemistry of the conversion $[\text{Ru}(\text{NO})(\text{Q})(\text{terpy})]^{(2+)} \rightarrow (3+)$ in $\text{CH}_3\text{CN} / 0.1 \text{ M Bu}_4\text{NPF}_6$.

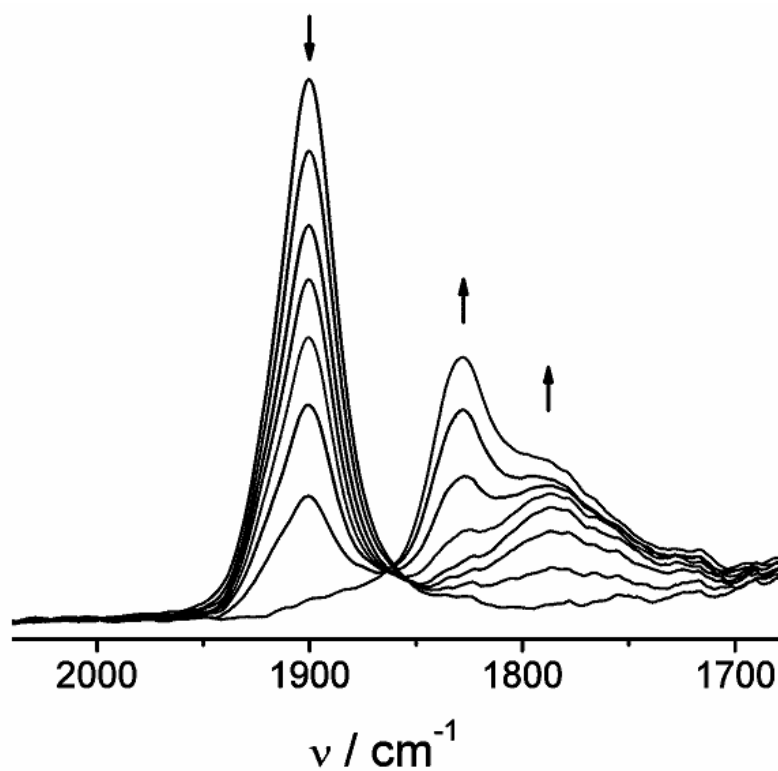


Figure 5.5.1.2. IR spectroelectrochemistry of the conversion $[\text{Ru}(\text{NO})(\text{Q})(\text{terpy})]^{(2+)} \rightarrow (+)$ in $\text{CH}_3\text{CN} / 0.1 \text{ M Bu}_4\text{NPF}_6$.

Table 5.5.1. Comparison of experimental with G03/PBE0 calculated^c NO stretching frequencies for $[\text{Ru}(\text{NO})(\text{Q})(\text{terpy})]^n$.

| n = 3 | | n = 2 | | n = 1 | |
|------------------------|------------------------|------------------------|------------------------|------------------------|------------------------|
| calc. | exp. | calc. | exp. | calc. | exp. |
| ν / cm^{-1} | ν / cm^{-1} | ν / cm^{-1} | ν / cm^{-1} | ν / cm^{-1} | ν / cm^{-1} |
| 1950 ^a | 1952 | 1900 ^a | 1900 | 1833 ^a | 1830 ^d |
| 1941 ^b | 1919 | | | 1700 ^b | 1786 ^d |

^a Calculated for ¹A state.

^b Calculated for ³A state.

^c Scaling factor 0.9326.

^d Part of broad absorption.

5.5.2. The complex $[\text{Ru}(\text{NO})(\text{Q})(\text{tppz})](\text{PF}_6)_2$

Similarly, as in 5.5.2.1 a moderate shift of NO-stretching frequency from 1902 cm^{-1} to broad 1800 cm^{-1} on spectroelectrochemical reduction, suggests that neither the NO ligand nor the metal are involved to a major extent in the reductive electron transfer process but that the iminoquinone ligand is the main redox component of this system.

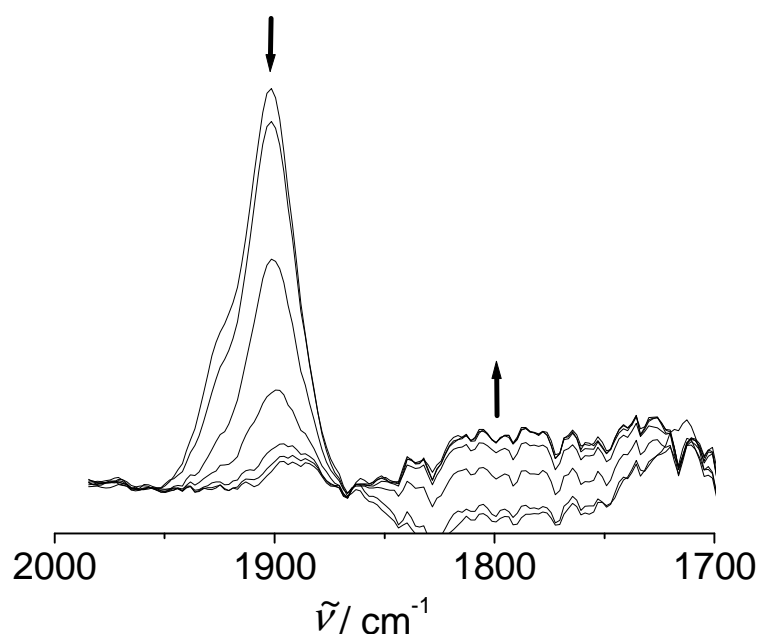


Figure 5.5.2.1. IR spectroelectrochemistry of the conversion $[\text{Ru}(\text{NO})(\text{Q})(\text{tppz})]^{(2+)} \rightarrow ^{(+)}$ in $\text{CH}_3\text{CN} / 0.1 \text{ M Bu}_4\text{NPF}_6$.

5.6. EPR spectroscopy

It was possible to study the isolated odd-electron paramagnetic complexes $[\text{Ru}(\text{NO})(\text{Q})(\text{trpy})](\text{PF}_6)_2$ and $[\text{Ru}(\text{NO})(\text{Q})(\text{tppz})](\text{PF}_6)_2$ by EPR spectroscopy. X-band EPR of both complexes and high frequency EPR for $[\text{Ru}(\text{NO})(\text{Q})(\text{trpy})](\text{PF}_6)_2$ were measured and the spectra are shown in Figures 5.6.1-3.

5.6.1. The complex $[\text{Ru}(\text{NO})(\text{Q})(\text{terpy})](\text{PF}_6)_2$

EPR spectroscopy of $[\text{Ru}(\text{NO})(\text{Q})(\text{terpy})](\text{PF}_6)_2$ suggests very little participation of the metal at the singly occupied MO (SOMO). Specifically, a very small ^{76}g anisotropy $g_1-g_3 = 0.0068$ was observed even at very high frequency (285 GHz, Figure 5.6.2), and an only partially hyperfine-resolved signal at X-band frequency (9.5 GHz) (Figure 5.6.1). Whereas the former reflects the marginal effect of the metal with its high spin-orbit coupling constant,^{24a,26} the latter indicates a small but unresolved contribution from NO to the overall spin distribution and a diminished^{23a} $^{14}\text{N}(\text{imine})$ EPR coupling constant. The corresponding ^{14}N coupling constants were calculated at 0.46 mT (imino-N) and 0.09 mT (nitrosyl-N) which would explain experimental result of an insufficiently resolved EPR spectrum at ambient temperature. *o*-Iminobenzosemiquinones without additional spin delocalization sites have typical ^{14}N hyperfine splitting of about 0.7 mT.^{23a}

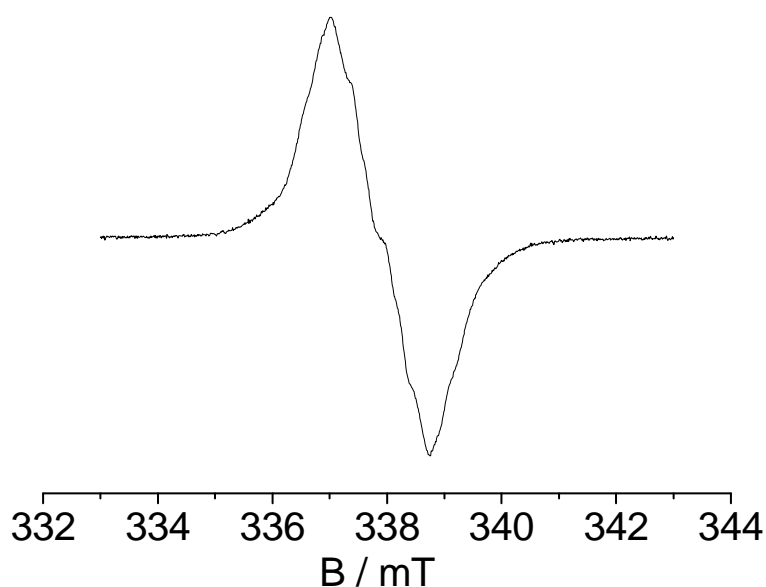


Figure 5.6.1. X-band (9.5 GHz) EPR spectrum of $[\text{Ru}(\text{NO})(\text{Q})(\text{terpy})](\text{PF}_6)_2$ in CH_2Cl_2 at 295 K.

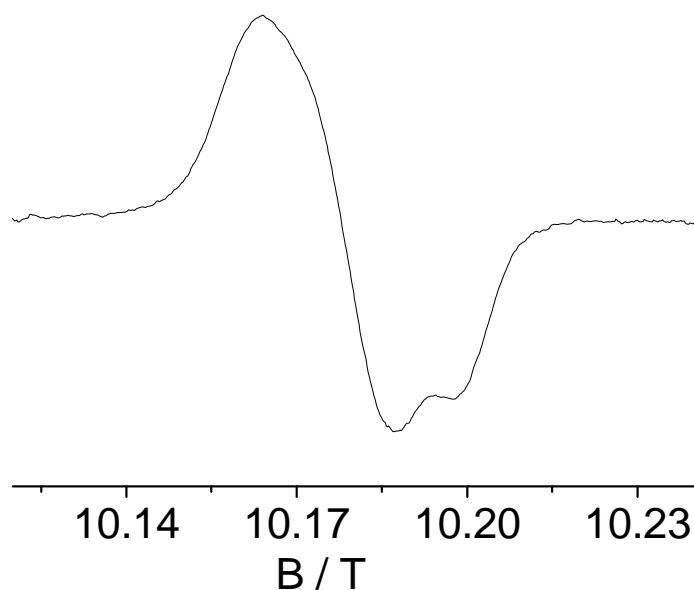


Figure 5.6.2. High-frequency (285 GHz) EPR spectrum of $[\text{Ru}(\text{NO})(\text{Q})(\text{terpy})](\text{PF}_6)_2$ in glassy frozen $\text{CH}_2\text{Cl}_2/\text{toluene}$ at 5 K.

Table 5.6.1. EPR data of complexes $[\text{Ru}(\text{NO})(\text{Q})(\text{terpy})](\text{PF}_6)_2$ and $[\text{Ru}(\text{NO})(\text{Q})(\text{terpy})](\text{PF}_6)_2$

| Complex | ^a g_{iso} | ^b g_1 | ^b g_2 | ^b g_3 | ^c Δg |
|--|-------------------------------|--------------------|--------------------|--------------------|-------------------------|
| $[\text{Ru}(\text{NO})(\text{Q})(\text{trpy})](\text{PF}_6)_2$ | 2.0024 | 2.0036 | 2.0036 | 1.9968 | 0.0068 |
| $[\text{Ru}(\text{NO})(\text{Q})(\text{tppz})](\text{PF}_6)_2$ | 2.0012 | n.o. | n.o. | n.o. | n.o. |

^a g_{iso} : isotropic g value obtained from X band experiment at 295 K in CH_2Cl_2 .

^b From 285 GHz EPR at 5 K in dichloromethane/toluene (4/1).

^c $\Delta g = g_1 - g_3$.

5.6.2. The complex $[\text{Ru}(\text{NO})(\text{Q})(\text{tppz})](\text{PF}_6)_2$

A similar X-band EPR spectrum pattern as in Figure 5.6.1 is observed for the tppz complex $[\text{Ru}(\text{NO})(\text{Q})(\text{tppz})](\text{PF}_6)_2$ (Figure 5.6.3). The poorly hyperfine-resolved signal suggests a small but unresolved contribution from NO to the overall spin density, similar like $[\text{Ru}(\text{NO})(\text{Q})(\text{terpy})](\text{PF}_6)_2$ complex.

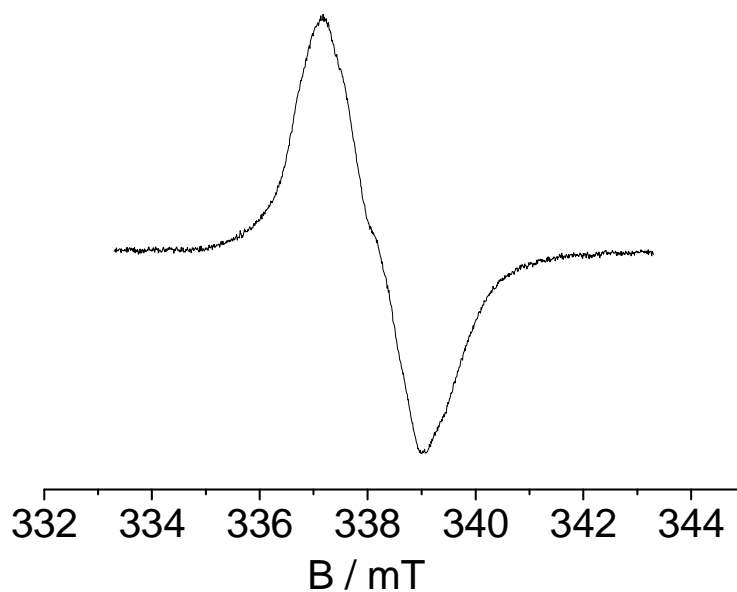


Figure 5.6.3. X-band (9.5 GHz) EPR spectrum of $[\text{Ru}(\text{NO})(\text{Q})(\text{tppz})](\text{PF}_6)_2$ in CH_2Cl_2 at 295 K.

5.7. DFT calculations

DFT calculations for the complex $[\text{Ru}(\text{NO})(\text{Q})(\text{terpy})]^{2+}$ reproduce both the structural (Figure 5.3.1, Table 5.3.1-2) and nitrosyl stretching features (Table 5.5.1) and provide a spin density representation (Figure 5.7.1) with about 15% contribution from the NO group. The calculated Ru–N–O angle and the metrical parameters in the quinonoid ligand are comparable with experimental values.

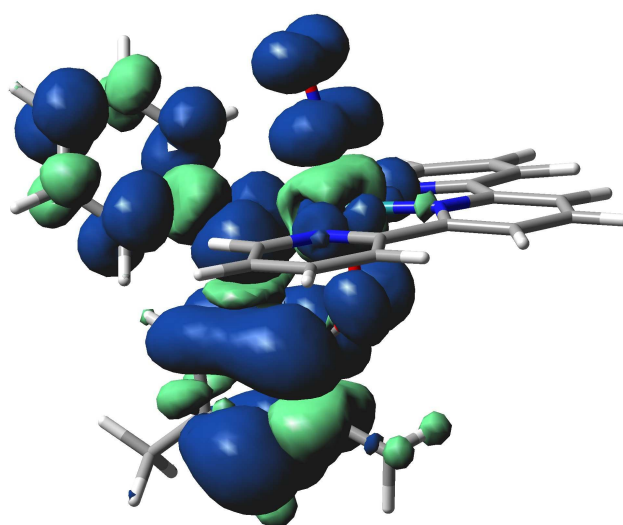


Figure 5.7.1. Representation of spin density in $[\text{Ru}(\text{NO})(\text{Q})(\text{terpy})]^{2+}$.

In addition to existing in three relatively persistent charge states (+/2+/3+), the complexes display a considerable variety of electronic and structural alternatives:

1. The combination of three electron transfer active components, viz., Ru^{II/III/IV}, Q^{0/•-/2-} and NO^{+•/-}, allows for several reasonable alternatives (“valence isomers”) in each charge form (cf. Scheme 1).
2. Positional isomerism of the unsymmetrical chelate Qⁿ relative to Ru(*mer*-terpy)(NO) is possible (A: O *trans* to NO, B: NPh *trans* to NO).

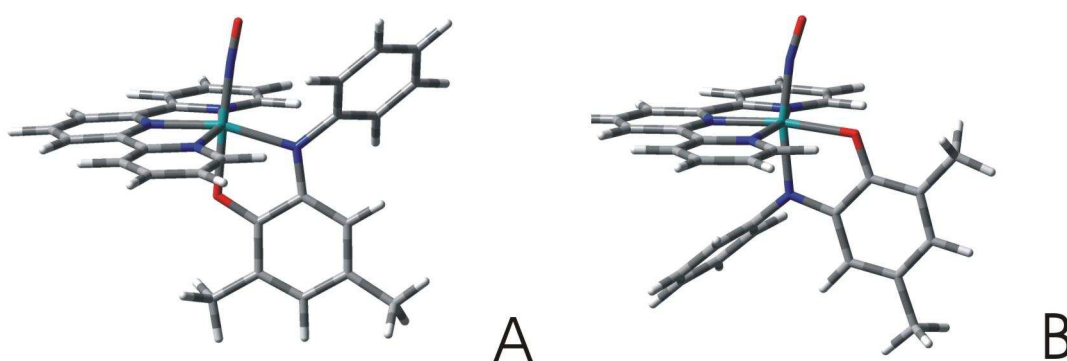


Figure 5.7.2. The most stable DFT optimized structures of $[\text{Ru}(\text{NO})(\text{Q})(\text{terpy})]^{2+}$ positional isomers A(left) and B(right). Configuration A corresponds to the structure listed in Table 5.3.2.

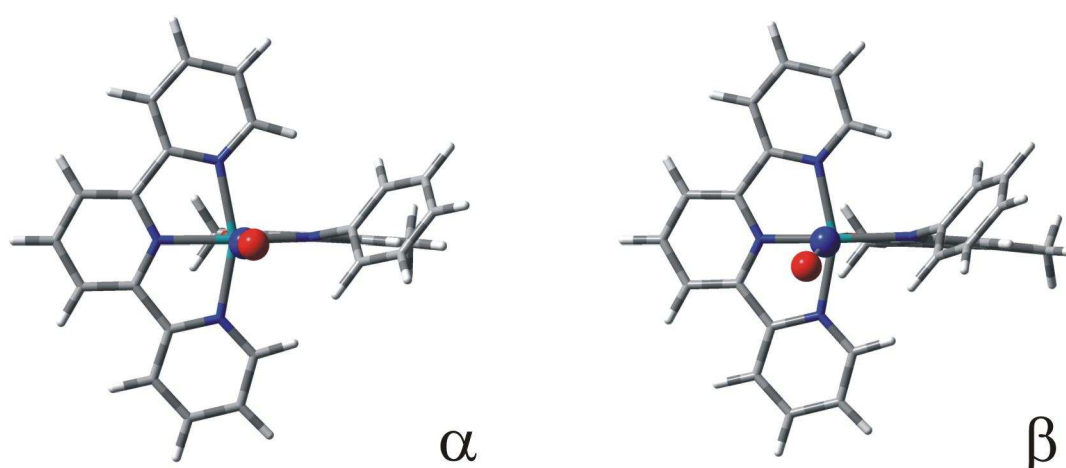


Figure 5.7.3. DFT optimized structures corresponding to different NO orientations in positional isomer A of $[\text{Ru}(\text{NO})(\text{Q})(\text{terpy})]^{2+}$. Ru–N–O angles of 176.3° and 140.9° for rotamers α and β , respectively. The energy minimum for form β was calculated to be 0.3 kcal/mol higher than that of form α .

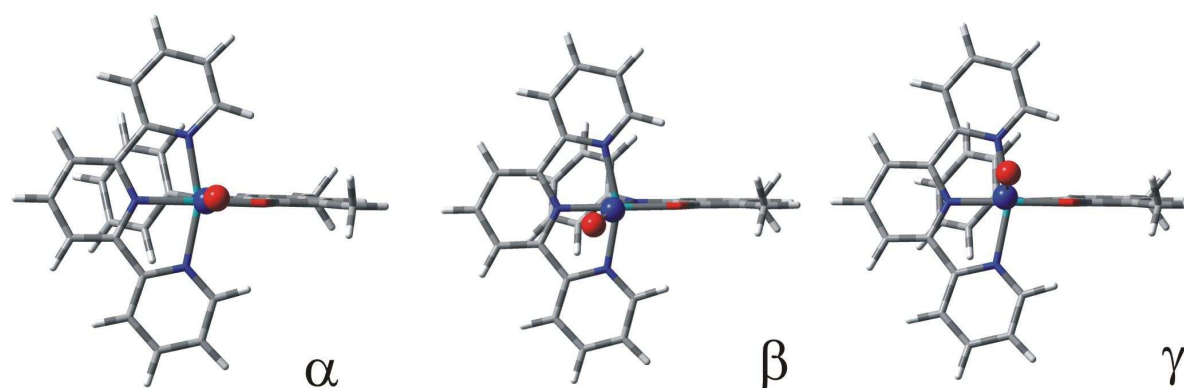


Figure 5.7.4. DFT optimized structures corresponding to different NO orientations in the positional isomer B of $[\text{Ru}(\text{NO})(\text{Q})(\text{terpy})]^{2+}$. Ru–N–O angles of 169.5° , 142.3° and 141.7° were calculated for rotamers α , β and γ , respectively. The energy minima for forms β and γ are 0.5 and 1.9 kcal/mol higher than that of form α , respectively.

3. Spin isomerism is likely when more than one ($S = 1/2$) components such as Ru^{III} , $\text{Q}^{\bullet-}$, or NO^\bullet are simultaneously present in the complex (e.g. singlet vs. triplet states).
4. Even slight bending of the Ru–NO moiety relative to the Ru(terpy) plane may lead to conformational isomers with separate energy minima for favored rotamers (α , β , γ , Figures 5.7.2-4).
5. The phenyl substituent on the N atom of Q^{n} may engage in π/π interaction with the Ru(terpy) plane in configuration B.

The use of G03/PBE0 gave the conformation $\text{A}\alpha$ as the most stable positional and rotational isomer (Figure 5.7.2-3). The energy minimum for the positional the isomer B (Figure 5.7.2) was found with the rotamer α (Figure 5.7.4), $\text{B}\alpha$ lies 2.07 kcal/mol higher in energy than $\text{A}\alpha$. Other rotamers β and γ (Figure 5.7.4) with more bent Ru–N–O and slightly higher NO spin densities lie slightly higher in energy, suggesting some degree of intramolecular charge mobility involving the nitrosyl ligand.

Geometry optimization for $[\text{Ru}(\text{NO})(\text{Q})(\text{terpy})]^{3+}$ in configuration A led to the singlet state of conformation α as the most stable form; the triplet state was found to lie higher by 9.8 kcal/mol. Close to linear arrangement is expected for Ru–(NO^+) (Scheme 5.4.1). In the case of positional isomer B the singlet state conformation $\text{B}\alpha$ was found as the most stable form, it was calculated 9.7 kcal/mol lower in energy than the triplet state. Conformation $\text{B}\alpha$ lies 4.9 kcal/mol higher in energy than $\text{A}\alpha$.

In case of configuration A of $[\text{Ru}(\text{NO})(\text{Q})(\text{terpy})]^+$, the calculation yields as lowest energy species the triplet state of the bent (141.6° for Ru–N–O) rotamer β . The corresponding low NO stretching frequency is calculated at 1700 cm^{-1} (Table 5.5.1), which is not compatible with a $\text{Ru}^{\text{II}}(\text{Q}^{\bullet-})(\text{NO}^{\bullet})$ oxidation state configuration. The next energy minimum is calculated to lie 11.3 kcal/mol higher for the singlet state in the less bent (179.1° for Ru–N–O) $A\alpha$ form of $[\text{Ru}(\text{NO})(\text{Q})(\text{terpy})]^+$, for which a stretching frequency value of 1833 cm^{-1} was calculated which supports the experimentally obtained value 1830 cm^{-1} within a broad absorption range. The observation suggests $\text{Ru}^{\text{II}}(\text{NO}^+)(\text{Q}^{2-})$ as valid oxidation state description. Solvent and counter effects can be responsible for the apparent discrepancy.

5.8. Conclusion

Two paramagnetic complexes $[\text{Ru}(\text{NO})(\text{Q})(\text{terpy})](\text{PF}_6)_2$ and $[\text{Ru}(\text{NO})(\text{Q})(\text{tppz})](\text{PF}_6)_2$ were prepared and the most stable positional isomer of $[\text{Ru}(\text{NO})(\text{Q})(\text{terpy})](\text{PF}_6)_2$ with NO *trans* to the O donor atom of Q was isolated and characterized by single crystal X-ray analysis. It was not possible to obtain single crystals of $[\text{Ru}(\text{NO})(\text{Q})(\text{tppz})](\text{PF}_6)_2$.

In conjunction with the experimental Ru–N–O angle of $175.2(3)^\circ$ and with $\nu(\text{NO}) = 1900\text{ cm}^{-1}$, the EPR studies at 9.5 and 285 GHz reveal a narrow radical-type signal, suggesting $[\text{Ru}^{\text{II}}(\text{NO}^+)(\text{Q}^{\bullet-})(\text{terpy})]^{2+}$ as the most valid oxidation state formulation. DFT calculations confirm this assignment but suggest about 15% NO character of the SOMO, in agreement with the EPR hyperfine features.

Though the crystal structure of $[\text{Ru}(\text{NO})(\text{Q})(\text{tppz})](\text{PF}_6)_2$ was not determined but a similar experimental value of $\nu(\text{NO}) = 1902\text{ cm}^{-1}$ and a radical type EPR signal at 9.5 GHz corresponding to $[\text{Ru}(\text{NO})(\text{Q})(\text{terpy})](\text{PF}_6)_2$ can be assigned to the oxidation state formulation $[\text{Ru}^{\text{II}}(\text{NO}^+)(\text{Q}^{\bullet-})(\text{tppz})]^{2+}$.

Reduction of both complexes and oxidation of the terpy complex cause moderate $\nu(\text{NO})$ shifts to lower and higher frequencies, respectively. This result suggests that neither the NO ligand nor the metal are involved to a major extent in the oxidative or reductive electron transfer but that the iminoquinone ligand is the main redox component of this systems.

CHAPTER 6

A Dinuclear Ruthenium Complex with Tppz as a Bridging Ligand and Non-innocent *o*-Iminobenzoquinone Terminal Ligands

6.1. Introduction

Studies of the electronic interaction between electroactive transition metal centers via a molecular bridge have gratefully contributed to our current understanding in redox reactivity^{67,78} and of its potential in information transfer⁷⁹ and energy-relevant research.⁸⁰ The classical example of the Creutz-Taube ion **1**^{67a} (Figure 6.1.1), a delocalized mixed-valent diruthenium(III, II) species,⁶⁷ has stimulated a wide variety of theoretical,⁸¹ methodical⁸² and conceptual advances.⁸⁴

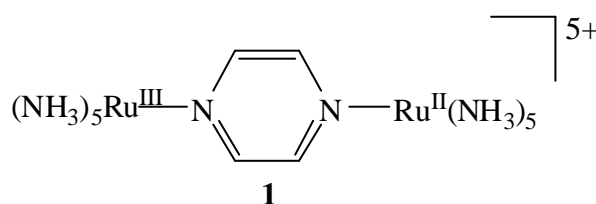
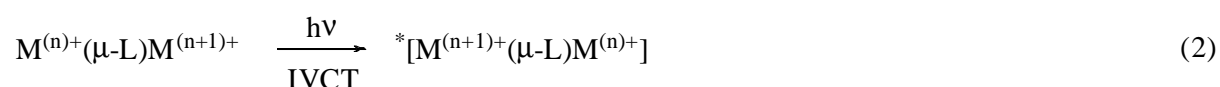
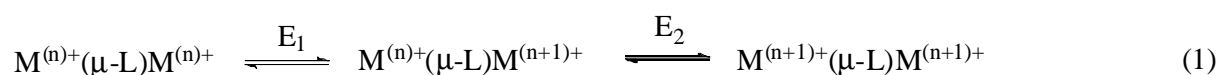


Figure 6.1.1. The Creutz-Taube ion.

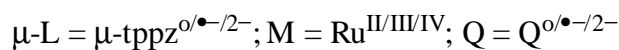
However, in this and many related cases the interesting centers are restricted to the metal ions so that a three-site arrangement, metal-bridge-metal (Scheme 6.1.1: A), could be developed as an adequate description of the bridge-mediated communication (“superexchange”).^{67,81} The role of the organic, frequently π -conjugated bridge has been probed by studying the effect of its variation^{67,83} on the electrochemical and electronic coupling, i.e. on the splitting of redox waves at E1 and E2 for stepwise electron transfer (1), and on the electronic transition to the “inter-valence” charge transfer (IVCT) excited state (2).^{67,78,89}



The coupling of *reaction centers* consisting of more than one atom has been investigated by studying electron/atom transfer sequences⁸⁵ and in a recent, only partially successful attempt

to couple two {Ru(NO)} entities via a conjugated bridge.⁸⁶ Herein the mediated coupling of two substituted mono-*o*-iminobenzoquinonato-ruthenium moieties Q^nRu^m , $Q^0 = 4,6\text{-di-}tert\text{-butyl-N-phenyl-}o\text{-iminobenzoquinone}$, with variable oxidation states of both the and of the (non-innocent) quinonoid ligand,^{32,33} through a bis-tridentate 2,3,5,6-tetrakis(2-pyridyl)pyrazine, $\mu\text{-tppz}$ served as the molecular bridge⁸⁷⁻⁸⁹ $[(Q)ClRu(\mu\text{-tppz})RuCl(Q)](PF_6)_2$, $2(PF_6)_2$, are described. The complex $[Cl(Q)Ru(\mu\text{-tppz})Ru(Q)Cl](PF_6)_2$, containing a five component redox system $[Q^n\text{-}Ru^m\text{-}(\mu\text{-tppz}^x)\text{-}Ru^{m'}\text{-}Q^n]$ (Scheme 6.1.1: B), has been structurally characterized and the accessible redox process (two oxidations and four reductions) were monitored by EPR and UV-Vis-NIR spectroelectrochemistry in order to assign the appropriate oxidation states to all five redox-active components. Tppz is known as a π accepting and thus also potentially non-innocent bis-tridentate bridge in dinuclear radical, mixed-valent and other paramagnetic compounds^{87,88} and in charge conducting coordinating polymers.⁸⁹

Scheme 6.1.1.



6.2. Synthesis and characterization

The precursor complex $Cl_3Ru(\mu\text{-tppz})RuCl_3$ was prepared according to a reported procedure.⁷⁷ The ligand 2-anilino-4,6-di-*tert*-butylphenol was prepared as reported.³³ The dinuclear complex $[(Q)ClRu(\mu\text{-tppz})RuCl(Q)]^{2+}$, $[2]^{2+}$ was synthesized *via* the reaction of the precursor complex $Cl_3Ru(\mu\text{-tppz})RuCl_3$ and the ligand 2-anilino-4,6-di-*tert*-butylphenol (H_2Q) in the presence of CH_3COONa and $LiCl$ in ethanolic medium under an atmospheric condition. The complex was isolated as the phosphate salt $[2](PF_6)_2$. During the chromatographic purification of $[2](PF_6)_2$ on an alumina column, the blue monomeric complex was eluted initially, followed by the green dinuclear complex $[2](PF_6)_2$. The complex shows the presence of only one of the two possible positional isomers (*syn*, *anti*) (Figure 6.2.1) through $^1H\text{-NMR}$ spectroscopy. The complex exhibited satisfactory microanalytical data (see Experimental Section). The formation of $[2](PF_6)_2$ was confirmed by

electrospray mass spectroscopy which showed signals at $m/z = 626.15$, corresponding to $[2]^{2+}/2$ (calculated molecular mass/2, 626.16).

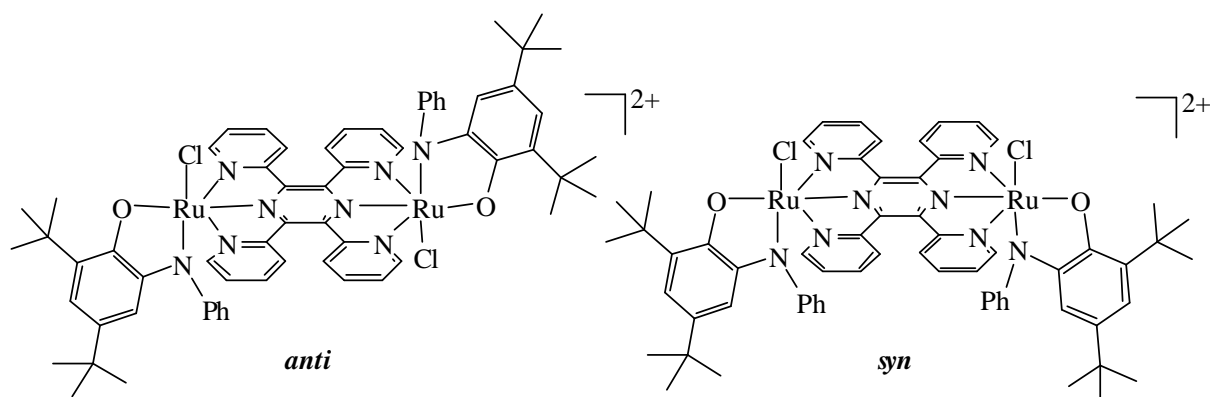


Figure 6.2.1. Representation of the two positional isomers (*anti*, *syn*) of the complex $[2]^{2+}$.

6.3. Crystal structure

Single crystals were obtained as $[2](PF_6)_2 \cdot (C_7H_8)$ from acetonitrile/toluene via the diffusion method. The molecular structure of the complex is shown in Figure 6.3.1. Crystallographic data are summarized in Chapter 9.5.7. Selected bond lengths and bond angles are listed in Table 6.3.1.

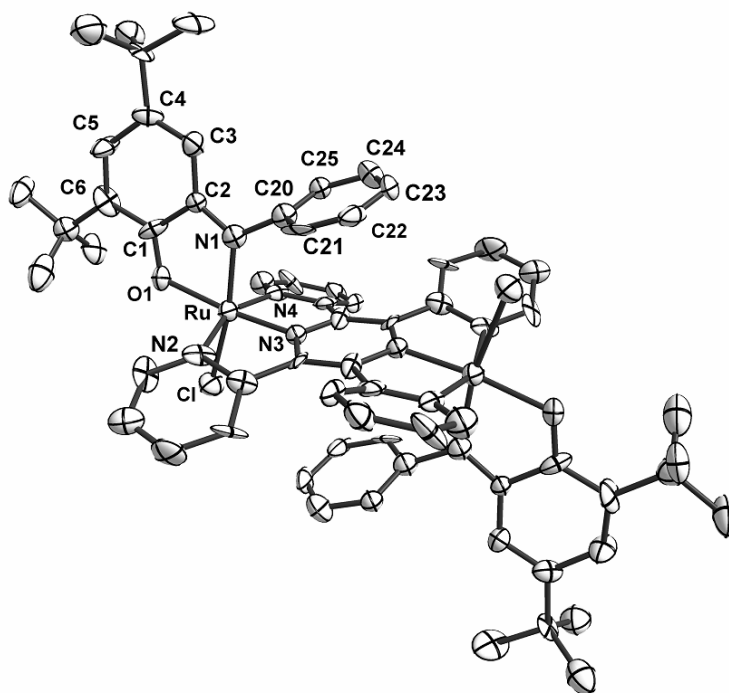


Figure 6.3.1. Molecular structure of the dication of $[2](PF_6)_2$ in the crystal.

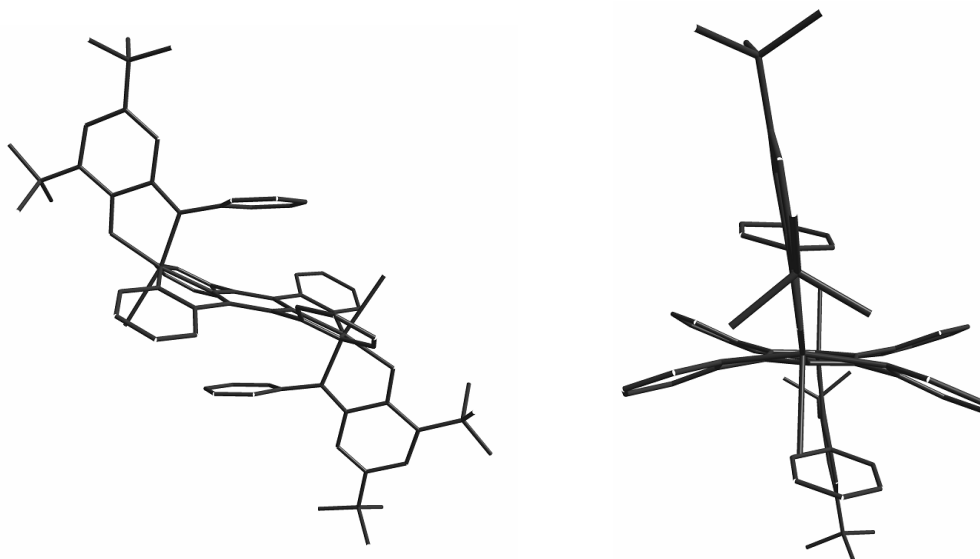


Figure 6.3.2. Structure of the dication of $[2](PF_6)_2$ showing a $\pi/\pi/\pi$ “triple-decker” stacking interaction (left) and conformation of the bridging ligand.

The crystal structure analysis reveals the *anti* isomer, with two *trans* chloride ligands. It also exhibits that chloride ligands are *trans* to each N–Ph part. The N-phenyl substituents of the Q ligands and the central pyrazine ring of the tppz bridge exhibit a $\pi/\pi/\pi$ “triple-decker” stacking interaction (Figure 6.3.2) with N3–C20 as the shortest distances 2.993 Å, the distances between the pyrazine-bridged metal ions is 6.544 Å. The pendent phenyl ring cannot manage to be parallel with the central pyrazine ring. The torsion angles are 21.1° and 24.4°. The two peripheral 4,6-di-*tert*-butyl-N-phenyl-*o*-benzosemiquinonato ligand are present according to established structure criteria such as the intermediate C–O and C=C (meta) distances. Specifically, the oxidation state assignment $[(Q^{\bullet-})-Ru^{III}-(\mu\text{-tppz}^0)-Ru^{III}-(Q^{\bullet-})]$ follows from the fit with statistically derived bond parameters for *o*-C₆H₄XY ligands which arrived at 1.30, 1.35 and 1.36 Å for the CO, CNH and C=C(meta) bonds in *o*-iminobenzosemiquinones, respectively. The C=C(meta) bond is most sensitive among the intra-ring C–C bonds because it clearly shows the transition from a short double bond value in the quinone form (alternating bonds) to an aromatic C–C bond order 1.5 in the fully reduced state. The corresponding experimental values for $[2]^{2+}$ are 1.292(11), 1.321(11) and 1.374(11) Å, respectively. The observed diamagnetism and the semiquinone assignment for Q implies strong antiferromagnetic coupling between $Q^{\bullet-}$ ($S = 1/2$) and coordinated Ru^{III} ($S = 1/2$) on either side of $[2]^{2+}$.

Table 6.3.1. Selected bond lengths (Å) and angles (°) for [2](PF₆)₂•(C₇H₈).

| | | | |
|--------------|-----------|--------------|----------|
| O1 – C1 | 1.292(11) | N3 – Ru – O1 | 171.2(3) |
| N1 – C2 | 1.321(11) | N2 – Ru – N3 | 80.0(3) |
| C6 – C5 | 1.379(13) | N3 – Ru – N4 | 79.1(3) |
| C5 – C4 | 1.469(13) | N4 – Ru – O1 | 103.6(3) |
| C4 – C3 | 1.369(12) | N4 – Ru – N1 | 90.3(3) |
| C1 – C2 | 1.460(12) | N2 – Ru – N1 | 102.5(3) |
| C3 – C2 | 1.430(13) | O1 – Ru – N1 | 77.4(3) |
| C1 – C6 | 1.433(13) | O1 – Ru – N2 | 98.8(3) |
| N1 – Ru – Cl | 167.3(2) | O1 – Ru – N4 | 103.6(3) |
| N2 – Ru – N4 | 156.2(3) | O1 – C1 – C2 | 114.7(8) |
| C2 – N1 – Ru | 117.8(6) | C1 – C2 – N1 | 112.5(9) |

6.4. Electrochemistry

The electrochemistry of the complexes [2](PF₆)₂ has been studied by cyclic voltammetry in CH₃CN solution containing 0.1 M Bu₄NPF₆ as supporting electrolyte. Ferrocene was used as an internal standard and all the redox potentials are referenced with respect to ferrocenium / ferrocene couple (Fc⁺/Fc) couple. The voltammogram is shown in Figure 6.4.1 and the results are listed in Table 6.4.1.

The complex [2](PF₆)₂ can be oxidized in two reversible steps and reduced in four reversible steps, a fifth, partially reversible wave was also detected. EPR and UV-Vis-NIR spectroelectrochemistry were used to analyze the electron configuration for these six additional redox states. Scheme 6.4.1 summarizes the alternatives and preferred interpretations are listed in the left-hand column.

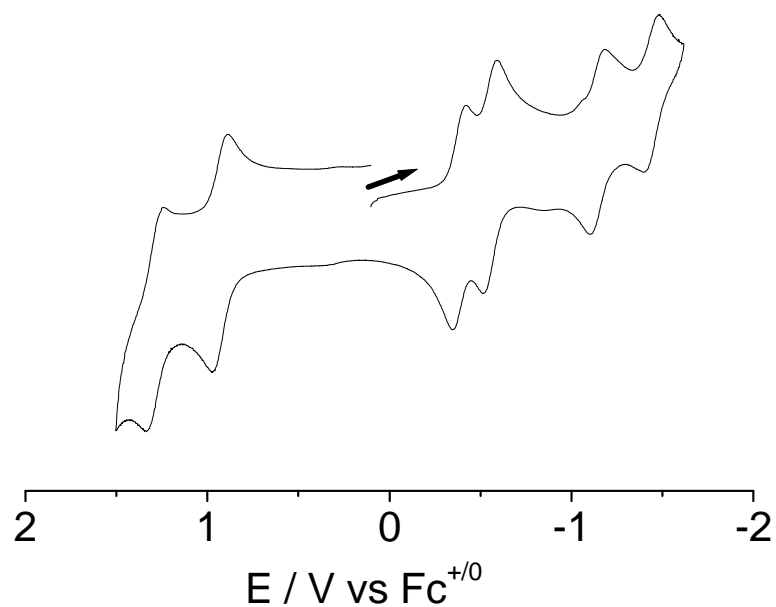


Figure 6.4.1. Cyclic voltammogram of $[2](PF_6)_2$ in $CH_3CN/0.1\ M\ Bu_4NPF_6$.

Table 6.4.1. Redox potentials for $2(PF_6)_2$ from cyclic voltammetry.

| E/V ($\Delta E/mV$) vs $Fc^{0/+}$ ^a | | | | | |
|--|------------|------------|------------|------------|------------|
| ox 1 | ox 2 | red 1 | red 2 | red 3 | red 4 |
| +1.29 (80) | +0.93 (85) | -0.38 (70) | -0.55 (80) | -1.15 (74) | -1.44 (90) |

^a in $CH_3CN/0.1\ M\ Bu_4NPF_6$, 100 mV/s, 298 K.

Scheme 6.4.1. Possible oxidation state distribution of $[2]^n$ ($n = 2-$ to 4).

| E (V) | K_c | assigned oxidation state distribution | alternative(s) |
|-------|------------|---|---|
| 1.29 | | $[\text{ClQ}^{\circ}\text{Ru}^{\text{III}}(\mu\text{-tppz})\text{Ru}^{\text{III}}\text{Q}^{\circ}\text{Cl}]^{4+}$ -e ⁻ ↓ +e ⁻ | or $[\text{ClQ}^{\bullet}\text{Ru}^{\text{IV}}(\mu\text{-tppz})\text{Ru}^{\text{IV}}\text{Q}^{\bullet}\text{Cl}]^{4+}$ |
| 0.93 | $10^{6.1}$ | $[\text{ClQ}^{\circ}\text{Ru}^{\text{II}}(\mu\text{-tppz})\text{Ru}^{\text{III}}\text{Q}^{\circ}\text{Cl}]^{3+}$ -e ⁻ ↓ +e ⁻ | or $[\text{ClQ}^{\circ}\text{Ru}^{\text{III}}(\mu\text{-tppz})\text{Ru}^{\text{III}}\text{Q}^{\bullet}\text{Cl}]^{3+}$ or $[\text{ClQ}^{\bullet}\text{Ru}^{\text{IV}}(\mu\text{-tppz})\text{Ru}^{\text{III}}\text{Q}^{\bullet}\text{Cl}]^{3+}$ |
| -0.38 | | $[\text{ClQ}^{\bullet}\text{Ru}^{\text{III}}(\mu\text{-tppz})\text{Ru}^{\text{III}}\text{Q}^{\bullet}\text{Cl}]^{2+}$ -e ⁻ ↓ +e ⁻ | |
| -0.55 | $10^{2.9}$ | $[\text{ClQ}^{\bullet}\text{Ru}^{\text{II}}(\mu\text{-tppz})\text{Ru}^{\text{III}}\text{Q}^{\bullet}\text{Cl}]^{+}$ -e ⁻ ↓ +e ⁻ | or $[\text{ClQ}^{\bullet}\text{Ru}^{\text{III}}(\mu\text{-tppz}^{\bullet})\text{Ru}^{\text{III}}\text{Q}^{\bullet}\text{Cl}]^{+}$ or $[\text{ClQ}^{2-}\text{Ru}^{\text{III}}(\mu\text{-tppz})\text{Ru}^{\text{III}}\text{Q}^{\bullet}\text{Cl}]^{+}$ |
| -1.15 | | $[\text{ClQ}^{\bullet}\text{Ru}^{\text{II}}(\mu\text{-tppz})\text{Ru}^{\text{II}}\text{Q}^{\bullet}\text{Cl}]$ -e ⁻ ↓ +e ⁻ | or $[\text{ClQ}^{\bullet}\text{Ru}^{\text{III}}(\mu\text{-tppz}^{2-})\text{Ru}^{\text{III}}\text{Q}^{\bullet}\text{Cl}]$ or $[\text{ClQ}^{2-}\text{Ru}^{\text{III}}(\mu\text{-tppz})\text{Ru}^{\text{III}}\text{Q}^{2-}\text{Cl}]$ |
| -1.44 | $10^{4.9}$ | $[\text{ClQ}^{\bullet}\text{Ru}^{\text{II}}(\mu\text{-tppz}^{\bullet})\text{Ru}^{\text{II}}\text{Q}^{\bullet}\text{Cl}]^{-}$ -e ⁻ ↓ +e ⁻ | or $[\text{ClQ}^{2-}\text{Ru}^{\text{II}}(\mu\text{-tppz})\text{Ru}^{\text{II}}\text{Q}^{\bullet}\text{Cl}]^{-}$ |
| -1.86 | | $[\text{ClQ}^{\bullet}\text{Ru}^{\text{II}}(\mu\text{-tppz}^{2-})\text{Ru}^{\text{II}}\text{Q}^{\bullet}\text{Cl}]^{2-}$ -e ⁻ ↓ +e ⁻ | or $[\text{ClQ}^{2-}\text{Ru}^{\text{II}}(\mu\text{-tppz})\text{Ru}^{\text{II}}\text{Q}^{2-}\text{Cl}]^{2-}$ |

6.5. EPR spectroscopy

The six reversible electron transfer processes are monitored by generating odd electron species in situ electrolysis for EPR spectroscopy. Oxidation of diamagnetic, EPR-silent $[2]^{2+}$ results in the appearance of a rhombic EPR signal (Figure 6.5.1, $g_1 = 2.643$, $g_2 = 2.101$, $g_3 = 1.785$) at 110 K in $\text{CH}_3\text{CN}/0.1 \text{ M Bu}_4\text{NPF}_6$ (no signal at 295 K) as is typical for distorted ruthenium(III) in its low-spin d^5 configuration.⁹⁰ Among the several alternatives as given in Scheme 6.4.1 the $[\text{Cl}(\text{Q}^0)\text{Ru}^{\text{II}}(\mu\text{-tppz})\text{Ru}^{\text{III}}(\text{Q}^0)\text{Cl}]^{3+}$ would explain this EPR result indicating a mixed-valent configuration. UV-Vis-NIR results support this assignment (see section 6.6).

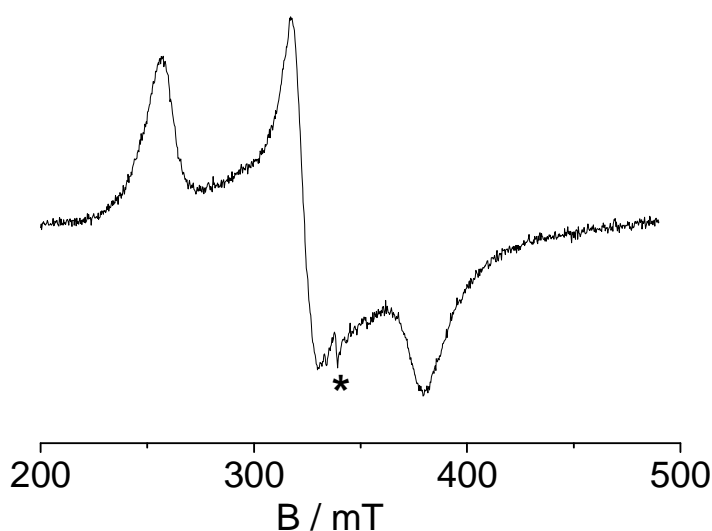


Figure 6.5.1. EPR spectrum of electrogenerated 2^{3+} at 110 K in $\text{CH}_3\text{CN}/0.1 \text{ M Bu}_4\text{NPF}_6$. (*: cavity signal).

The reduction sequence of $[2]^{2+}$ starts with the EPR detected formation of an *o*-iminoquinone radical species ($g_{\text{iso}} = 2.0015$) coordinated to one ruthenium center with hyperfine coupling from ^{14}N ($I = 1$, 99.63%) at 0.50 mT (1 N) and from ^{99}Ru ($I = 5/2$, 12.7%) and ^{101}Ru ($I = 5/2$, 17%) at about 2.1 mT (1 Ru).^{91,23a} Figure 6.5.2(A) confirms this analysis which implies reduction of one ruthenium(III) ion in $[\text{Cl}(\text{Q}^{\bullet})\text{Ru}^{\text{II}}(\mu\text{-tppz}^{\bullet})\text{Ru}^{\text{III}}(\text{Q}^{\bullet})\text{Cl}]^+$; the reduction of reducible^{63a,89} tppz would produce $[\text{Cl}(\text{Q}^{\bullet})\text{Ru}^{\text{III}}(\mu\text{-tppz}^{\bullet})\text{Ru}^{\text{III}}(\text{Q}^{\bullet})\text{Cl}]^+$ which would produce an EPR spectrum with hyperfine coupling to two (pyrazine)N and to two Ru centers.

The closely following second reduction (comproportionation constant $K_c = 10^{2.9}$ for the $[2]^+$ intermediate) shows an EPR spectrum (Figure 6.5.2(B)) at $g_{\text{iso}} = 2.0033$ with $a(^{14}\text{N}) = 0.75 \text{ mT}$ (1 N) and $a(^{99,101}\text{Ru}) = 1.35 \text{ mT}$ (1 Ru). No triplet features (half-field EPR signal) were observed for the neutral $[\text{Cl}(\text{Q}^{\bullet})\text{Ru}^{\text{II}}(\mu\text{-tppz})\text{Ru}^{\text{II}}(\text{Q}^{\bullet})\text{Cl}]$, indicating little magnetic

interaction between the iminosemiquinone radicals separated by $[\text{ClRu}(\mu\text{-tppz})\text{RuCl}]^{2+}$. The smaller metal hyperfine coupling and larger iminosemiquinone-N coupling constant in the doubly reduced species reflect different spin shifts which result from a balanced situation in the neutral compound to a more polarized situation in the monocation. Nevertheless, the ^{14}N values are in the expected range for iminosemiquinones²⁶ and the $^{99,101}\text{Ru}$ satellite coupling is typical for Ru(II) semiquinone complexes.^{23a,92} DFT calculations confirm that the first two reduction steps involve orbitals having large contribution from Q ligands (see section 6.7).

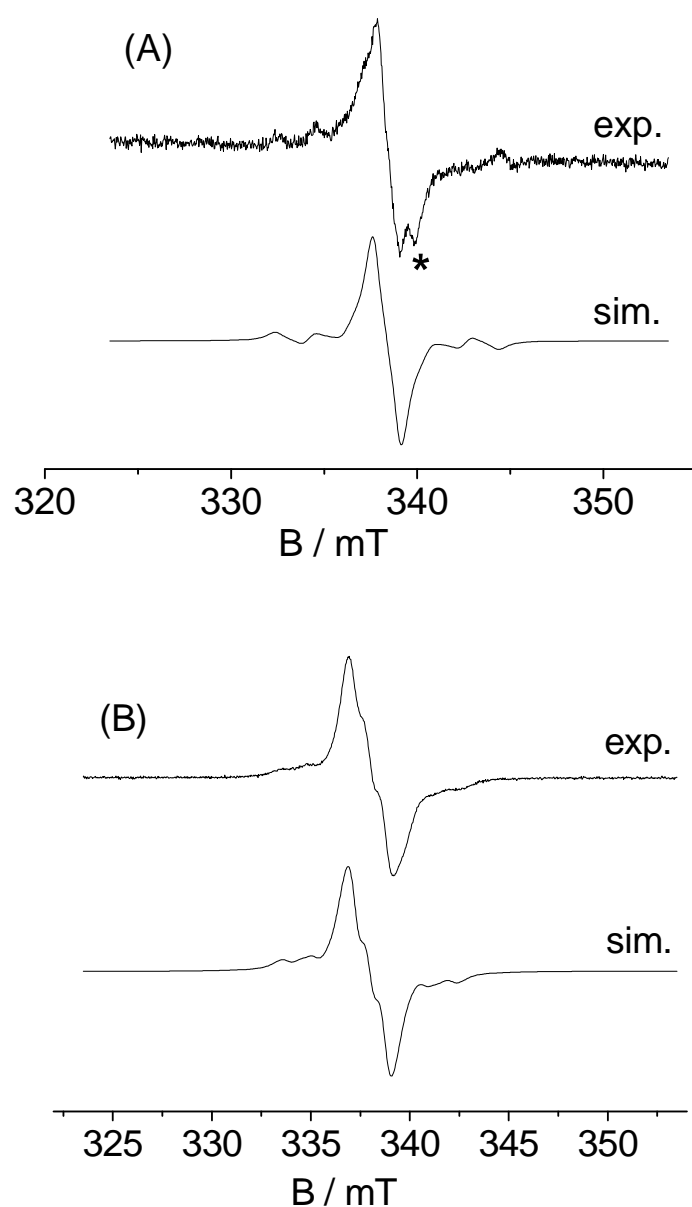


Figure 6.5.2. EPR spectra of electrogenerated $[\mathbf{2}]^+$ (A) and $[\mathbf{2}]^0$ (B) at 295 K in $\text{CH}_3\text{CN}/0.1 \text{ M Bu}_4\text{NPF}_6$, with simulation (*: cavity signal).

On the third reduction the EPR signal at $g_{\text{iso}} = 1.9987$ ($g_1 = 2.015$, $g_2 = 1.998$, $g_3 = 1.985$ at 110 K, Figure 6.5.3) without detectable metal hyperfine splitting confirms^{87,89} the notion of tppz-centered spin, resulting from a three-spin situation $Q^{\cdot-}/\text{tppz}^{\cdot-}/Q^{\cdot-}$ with antiparallel spin-spin interaction of the semiquinone ligands ($\uparrow\uparrow\downarrow$). Related copper(II)-bridged bis-iminosemiquinones were discussed with respect to variable spin exchange patterns.^{33,68}

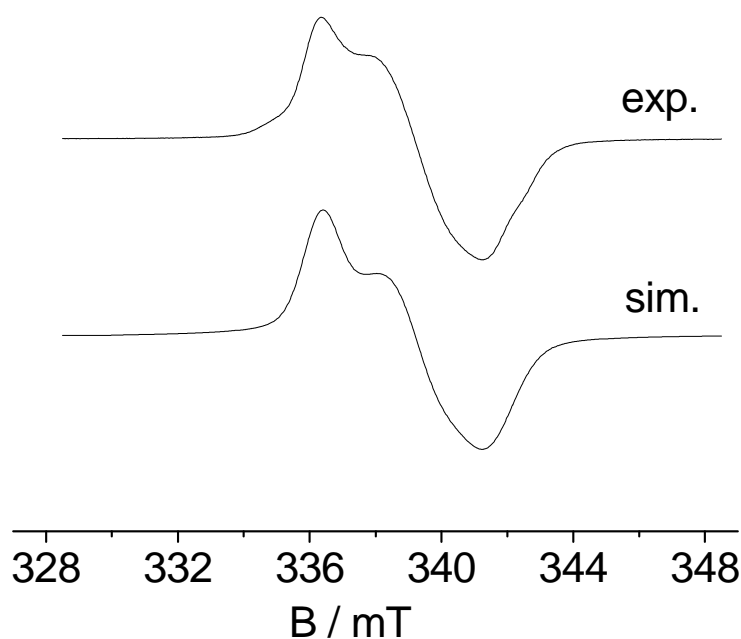


Figure 6.5.3. EPR spectrum of electrogenerated $2^{\cdot-}$ at 110 K in $\text{CH}_3\text{CN}/0.1 \text{ M Bu}_4\text{NPF}_6$, with simulation.

Table 6.5.1. EPR data.

| ^a Complex | g_{iso} | g_1 | g_2 | g_3 | ^d g_{av} | ^e Δg |
|---------------------------|------------------|-------|-------|-------|------------------------------|-------------------------|
| ^b 2^{3+} | ----- | 2.643 | 2.101 | 1.785 | 2.205 | 0.858 |
| ^c 2^+ | 2.0015 | ----- | ----- | ----- | ----- | ----- |
| ^c 2^0 | 2.0033 | ----- | ----- | ----- | ----- | ----- |
| ^b $2^{\cdot-}$ | 1.9987 | 2.015 | 1.998 | 1.985 | 1.9993 | 0.03 |

^a in $\text{CH}_3\text{CN}/0.1 \text{ M Bu}_4\text{NPF}_6$. ^b at 110 K. ^c at 295 K. ^d $g_{\text{av}} = [(g_1^2 + g_2^2 + g_3^2)/3]^{1/2}$.

^e $\Delta g = g_1 - g_3$.

6.6. UV-Vis-NIR spectroelectrochemistry

The electronic configuration of two reversible oxidations and four reversible reductions are analyzed using UV-Vis-NIR spectroelectrochemistry in CH₃CN/0.1 M Bu₄NPF₆.

Oxidation of **2**²⁺ results the emergence and subsequent disappearance (on second oxidation) of an intense near-infrared band at 1853 nm ($\epsilon = 4150 \text{ M}^{-1}\text{cm}^{-1}$, $\Delta\nu_{1/2} = 1350 \text{ cm}^{-1}$) on spectroelectrochemical oxidation in CH₃CN/0.1 M Bu₄NPF₆ (Figure 6.6.1) strongly suggests a mixed-valent configuration $[\text{Cl}(\text{Q}^0)\text{Ru}^{\text{II}}(\mu\text{-tppz})\text{Ru}^{\text{III}}(\text{Q}^0)\text{Cl}]^{3+}$ with a low-energy IVCT transition and a sizeable comproportionation constant of $10^{6.1}$ (Complex **1** has $K_c = 10^{7.3}$ in acetonitrile; $\lambda_{\text{max}} = 1600 \text{ nm}$, $\epsilon = 5000 \text{ M}^{-1} \text{ cm}^{-1}$, $\Delta\nu_{1/2} = 1400 \text{ cm}^{-1}$ in water).^{67a,93} The reduction of one ruthenium(III) center from the initial configuration $[\text{Cl}(\text{Q}^{\bullet-})\text{Ru}^{\text{III}}(\mu\text{-tppz})\text{Ru}^{\text{III}}(\text{Q}^{\bullet-})\text{Cl}]^{2+}$ of **2**²⁺ on *oxidation* to **2**³⁺ is made possible through the twofold oxidation of the iminosemiquinone to the iminoquinone state. Such “oxidation-leading-to-oxidation” mechanisms, also addressed as “redox-induced electron transfer” (RIET),⁹⁴ have raised in the context of mixed-valency^{67,83} and valence tautomerism.⁹⁵ Some salient examples have been reviewed very recently and another example involving group 8 metal coordination chemistry of singlet diradical species has been reported.⁹⁶ The reverse pattern, a “reduction-leading-to-oxidation” mechanism, also based on intramolecular valence redistribution, has also been discussed for oligonuclear ruthenium complexes.⁹⁷ The second oxidation to **2**⁴⁺ is likely to produce $[\text{Cl}(\text{Q}^0)\text{Ru}^{\text{III}}(\mu\text{-tppz})\text{Ru}^{\text{III}}(\text{Q}^0)\text{Cl}]^{4+}$, all three forms **2**²⁺, **2**³⁺ and **2**⁴⁺ exhibit an intense ($\epsilon > 10000 \text{ M}^{-1} \text{ cm}^{-1}$) MLCT/LLCT charge transfer band (Ru, Q^{•-} → $\pi^*(\text{tppz})$) at 600–700 nm.

On one-electron reduction **2**²⁺ → **2**⁺ the lowest energy charge-transfer band at 684 nm ($\epsilon = 28750 \text{ M}^{-1} \text{ cm}^{-1}$) undergoes a substantial decrease in intensity and further diminishes on second reduction **2**⁺ → **2**⁰ along with a new band 750 nm and a shoulder around 1033 nm (Figure 6.6.2). EPR and DFT results imply that the two successive closely spaced reduction occurred preferentially on the two metal centers resulting the $[\text{Cl}(\text{Q}^{\bullet-})\text{Ru}^{\text{II}}(\mu\text{-tppz})\text{Ru}^{\text{II}}(\text{Q}^{\bullet-})\text{Cl}]$ electronic configuration. Thus the new band 750 nm and the shoulder 1033 nm after the second reduction could be assigned Q^{•-}/tppz targeted MLCT and Q^{•-} → $\pi^*(\text{tppz})$ LLCT transitions.

On the third reduction a characteristic absorption appears at ca. 960 nm (Figure 6.6.3) which is typical for tppz^{•-}.⁸⁷⁻⁸⁹ The fourth reduction is also believed to occur at the tppz bridge because the absorption intensity emerging at about 1200 nm (Figure 6.6.3) has similarly been observed for other diruthenium complexes tppz²⁻.⁸⁷

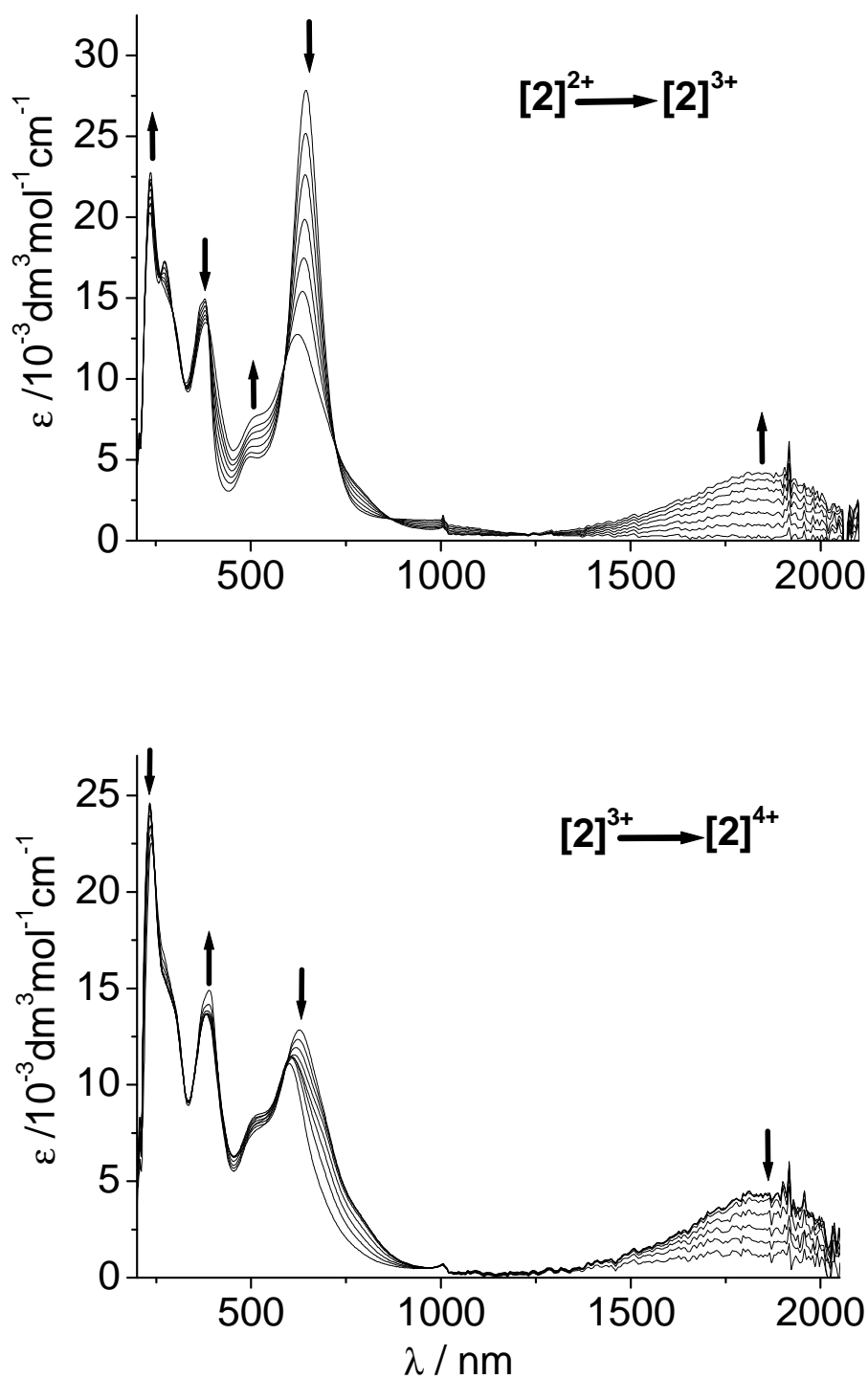


Figure 6.6.1. UV/Vis/NIR-Spectroelectrochemical response of system [2]²⁺ on oxidation in CH₃CN/0.1 M Bu₄NPF₆.

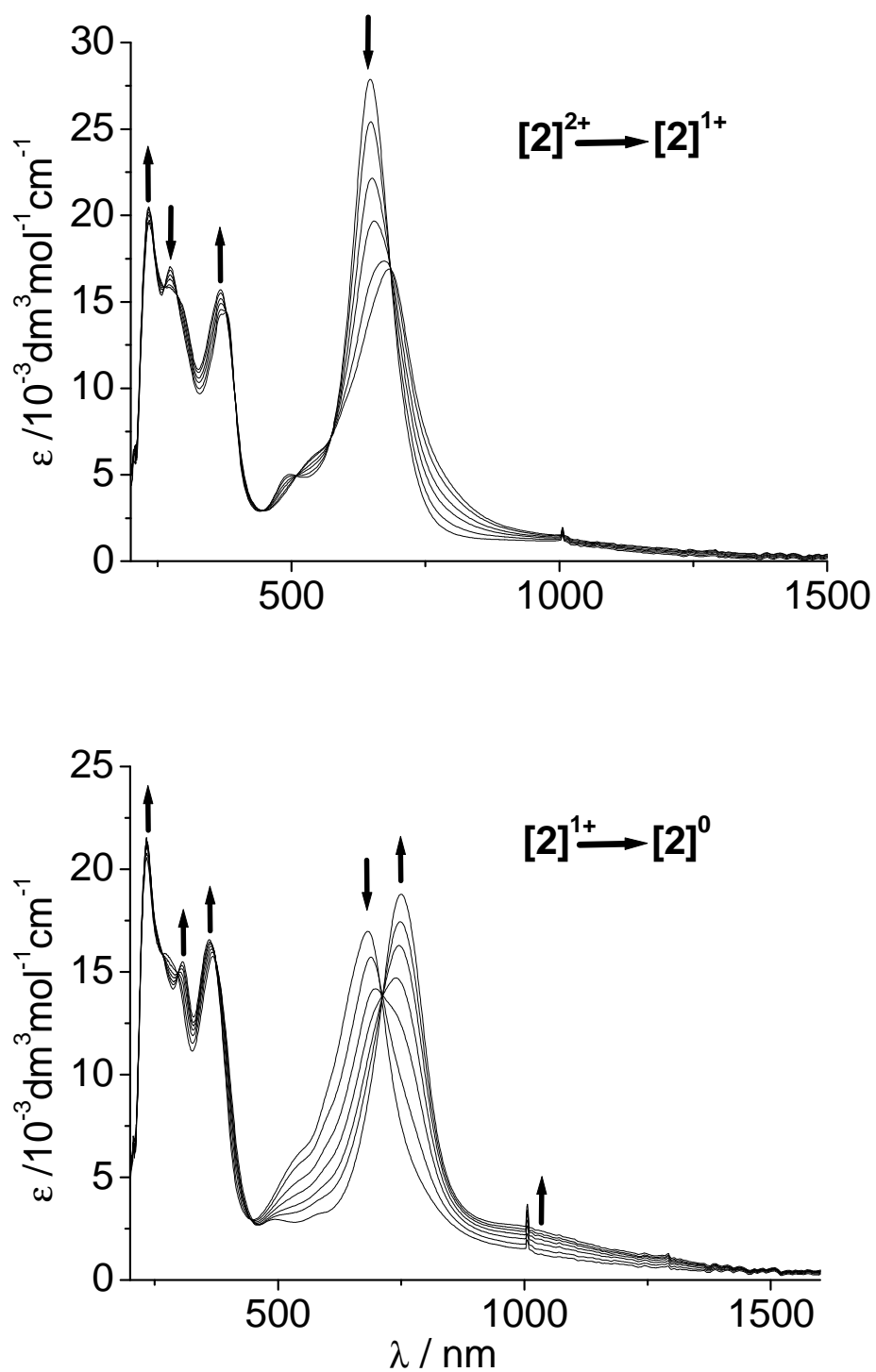


Figure 6.6.2. UV/Vis/NIR-Spectroelectrochemical response of system 2^{2+} on reduction in $\text{CH}_3\text{CN}/0.1 \text{ M Bu}_4\text{NPF}_6$ (first two steps).

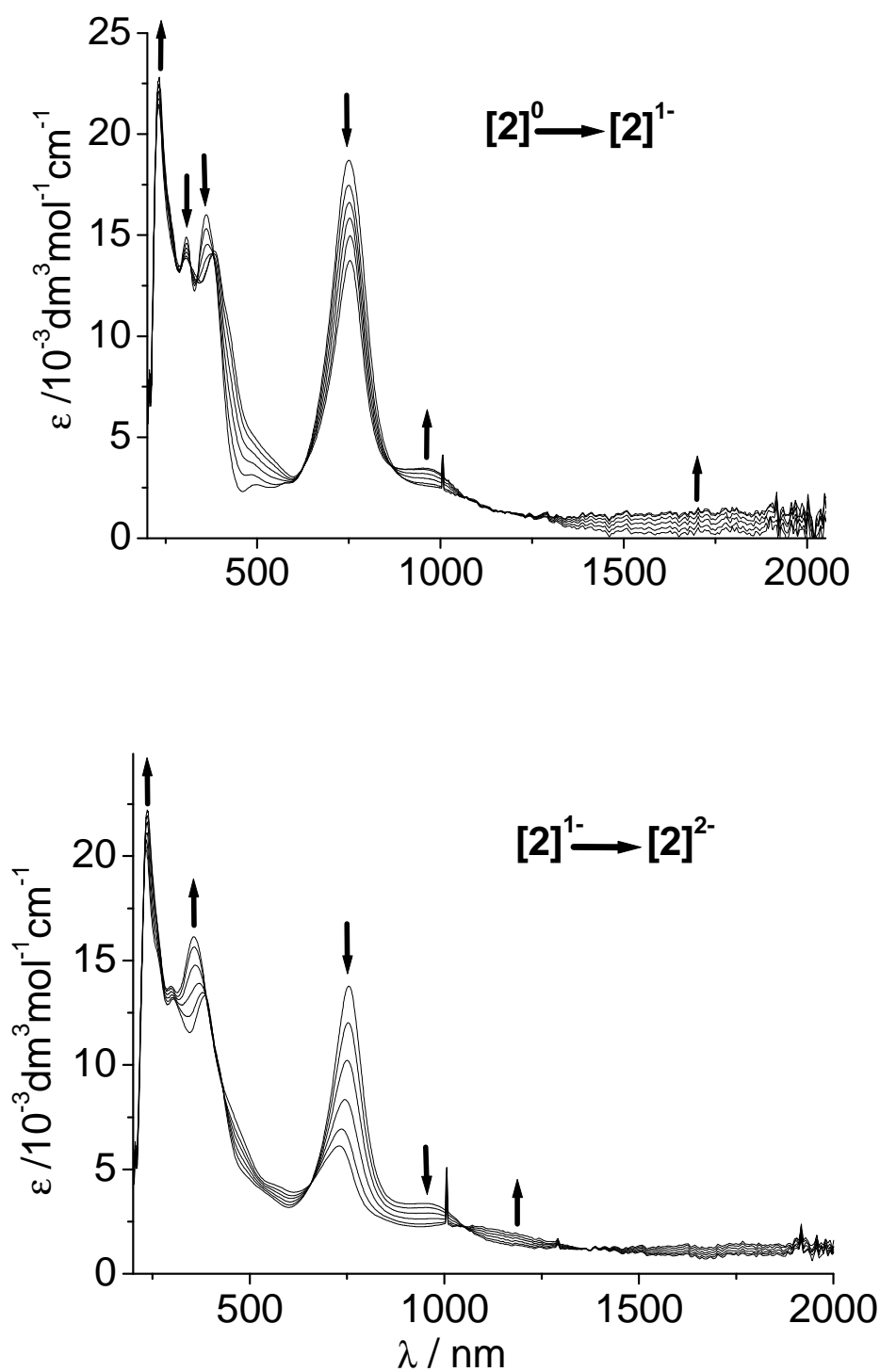


Figure 6.6.3. UV/Vis/NIR-Spectroelectrochemical response of system $[2]^{2+}$ on reduction in $\text{CH}_3\text{CN}/0.1 \text{ M Bu}_4\text{NPF}_6$ (third and fourth step).

6.7. DFT calculations

The electronic structures of $[\text{Cl}(\text{Q})\text{Ru}(\mu\text{-tppz})\text{Ru}(\text{Q})\text{Cl}]^{n+}$ ($n = 1, 2, 3$) were calculated by the density functional theory (DFT) method. Electronic transitions were calculated by the time-dependent DFT (TD DFT) method.

The composition of frontier orbitals as listed in Table 6.7.1 and depicted in Figure 6.7.1 and the qualitative DFT-calculated MO energy diagram of $\mathbf{2}^{2+}$ in Figure 6.7.2 show that the highest occupied molecular orbital (HOMO) (Figure 6.7.1) is predominantly centered at the Ru–Cl moieties and that the lower lying occupied orbitals have also mainly ruthenium character. The set of two energetically close lowest lying unoccupied MOs (LUMOs) with large contributions from π^*_Q orbitals is followed by two nearly degenerate π^*_{tppz} based unoccupied orbitals. Using this information and TD DFT methodology, the intense absorption at 684 nm in $\mathbf{2}^{2+}$ can be assigned to an MLCT transition from the HOMO to the LUMO+2 (Table 6.7.2). Figure 6.7.3 confirms that the DFT calculated spin density in $\mathbf{2}^{3+}$ is mainly localized on the metal centers, with some contribution from Cl and slightly negative spin density on the tppz bridging ligand. G03/PBE0 calculations yield cumulated spin densities of 1.116, 0.186 and -0.280 for Ru, Cl and tppz, respectively. No significant spin density was calculated for the Q ligand in $\mathbf{2}^{3+}$.

DFT calculations confirm that the first two reduction steps involve orbitals having large contributions from the Q ligand (Table 6.7.1, Figure 6.7.1). The spin density of the one-electron reduced form is calculated to be mainly delocalized over the π^* systems (Q, with smaller contributions from $\mu\text{-tppz}$) and with little participation of Ru, as shown in Figure 6.7.3. The cumulated densities for $\mathbf{2}^+$ are 0.719, -0.097 and 0.377 for Q, Ru and tppz respectively.

Table 6.7.1. DFT G03/PBE0 calculated one-electron energies and compositions of selected highest occupied and lowest unoccupied molecular orbitals of $[\text{Cl}(\text{Q})\text{Ru}(\mu\text{-tppz})\text{Ru}(\text{Q})\text{Cl}]^{2+}$ expressed in terms of composing fragments.

| MO | E (eV) | Prevailing character | Ru | tppz | Q | Cl |
|--------------|--------|--------------------------|----|------|----|----|
| Unoccupied - | | | | | | |
| LUMO+4 | -6.49 | π^* tppz | 6 | 92 | 1 | 1 |
| LUMO+3 | -7.36 | π^* tppz + Ru | 14 | 67 | 18 | 0 |
| LUMO+2 | -7.38 | π^* tppz + Ru | 20 | 69 | 9 | 2 |
| LUMO+1 | -7.69 | π^* Q + Ru | 17 | 6 | 76 | 1 |
| LUMO | -7.87 | π^* Q + π^* tppz | 6 | 37 | 55 | 1 |
| Occupied | | | | | | |
| HOMO | -10.03 | Ru + Cl | 55 | 11 | 9 | 24 |
| HOMO-1 | -10.34 | Ru + Q + Cl | 39 | 5 | 37 | 19 |
| HOMO-2 | -10.36 | Ru + Q + Cl | 38 | 5 | 37 | 20 |
| HOMO-3 | -10.60 | Cl + Ru | 26 | 18 | 7 | 48 |
| HOMO-4 | -10.85 | Ru + Q | 48 | 14 | 48 | 0 |
| HOMO-5 | -10.96 | Ru + Q | 41 | 9 | 47 | 4 |
| HOMO-6 | -11.04 | Q | 12 | 4 | 53 | 31 |
| HOMO-7 | -11.09 | Q | 21 | 6 | 44 | 29 |

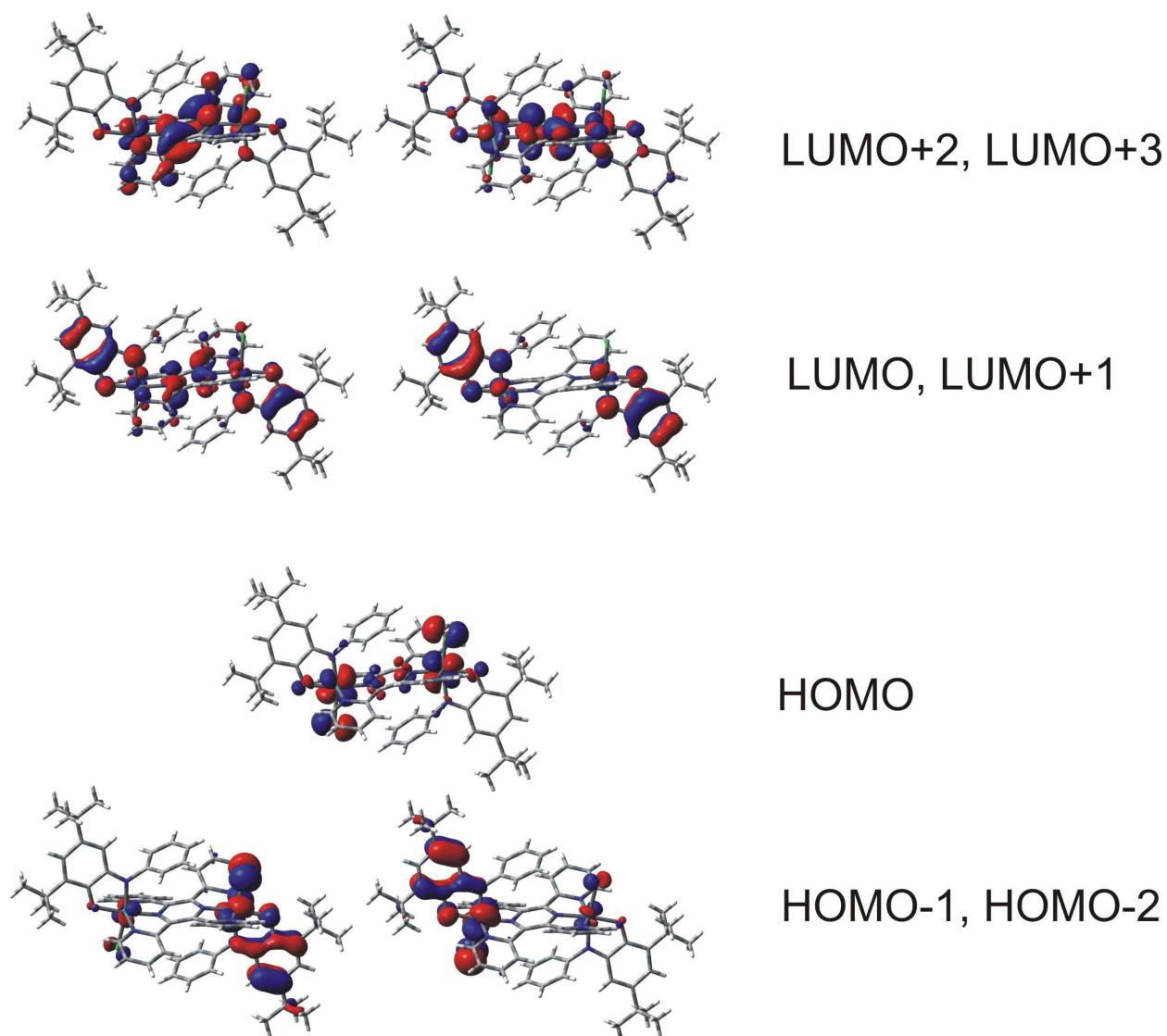


Figure 6.7.1. Representation frontier orbitals of 2^{2+} .

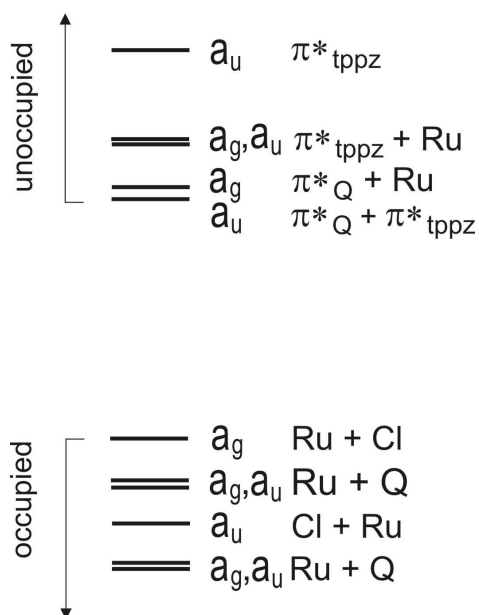


Figure 6.7.2. Qualitative DFT calculated MO scheme of $[\mathbf{2}]^{2+}$. Approximate C_i symmetry is used for the labeling of molecular orbitals.

Table 6.7.2. Selected G03/PBE0/CPCM calculated lowest allowed TD-DFT singlet transitions for $[\mathbf{2}]^{2+}$.

| state | main character (in %) | calc. | exp. | |
|----------------|--|--------------------------------|------------------|-----------------------------------|
| | | transition energy ^a | oscill. strength | $\lambda_{\text{max}}/\epsilon^b$ |
| ¹ A | 42(HOMO-2→LUMO); 43 (HOMO-1→LUMO+1) | 1.51(817) | 0.018 | 684 (28750) |
| ¹ A | 75 (HOMO→LUMO+3) | 1.98 (625) | 0.025 | |
| ¹ A | 70 (HOMO→LUMO+2) | 2.08 (595) | 0.434 | |
| ¹ A | 88 ((HOMO-2→LUMO+2) | 2.19 (565) | 0.209 | |
| ¹ A | mixed | 2.36 (523) | 0.211 | 489 (sh) |
| ¹ A | 66 (HOMO-4→LUMO) | 2.41 (514) | 0.156 | |
| ¹ A | 75 ((HOMO-5→LUMO+1) | 2.81 (441) | 0.130 | 378 (14850) |

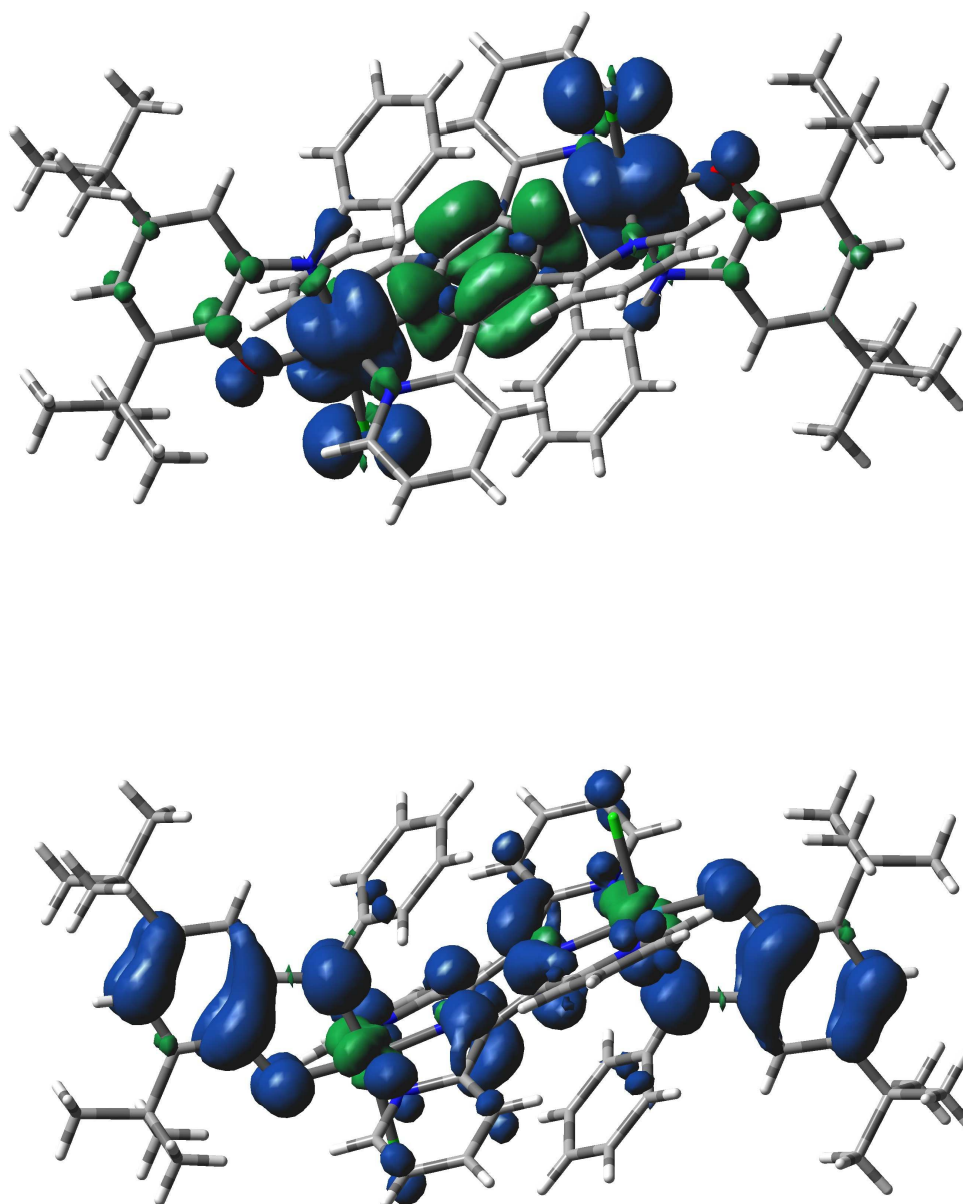


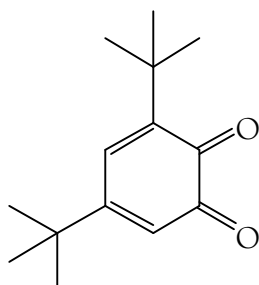
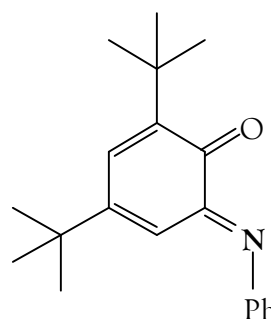
Figure 6.7.3. DFT calculated spin densities of $[2]^{3+}$ (top) and $[2]^+$ (bottom).

6.8. Conclusion

Having combined the concepts of non-innocent ligand (NIL) behavior² and intramolecular electronic exchange between equivalent electron transfer sites across active bridges (BL),⁶⁷ a first symmetrical five-center system $[\text{Cl}(\text{Q})\text{Ru}(\mu\text{-tppz})\text{Ru}(\text{Q})\text{Cl}]^n = \text{NIL} // \text{M} // \text{BL} // \text{M} // \text{NIL}$, combining two non-innocent ligand/metal (NIL/M) situations^{2,23} with a classical pyrazine-bridged diruthenium configuration for mixed-valency^{67,97} are presented. Starting from a structurally defined iminosemiquinonato-ruthenium(III) containing precursor, a total of 6 additional redox states involving $\text{Ru}^{\text{III,II}}$, $\text{tppz}^{\text{o},\bullet,-,2-}$, and $\text{Q}^{\text{o},\bullet,-,2-}$ were reversibly accessible by EPR and UV-VIS-NIR spectroelectrochemistry, illustrating remarkable alternatives for intramolecular electron transfer such as mixed valency, redox-induced electron transfer, and three-spin exchange. EPR spectroelectrochemistry has turned out to be a particularly valuable tool, in agreement with DFT calculated spin densities it revealed metal-based spin for the oxidized state and various combinations of ligand-based spin for the first three reduced forms of $[\text{Cl}(\text{Q})\text{Ru}(\mu\text{-tppz})\text{Ru}(\text{Q})\text{Cl}](\text{PF}_6)_2$. These informations have allowed us to identify the most appropriate oxidations state combinations for the individual charge forms as listed in Scheme 6.4.1. The results demonstrate that not only conventional transition metal ions,^{67a} non-metal electron transfer sites,^{98,99} metal clusters,⁹⁷ or bond-breaking and -re-forming reaction centers¹⁰ can be electronically coupled by active bridges but also composite electron transfer moieties such as metal/non-innocent ligand entities, adding another dimension to mixed-valence chemistry. It remains to be investigated whether even more extended and complex configurations involving non-innocent terminal or bridging ligands and electro- and spin-active metal centers can be constructed and their intramolecular spin and valence exchange behavior analyzed.

CHAPTER 7**Spectroelectrochemical (UV-Vis-NIR and EPR) and Theoretical Studies of the Redox Series $[M(Q_O)_3]^n$ ($Q_O = 3,5$ -Di-*tert*-butyl-*o*-benzoquinone $M = Ru$ and Os) and $[M(Q)_3]^n$ ($Q = 4,6$ -Di-*tert*-butyl-*N*-phenyl-*o*-iminobenzoquinone, $M = Ru$), $n = +2$ to -2** **7.1. Introduction**

A great amount of work^{7,8,32} has been carried out in establishing the interaction between redox-active transition-metals and *o*-benzoquinone or *o*-iminobenzoquinone π systems. These ligands can bind to the metal centre in three different electronic forms, viz., as *o*-benzoquinone/*o*-iminoquinone (Q_O^0/Q^0), as *o*-semiquinonato/*o*-iminosemiquinonato ($Q_O^{\cdot-}/Q^{\cdot-}$), or as catecholato/*o*-anilidophenolato (Q_O^{2-}/Q^{2-}) ligands. The mixing of metal and ligand based frontier orbitals is a remarkable phenomenon^{27,33} for complexes containing quinone ligands. Ruthenium or osmium-quinonoid systems show considerable mixing^{26,60b} between the orbitals of the metal and the quinonoid moiety and thus ambiguities arise to assign their precise valence-state configurations in different redox forms. The $M(Q_O)_3$ complexes of Ru and Os have been reported¹⁰¹ by Pierpont and coworkers, where Q_O corresponds to 3,5-di-*tert*-butyl-*o*-benzoquinone. The Ru complex has been formulated^{101,102} as containing three semiquinonato ($Q_O^{\cdot-}$) ligands and the Os complex with three catecholato (Q_O^{2-}) ligands. However, no detail spectroscopic investigations have been presented estimating the metal-ligand orbital mixing in the respective accessible redox states.

3,5-di-*tert*-butyl-*o*-benzoquinone (Q_O)4,6-di-*tert*-butyl-*N*-phenyl-*o*-iminobenzoquinone (Q)**Figure 7.1.1.** Molecular formulae of two non-innocent ligands (quinone forms).

This Chapter describes reported complexes $\text{Ru}(\text{Q}_\text{O})_3$ and $\text{Os}(\text{Q}_\text{O})_3$ along with the newly synthesized $\text{Ru}(\text{Q})_3$ complex where Q corresponds to well applied and recently reviewed^{3a} 4,6-di-*tert*-butyl-N-phenyl-*o*-iminobenzoquinone ligand (Table 7.1.1, Figure 7.1.1). The complexes were studied with the aim of establishing the electronic configuration in the oxidized and reduced forms using EPR and UV-Vis-NIR spectroelectrochemistry techniques and finally DFT and TD-DFT calculations have been performed to interpret these experimental results.

Table 7.1.1. Numbering of the complexes.

| Complex | no. |
|----------------------------------|----------|
| $\text{Ru}(\text{Q})_3$ | 1 |
| $\text{Os}(\text{Q})_3$ | 2 |
| $\text{Ru}(\text{Q}_\text{N})_3$ | 3 |

7.2. Syntheses and characterization

Complexes **1** and **2** were prepared according to the literature procedure.¹⁰¹ The diamagnetic complexes **1** and **2** were formulated with $\text{Ru}^{\text{III}}(\text{Q}_\text{O}^{\cdot-})_3$ and $\text{Os}^{\text{VI}}(\text{Q}_\text{O}^{2-})_3$ electronic configurations by Pierpont and coworkers.^{101,102} The complexes show narrow ^1H -NMR line attributed strong antiferromagnetic coupling¹⁰¹ between the unpaired spins (in the case of the Ru compound).

The new diamagnetic complex **3** was prepared by the reaction of RuCl_3 and 2-anilino-4,6-di-*tert*-butylphenol (H_2Q) in methanol and in the presence of KOH under atmospheric condition followed by chromatographic purification using a neutral alumina column. The complex was characterized by elemental analysis, electrospray mass and ^1H -NMR spectroscopy. The complex **3** can exist in *fac* (facial) or *mer* (meridional) diastereoisomeric form (Figure 7.2.1). The ^1H -NMR spectrum of **3** (Figure 7.2.2), recorded in CD_2Cl_2 at room temperature, exhibits five distinct ^tBu signals, with two signals overlapped, and three sets of each 2H and 5H aromatic protons, corresponding to three magnetically non-equivalent Q ligands and justifying the meridional configuration of **3**. The appearance of three non-equivalent IR stretching bands at 2952, 2903 and 2863 cm^{-1} also supports this justification.

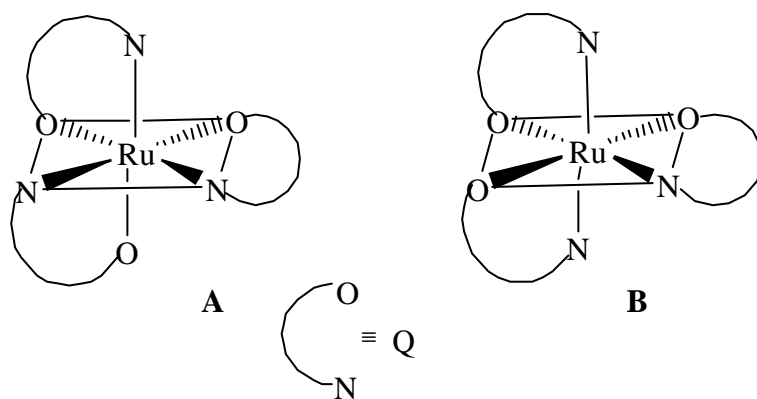


Figure 7.2.1. Two possible diastereoisomers: *fac* (facial) (A) and *mer* (meridional) (B).

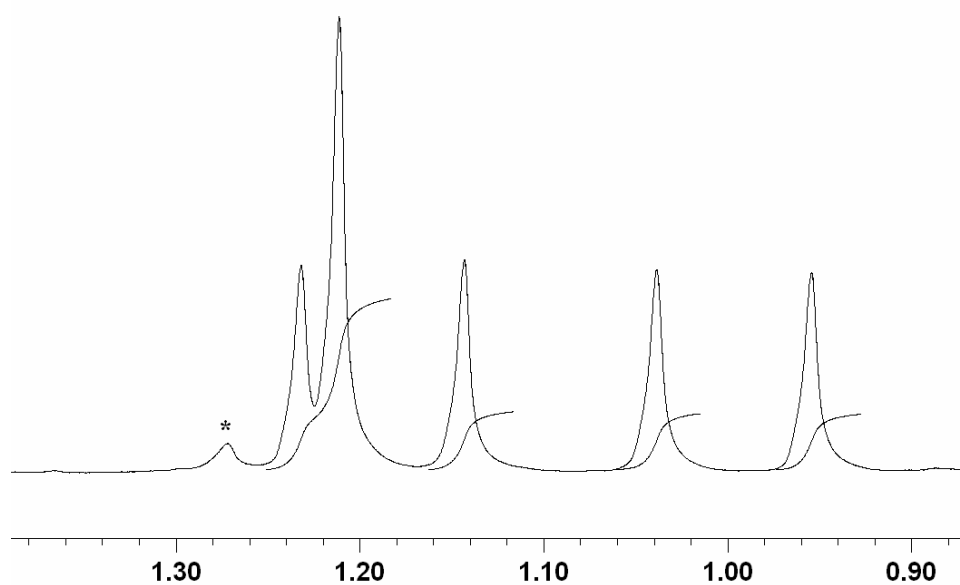
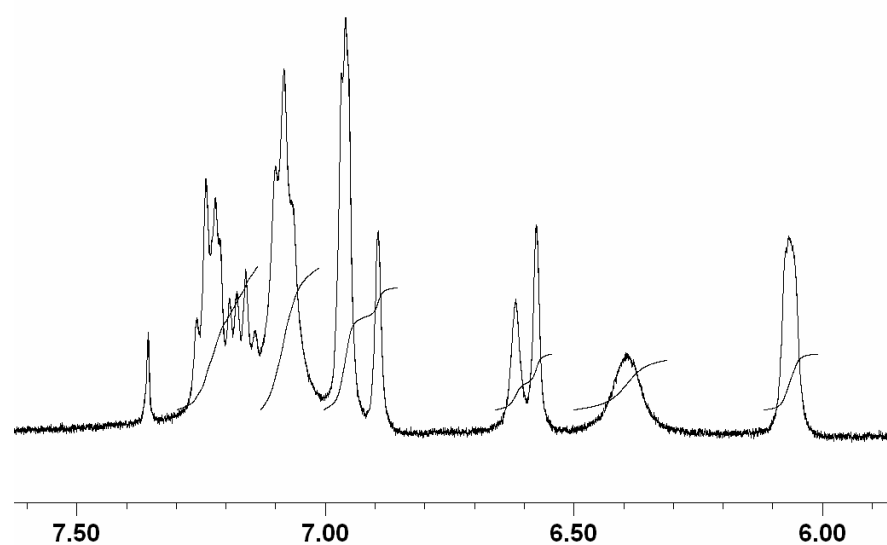


Figure 7.2.2. $^1\text{H-NMR}$ spectra of the complex **3**: aromatic (top) and aliphatic (bottom; * indicates signals from the solvent) region.

7.3. Electrochemistry

The electrochemistry of the complexes **1**, **2** and **3** has been studied by cyclic voltammetry in CH_2Cl_2 solution containing 0.1 M Bu_4NPF_6 as supporting electrolyte. Ferrocene was used as an internal standard and all the redox potentials are referenced with respect to ferrocenium / ferrocene (Fc^+/Fc) couple. The voltammograms are shown in Figure 7.3.1 and results are summarized in Table 7.3.1.

The complexes **1** and **2** undergo two oxidations and two reductions (Figure 7.3.1). The second oxidation was found to be an irreversible process in case of **2**. The separations in potentials between the first oxidation (ox1) and first reduction (red1), $\Delta E = 0.85$ and 0.96 for **1** and **2** converts to comproportionation constants $K_c = 10^{14.4}$ and $10^{16.3}$ respectively.

The cyclic voltammogram of **3** (Figure 7.3.1) displays four redox responses and essentially involve the ligand-centered process. The second reduction was found to be a quasi-reversible process. The separation in potentials between the first oxidation (ox1) and reduction (red1), $\Delta E = 0.84$ V translates to a comproportionation constant $K_c = 10^{14.2}$. The more electron donating nature of the Q^- ligand in **3** makes the oxidation processes (ox1 and ox2) much easier and the reduction processes (red1 and red2), more difficult, compared to the complexes **1** and **2** (Table 7.3.1).

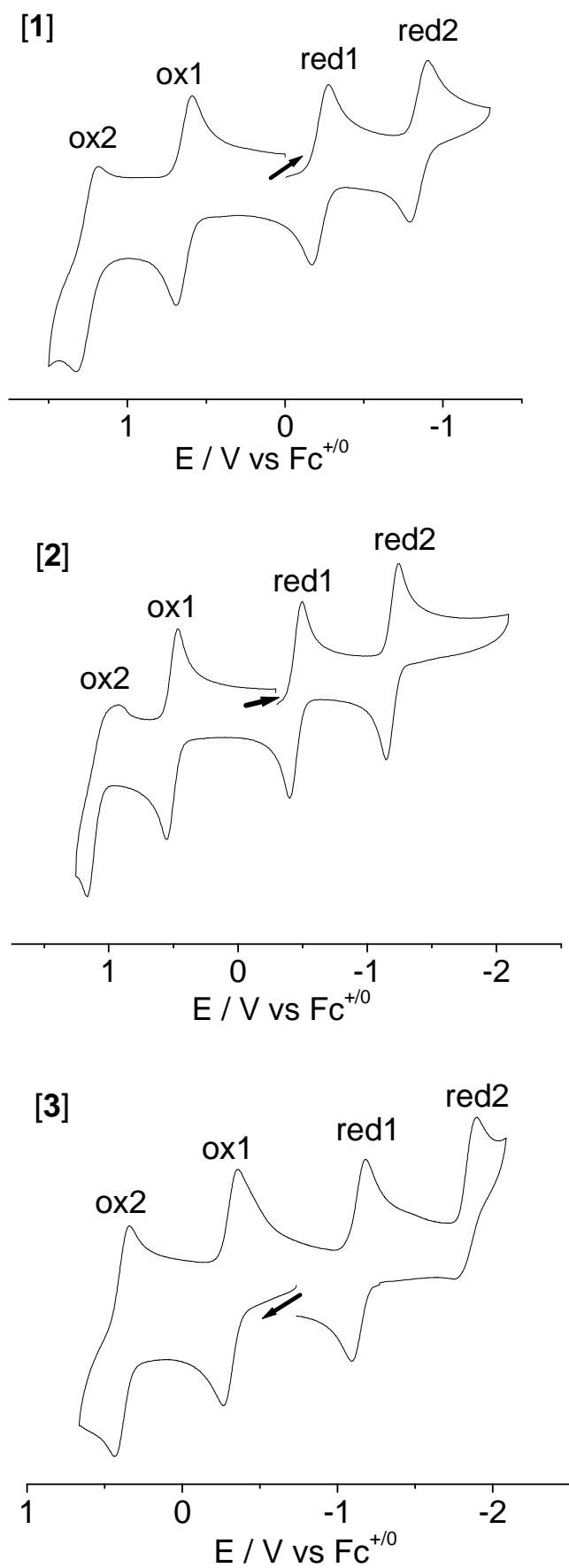


Figure 7.3.1. Cyclic voltammograms of **1**, **2**, and **3** in $\text{CH}_2\text{Cl}_2/0.1 \text{ M Bu}_4\text{NPF}_6$.

Table 7.3.1. Redox potentials of the complexes.

| Complex | E/V (ΔE_p /mV) vs Fc ^{0/+} ^a | | | |
|----------|---|--------------------|------------|--------------------|
| | ox1 | ox2 | red1 | red2 |
| 1 | +0.35(94) | +0.96(104) | -0.50(105) | -1.13(115) |
| 2 | +0.51(81) | +1.17 ^b | -0.45(103) | -1.20(94) |
| 3 | -0.30(86) | +0.40(93) | -1.14(99) | -1.91 ^b |

^a CH₂Cl₂/0.1 M Bu₄NPF₆, 100 mV/s, 295 K, ^b Peak potentials for irreversible process.

7.4. EPR spectroscopy

To assign the sites of the redox processes, the X-band EPR measurements were done for all three complexes generating odd electron species electrochemically. Complexes **1** and **2** and the complex **3** with the *o*-iminobenzoquinone are discussed in separate sections. The data for all three complexes are listed in Table 7.4.1.

7.4.1. The complexes [1] and [2]

One-electron reduction of the diamagnetic complex **1** results in a signal with (Figure 7.4.1(top)) slight splitting of the *g* component (with $g_1 = 2.041$ and $g_2 = g_3 = 1.9906$) at $g_{av} = 2.0075$ in glassy frozen solution at 100 K (very weak signal at 295 K). The $\Delta g = g_1 - g_3 = 0.0504$, suitable to evaluate the amount of spin on the heavy metal^{26,64}, indicates significant amount of ruthenium contribution to the SUMO. These results suggest a metal/ligand mixed-spin intermediate **1**⁻, in agreement with DFT calculation results (see later). Electrochemically generated one-electron reduced species **2**⁻ exhibits unresolved EPR signal (Figure 7.4.1(bottom)) at $g_{iso} = 2.0258$ in glassy frozen solution at 100 K (no signal at 295 K). No detectable *g* anisotropy was observed because of the large line-width. The higher g_{iso} value of osmium analogue compared to g_{av} of ruthenium analogue suggests relatively more osmium contribution in the SUMO compared to the ruthenium analogue, in addition to the effect of bigger spin-orbit coupling in osmium system.²⁶ DFT calculated spin density justify this experimental result (see section 7.6.1).

Oxidation of **1** results in the appearance of an isotropic EPR signal at $g_{\text{iso}} = 1.9909$ at 295 K (Figure 7.4.2 (top)); however, in glassy frozen solution at 110 K an appreciable g component splitting is observed with $g_1 = 2.0037$, $g_2 = 1.9912$ and $g_3 = 1.977$ (Figure 7.4.2 (bottom)). The isotropic g value which is very close to the value of 2.0023 for the free electron and the still rather small $\Delta g = 0.027$ collectively suggest a ligand localized SOMO with marginal contribution from the metal. No EPR signal was observed for the electrochemically generated one-electron oxidized species **2**⁺ at 295 K; however an almost isotropic signal at $g_{\text{iso}} = 2.027$ with no splitting, was observed in glassy frozen solution at 110 K (Figure 7.4.3).

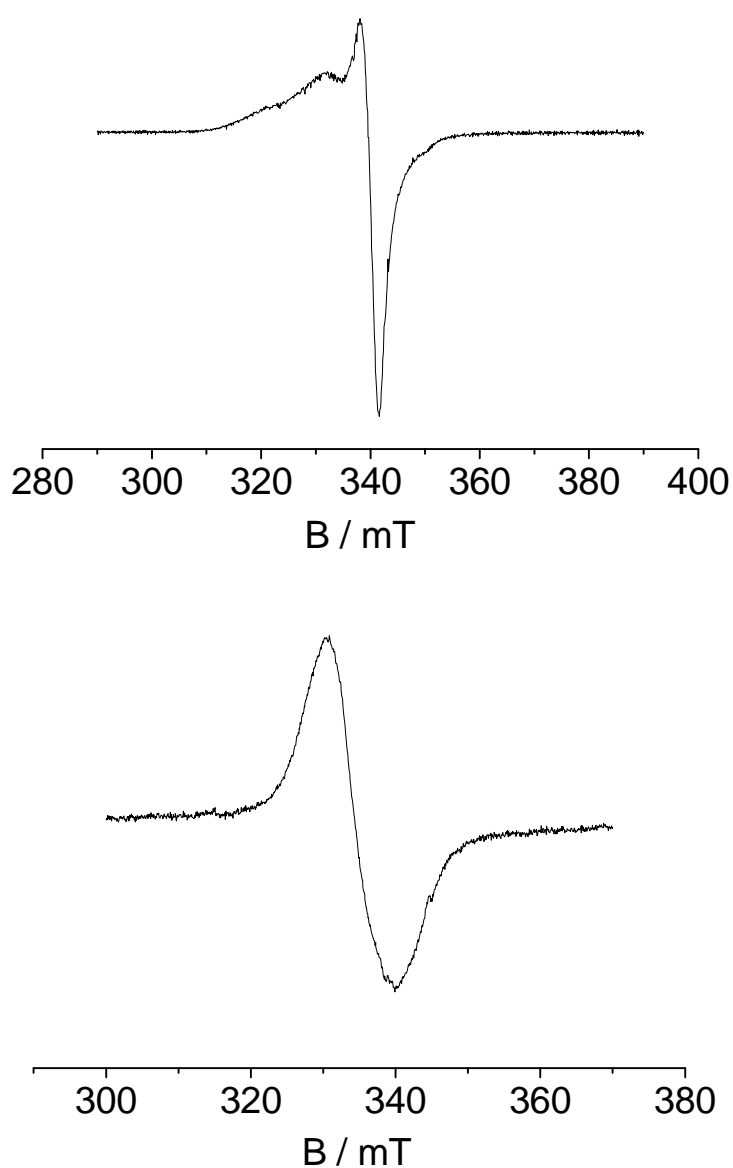


Figure 7.4.1. X-band EPR spectra of electrochemically generated [**1**]^{•-} (top) and [**2**]^{•-} (bottom) at 110 K in CH₂Cl₂/0.1 M Bu₄NPF₆.

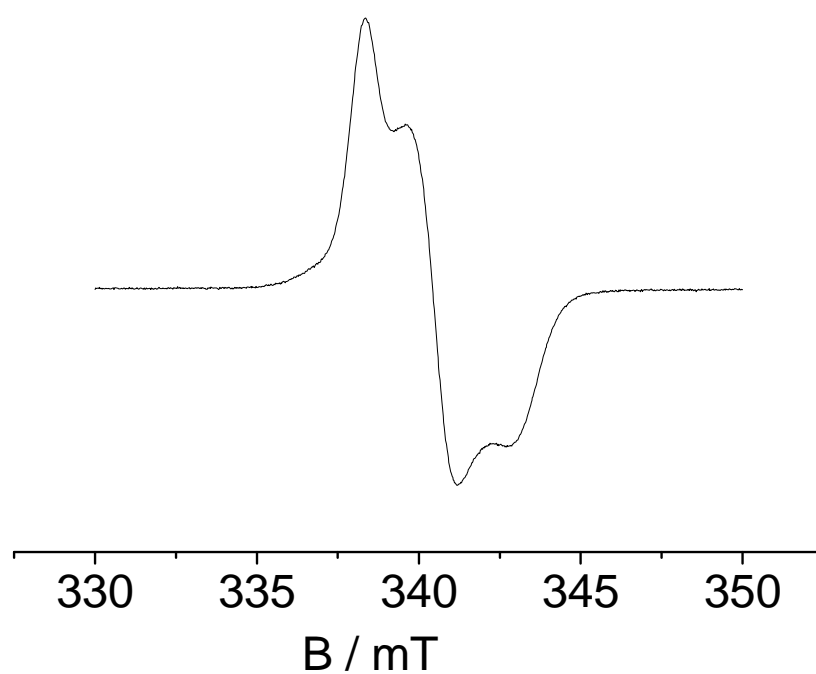
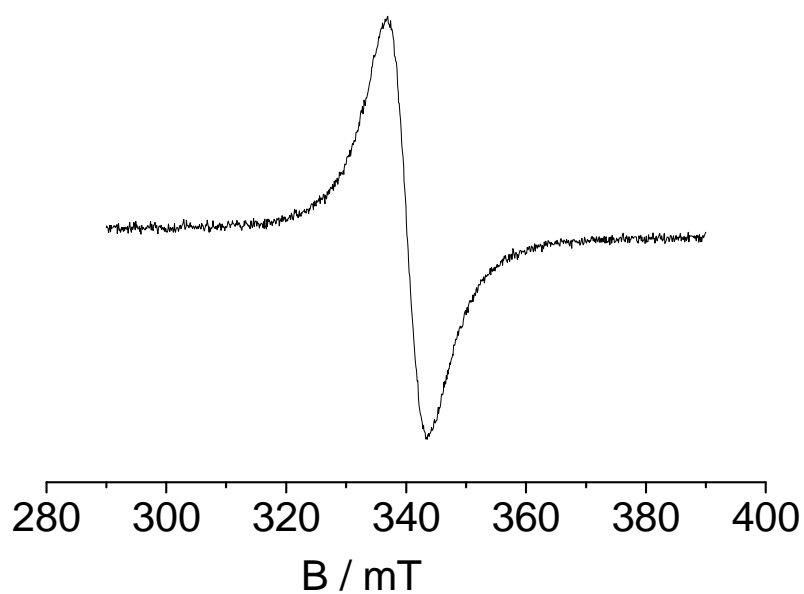


Figure 7.4.2. X-band EPR spectra of electrochemically generated $[1]^+$ at 295 K (top) and at 110 K (bottom) in $\text{CH}_2\text{Cl}_2/0.1 \text{ M Bu}_4\text{NPF}_6$.

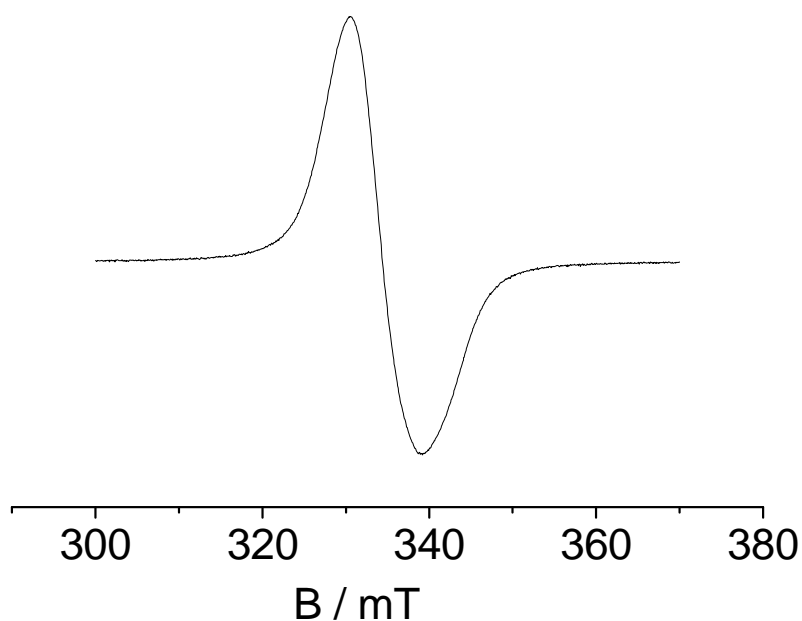


Figure 7.4.3. X band EPR spectrum of electrochemically generated $[2]^+$ at 110 K in $\text{CH}_2\text{Cl}_2/0.1 \text{ M Bu}_4\text{NPF}_6$.

7.4.2. The complex [3]

On one-electron oxidation to the intermediate 3^+ an intense unresolved EPR signal (Figure 7.4.4) without detectable g anisotropy at X-band frequency was observed ($g_{\text{iso}} = 1.9945$), both at room temperature and at 110 K. The absence of noticeable g component splitting signifies a very small metal contribution to the spin density in 3^+ as supported by DFT calculations. In contrast, one-electron reduction yields an isotropic g of 2.0018 (Figure 7.4.5(top)), very close to the free electron value; however in glassy frozen solution at 110 K there is an appreciable component splitting observable with $g_1 = 2.046$, $g_2 = 1.994$ and $g_3 = 1.973$ and $\Delta g = 0.0727$ (Figure 7.4.5(bottom)). The value indicates a mixed metal/ligand spin intermediate 3^- , in agreement with DFT calculation results (see later).

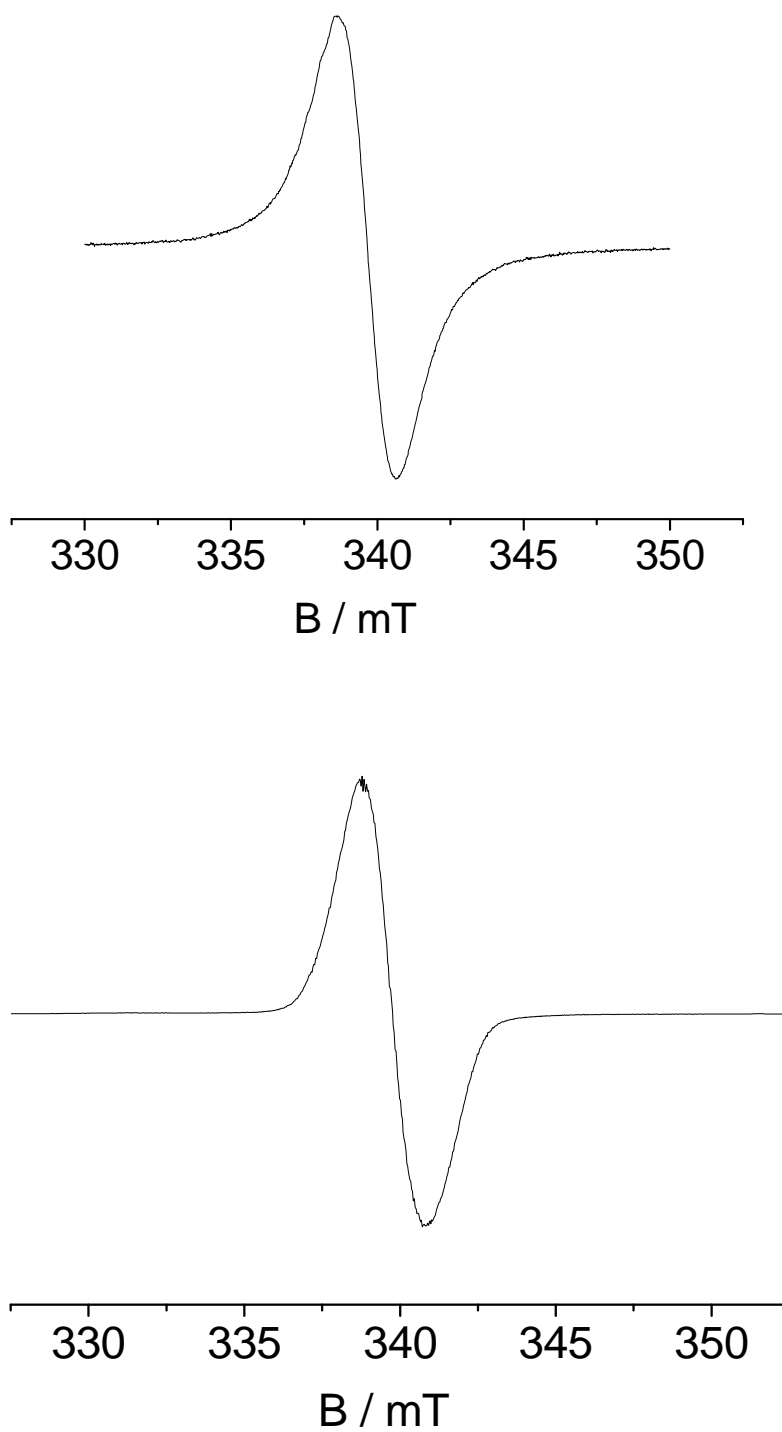


Figure 7.4.4. X-band EPR spectra of electrochemically generated 3^+ at 295 K (top) and at 110 K (bottom) in $\text{CH}_2\text{Cl}_2/0.1 \text{ M Bu}_4\text{NPF}_6$.

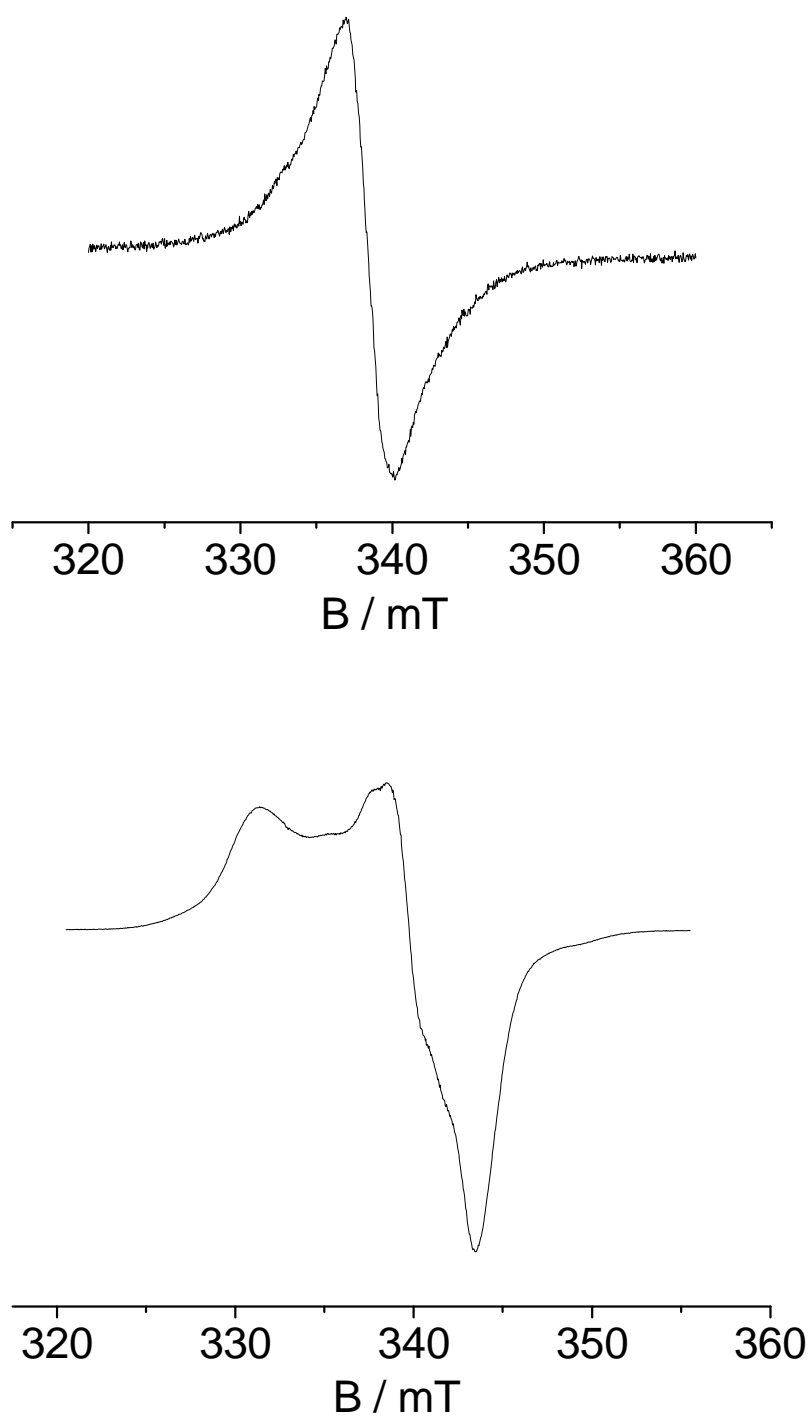


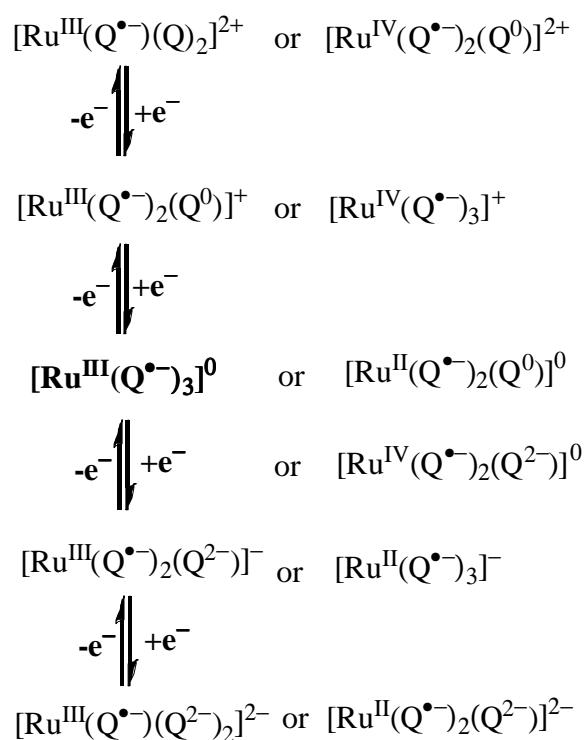
Figure 7.4.5. X-band EPR spectra of electrochemically generated 3^- at 295 K (top) and at 110 K (bottom) in $\text{CH}_2\text{Cl}_2/0.1 \text{ M Bu}_4\text{NPF}_6$.

Table 7.4.1. EPR data of complexes $[1]^n$, $[2]^n$ and $[3]^n$ ($n = -, +$).

| Complex ^a | g (at 295 K) | g (110 K) | Δg^b | g_{av}^c |
|----------------------|------------------|--|--------------|------------|
| 1^- | very weak signal | $g_1 = 2.041$ $g_2 = g_3 = 1.9906$ | 0.0504 | 2.0075 |
| 1^+ | 1.991 | $g_1 = 2.0037$ $g_2 = 1.9912$ $g_3 = 1.9767$ | 0.0270 | 1.9906 |
| 2^- | no signal | 2.0258 | ----- | ----- |
| 2^+ | no signal | 2.0274 | ----- | ----- |
| 3^- | 2.0018 | $g_1 = 2.0456$ $g_2 = 1.994$ $g_3 = 1.973$ | 0.0727 | 2.0043 |
| 3^+ | 1.9945 | 1.9945 | ----- | ----- |

^a in $CH_2Cl_2/0.1$ M Bu_4NPF_6 . ^b $\Delta g = g_1 - g_3$. ^c $g_{av} = [(g_1^2 + g_2^2 + g_3^2)/3]^{1/2}$.

Scheme 7.4.1. Alternative formulations for the oxidized and reduced states of $[Ru(Q)_3]$ [**3**].



7.5. UV-Vis-NIR spectroelectrochemistry

To obtain more information about the electronic distribution in various accessible redox processes, UV-Vis-NIR spectroelectrochemical changes of all three complexes **1**, **2** and **3** were monitored using an OTTLE cell.⁶⁶ The data are summarized in Table 7.5.1.

Compound **1** exhibits NIR absorption with a band maximum at 1220 nm, in addition to several shoulders and a broad band maximum at 585 nm (Figure 7.5.1). For the Os compound **2**, the band maximum in the NIR absorption region is blue-shifted to 1006 nm and several shoulders, with a band maximum at 596 nm were observed (Figure 7.5.2). As will be discussed later, the NIR absorption band can be assigned as mixed LMCT/IL transition from the HOMO into the sets of LUMOs (Figure 7.6.2-3, Table 7.6.1–2). The bands around 673 nm and 1000 nm for **1**⁺ (Figure 7.5.1 (top)) and 555 nm and 882 nm for **2**⁺ (Figure 7.5.2 (top)) are assigned as semiquinone-to-quinone transitions, indicating a preferential ligand based oxidation. Both complexes show a decrease in NIR band intensity on first oxidation, and the bands disappear on second oxidation (Figure 7.5.1 and 7.5.2 (bottom)). For the doubly oxidized state, the previous HOMO is now empty and no NIR transition can occur from this level. Reduction of both the complexes to **1**⁻ (Figure 7.5.3) and **2**⁻ (Figure 7.5.4) results in the long-wavelength NIR intensity to diminish and an intense band at 932 nm and 799 nm appear respectively. Based on the EPR results and DFT calculations they can be attributed to LMCT/MLCT mixed transitions which disappear on second reduction.

The symmetry of system **3**ⁿ and the presence of three highly non-innocent ligands are responsible for extended absorption³³⁻³⁵ (Figure 7.5.4(top)) with a band maximum at 1278 nm (HOMO → LUMO), in addition to several shoulders and a band at 563 nm. Oxidation to **3**⁺ causes the NIR band to diminish while a very broad, weak band at about 2500 nm as well as absorption features at about 900 and 600 nm emerge (Figure 7.5.5(top)). The later remains hardly changed on second oxidation (Figure 7.5.5(bottom)), whereas the IR band disappears and the 900 nm band system shifts to 775 nm. The very broad absorption band around 2500 nm is not untypical for intervalence charge transfer (IVCT) transitions between coordinated but weakly interacting non-innocent ligands of different charge and oxidation state.¹⁰¹⁻¹⁰⁴ The formation $[\text{Ru}^{\text{III}}(\text{Q}^{\bullet-})_2(\text{Q})^0]$ would provide such an opportunity (formally a semiquinone-to-quinone transition, SOMO → LUMO). For the doubly oxidized state the HOMO is now empty and no NIR transition can occur from this level. Intense charge transfer transitions involving the metal remain. Reduction of **3** to **3**⁻ causes the long-wavelength NIR intensity to diminish while an intense absorption emerges at 817 nm (Figure 7.5.6).

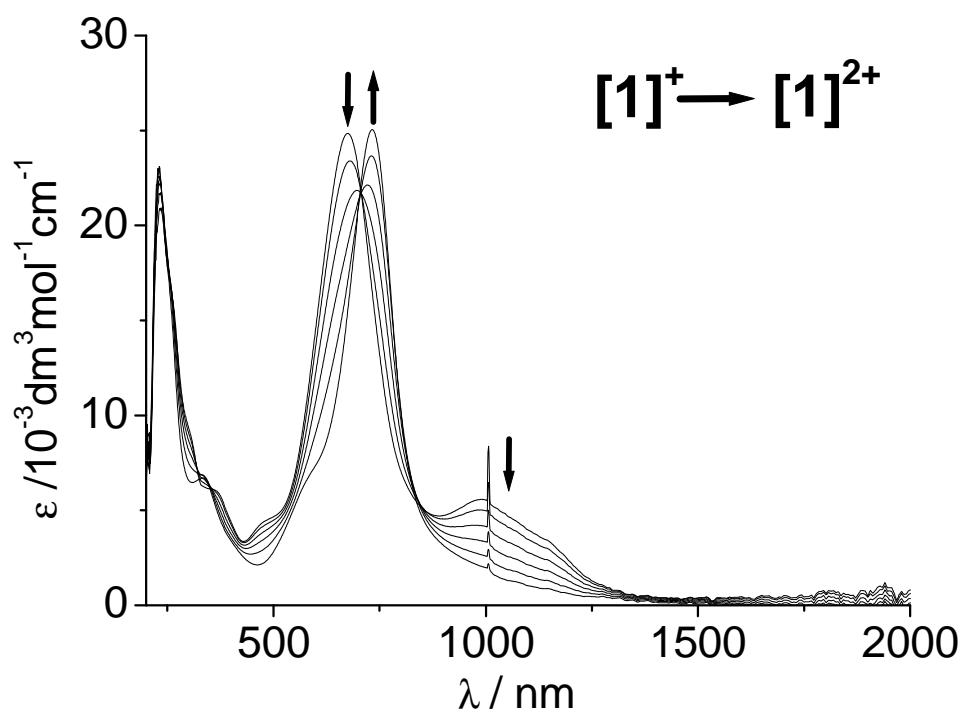
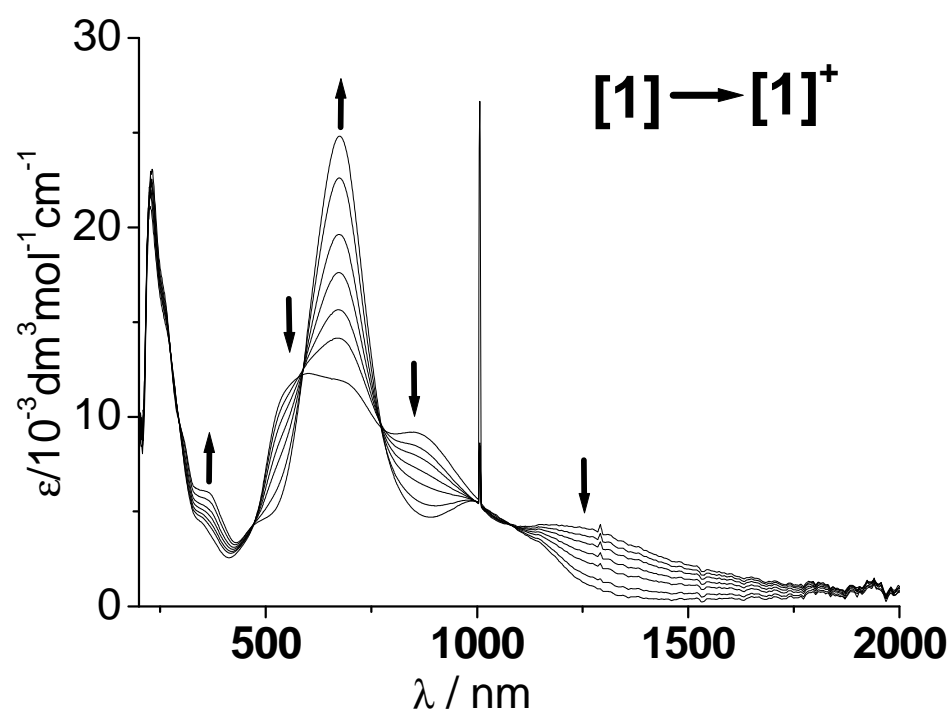


Figure 7.5.1. UV-Vis-NIR spectroelectrochemistry of the conversion $[1]^{(0) \rightarrow (+)}$ (top) and $[1]^{(+)} \rightarrow (2+)$ (bottom) in $\text{CH}_2\text{Cl}_2/0.1 \text{ M Bu}_4\text{NPF}_6$.

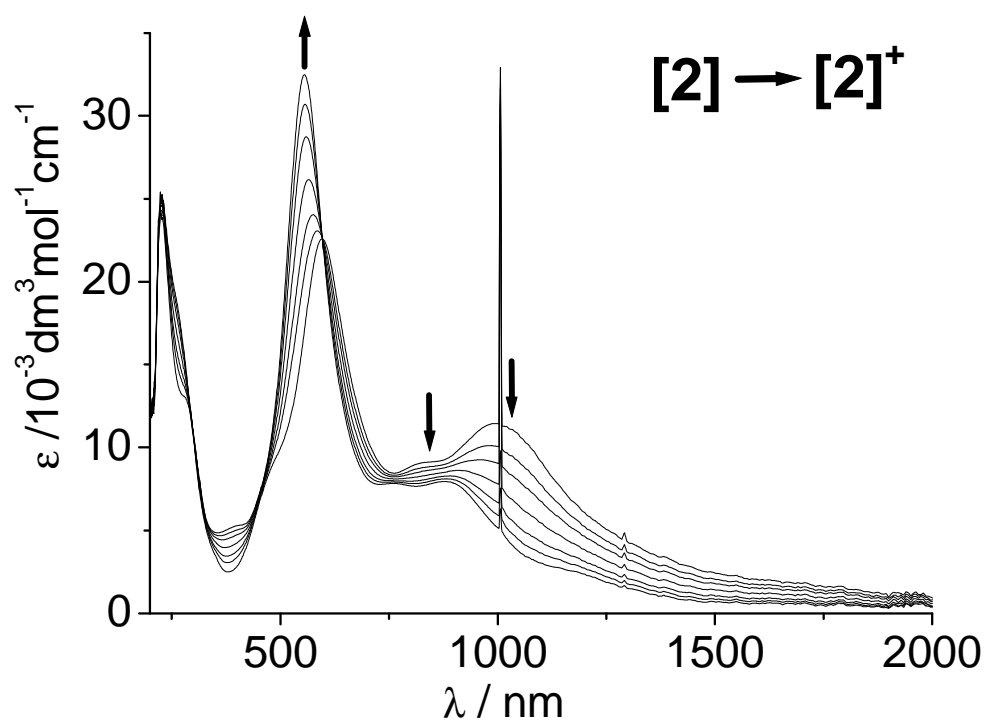


Figure 7.5.2. UV-Vis-NIR spectroelectrochemistry of the conversion $[2]^{(0)} \rightarrow [2]^{(+)}$ (top) in $\text{CH}_2\text{Cl}_2/0.1 \text{ M Bu}_4\text{NPF}_6$.

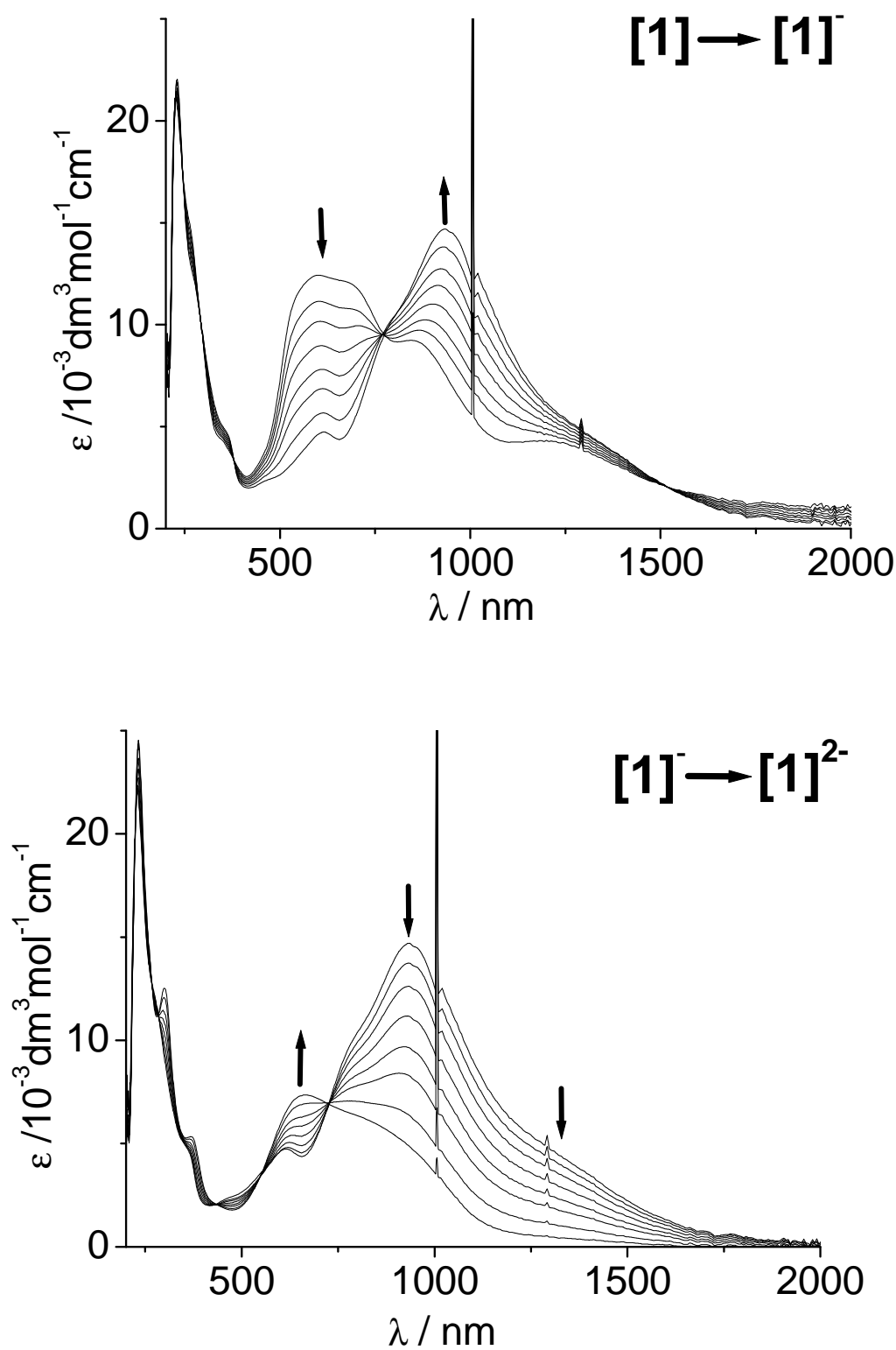


Figure 7.5.3. UV-Vis-NIR spectroelectrochemistry of the conversion $[1]^{(0) \rightarrow (-)}$ (top) and $[1]^{(-) \rightarrow (2-)}$ (bottom) in $\text{CH}_2\text{Cl}_2/0.1 \text{ M Bu}_4\text{NPF}_6$.

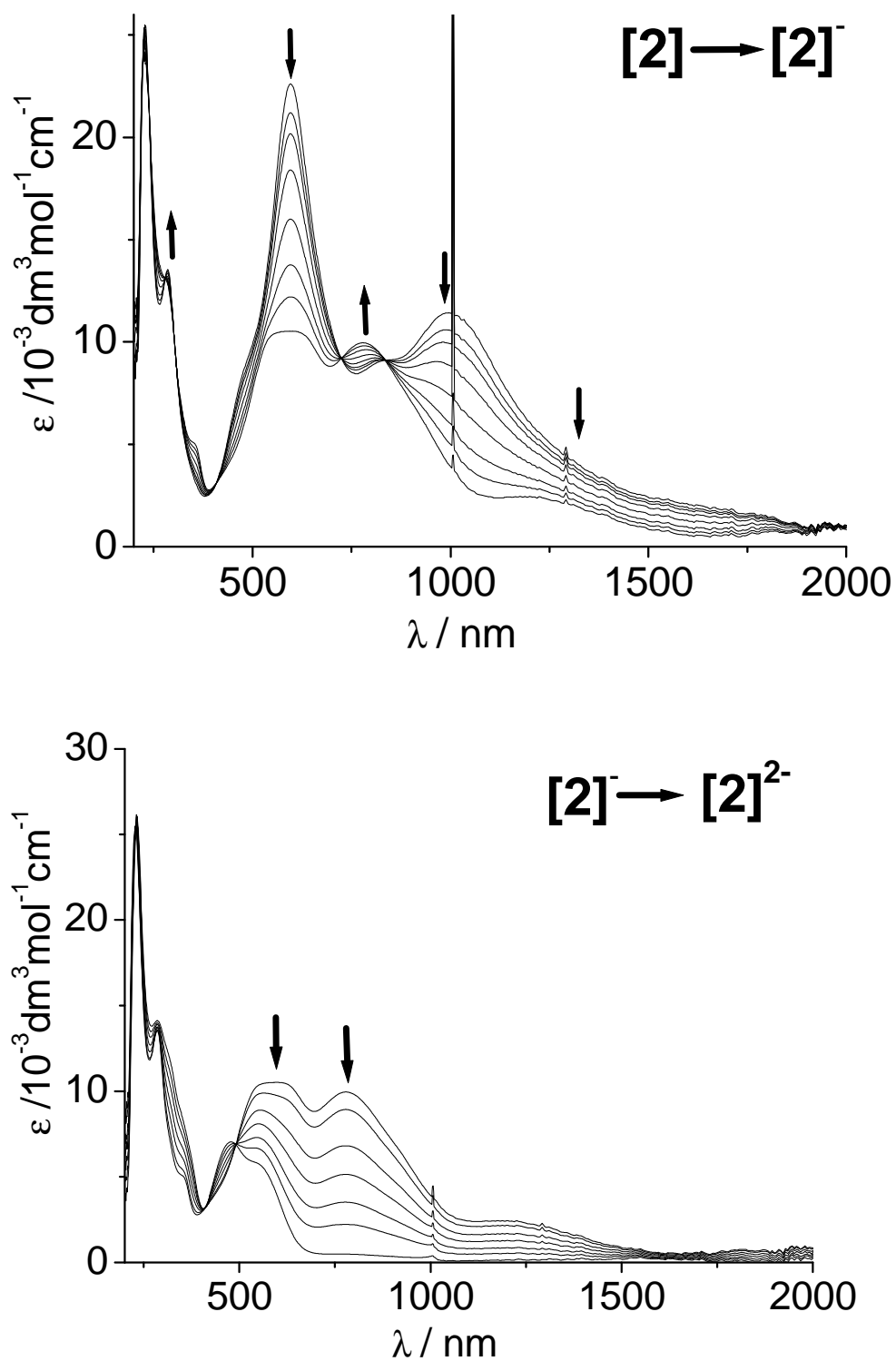


Figure 7.5.4. UV-Vis-NIR spectroelectrochemistry of the conversion $[2]^{(0) \rightarrow (-)}$ (top) and $[2]^{(-) \rightarrow (2-)}$ (bottom) in $\text{CH}_2\text{Cl}_2/0.1 \text{ M Bu}_4\text{NPF}_6$.

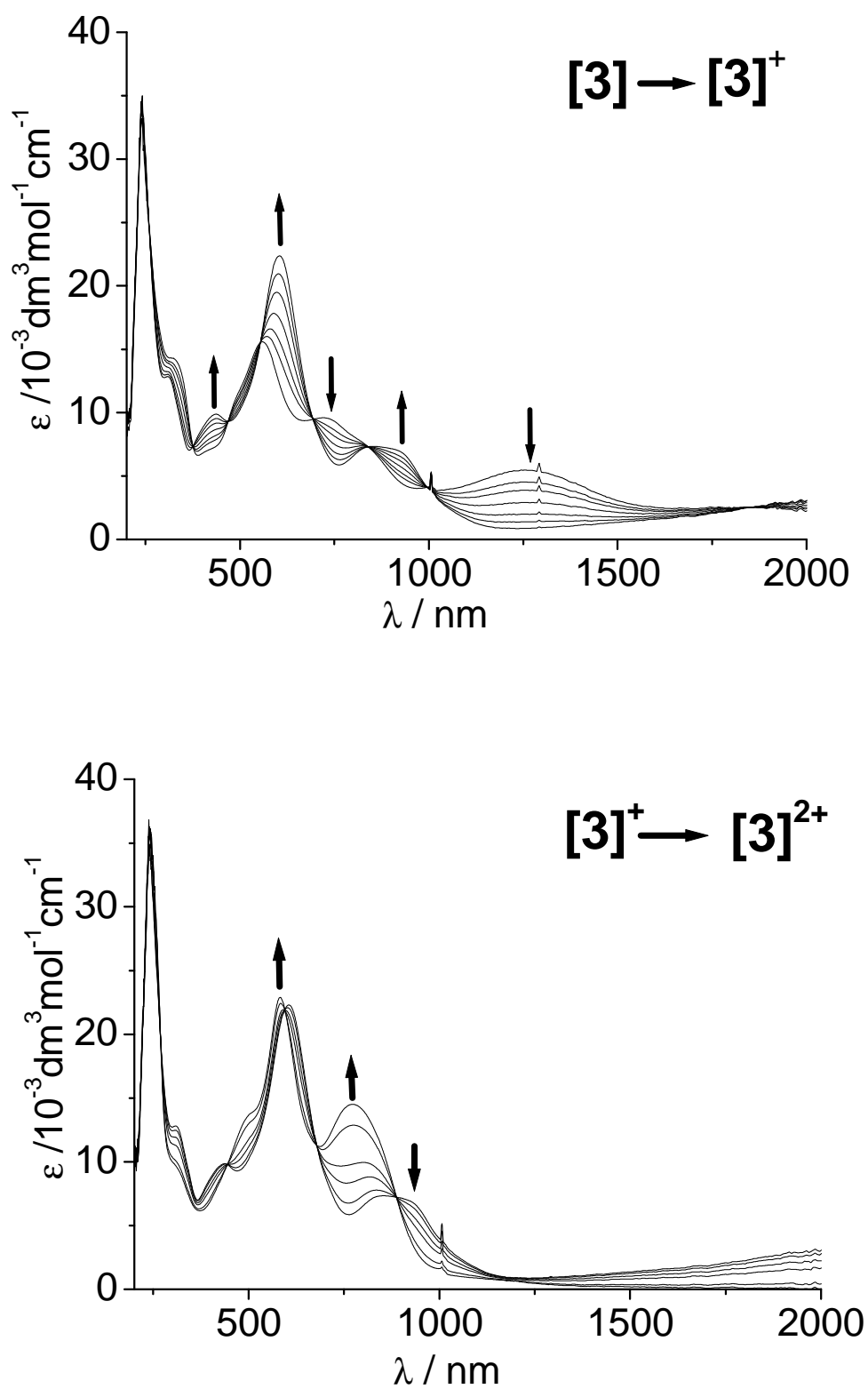


Figure 7.5.5. UV-Vis-NIR spectroelectrochemistry of the conversion $[3]^{(0) \rightarrow (+)}$ (top) and $[3]^{(+)} \rightarrow (2+)$ (bottom) in $\text{CH}_2\text{Cl}_2/0.1 \text{ M Bu}_4\text{NPF}_6$.

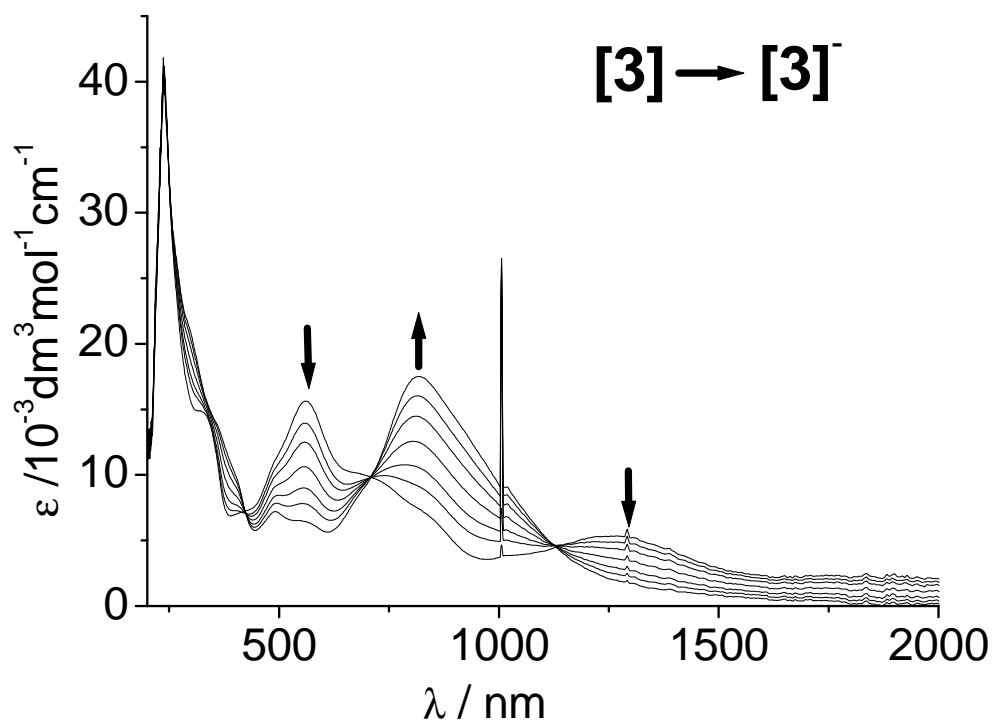


Figure 7.5.6. UV-Vis-NIR spectroelectrochemistry of the conversion $[3]^{(0) \rightarrow (-)}$ in $\text{CH}_2\text{Cl}_2/0.1 \text{ M Bu}_4\text{NPF}_6$.

Table 7.5.1. Absorption data from spectroelectrochemistry.

| ^a Complex | $\lambda_{\max} / \text{nm} (\epsilon / \text{M}^{-1}\text{cm}^{-1})$ |
|-----------------------|---|
| 1²⁺ | 334 (6800), 735 (25200), 1009 (1900), 1168 (sh) |
| 1⁺ | 365 (6100), 673 (24900), 999 (5600), 1139 (sh) |
| 1⁰ | 585 (12300), 687 (11800), 860 (9200), 1220 (4300) |
| 1⁻ | 614 (4800), 767 (sh), 932 (14700), 1292 (sh) |
| 1²⁻ | 301 (12600), 368 (5400), 650 (7300), 870 (5900) |
| 2⁺ | 555 (32500), 882 (7900), 1180 (sh) |
| 2⁰ | 596 (22600), 826 (9100), 1006 (11500) |
| 2⁻ | 284 (13700), 588 (10500), 799 (10000), 1208 (2400) |
| 2²⁻ | 284 (14100), 478 (7000), 547 (5800) |
| 3²⁺ | 502 (sh), 584 (23000), 770 (14500) |
| 3⁺ | 437 (9900), 604 (22400), 837 (7300), 925 (6900) |
| 3⁰ | 332 (14100), 553 (15600), 725 (9600), 1278 (5500) |
| 3⁻ | 490 (7200), 567 (6400), 817 (17400) |

^a from spectroelectrochemistry in CH₂Cl₂/0.1 M Bu₄NPF₆

7.6. DFT calculations

7.6.1. The complexes [1] and [2]

Figure 7.6.1(left) shows that the DFT calculated spin density in $\mathbf{1}^+$ is mainly localized on Q ligands. G03/PBE0 calculations yield spin densities of 0.405 for each Q and -0.215 for Ru. This is further confirmed by the ADF/BP calculated isotropic g factor value of 2.005 ($g_{11} = 2.007$, $g_{22} = 2.004$, $g_{33} = 2.003$) which is in good agreement with the experimental g factor value of 1.999 (see Table 7.4.1). However the G03/PBE0 calculations of $\mathbf{2}^+$ indicate a different participation of Os at the spin density (0.323 for each Q and 0.032 for Os). The calculated g factor shows larger anisotropy values of $g_{\text{iso}} = 1.996$ ($g_{11} = 2.012$, $g_{22} = 2.005$, $g_{33} = 1.971$).

In the course of reduction the electron is accepted by the set of almost degenerate LUMO and LUMO+1 orbitals with approximately 27% or 37% contribution of metal in $\mathbf{1}^-$ or $\mathbf{2}^-$, respectively. The ADF/BP calculations give spin densities of 0.480 for Ru and of 0.171 for each Q ligand for $\mathbf{1}^-$, and of 0.622 for Os and of 0.171 for each Q ligand for $\mathbf{2}^-$.

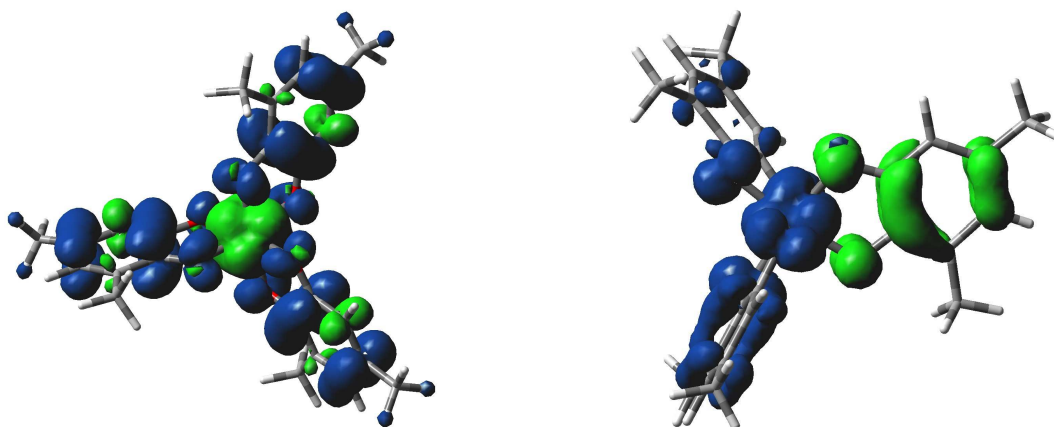


Figure 7.6.1. DFT calculated spin densities of $\mathbf{1}^+$ (left) and $\mathbf{1}^-$ (right). Blue areas indicate positive and green areas negative spin densities.

TD DFT calculations including solvent effect incorporation interpret the experimental optical spectra of neutral complexes $\mathbf{1}$ and $\mathbf{2}$ as shown in Tables 7.6.1 and 7.6.2, respectively. The dominating excitations contributing to the two lowest lying transitions in visible region are schematically drawn in Figures 7.6.2 and Figure 7.6.3. The calculations slightly underestimate the energy of the lowest lying transition of $\mathbf{1}$ found at 1220 nm (calculated at about 1350 nm). This transition can be characterized as mixed LMCT/IL transition from HOMO into the set of

LUMOs. The intense band around 687 nm is again reasonably reproduced by TD DFT calculation and it is formed by mixed MLCT/IL excitations from HOMO–2 and HOMO–3 into the LUMO and LUMO+1. TD DFT calculations well reproduce the shift of excitations to higher energy when going from **1** to **2** (Ru → Os).

Table 7.6.1. Selected G03/PBE0/CPCM calculated lowest allowed TD-DFT singlet transitions for complex **1**.

| State | Main character (in %) | calculated | | Experiment |
|------------------|---------------------------------------|----------------------------|-----------|-----------------------------|
| | | trans. energy ^a | osc. Str. | $\lambda_{\max}/\epsilon^b$ |
| a ¹ A | 85 (HOMO→LUMO) | 0.90 (1375) | 0.083 | |
| b ¹ A | 91 (HOMO→LUMO+1) | 1.04 (1350) | 0.082 | 1220 (4300) |
| c ¹ A | mixed (HOMO–2, HOMO–3 → LUMO, LUMO+1) | 1.44 (858) | 0.003 | 860 |
| d ¹ A | mixed (HOMO–2, HOMO–3 → LUMO, LUMO+1) | 1.94 (639) | 0.329 | |
| e ¹ A | mixed (HOMO–2, HOMO–3 → LUMO, LUMO+1) | 1.97 (631) | 0.315 | 687 (11800), |
| e ¹ A | mixed (HOMO–4, HOMO–5→LUMO, LUMO+1) | 2.27 (547) | 0.064 | |
| g ¹ A | mixed (HOMO–4, HOMO–5→LUMO, LUMO+1) | 2.29 (541) | 0.042 | 585 (12300), |

Table 7.6.2. Selected G03/PBE0/CPCM calculated lowest allowed TD-DFT singlet transitions for complex **2**.

| State | Main character (in %) | calculated | | Experiment |
|------------------|---------------------------------------|----------------------------|-----------|-----------------------------|
| | | trans. energy ^a | osc. Str. | $\lambda_{\max}/\epsilon^b$ |
| A ¹ A | 96 (HOMO→LUMO) | 1.18 (1050) | 0.079 | |
| B ¹ A | 91 (HOMO→LUMO+1) | 1.21 (1027) | 0.085 | 1006 (11500) |
| c ¹ A | mixed (HOMO–2, HOMO–3 → LUMO, LUMO+1) | 1.68 (738) | 0.003 | 826 |
| D ¹ A | mixed (HOMO–2, HOMO–3 → LUMO, LUMO+1) | 2.11 (585) | 0.330 | |
| e ¹ A | mixed (HOMO–2, HOMO–3 → LUMO, LUMO+1) | 2.16 (573) | 0.309 | 596 (22600) |
| f ¹ A | 70 (HOMO–3→LUMO+1) | 2.25 (551) | 0.087 | |

^a Transition energies in eV (or wavelengths in nm); ^b Absorption maxima in nm, molar extinction coefficients in $10^{-3} \text{ M}^{-1} \text{ cm}^{-1}$

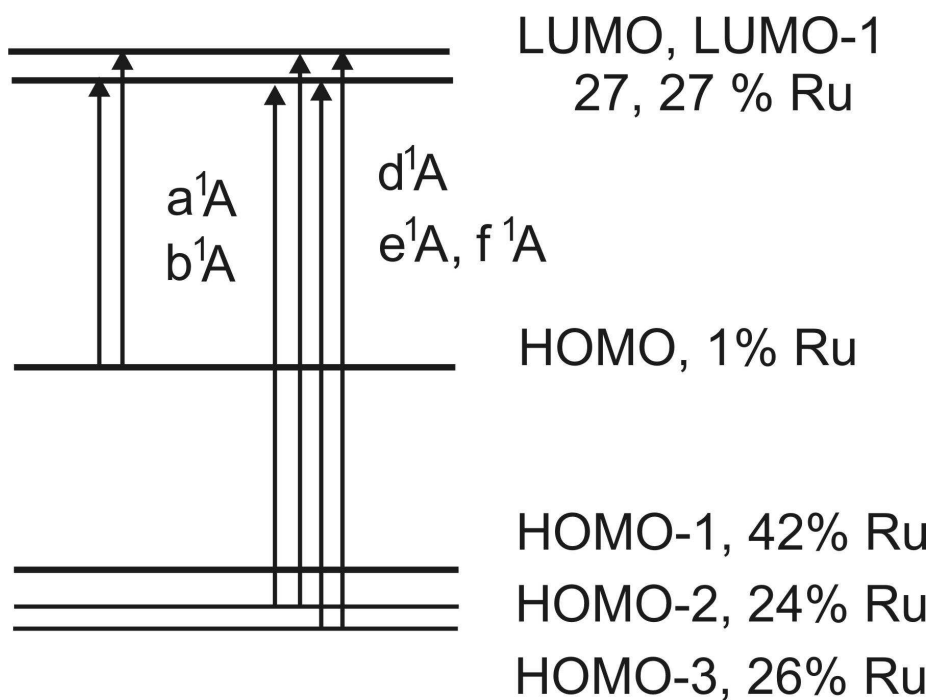


Figure 7.6.2. The qualitative MO scheme of complex **1**. Arrows indicate the main contributions to the lowest allowed TD DFT calculated transitions.

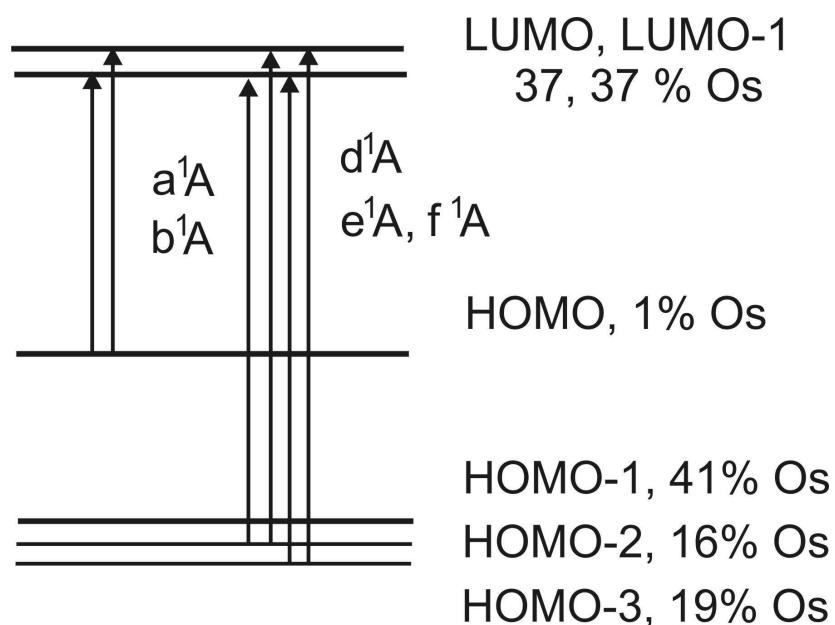


Figure 7.6.3. The qualitative MO scheme of complex **2**. Arrows indicate the main contributions to the lowest allowed TD DFT calculated transitions.

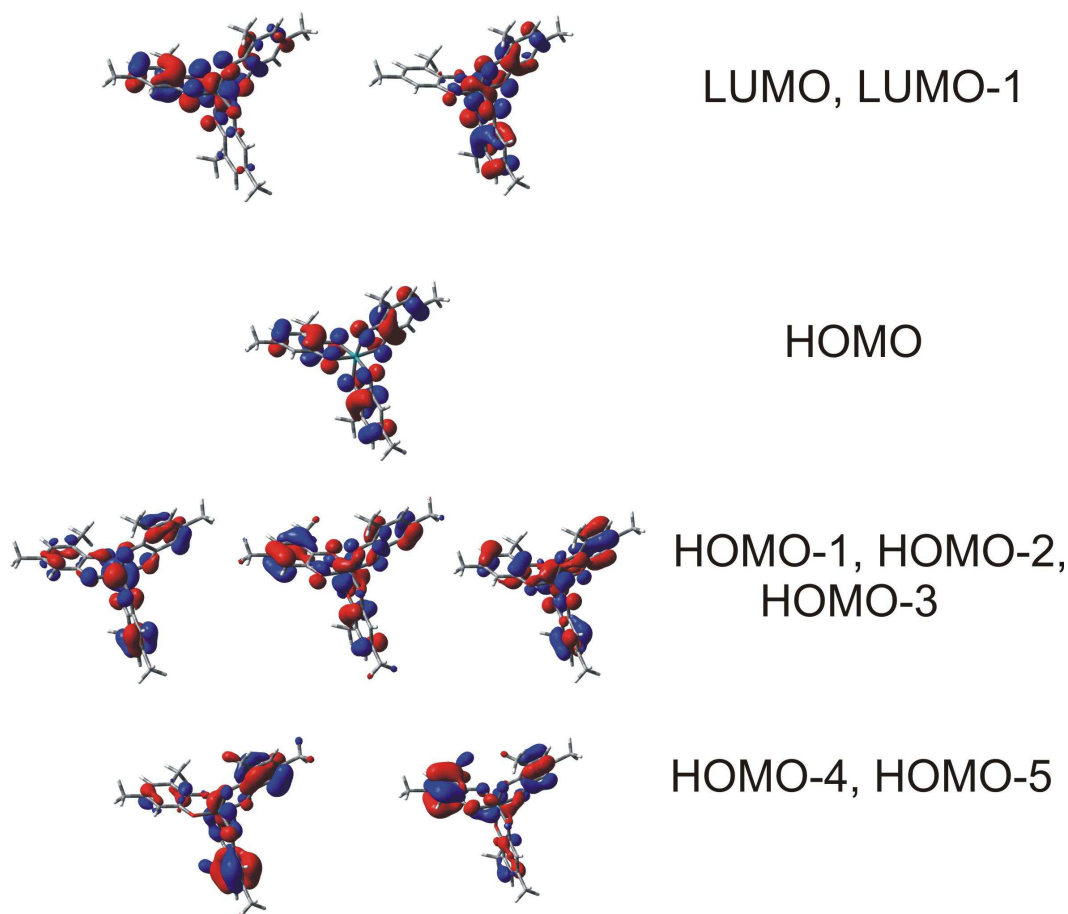


Figure 7.6.4. The representation of the frontier orbitals of complex **1**.

7.6.2. The complex [3]

The optimized structure of the *mer* configuration of complex **3** is shown in Figure 7.6.5. Figure 7.6.6(left) shows that DFT calculated spin densities are mainly localized on Q. The ADF/BP calculations yield spin densities of 0.405 for each Q. This is confirmed by calculated isotropic g factor value of 2.0049 which is in good agreement with the experimentally obtained value of 1.9945 for 3^+ . Further investigation has been done by calculating the three g component with the values of $g_{11} = 2.0074$, $g_{22} = 2.044$, $g_{33} = 2.029$ and very small $\Delta g = 0.0016$, suggests that ligand contribution predominates to form the HOMO.

In the course of the reduction the electron is taken into the set of LUMOs with partially contributing 4d orbitals of Ru. The set of almost degenerate LUMO and LUMO+1 contains approximately 25% contribution from Ru $d\pi$ orbitals, suggesting a metal/ligand mixed spin intermediate. ADF/BP calculations give spin densities of 0.407 for Ru and of 0.198 for each of the Q ligands. The observed g anisotropy at X band frequency with $\Delta g = 0.0727$ suggest the appreciable metal contribution to the SOMO.

TD-DFT methodology reasonably interprets the experimental spectrum of neutral complex as seen in Table 7.6.3. The qualitative MO scheme and the corresponding frontier orbitals are shown in Figure 7.6.7. The lowest lying allowed feature around 1278 nm can be characterized as mixed LMCT/IL transition from the HOMO into the set of LUMOs, and the intense band around 560 nm is formed by mixed MLCT/IL excitations from HOMO-2 and HOMO-3 into the LUMO and LUMO+1. The calculated transitions of 3^{2+} (Table 7.6.2) are shifted to lower energies in comparison with the neutral complex **3**, in agreement with the experiment. The lowest lying transitions of dication can be characterized as predominantly MLCT transitions.

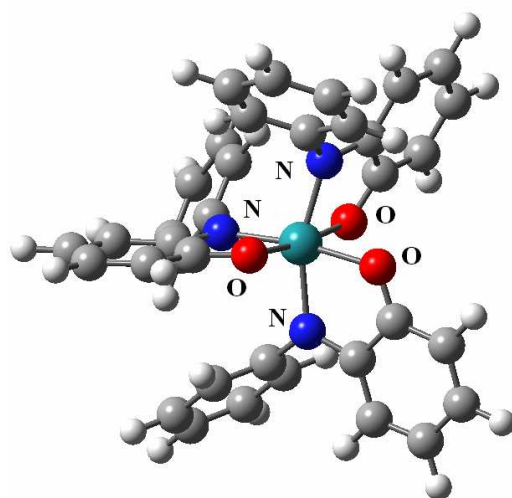


Figure 7.6.5. G03/PBE0 optimized structure of complex **3** (*mer* configuration).

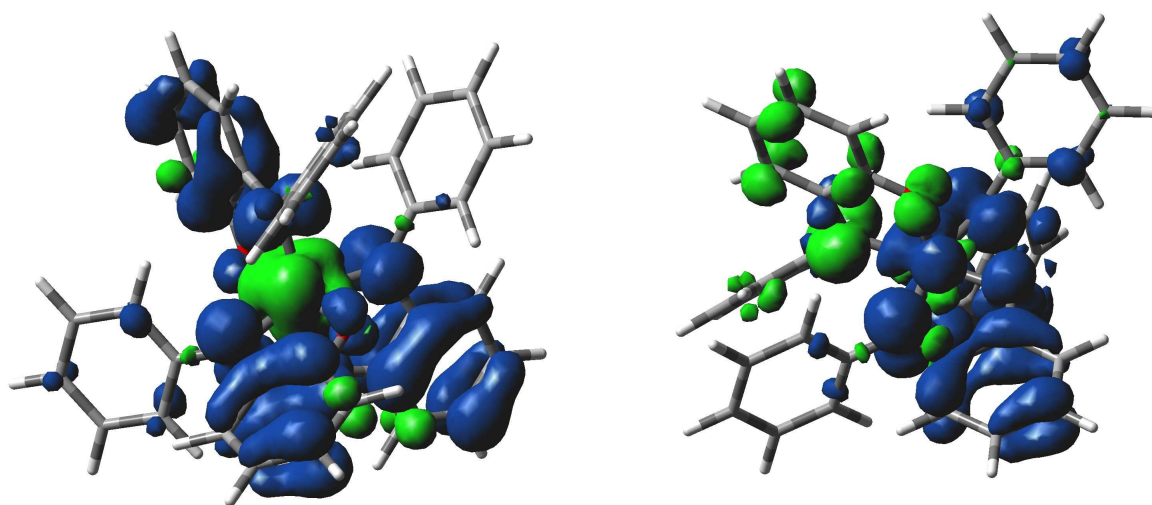


Figure 7.6.6. DFT calculated spin densities for 3^+ (left) and 3^- (right)

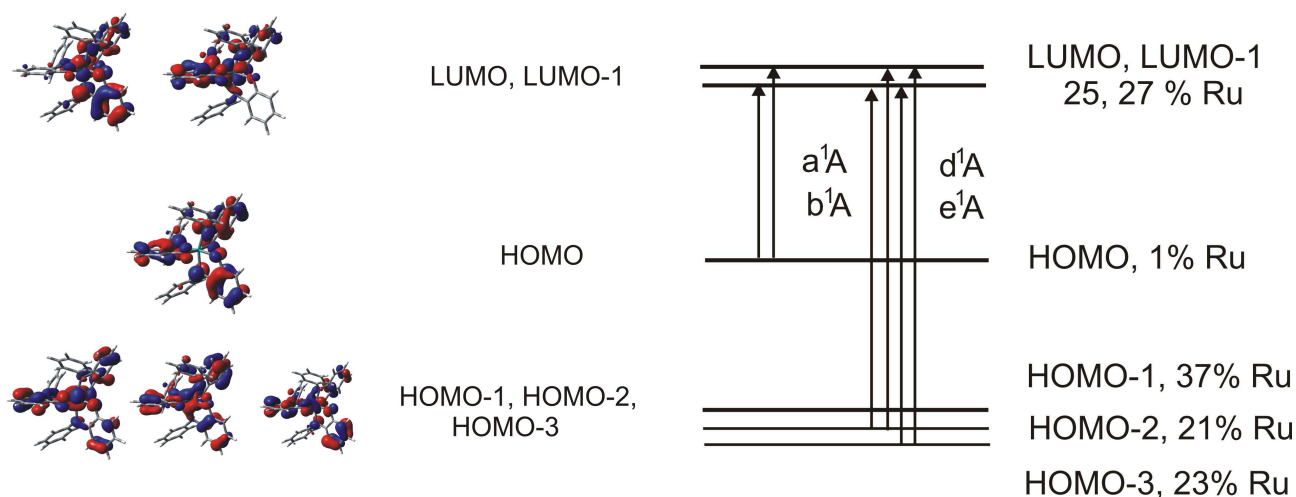


Figure 7.6.7. The representation of frontier orbitals (left) and the qualitative MO scheme of [3] (right). Arrows indicate the main contributions to the lowest allowed TD DFT calculated transitions.

Table 7.6.3. Selected G03/PBE0/CPCM calculated lowest allowed TD-DFT singlet transitions for **3**.

| state | main character (in %) | calculated | | experiment |
|--------|---------------------------------------|----------------------------|-----------|-----------------------------|
| | | trans. energy ^a | osc. Str. | $\lambda_{\max}/\epsilon^b$ |
| a^1A | 96 (HOMO→LUMO) | 0.96 (1289) | 0.109 | 1278 (5500) |
| b^1A | 91 (HOMO→LUMO+1) | 1.04 (1197) | 0.081 | |
| c^1A | 88 ((HOMO-1→LUMO) | 1.39 (894) | 0.010 | 725 (9600) |
| d^1A | Mixed | 1.89 (656) | 0.019 | |
| e^1A | 65 (HOMO-2→LUMO); 25 (HOMO-3→LUMO+1) | 2.21 (561) | 0.139 | 553 (15600) |
| f^1A | 55 ((HOMO-3→LUMO); 31 (HOMO-2→LUMO+1) | 2.25 (551) | 0.241 | |
| g^1A | 60 (HOMO-5→LUMO); | 2.72 (455) | 0.065 | 332 (14100) |
| h^1A | 45 (HOMO-6→LUMO); 21 (HOMO-7→LUMO) | 2.75 (451) | 0.103 | |
| i^1A | Mixed | 2.91 (426) | 0.083 | |
| j^1A | 88 (HOMO→LUMO+3) | 3.53 (351) | 0.052 | |

Table 7.6.4. Selected G03/PBE0/CPCM calculated lowest allowed TD-DFT singlet transitions for 3^{2+} .

| state | main character (in %) | calculated | | experiment |
|------------------|-----------------------|----------------------------|-----------|-----------------------------|
| | | trans. energy ^a | osc. str. | $\lambda_{\max}/\epsilon^b$ |
| a ¹ A | 88 (HOMO-1→LUMO) | 1.61 (768) | 0.079 | 770 (14500) |
| b ¹ A | 85 (HOMO-2→LUMO) | 1.74 (709) | 0.089 | |
| c ¹ A | 88 ((HOMO-3→LUMO) | 2.05 (606) | 0.068 | 584 (23000) |
| d ¹ A | Mixed | 2.13 (581) | 0.062 | |
| e ¹ A | Mixed | 2.16 (574) | 0.063 | |
| f ¹ A | Mixed | 2.24 (552) | 0.105 | |
| g ¹ A | Mixed | 2.51 (495) | 0.060 | 502 (sh) |
| h ¹ A | Mixed | 2.63 (471) | 0.102 | |

7.7. Conclusion

The newly synthesized neutral compound **3** obtained as *mer* isomer has been assigned to $\text{Ru}^{\text{III}}(\text{Q}^{\bullet-})_3$ electronic configuration. The compound is EPR-silent and shows unshifted ¹H NMR lines, attributing strong antiferromagnetic coupling between the unpaired spin. More electron rich 4,6-di-*tert*-butyl-N-phenyl-*o*-benzoquinone (Q^{n}) ligand makes the oxidations easier and reductions difficult for complex **3** compare to 3,5-di-*tert*-butyl-*o*-benzoquinone based complexes **1** and **2**.

Compound **3** has a predominantly ligand-centered HOMO as evident from the EPR signal of the intermediate 3^+ (no *g* anisotropy detected at X-band frequency) which suggests preferentially $[\text{Ru}^{\text{III}}(\text{Q}^{\bullet-})_3] \rightarrow [\text{Ru}^{\text{III}}(\text{Q}^{\bullet-})_2(\text{Q}^0)]^+$ process and as supported by DFT calculations. For the doubly oxidized state the HOMO is now empty and no NIR transition can occur from this level. Intense charge transfer transitions involving the metal remain thus could be formulated as $[\text{Ru}^{\text{III}}(\text{Q}^{\bullet-})(\text{Q}^0)_2]^{2+}$.

On the other side, electron addition proceeds to yield a metal/ligand spin intermediate 3^- . The first reduction could either be associated with the ruthenium (III) or $\text{Q}^{\bullet-}$ center as both are susceptible to one-electron reduction and the resultant reduced species would than be formulated as $[\text{Ru}^{\text{III}}(\text{Q}^{\bullet-})_2(\text{Q}^{2-})]^-$ or $[\text{Ru}^{\text{II}}(\text{Q}^{\bullet-})_3]^-$. An appreciable *g* component splitting in glassy frozen solution at 110 K observable with $\Delta g = 0.0727$ suggest to form $[\text{Ru}^{\text{III}}(\text{Q}^{\bullet-})_2(\text{Q}^{2-})]^-$, in agreement with ca. 25% calculated metal character of the LUMO.

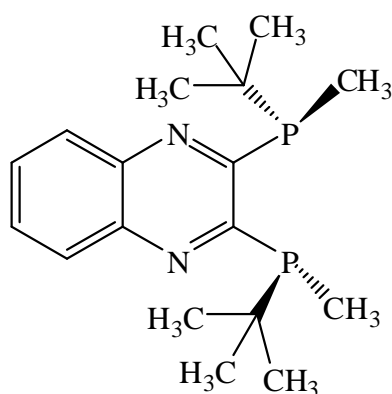
For the compounds **1** and **2** the electron is withdrawn successively from the ligand localized orbital with marginal contribution from metal as evident from the EPR signals of the respective oxidized species (small g anisotropy for **1**⁺ and no g anisotropy but relatively higher value of g compare to the free electron value for **2**⁺). DFT calculations support this results and it shows relatively greater contribution of Os compare to Ru in their respective HOMO. In the course of reduction a metal/ligand mixed spin intermediate situation arises in both, **1**⁻ and **2**⁻ according to EPR (see Section 7.4), in agreement with 27% and 37% metal contribution to their LUMO.

CHAPTER 8

Rhenium and Platinum Complexes of the Diphosphine Chelate Ligand *R,R*-QuinoxP

8.1. Introduction

Chiral 1,4-diphosphine³⁶ ligands capable of forming five- or six-membered metal-chelate rings have long been established as essential components of successful enantioselective catalysis systems, involving especially hydrogenation and C–C bond forming reactions.³³ For practical applications, however, the necessity to work with air-sensitive alkylphosphines has been a drawback, which is why strategies to overcome this inconvenience and simultaneously preserve or even improve the catalytic activity and selectivity have been sought. Imamoto and coworkers have recently presented a class of diphosphine ligands which fulfil these requirements, using the rigid and π electron-deficient quinoxaline heterocycle as a platform to which the dialkylphosphinosubstituents could be attached in 2,3 position.^{37,38} The resulting molecules such as 2,3-bis(*tert*-butylmethylphosphino)quinoxaline (QuinoxP)³⁷ and related diphosphines³⁸ were employed in connection with rhodium and palladium components for asymmetric hydrogenation and carbon–carbon bond formation.



R,R-QuinoxP = 2,3-bis(*tert*-butylmethylphosphino)quinoxaline (L)

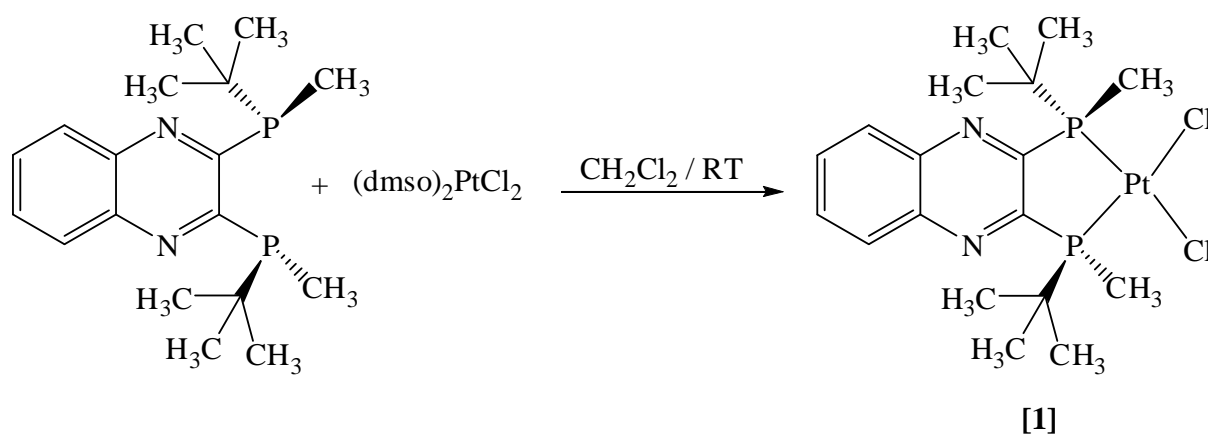
Considering the tendency of quinoxalines,³⁹ specially metal coordinate ones,⁴⁰ to undergo reversible electron uptake to form persistent, EPR-detectable radical anion species, the *R,R* isomer L of QuinoxP has been used in order to get the metal complexes.

The present chapter describes the reactions of metal precursors $\text{Pt}(\text{dmsO})_2\text{Cl}_2$ and $\text{Re}(\text{CO})_5\text{Cl}$ with the *R,R* isomer L of QuinoxP resulting in two air stable neutral mononuclear

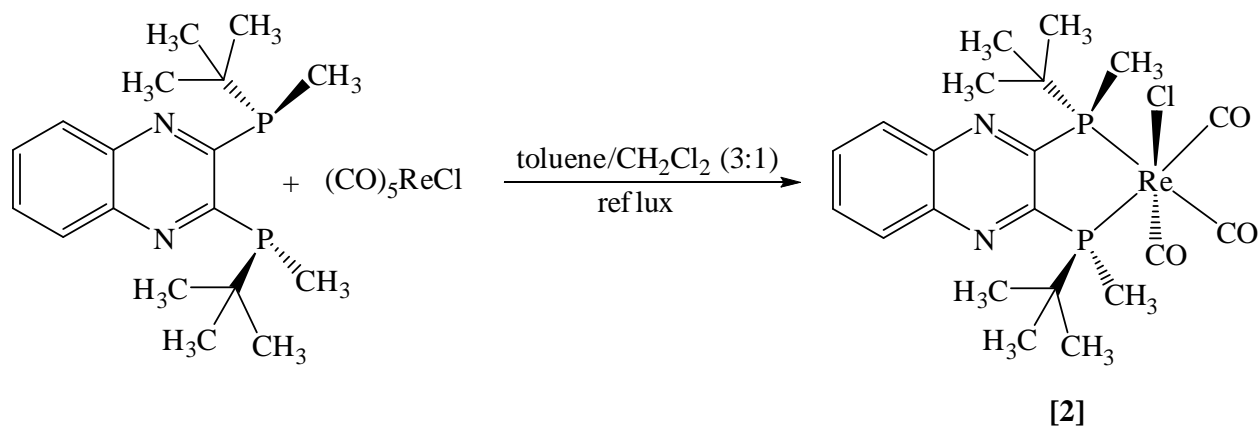
complexes with the formulations (L)PtCl₂ [1] and (L)Re(CO)₃Cl [2], including their single crystal X-ray crystal structures. The electron transfer behaviour of the complexes [1] and [2] has been investigated by cyclic voltammetry and by EPR, UV-Vis and IR spectroelectrochemistry.

8.2. Syntheses and characterization

The complex [(L)PtCl₂] [1] was synthesized by reacting the free ligand **L** with the metal precursor Pt(dmsO)₂Cl₂ according to the Scheme 8.2.1.



Scheme 8.2.1. Synthesis of (L)PtCl₂ [1]



Scheme 8.2.2. Synthesis of (L)Re(CO)₃Cl [2]

The yellow colored complex **1** was characterized by ^1H , ^{31}P NMR spectroscopy and elemental analysis. Measurable yellow single crystals were obtained by slow diffusion of hexane into a dichloromethane solution of **1**.

A mixture of $\text{Re}(\text{CO})_5\text{Cl}$ and of the free ligand **L** in toluene-dichloromethane mixture was heated to reflux for 4 h under an argon atmosphere to obtain the complex $(\text{L})\text{Re}(\text{CO})_3\text{Cl}$ [**2**] (Scheme 8.2.2). Addition of diethyl ether to a concentrated dichloromethane solution of **2** gave the desired yellow product which was further purified by recrystallization from a mixture of dichloromethane and diethyl ether. The complex **2** was characterized by ^1H , ^{31}P spectroscopy and elemental analysis. Single crystals were obtained from dichloromethane/hexane (1/1) mixture as dichloromethane solvate. Splitting of the P-methyl and P-*tert*-butyl signals in the ^1H -NMR spectrum (Figure 8.2.2) and the appearance of different P signals (Figure 8.2.4) in ^{31}P -NMR data reflect the different chemical environment above and below the π plane of L which is as a consequence of the *fac*- $\text{Re}(\text{CO})\text{Cl}$ configuration of the Re center in **2**. Only one set of P-methyl and P-*tert*-butyl signals in the ^1H -NMR spectrum (Figure 8.2.1) and one P signal in the ^{31}P NMR spectrum (Figure 8.2.3) were observed in the case of free ligand L.

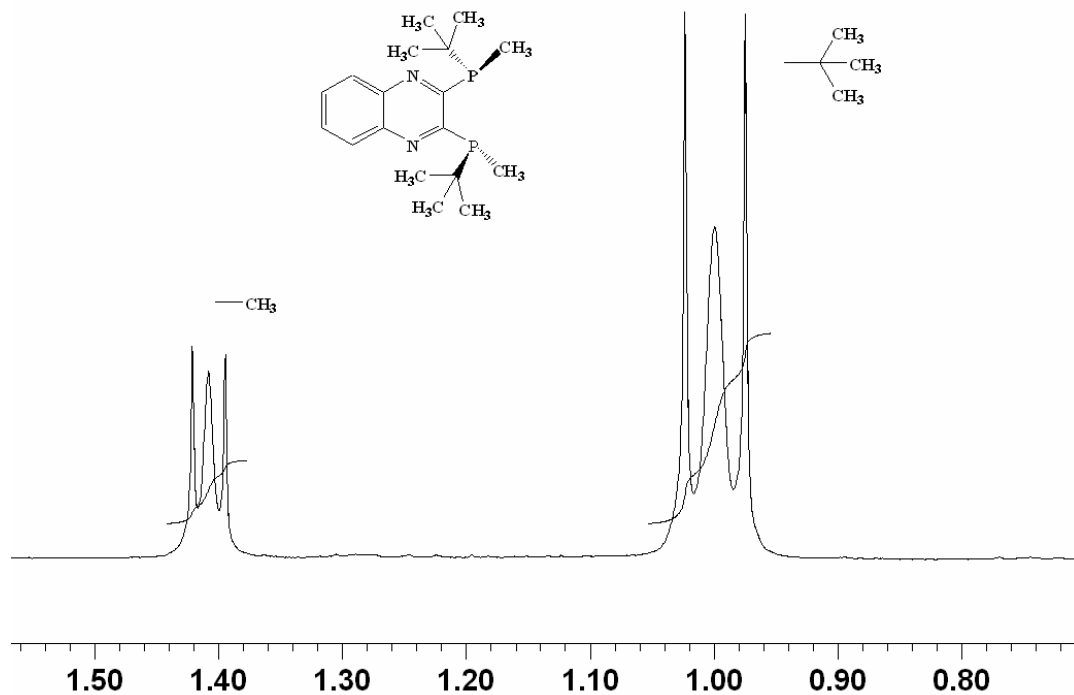


Figure 8.2.1. ¹H-NMR spectrum of the free ligand **L** in CDCl₃ at 250 MHz (aliphatic region).

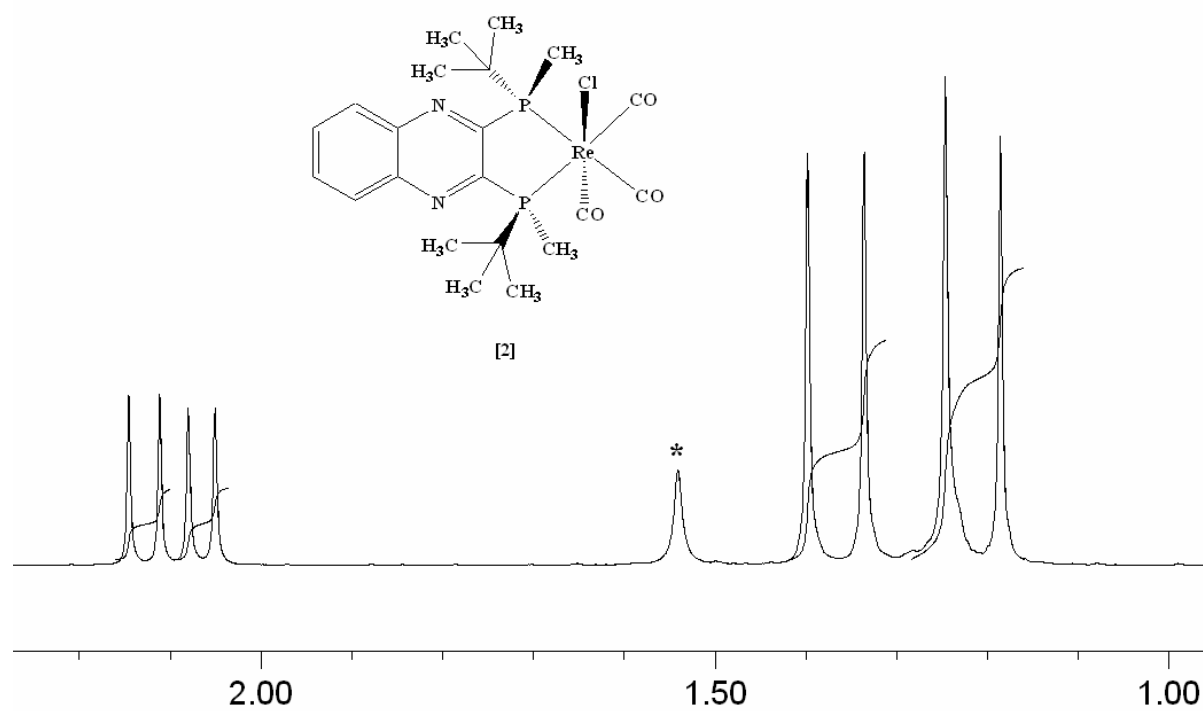


Figure 8.2.2. ¹H-NMR spectrum of **2** in CDCl₃ at 250 MHz (aliphatic region). *indicates signal from solvent

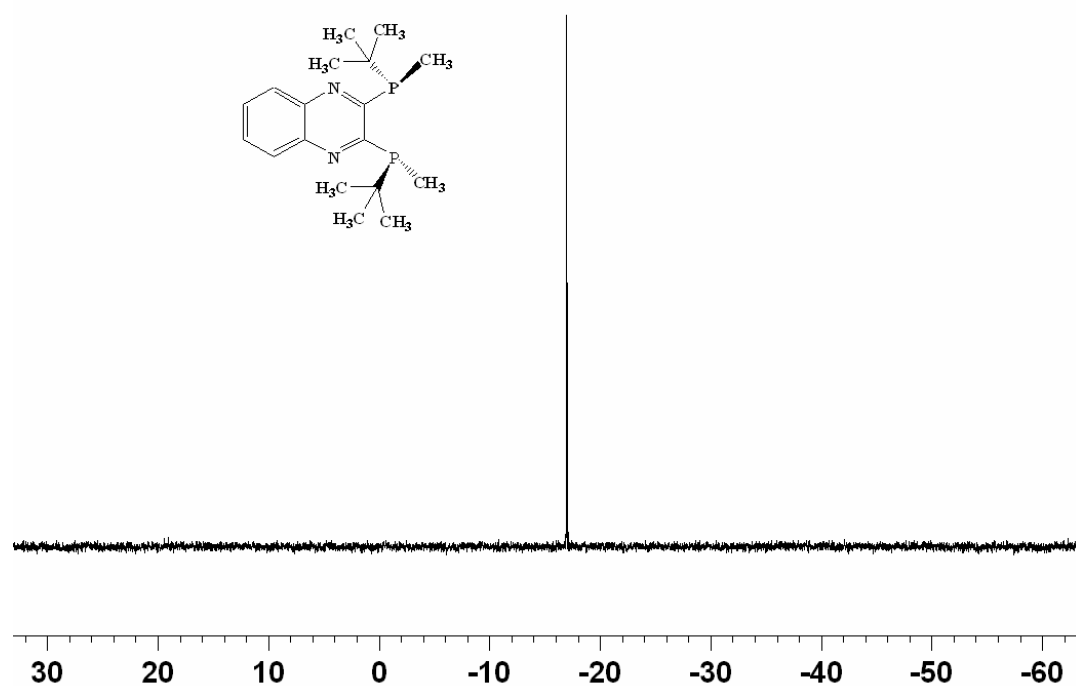


Figure 8.2.3. ^{31}P -NMR spectrum of the free ligand **L** in CD_3CN at 250 MHz.

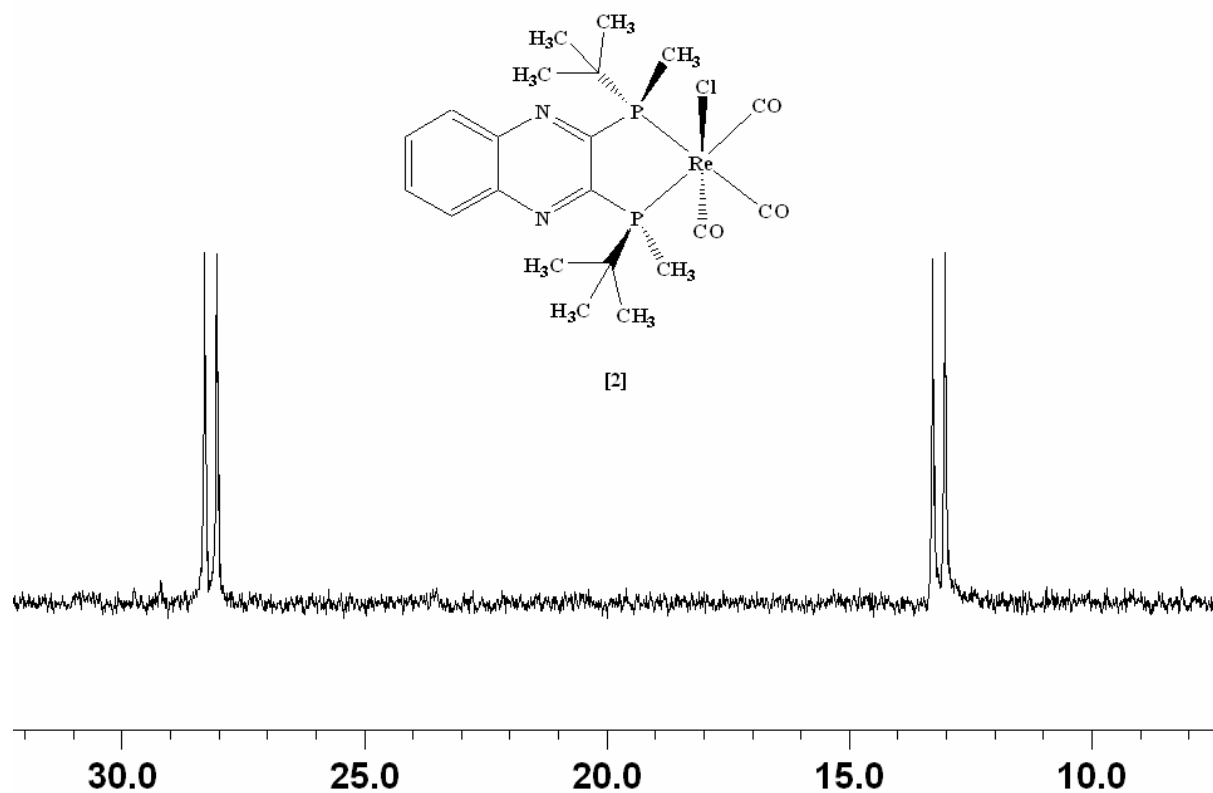


Figure 8.2.4. ^{31}P -NMR spectrum of **2** in CDCl_3 at 250 MHz.

8.3. Crystal structures

Single crystals were obtained as dichloromethane solvates by slow diffusion of n-hexane into a dichloromethane solution of [1]. Complex [2] was crystallized from CH₂Cl₂/n-hexane at -25 °C. Crystallographic data of both complexes are given in Chapters 9.5.8–9.5.9. The molecular structures of the complexes are shown in Figure 8.3.1 and 8.3.2. Selected bond lengths and angles are listed in Table 8.3.1 and 8.3.2. The structures show the expected formation of five-membered chelate rings involving the two *ortho*-positioned dialkylphosphino groups (*R* configuration) and the four-coordinate d⁸ metal [1] or six-coordinate d⁶ configured metal centers [2]. The five-membered rings are approximately planar, adopting only a slightly twisted configuration. The two Re–CO bonds deviate by approximately 13° from the chelate plane due to the steric repulsion between the chloride and carbonyl groups with the bulky *tert*-butyl group.

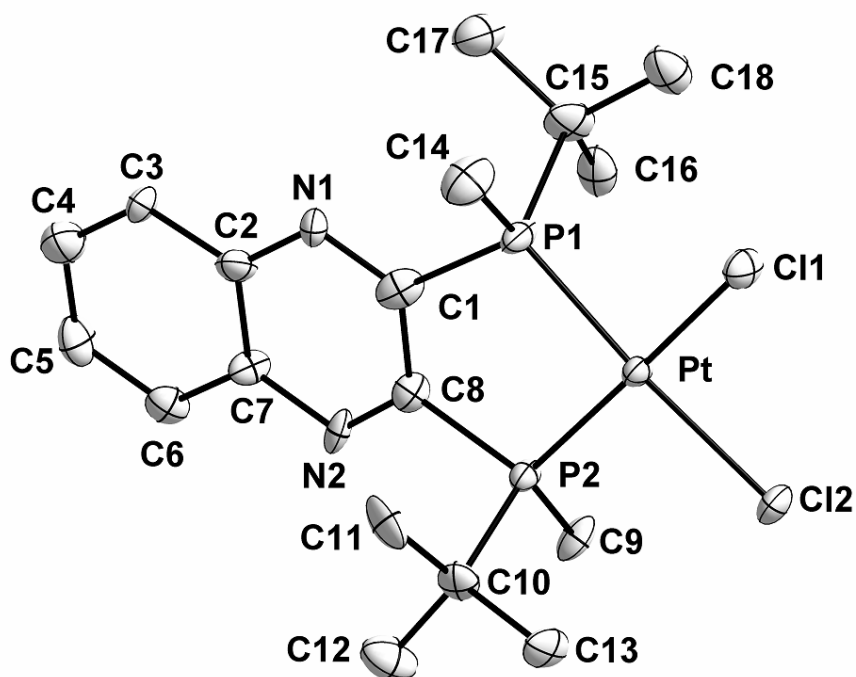


Figure 8.3.1. Molecular structure of [(L)PtCl₂] [1].

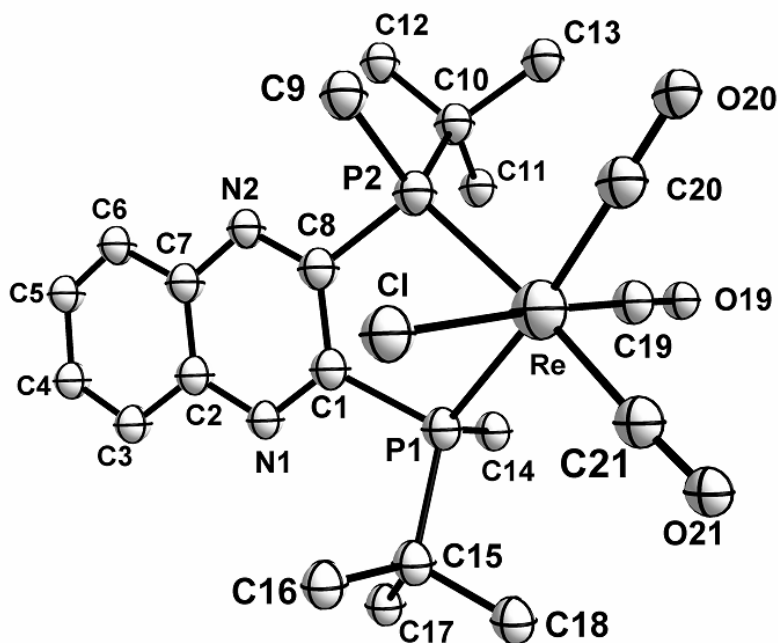


Figure 8.3.2. Molecular structure of [(L)Re(CO)₃Cl] [2].

Table 8.3.1. Selected bond lengths (Å) and angles (°) for [(L)PtCl₂] [1].

| Bond lengths (Å) | | | |
|------------------|-----------|------------|-----------|
| Pt–Cl(1) | 2.363(2) | Pt–Cl(2) | 2.361(2) |
| Pt–P(2) | 2.219(2) | Pt–P(1) | 2.219(2) |
| P(1)–C(14) | 1.807(9) | P(1)–C(15) | 1.893(8) |
| P(2)–C(9) | 1.799(8) | P(2)–C(10) | 1.862(7) |
| P(1)–C(1) | 1.835(9) | P(2)–C(8) | 1.831(8) |
| C(1)–C(8) | 1.425(11) | C(1)–N(1) | 1.314(11) |
| C(2)–C(7) | 1.436(10) | C(2)–C(3) | 1.404(11) |
| C(3)–C(4) | 1.384(12) | C(4)–C(5) | 1.406(12) |
| C(5)–C(6) | 1.378(12) | C(6)–C(7) | 1.425(11) |
| C(7)–N(2) | 1.365(10) | | |

| Bond angles (°) | | | |
|-----------------|-----------|------------------|-----------|
| P(1)–Pt–Cl(1) | 91.20(8) | P(1)–Pt–Cl(2) | 171.11(7) |
| P(2)–Pt–Cl(1) | 171.66(7) | P(2)–Pt–Cl(2) | 91.01(7) |
| P(2)–Pt–P(1) | 88.57(8) | Cl(1)–Pt–Cl(1) | 90.50(7) |
| C(9)–P(2)–C(10) | 108.9(4) | C(15)–P(1)–C(14) | 108.6(4) |

Table 8.3.2. Selected bond lengths (Å) and angles (°) for (L)Re(CO)₃(Cl) [2].

| Bond lengths (Å) | | | |
|------------------|-----------|------------|-----------|
| Re–Cl | 2.503(2) | Re–P(1) | 2.438(2) |
| Re – C(19) | 1.939(7) | Re – C(20) | 1.937(5) |
| Re–C(21) | 1.968(4) | C(6)–C(7) | 1.398(16) |
| C(7)–N(2) | 1.383(14) | Re– P(2) | 2.461(2) |
| P(1)–C(14) | 1.842(9) | P(1)–C(15) | 1.864(8) |
| P(2)–C(9) | 1.820(8) | P(2)–C(10) | 1.870(7) |
| P(1)–C(1) | 1.848(12) | P(2)–C(8) | 1.847(11) |
| C(1)–C(8) | 1.444(9) | C(1)–N(1) | 1.353(13) |
| C(2)–C(7) | 1.403(9) | C(2)–C(3) | 1.445(16) |
| C(3)–C(4) | 1.373(18) | C(4)–C(5) | 1.396(11) |
| C(5)–C(6) | 1.352(12) | C(6)–C(7) | 1.398(16) |

| Bond angles (°) | | | |
|-----------------|-----------|---------------|----------|
| P(1)–Re–Cl | 87.71(8) | P(2)–Re–Cl | 83.30(7) |
| P(1)–Re–C(20) | 171.90(9) | P(1)– Re–P(2) | 82.50(6) |
| P(1)–Re–C(21) | 97.48(8) | P(2)–Re–C(20) | 89.99(1) |
| P(2)–Re–C(21) | 170.41(5) | P(2)–Re–C(19) | 97.78(7) |
| C(19)–Re–Cl | 176.68(6) | C(20)–Re–Cl | 94.43(7) |

8.4. Electrochemistry

The free ligand 2,3-bis(*tert*-butylmethylphosphino)quinoxaline (**L**) undergoes an electrochemically reversible one-electron reduction at -2.05 V (Table 8.4.1) vs ferrocenium/ferrocene (Figure 8.4.1); the parent quinoxaline has $E_{1/2} = -2.18$ V.

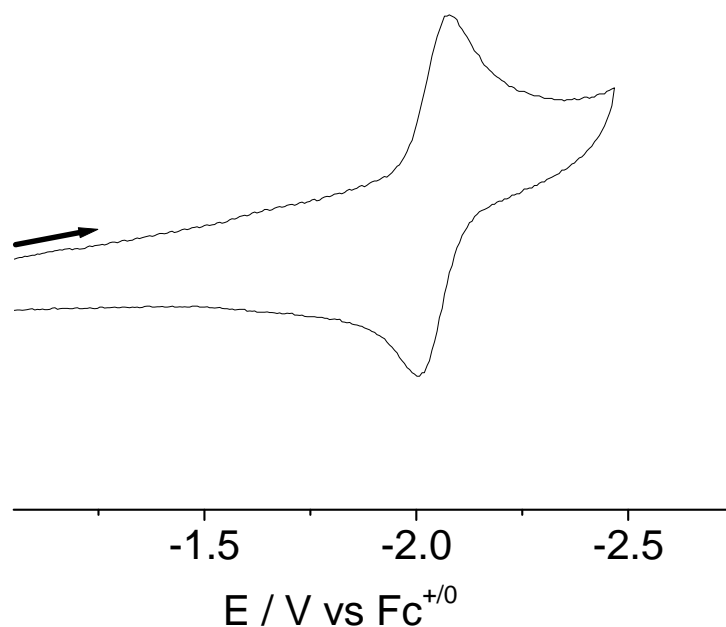


Figure 8.4.1. Cyclic voltammetry of **L** in $\text{CH}_2\text{Cl}_2/0.1\text{M Bu}_4\text{NPF}_6$ at a 100 mV/s scan rate.

Cyclic voltammetric studies of both the complexes **1** and **2** have been performed in $\text{CH}_2\text{Cl}_2/0.1\text{M Bu}_4\text{NPF}_6$. The both complexes **1** and **2** show a one-electron reversible reduction process at -1.56 V (Figure 8.4.2) and -1.70 V (Figure 8.4.3) vs $\text{Fc}^{+/0}$ respectively, facilitated in comparison to that of the free ligand (Table 3.4.1). The second reduction could not be observed in CH_2Cl_2 or CH_3CN , suggesting a large comproportionation constant for the one electron reduced intermediate, as would be expected for 1,4-diazine redox systems.^{40b}

The rhenium(I) compound **2** exhibits a partially reversible oxidation (Figure 8.4.3) at a potential $+1.11$ V versus $\text{Fc}^{+/0}$ higher than that for the (irreversible) oxidation of **L**. This result reflects the involvement of phosphine lone pairs in metal binding and suggests a metal-based oxidation to labile rhenium(II); unfortunately, the spectroelectrochemical measurement suffered from extensive decomposition of electro-generated $\mathbf{2}^+$. Reversible one-electron reduction could be monitored by EPR, IR and UV-Vis spectroelectrochemistry for the Re^{I} species **2** and by EPR spectroelectrochemistry for the platinum(II) complex **1**.

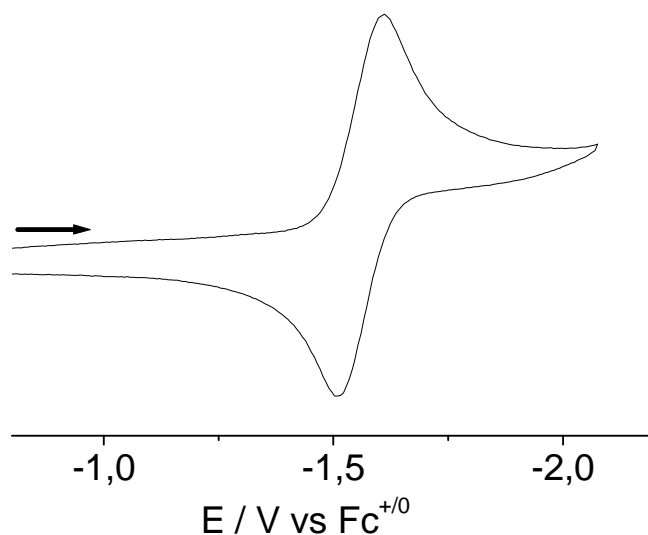


Figure 8.4.2. Cyclic voltammogram of [1] in $\text{CH}_2\text{Cl}_2/0.1\text{M Bu}_4\text{NPF}_6$ at 100 mV/s scan rate.

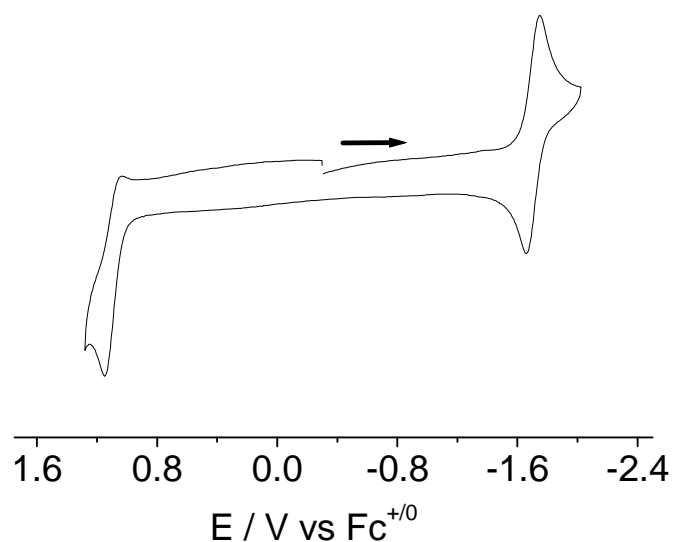


Figure 8.4.3. Cyclic voltammogram of [2] in $\text{CH}_2\text{Cl}_2/0.1\text{M Bu}_4\text{NPF}_6$ at 100 mV/s scan rate.

Table 8.4.1 Redox potentials of the free ligand **L** and its neutral complexes.

| | L | 1 | 2 |
|-------------------|---------------------|---------------------|---------------------|
| $E(\text{red})^a$ | -2.05 ($E_{1/2}$) | -1.56 ($E_{1/2}$) | -1.70 ($E_{1/2}$) |
| $E(\text{ox})^a$ | +0.36 ($E_{p,a}$) | >1.5 | +1.11 ($E_{p,a}$) |

^a in $\text{CH}_2\text{Cl}_2/0.1\text{ M Bu}_4\text{NPF}_6$. Potentials are given in V vs $\text{Fc}^{0/+}$, with half-wave ($E_{1/2}$) potential for reversible process or peak potentials (E_{pc} , E_{pa}) for irreversible process.

8.5. IR spectroelectrochemistry

IR spectroelectrochemistry measurement was carried for the complex **2** in the OTTLE cell⁶⁶ focusing on the carbonyl stretching region to investigate the site of the reduction process. The compound exhibits three CO bands at 2032 cm⁻¹, 1953 cm⁻¹ and 1895 cm⁻¹ in CH₂Cl₂ for the *fac*-(CO)₃Re moiety (Figure 8.5.1, Table 8.5.1). Upon one-electron reduction the expected shifts of all bands to lower energies are observed. However, the comparatively small low-energy shift to about 20 cm⁻¹ for the three CO stretching bands indicates marginal involvement of *fac*-(CO)₃Re fragment in the spin distribution on reduction of **2**. For comparison, the CO bands of (abpy)Re(CO)₃Cl (abpy = 2,2'-azobis(pyridine)) show an average shift of 40 cm⁻¹ on reduction.^{105,106}

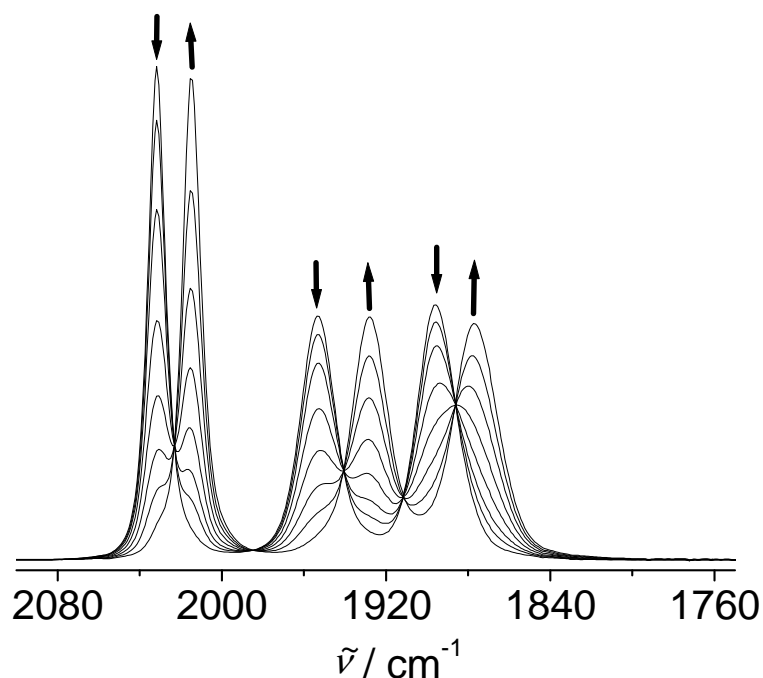


Figure 8.5.1. IR spectroelectrochemistry of the conversion **2** to **2**^{•-} in CH₂Cl₂ / 0.1 M Bu₄NPF₆.

Table 8.5.1. IR vibrational data obtained from spectroelectrochemistry.

| 2ⁿ | v (CO)^a / cm⁻¹ |
|----------------------|---|
| n = 0 | 2032, 1953, 1895 |
| n = -1 | 2014, 1928, 1877 |

^a Measurements in CH₂Cl₂/0.1 M Bu₄NPF₆.

8.6. EPR spectroscopy

The free ligand L and the metal complexes **1** and **2** could be reduced electrochemically *in situ* in CH₂Cl₂/ 0.1 M Bu₄NPF₆ to yield L^{•-}, **1**^{•-} and **2**^{•-} which were studied by means of X-band EPR spectroscopy. The radical anion produced, L^{•-}, shows an only partially resolved EPR signal (Figure 8.6.1) at $g_{\text{iso}} = 2.0030$ with a total spectral width of about 4 mT. Due to insufficient resolution, the complex spectrum could not yet be analyzed. Nevertheless, this result confirms the π -electron deficiency of quinoxaline,¹⁰⁷ enhanced further by the established electron-withdrawing effect of dialkylphosphino substituents.¹⁰⁸⁻¹¹⁰ EPR studies of radical complexes with heavy transition metals such as Pt or Re can provide sizable effects, including g factor shifts, g factor anisotropy and metal hyperfine coupling. While the former is caused by the large spin-orbit coupling constants of these ions,¹¹¹ both the ¹⁹⁵Pt (33.8% natural abundance, $I = 1/2$) and ^{185,187}Re isotopes (100%, $I = 5/2$, very similar nuclear magnetic moments) are distinguished by unusually large isotropic hyperfine coupling constants. The EPR spectra of **1**^{•-} (Figure 8.6.2) and **2**^{•-} (Figure 8.6.3) show g values close to that of the ligand radical anion ($g = 2.0030$), confirming the marginal contribution of the metals to the singly occupied molecular orbital. This result is supported by the lack of detectable g anisotropy at X-band frequency (9.5 GHz). Whereas **2**^{•-} did not show sufficient EPR resolution for hyperfine structure analysis, except for significantly higher spectral width due to ^{185,187}Re splitting at the order of 5 G, the radical **1**^{•-} exhibits a sizable ¹⁹⁵Pt hyperfine coupling of 24 G, the typically large ¹⁴N ($I = 1$) coupling parameter of quinoxalines (5.7 G)^{40b,107} as well as smaller ¹H and ³¹P splitting. Both kinds of nuclei have $I = 1/2$ quinoxaline anion was reported with 3.3 G (2H), 2.4 G (2H), and 1.45 G (2H).¹¹ The value of 24 G for ¹⁹⁵Pt is still below the approximately 40–50 G of typical (Het^{•-})PtCl₂ complexes, e.g. the heterocycles Het = bpy, bpym,^{112,113} and is certainly much smaller than what would be expected for mononuclear platinum(I) complexes.¹¹⁴

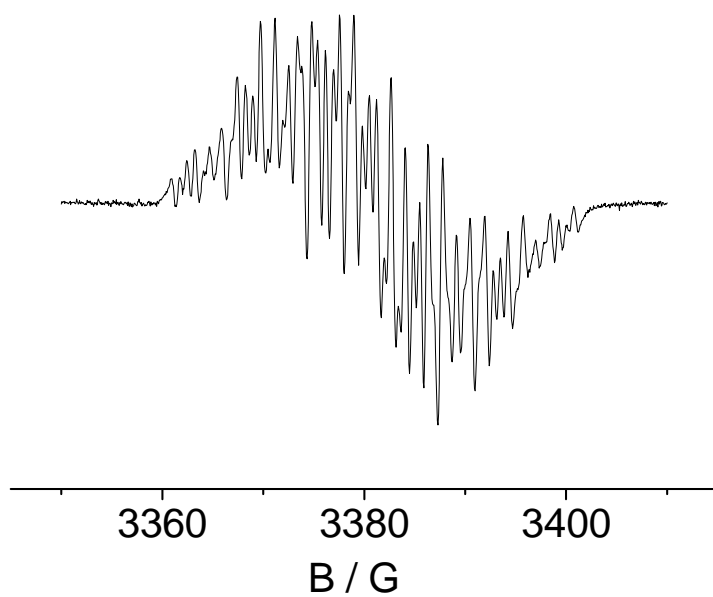


Figure 8.6.1. EPR spectrum of electrochemically generated $L^{\bullet-}$ at 289 K in $CH_2Cl_2/0.1 M$ Bu_4NPF_6 .

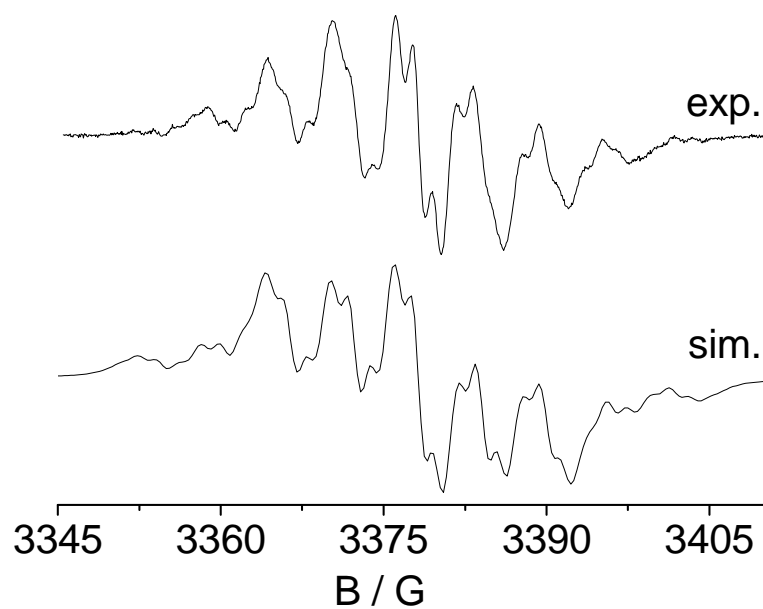


Figure 8.6.2. EPR spectrum of electrochemically generated $1^{\bullet-}$ at 298 K in $CH_2Cl_2/0.1 M$ Bu_4NPF_6 (top) with simulation (bottom).

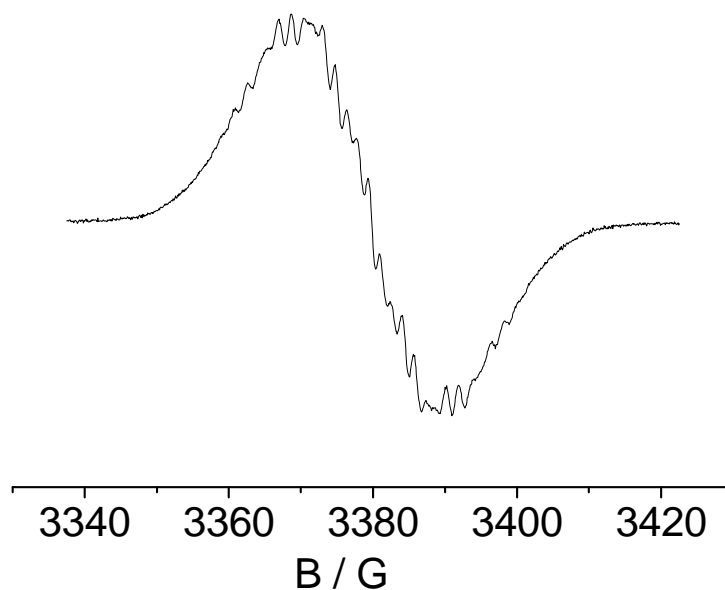


Figure 8.6.3. EPR spectrum of electrochemically generated $2^{\bullet-}$ at 298 K in $\text{CH}_2\text{Cl}_2/0.1 \text{ M Bu}_4\text{NPF}_6$.

Table 8.6.1. EPR data for free ligand $\text{L}^{\bullet-}$, $1^{\bullet-}$ and $2^{\bullet-}$.

| | $\text{L}^{\bullet-}$ | $1^{\bullet-}$ | $2^{\bullet-}$ |
|---|---|---|---|
| g | 2.0030 ^a | 2.0045 ^b | 2.0032 ^b 2.0032 ^c |
| A | partially resolved (40 G spectral width) | $A(^{195}\text{Pt}) = 24 \text{ G (1Pt)}$ $A(^{14}\text{N}) = 5.8 \text{ G (2N)}$ $A(^1\text{H}) = 1.7 \text{ G (2H)}$ $A(^{31}\text{P}) = 1.7 \text{ G (2P)}$ | partially resolved (70 G spectral width) |

^a in situ electrochemical reduction in acetonitrile at RT.

^b in situ electrochemical reduction in dichloromethane at RT.

^c in situ electrochemical reduction in dichloromethane at 110 K.

8.7. UV-Vis spectroelectrochemistry

Both complexes **1** and **2** display metal-to-(acceptor) ligand charge transfer (MLCT) absorptions in the near-UV region (Table 8.7.1). The location of reversible one electron reduction process of **2** to $\mathbf{2}^{\bullet-}$ was examined by applying the spectroelectrochemical techniques. The formation of $\mathbf{2}^{\bullet-}$ is accompanied by the emergence of an intense band system in the visible (563 nm) region (Figure 8.7.1). Quinoxaline radical anions are distinguished by long-wavelength absorptions around 600 nm.¹¹⁵ Therefore the observed bands in $\mathbf{2}^{\bullet-}$ can be assigned to intraligand and (bathochromically shifted) MLCT transitions. It can be concluded that there is only a marginal involvement of the *fac*-Re(CO)₃Cl fragment in the spin distribution on reduction.

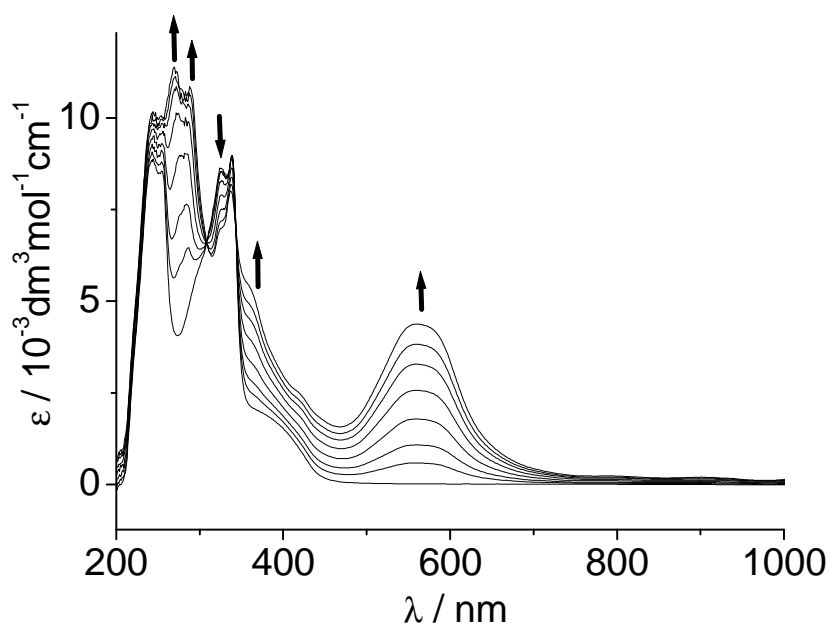


Figure 8.7.1. UV-Vis spectroelectrochemistry of the conversion **2** to $\mathbf{2}^{\bullet-}$ in CH₂Cl₂/0.1 M Bu₄NPF₆

Table 8.7.1. Electronic spectral data for $\mathbf{1}^0$ and $\mathbf{2}^n$ [$n = -1, 0$]

| Complex ^a | $\lambda_{\text{max}} / \text{nm} (\epsilon / \text{M}^{-1}\text{cm}^{-1})$ |
|-------------------------|---|
| $\mathbf{1}^0$ | 329 (9300), 340 (10600), 395 (sh) |
| $\mathbf{2}^0$ | 325 (8600), 338 (8900), 390 (sh) |
| $\mathbf{2}^{\bullet-}$ | 269 (11400), 289 (10800), 335 (8000), 360 (sh), 563 (4400) |

^a Measurements in CH₂Cl₂/0.1 M Bu₄NPF₆.

8.8. Conclusion and outlook

The two metal complexes **1** and **2** have been synthesised by reacting two standard metal precursor $\text{Pt}(\text{dmsO})_2\text{Cl}_2$ and $\text{Re}(\text{CO})_5\text{Cl}$ with the *R,R* isomer L of QuinoxP and characterized by ^1H , ^{31}P -NMR spectroscopy, elemental analysis and IR spectroscopy. Coordination was found to occur via P donor atoms as indicated crystal structures and NMR studies; the quinoxaline N donors do not participate in any coordination to the metals. The stereochemical arrangements observed illustrate the enantioselectivity reported for catalysis involving complexes of L. Electron acceptance by the quinoxaline heterocycle is responsible not only for the improved stability of L towards air but also for rather facile reduction of the complexes to the persistent radical anions **1** $^{\cdot-}$ and **2** $^{\cdot-}$. EPR, UV-Vis and IR spectroelectrochemistry collectively suggest a formulation of $(\text{L}^{\cdot-})\text{MX}_n$ in which the electron has been added to the heterocyclic π system of the molecule (spin localization on quinoxaline), the facile reduction to stable radical anion complexes, at least for the 5d element species involving Re(I) and Pt(II), is remarkable. These experiments also indicate the primary localization of the unpaired electron in the quinoxaline heterocycle with rather little spin delocalization to the metal centres via the phosphorus atoms. In this respect the complexes resemble other phosphino-substituted organic radical ligands¹⁵ or molecules such as dipyrrodo[3,2-a:2',3'-c]phenazine (dppz), where the coordinating (chelating) group and the spin bearing section are spatially separated and electrochemically decoupled, a behaviour which may be exploited under strongly reducing situation.

CHAPTER 9

Experimental

9.1. Instrumentation

Elemental analysis

C, H, N analyses were carried out on a Perkin elmer analyzer 240 by Ms. B. Förtsch.

NMR spectroscopy

^1H and ^{31}P -NMR experiments at 250 MHz and 400 MHz were carried out by Ms. K. Török on a Bruker AC 250 spectrometer and Bruker AM 400 MHz spectrometer. Tetramethylsilane (TMS) was used as external chemical shift standard.

EPR spectroscopy

X-band EPR spectra at about 9.5 GHz were obtained on a Bruker system ESP 300 equipped with a HEWLETT-PACKARD frequency counter 5350B, a Bruker ER035M gaussmeter for g-value determination. For measurements between 110-300 K, the same instrumental configurations were used with a liquid nitrogen cryostat. Spectra at 285 GHz were taken on a laboratory-made spectrometer at the Grenoble High magnetic Field laboratory in frozen solutions at 5 K.

ESI-mass spectroscopy

ESI mass spectra were recorded on Bruker Daltonics-microTOF-Q by Dr. J. Opitz, Mr. J. Trinkner and Ms. K. Wohlbold.

IR spectroscopy

IR spectra were obtained using Perkin-Elmer FTIR 684 and 283 instruments or Nicolet 6700 FTIR instrument. The solid state IR measurements were performed with an ATR unit (smart orbit with diamond crystal) on Nicolet 6700 FTIR instrument. The solution measurements were performed through CaF_2 windows.

UV-Vis-NIR spectroscopy

Absorption spectra were recorded on J&M TIDAS and Simadzu UV 3101 PC spectrometers. The measurements were done in solution using quartz cuvettes of 1 cm or 1 mm path length.

UV-Vis-NIR and IR spectroelectrochemistry

UV-Vis-NIR and IR spectroelectrochemistry measurements were performed under argon atmosphere using an optically transparent electrode (OTTLE) cell developed by Mr. Krejčík. The windows of the cell consist of CaF₂ plates. Between the plates there is a spacer into which the working (platinum mesh), auxiliary (platinum mesh) and reference electrodes (silver wire as pseudo reference) are melt-sealed.

Cyclic voltammetry

Cyclic and square-wave voltammetry measurements were performed on an EG&G PAR 273 potentiostat. The measurements were carried out under an argon atmosphere in 0.1 M tetrabutylammonium hexafluorophosphate or in 0.1 M tetrabutylammonium perchlorate solutions using a three-electrode configuration (glassy carbon as working electrode, platinum as counter electrode and silver as pseudoreference electrode). The ferrocene/ferrocenium couple served as internal reference. Polarography was performed using a PAR 263A instrument.

9.2. Solvents and working conditions

All metal complexes were synthesized under argon atmosphere using conventional Schlenk techniques. Solvents were dried by refluxing under argon over calcium hydride (dichloromethane, acetonitrile, methanol, ethanol and hexane), calcium chloride (acetone), sodium (toluene) or lithium aluminium hydride (diethyl ether). They were degassed by freeze-pump-thaw method.

9.3. DFT calculations

DFT calculations were performed by Dr. S. Zalis from J. Heyrovský Institute of Physical Chemistry, Prague.

[(OEP)Ru(NO)(H₂O)]ⁿ (n = 1, 2) and [(OEP)Ru(NO)(py)]ⁿ (n = 0, 1)

The electronic structures of all complexes were calculated by density functional theory (DFT) methods using the Gaussian 03¹¹⁶ and ADF2006.01¹¹⁷ program packages. In order to simplify some of the calculations the ethyl substituent was replaced by methyl in [(OEP)Ru(NO)(H₂O)]ⁿ, leading to [(OMP)Ru(NO)(H₂O)]ⁿ. The calculations of the vibrational

frequencies were performed at optimized geometries. Low-lying excited states were calculated by the time-dependent DFT (TD-DFT) method.

The hybrid functional of Perdew, Burke and Ernzerhof¹¹⁸ (PBE0) was used within Gaussian (G03/PBE0) together with 6-31G* polarized double- ζ basis sets¹¹⁹ for C, N, H and O atoms and effective core pseudopotentials and corresponding optimized sets of basis functions for Ru atoms.¹²⁰ The triple- ζ basis augmented by diffuse functions (aug-cc-pvtz)¹²¹ was used for O within the H₂O ligand. The vibrational analysis was done with the “pure” density functional BPW91.^{122,123} The polarizable conductor calculation model (CPCM)¹²⁴ was used for modeling of the solvent influence in TD DFT calculations.

Slater-type orbital (STO) basis sets of triple- ζ quality with two polarization functions for the Ru atom and of triple- ζ quality with one polarization function for the remaining atoms were employed within ADF2006.01. The inner shells were represented by the frozen core approximation (1s for C, N, O, 1s-3d for Ru were kept frozen). The calculations were done with the functional including Becke’s gradient correction¹²² to the local exchange expression in conjunction with Perdew’s gradient correction¹²⁴ to the local correlation (ADF/BP). The scalar relativistic (SR) zero order regular approximation (ZORA) was used within ADF calculations. The *g* tensor was obtained from a spin-nonpolarized wave function after incorporating the spin-orbit (SO) coupling. *A* and *g* tensors were obtained by first-order perturbation theory from a ZORA Hamiltonian in the presence of a time-independent magnetic field.^{125,126} Core electrons were included in calculations of *A* tensors.

[(terpy)Ru(Q)(NO)]ⁿ⁺ (n = 1, 2, 3)

DFT Calculations were performed using the Gaussian 03¹¹⁶ and ADF2008.01¹¹⁷ program packages. In order to simplify calculations the *tert.*-Bu substituents were replaced by methyl groups. The calculation of the vibrational frequency was performed at optimized geometry, no imaginary frequency was found. The hybrid functional of Perdew, Burke and Ernzerhof¹¹⁸ (PBE0) was used within Gaussian (G03/PBE0) together with 6-31G* polarized double- ζ basis sets¹¹⁹ for C, N, H and O atoms and effective core pseudopotentials and corresponding optimized sets of basis functions for Ru.¹²⁰ The vibrational analysis was done with the “pure” density functional BPW91.^{122,123} Slater type orbital (STO) basis sets of triple- ζ quality with two polarization functions for the Ru atom and of triple- ζ quality with one polarization function for the remaining atoms were employed within ADF2008.01. The inner shells were represented by the frozen core approximation (1s for C, N, O, 1s-3d for Ru were kept frozen). The calculations were done with the functional including Becke’s gradient correction¹²² to the

local exchange expression in conjunction with Perdew's gradient correction¹²⁴ to the local correlation (ADF/BP). The scalar relativistic (SR) zero order regular approximation (ZORA) was used within ADF calculations. The g tensor was obtained from a spin-nonpolarized wave function after incorporating the spin-orbit (SO) coupling. A and g tensors were obtained by first-order perturbation theory from a ZORA Hamiltonian in the presence of a time-independent magnetic field.^{125,126} Core electrons were included in calculations of A tensors. The vibrational analysis was done with the "pure" density functional BPW91.

$[(Q)ClRu(\mu\text{-tppz})RuCl(Q)]^{n+}$ ($n = 1, 2, 3$)

The electronic structures of $[Cl(Q)Ru(\mu\text{-tppz})Ru(Q)Cl]^{n+}$ ($n = 1, 2, 3$) were calculated by the density functional theory (DFT) method using the Gaussian 03¹¹⁶ and ADF2008.01¹¹⁷ program packages using the experimental (crystal) structure of $[Cl(Q)Ru(\mu\text{-tppz})Ru(Q)Cl](PF_6)_2$. Electronic transitions were calculated by the time-dependent DFT (TD DFT) method.

The hybrid functional of Perdew, Burke and Ernzerhof¹¹⁸ (PBE0) was used within Gaussian (G03/PBE0) together with 6-31G* polarized double- ζ basis sets¹¹⁹ for C, N, H and O atoms and effective core pseudopotentials and corresponding optimized sets of basis functions for the Ru atoms.¹²⁰ The solvent was described by the polarizable conductor calculation model (CPCM)¹²⁷ in TD DFT calculations.

Slater-type orbital (STO) basis sets of triple- ζ quality with two polarization functions for the Ru atom and of triple- ζ quality with one polarization function for the remaining atoms were employed within ADF2008.01. The inner shells were represented by the frozen core approximation (1s for C, N, O, 1s-3d for Ru were kept frozen). The calculations were done with the functional including Becke's gradient correction to the local exchange expression in conjunction with Perdew's gradient correction to the local correlation (ADF/BP).^{122,123} The scalar relativistic (SR) zero order regular approximation (ZORA) was used within ADF calculations. The g tensor was obtained from a spin-nonpolarized wave function after incorporating the spin-orbit (SO) coupling. A and g tensors were obtained by first-order perturbation theory from a ZORA Hamiltonian in the presence of a time-independent magnetic field.^{125,126} Core electrons were included in calculations of A tensors.

[Ru(Q₀)₃]ⁿ and [Os(Q₀)₃]ⁿ (n = -1, 0, 1)

The electronic structures of [Ru(sq)₃] and [Os(sq)₃] were calculated by the density functional theory (DFT) method using the Gaussian 03¹¹⁶ and ADF2008.01¹¹⁷ program packages on experimental structure. Electronic transitions were calculated by the time-dependent DFT (TD DFT) method.

The hybrid functional of Perdew, Burke and Ernzerhof¹¹⁸ (PBE0) was used within Gaussian (G03/PBE0) together with 6-31G* polarized double- ζ basis sets¹¹⁹ for C, H and O atoms and effective core pseudopotentials and corresponding optimized sets of basis functions for the Ru atoms.¹²⁰ The solvent was described by the polarizable conductor calculation model (CPCM)¹²⁷ in TD DFT calculations.

Slater-type orbital (STO) basis sets of triple- ζ quality with two polarization functions for the Ru atom and of triple- ζ quality with one polarization function for the remaining atoms were employed within ADF2008.01. The inner shells were represented by the frozen core approximation (1s for C, N, O, 1s-3d for Ru were kept frozen). The calculations were done with the functional including Becke's gradient correction¹²² to the local exchange expression in conjunction with Perdew's gradient correction to the local correlation (ADF/BP).¹²⁴ The scalar relativistic (SR) zero order regular approximation (ZORA) was used within ADF calculations. The *g* tensor was obtained from a spin-nonpolarized wave function after incorporating the spin-orbit (SO) coupling. *A* and *g* tensors were obtained by first-order perturbation theory from a ZORA Hamiltonian in the presence of a time-independent magnetic field.^{125,126} Core electrons were included in calculations of *A* tensors.

[Ru(Q)₃]ⁿ (n = -1,0,1)

The electronic structures of all complexes were calculated by density functional theory (DFT) methods using the Gaussian 03¹¹⁶ and ADF2008.01¹¹⁷ program packages. The calculations of the vibrational frequencies were performed at optimized geometries. Low-lying excited states were calculated by the time-dependent DFT (TD-DFT) method.

The hybrid functional of Perdew, Burke and Ernzerhof¹¹⁸ (PBE0) was used within Gaussian (G03/PBE0) together with 6-31G* polarized double- ζ basis sets¹¹⁹ for C, N, H and O atoms and effective core pseudopotentials and corresponding optimized sets of basis functions for Ru atoms.¹²⁰ The polarizable conductor calculation model (CPCM)¹²⁷ was used for modeling of the solvent influence in TD DFT calculations.

Slater-type orbital (STO) basis sets of triple- ζ quality with two polarization functions for the Ru atom and of triple- ζ quality with one polarization function for the remaining atoms were employed within ADF2008.01. The inner shells were represented by the frozen core approximation (1s for C, N, O, 1s-3d for Ru were kept frozen). The calculations were done with the functional including Becke's gradient correction¹²² to the local exchange expression in conjunction with Perdew's gradient correction to the local correlation (ADF/BP).¹²⁴ The scalar relativistic (SR) zero order regular approximation (ZORA) was used within ADF calculations. The g tensor was obtained from a spin-nonpolarized wave function after incorporating the spin-orbit (SO) coupling. A and g tensors were obtained by first-order perturbation theory from a ZORA Hamiltonian in the presence of a time-independent magnetic field.^{1125,126} Core electrons were included in calculations of A tensors.

9.4. Syntheses

9.4.1. Commercially available compounds

- [Ru(OEP)(CO)], NaNO₂, *tetra*-2-pyridinyl-pyrazine, 3,5-di-*tert*-butylcatechol, (*R,R*)-2,3-Bis(*tert*-butylmethyl-phosphino)quinoxaline, AgClO₄, AgPF₆ and OsO₄ from Aldrich.
- NOBF₄, NOPF₆, 2,2':6',2''-terpyridine and 60% HPF₆ from Alfa Aesar.
- KCN, Ph₄PCl, pyridine, 4-cyanopyridine and 4-*N,N*-dimethylaminopyridine from Fluka.
- KReO₄ from Strem.
- Re(CO)₅Cl from Acros.
- Hydroxylammoniumchloride and aniline from Merck.
- The precursor complex Pt(dmsO)₂Cl₂ was obtained from Dr. Ece Bulak.

9.4.2. Syntheses of reported compounds

The ligand 2-anilino-4,6-di-*tert*-butylphenol³³ and the precursor complex Cl₃Ru(μ -tppz)RuCl₃,⁷⁷ [(OEP)Ru(NO)(H₂O)](BF₄) were prepared according to literature procedures.

9.4.3. Synthesis of $(\text{PPh}_4)_4[(\text{CN})_4(\text{NO})\text{Re}(\mu\text{-O})\text{Re}(\text{NO})(\text{CN})_4]$

A mixture of KReO_4 (1 g, 3.5 mmol), KCN (2.3 gm, 35.3 mmol) and KOH (5.9 g, 105.3 mmol) were dissolved in a minimum volume of hot water (*ca.* 90 °C). Solid $\text{NH}_2\text{OH}\cdot\text{HCl}$ (3.65 g, 52.5 mmol) was added portion wise into it with constant stirring. A deep red color solution was obtained during the course of the addition. Stirring was continued for another 1.5 h. The solution was then cooled to 0 °C and the ice-cold solution was subsequently poured into chilled dry *i*-PrOH (100 mL) and stirred for 10 min keeping the temperature of the solution at 0 °C. A deep red colored oily solid was separated out. The colorless liquid was carefully decanted off. The oil was poured into the cold *i*-PrOH (100 mL) and the mixture was stirred until the oil thickened. This process was repeated 3-4 times using fresh *i*-PrOH in each operation. The deep red solid so obtained was washed thoroughly with cold *i*-PrOH and then dried in vacuum. The crude product was extracted with MeOH and filtered through a frit. Addition of hexane/diethylether (1:1) mixture to the cold MeOH extract resulted in a microcrystalline solid which was filtered and washed with cold *i*-PrOH. The solid product thus obtained was dissolved in minimum volume of distilled water. A saturated aqueous solution of Ph_4PCl was added into it and stirred for 1 h at room temperature. A deep purple colored solid material corresponding to the tetra(tetraphenylphosphonium) salt, $(\text{PPh}_4)_4[(\text{CN})_4(\text{NO})\text{Re}(\mu\text{-O})\text{Re}(\text{NO})(\text{CN})_4]$ was separated out from the solution. It was filtered and washed several times with chilled water. The purple colored solid was recrystallised from acetonitrile-diethyl ether solution which yielded analytically pure $(\text{PPh}_4)_4[(\text{CN})_4(\text{NO})\text{Re}(\mu\text{-O})\text{Re}(\text{NO})(\text{CN})_4]$. Single crystals of $(\text{PPh}_4)_4[(\text{CN})_4(\text{NO})\text{Re}(\mu\text{-O})\text{Re}(\text{NO})(\text{CN})_4]$ were obtained from dichloromethane/hexane (diffusion method) at room temperature.

Yield: 54 mg (2-3%)

IR (CH_3CN): $\nu_{\text{NO}}/\text{cm}^{-1} = 1670$ and 1710 . $\nu_{\text{CN}}/\text{cm}^{-1} = 2118$ and 2129 .

9.4.2. Syntheses of complexes with $[\text{Ru}(\text{terpy})\text{Cl}_3]$

$[(\text{terpy})\text{Ru}(\text{Q})\text{Cl}](\text{ClO}_4)$

Starting complex $[\text{Ru}^{\text{III}}(\text{terpy})\text{Cl}_3]$ (100 mg, 0.23 mmol), 2-anilino-4,6-di-*tert*-butylphenol ligand (L, 68 mg, 0.23 mmol) and NEt_3 were taken in 20 mL of ethanol, and the mixture was heated at reflux in air for 5 h under atmospheric conditions. The initial dark brown color

solution gradually changed to a deep purple. The solvent was then removed under reduced pressure. The solid dry mass was dissolved in minimum volume (5 mL) of acetonitrile/methanol (4:1) mixture, and an excess saturated aqueous solution of NaClO₄ was added to it. The solid precipitate thus obtained was filtered off and washed thoroughly by cold ethanol followed by ice-cold water. The product thus obtained was dried completely in vacuum. It was then purified on an alumina (neutral) column. The deep solution corresponding to the desired product was eluted with CH₂Cl₂/CH₃CN (1:1). Evaporation of the solvent under reduced pressure afforded the pure complex [(terpy)Ru(Q)Cl](ClO₄).

Yield: 60 mg (35%).

Mass spectrum: The positive ion electrospray mass spectrum in acetonitrile showed the molecular ion peak centered at $m/z = 676.4$ corresponding to [(terpy)Ru(Q)Cl]⁺ (calculated mass: 655.2).

Elemental analysis: C₃₅H₃₆Cl₂N₄O₅Ru (764.67 g/mol).

Calculated: C: 54.98% H: 4.75% N: 7.33%

Found: C: 54.93% H: 5.39% N: 7.00%

¹H NMR (400 MHz, acetone-*d*⁶): δ = 8.26 (d, *J* = 8.0 Hz, 2 H), 8.12 (d, *J* = 8.1 Hz, 2 H), 8.05 (m, 2 H), 7.97 (s, 1 H), 7.88 (t, *J* = 8.1, 8.2 Hz, 1 H), 7.49 (m, 4 H), 7.16 (t, *J* = 7.5, 1 H), 6.97 (m, 2 H), 6.53 (s, 1 H), 5.87 (d, *J* = 7.32 Hz, 2H), 1.80 (s, 9 H), 1.10 (s, 9 H).

UV-Vis (CH₃CN): λ_{max}/nm (ε/M⁻¹ cm⁻¹) = 570 (24100), 315 (29900), 270 (34100), 237 (44200).

[(terpy)Ru(Q)(NO₂)](ClO₄)

10 ml of degassed water was added to the 5 mL CH₃CN solution of [(terpy)Ru(Q)Cl](ClO₄) (100 mg, 0.13 mmol). Then mixture was heated at reflux for 30 min in argon atmosphere. An excess of AgClO₄ (135 mg, 0.65 mmol) was added to the above hot solution and the heating was continued for a further 2 h. The solution was then cooled and the precipitated AgCl was separated by filtration through a (G-4) frit over a celite bed. An excess of NaNO₂ (135 mg,

1.95 mmol) was added in to the filtrate and the mixture was heated to reflux again for 3h in argon atmosphere. During the course of the reaction deep purple color of [(terpy)Ru(Q)Cl](ClO₄) was changed to blue. On cooling to room temperature the blue nitro complex [(terpy)Ru(Q)(NO₂)](ClO₄) was precipitated out. It was filtered off followed by washed with chilled water, and dried in vacuum.

Yield: 60 mg (85%)

Mass spectrum: The positive ion electrospray mass spectrum in acetonitrile showed the molecular ion peak centered at $m/z = 676.2$ corresponding to [(terpy)Ru(Q)(NO₂)]⁺ (calculated mass: 675.8).

Elemental analysis: C₃₅H₃₆Cl₁N₅O₇Ru (775.23 g/mol).

Calculated: C: 54.23% H: 4.68% N: 9.03%

Found: C: 54.14% H: 4.55% N: 9.10%

¹H NMR (250 MHz, CD₃CN): $\delta = 8.62$ (d, $J = 8.1$ Hz, 2 H), 8.59 (d, $J = 8.1$ Hz, 2 H), 8.26 (m, 3 H), 7.88 (m, 3 H), 7.70 (m, 2 H), 7.22 (t, $J = 7.7, 7.3$ Hz, 1 H), 7.08 (t, $J = 8.1, 7.3$ Hz, 2 H), 6.68 (s, 1 H), 6.08 (d, $J = 7.3$ Hz, 2H).

UV-Vis (CH₂Cl₂): λ_{\max}/nm ($\epsilon/\text{M}^{-1}\text{cm}^{-1}$): 585 (27300), 364 (11000), 312 (23400), 276 (32300), 234 (36800).

[(terpy)Ru(Q)(NO)](PF₆)₂

An excess of 60% HPF₆ (0.4 mL) was added to the solution of [(terpy)Ru(Q)(NO₂)](ClO₄) (50 mg, 0.06 mmol, 10 mL CH₂Cl₂). The solution was stirred for 30 min in a dark condition under argon atmosphere during which resulted in a dark brown precipitate of [(terpy)Ru(Q)(NO)](PF₆)₂. The precipitate was isolated by filtration and washed with 3 mL of chilled CH₂Cl₂. It was further purified by recrystallization from a mixture of acetonitrile and diethyl ether.

Yield: 39 mg (65%).

Elemental analysis: C₃₅H₃₆F₁₂N₅O₂P₂Ru (949.72 g/mol).

| | | |
|-----------------------|----------|-----------|
| Calculated: C: 44.26% | H: 3.82% | N: 7.37 % |
| Found: C: 43.64% | H: 3.33% | N: 7.32 % |

IR: $\nu_{\text{CO}}/\text{cm}^{-1} = 1887$ s (solid) and 1900 s (CH₃CN).

EPR (CH₂Cl₂): $g_{\text{iso}} = 2.0024$.

9.4.5. Syntheses of mononuclear complexes with [Cl₃Ru(μ -tppz)RuCl₃]

[(tppz)Ru(Q)Cl](PF₆)

The precursor complex Cl₃Ru(μ -tppz)RuCl₃ (100 mg, 0.12 mmol) and 2-anilino-4,6-di-*tert*-butylphenol (L, 79 mg, 0.26 mmol) were refluxed for 6 h in 20 mL of ethanol in the presence of excess LiCl (52 mg, 1.2 mmol) and CH₃COONa (25 mg, 0.30 mmol) under atmospheric condition. The initial light green solution changed to deep green. After removal of the solvent the residue was dissolved in 5 mL of an acetonitrile/methanol (4/1) mixture, and an excess of a saturated aqueous solution of NH₄PF₆ was added. The precipitate thus obtained was collected and washed with ice-cold water. The crude product was purified by column chromatography (neutral alumina). The blue mononuclear complex [(tppz)Ru(Q)Cl](PF₆) was eluted by 4:1 CH₂Cl₂/CH₃CN mixture. Evaporation of solvent under reduced pressure yielded the pure compound.

Yield: 18 mg (15%).

Mass spectrum: The positive ion electrospray mass spectrum in acetonitrile showed the molecular ion peak centered at $m/z = 820.2$ corresponding to [(tppz)Ru(Q)Cl]⁺ (calculated mass: 820.4).

Elemental analysis: C₄₄H₄₁F₆ClN₇OPRu (965.35 g/mol).

| | | |
|-----------------------|----------|-----------|
| Calculated: C: 54.75% | H: 4.28% | N: 10.16% |
| Found: C: 54.60% | H: 4.22% | N: 10.11% |

^1H NMR (400 MHz, CD_3CN): $\delta = 7.23$ (d, $J = 9.1$ Hz, 2H), 7.70–7.46 (m, 9H), 7.93 (t, $J = 1.1$ Hz, 2H), 7.95 (t, $J = 1.1$, 2H), 8.03 (d, $J = 1.8$, 2H), 8.05 (d, $J = 1.8$, 2H), 8.07 (d, $J = 1.8$, 2H), 8.65–8.60 (m, 2H), 1.52 (s, 9H), 1.79 (s, 9H).

UV-Vis (CH_2Cl_2): $\lambda_{\text{max}}/\text{nm}$ ($\epsilon/\text{M}^{-1}\text{cm}^{-1}$): 582 (18600), 328 (18100), 261 (17600).

[(tppz)Ru(Q)(NO₂)](PF₆)

10 ml of degassed water was added to the 5 mL CH_3CN solution of [(tppz)Ru(Q)Cl](PF₆) (100 mg, 0.10 mmol). Then mixture was heated at reflux for 30 min in argon atmosphere. An excess of AgClO_4 (135 mg, 0.65 mmol) was added to the above hot solution and the heating was continued for a further 2 h. The solution was then cooled and the precipitated AgCl was separated by filtration through a (G-4) frit over a celite bed. An excess of NaNO_2 (135 mg, 1.95 mmol) was added in to the filtrate and the mixture was heated to reflux again for 3h in argon atmosphere. During the course of the reaction deep blue color of [(tppz)Ru(Q)Cl](PF₆) was changed to blue. An excess of a saturated aqueous solution of NH_4PF_6 was added and on cooling to room temperature the blue nitro complex [(tppz)Ru(Q)(NO₂)](PF₆) was precipitated out. It was filtered off followed by washed with chilled water, and dried in vacuum.

Yield: 60 mg (86%).

Mass spectrum: The positive ion electrospray mass spectrum in acetonitrile showed the molecular ion peak centered at $m/z = 831.2$ corresponding to [(tppz)Ru(Q)(NO₂)]⁺ (calculated mass: 830.9).

Elemental analysis: $\text{C}_{44}\text{H}_{41}\text{F}_6\text{N}_8\text{O}_3\text{PRu}$ (975.91 g/mol).

Calculated: C: 54.15% H: 4.23% N: 10.16%

Found: C: 54.20% H: 4.18% N: 10.22%

^1H NMR (250 MHz, CD_3CN): $\delta = 7.36$ (d, $J = 8.3$ Hz, 2H), 7.54 (t, $J = 5.73$, 7.45, 2H), 7.72–7.65 (m, 2H), 7.87–7.76 (m, 9H), 8.05 (d, $J = 1.1$, 1.5 2H), 8.08 (t, $J = 1.2$, 1.1, 2H), 8.11 (d, $J = 1.7$, 2H), 8.75–8.69 (m, 2H), 1.67 (s, 9H), 1.88 (s, 9H).

UV-Vis (CH_2Cl_2): $\lambda_{\text{max}}/\text{nm}$: 595, 353, 296.

[(tppz)Ru(Q)(NO)](PF₆)₂

An excess of 60% HPF₆ (0.4 mL) was added to the solution of [(tppz)Ru(Q)(NO₂)](PF₆) (50 mg, 0.05 mmol, 10 mL CH_2Cl_2). The solution was stirred for 30 min in a dark condition under argon atmosphere during which resulted in a dark brown precipitate of [(tppz)Ru(Q)(NO)](PF₆)₂. The precipitate was isolated by filtration and washed with 3 mL of chilled CH_2Cl_2 . It was further purified by recrystallization from a mixture of acetonitrile and diethyl ether.

Yield: 23 mg (40%).

Elemental analysis: C₄₄H₄₁F₁₂N₈O₂PRu (1104.88 g/mol).

| | | |
|-----------------------|----------|-----------|
| Calculated: C: 47.83% | H: 3.75% | N: 10.14% |
| Found: C: 47.35% | H: 3.72% | N: 10.00% |

IR: $\nu_{\text{NO}}/\text{cm}^{-1}$ = 1900 s (solid) and 1902 s (CH_3CN).

EPR (CH_2Cl_2): g_{iso} = 2.0012.

9.4.6. Synthesis of dinuclear complex with [Cl₃Ru(μ -tppz)RuCl₃]

[(Q)ClRu(μ -tppz)RuCl(Q)](PF₆)₂

The precursor complex Cl₃Ru(μ -tppz)RuCl₃ (100 mg, 0.12 mmol) and 2-anilino-4,6-di-*tert*-butylphenol (L, 79 mg, 0.26 mmol) were refluxed for 6 h in 20 mL of ethanol in the presence of excess LiCl (52 mg, 1.2 mmol) and CH₃COONa (25 mg, 0.30 mmol) under atmospheric condition. The initial light green solution changed to deep green. After removal of the solvent the residue was dissolved in 5 mL of an acetonitrile/methanol (4/1) mixture, and an excess of a saturated aqueous solution of NH₄PF₆ was added. The precipitate thus obtained was collected and washed with ice-cold water. The crude product was purified by column

chromatography (neutral alumina). The complex [(Q)ClRu(μ -tppz)RuCl(Q)](PF₆)₂ was eluted as a green zone using a CH₂Cl₂/CH₃CN mixture (5/3) as eluent. Evaporation of solvent under reduced pressure yielded the pure compound.

Yield: 40% (76 mg).

Mass spectrum: The positive ion electrospray mass spectrum in acetonitrile showed the molecular ion peak centered at $m/z = 626.1$ corresponding to [(Q)ClRu(μ -tppz)RuCl(Q)]²⁺/2 (calculated mass/2: 626.2).

Elemental analysis: C₆₄H₆₆Cl₂F₁₂N₈O₂P₂Ru₂ (1542.27 g/mol).

| | | |
|-----------------------|----------|----------|
| Calculated: C: 49.84% | H: 4.31% | N: 7.27% |
| Found: C: 50.03% | H: 4.40% | N: 7.17% |

¹H NMR (400 MHz, CD₃CN) $\delta = 8.25$ (t, 7.9, 7.9), 7.97 (s), 7.86–.69 (m), 7.52 (d, 7.8), 7.16–6.98 (m), 6.82 (t, 7.8, 7.2), 6.5 (s), 1.17 (s), 1.89 (s).

UV-Vis (CH₂Cl₂): λ_{\max}/nm ($\epsilon/\text{M}^{-1}\text{cm}^{-1}$): 234 (20300), 378 (14900), 489 (sh), 684 (28800).

9.4.7. Synthesis of [Ru(Q)₃]

Metal precursor RuCl₃·3H₂O (100 mg, 0.48 mmol), the ligand 2-anilino-4,6-di-*tert*-butylphenol (571 mg, 1.92 mmol) and KOH (215 mg, 3.84 mmol) were taken in 30 mL methanol. The solution was stirred for 24h at room temperature. The initial dark brown colored solution change to deep blue. The solvent was then removed under reduced pressure. The solid dry mass was dissolved in minimum volume of (5–7 mL) dichloromethane and the solution was filtered. The filtrate was collected and the solvent was removed under reduced pressure. The product was dried completely in vacuum. It was then purified on an alumina (neutral) column. The deep blue solution corresponding to the desired product was eluted with CH₂Cl₂. Evaporation of the solvent under reduced pressure afforded the pure complex [Ru(Q)₃].

Yield: 285 mg (60%).

Elemental analysis: C₆₀H₇₅N₃O₃Ru (987.35 g/mol).

| | | |
|-----------------------|----------|----------|
| Calculated: C: 72.99% | H: 7.66% | N: 4.26% |
| Found: C: 73.03% | H: 7.63% | N: 3.96% |

¹H NMR (250 MHz, CDCl₃): δ = 5.95 (s, 2 H), 6.36 (s, 2 H), 6.55 (s, 2H), 6.87 (m, 5 H), 7.03 (m, 5 H), 7.15 (m, 5 H), 0.91 (s, 9 H), 0.98 (s, 9 H), 1.11 (s, 9 H), 1.21 – 1.15 (m, 27 H).

UV/Vis (CH₂Cl₂): λ_{max}/nm (ε/M⁻¹ cm⁻¹): 332 (14100), 553 (15600), 725 (9600), 1278 (5500).

9.4.8. Syntheses of complexes with *R,R*-QuinoxP ligand

[(*R,R*-QuinoxP)PtCl₂]

To an amount of 63.5 mg of the quinoxaline ligand (0.19 mmol) dissolved in 20 ml dichloromethane was added dropwise a dichloromethane solution of 80 mg (0.19 mmol) Pt(dmsO)₂Cl₂. The mixture was stirred at room temp for 12 h under an argon atmosphere. The solvent was removed under reduced pressure until about 5 ml was left; addition of diethyl ether precipitated the product which was left at 0 °C overnight to complete precipitation. The solution was then filtered and the solid washed several times with diethyl ether until the filtrate becomes colorless. The solid thus obtained was recrystallized from dichloromethane/hexane (1/1) to obtain analytically pure compound.

Yield: 47 mg (82%).

Elemental analysis: C₁₈H₂₈Cl₂N₂P₂Pt (600.37 g/mol).

| | | |
|-----------------------|----------|----------|
| Calculated: C: 36.01% | H: 4.70% | N: 4.67% |
| Found: C: 35.88% | H: 4.76% | N: 4.41% |

¹H-NMR (CDCl₃): δ 1.19 (d, 18H, 6 CH₃, ³J(P-H) = 16.4 Hz), 2.25 (d, 6H, 2 CH₃, ²J(P-H) = 12.0 Hz, ³J(Pt-H) = 36.0 Hz), 7.98 – 8.08 (m, 2H), 8.27 – 8.37 (m, 2H).

^{31}P -NMR (CDCl_3): δ 30.65 (s, $^1J(\text{Pt} - \text{P}) = 3446.5$ Hz).

UV-Vis (CH_2Cl_2): $\lambda_{\text{max}}/\text{nm}$ ($\epsilon/\text{M}^{-1} \text{cm}^{-1}$): 395(sh), 340 (10600), 329 (9300).

[(*R,R*-QuinoxP)Re(CO)₃Cl]

A mixture of $\text{Re}(\text{CO})_5\text{Cl}$ (80 mg, 0.22 mmol) and of the quinoxaline ligand (73.9 mg, 0.22 mmol) in 40 mL of 3:1 toluene-dichloromethane was heated to reflux for 4 h under an argon atmosphere. The solvent was removed under reduced pressure to 10 ml and a solid was precipitated on addition of diethyl ether at 0 °C. The yellow precipitate was collected and washed several times with diethyl ether. The solid thus obtained was recrystallized from dichloromethane/hexane (1/1) to obtain analytically pure compound.

Yield: 125mg (88%).

Elemental analysis: $\text{C}_{21}\text{H}_{28}\text{Cl}_1\text{N}_1\text{O}_3\text{P}_2\text{Re}$ (626.05 g/mol).

Calculated: C: 39.41% H: 4.41% N: 4.38%

Found: C: 40.73% H: 4.57% N: 4.17%

^1H NMR (250 MHz, CDCl_3) : δ = 1.37 (d, 9H, 3 CH_3 , $^3J(\text{P-H}) = 15.51\text{Hz}$) , 1.21 (d, 9H, CH_3 , $^3J(\text{P-H}) = 15.26$ Hz), 2.13 (d, CH_3 ,3H , $^2J(\text{P-H}) = 8.79$ Hz), 2.16 (d, CH_3 ,3H , $^2J(\text{P-H}) = 7.93$ Hz), 7.85 – 7.97 (m, 2H), 8.15– 8.27 (m, 2H).

^{31}P NMR (250 MHz, CDCl_3): δ = 13.01 (d, $^3J(\text{P} - \text{P}) = 25.54$ Hz), 28.10 (d, $^3J(\text{P} - \text{P}) = 25.54$ Hz).

IR (CH_2Cl_2): $\nu_{\text{CO}}/\text{cm}^{-1} = 2032$ vs, 1953 s and 1895 s.

UV-Vis (CH_2Cl_2): $\lambda_{\text{max}}/\text{nm}$ ($\epsilon/\text{M}^{-1} \text{cm}^{-1}$) = 325 (8660), 338 (8960), 390 (sh).

9.5. Crystallography

Crystallographic data collection was carried out by Dr. F. Lissner, Dr. I. Hartenbach, Dr. S. Strobel and Priv.-Doz. Dr. M. Niemeyer from the University of Stuttgart. Structure solving was done by Dr. F. Lissner, Dr. I. Hartenbach, Dr. S. Strobel and Priv. Doz. Dr. M. Niemeyer. Data collection was performed on four circle diffractometer NONIUS Kappa-CCD or Siemens P4 with a Mo-K α radiation of 0.71073 Å (graphite-monochromatized) at 293 K or 173 K. The crystals were sealed in capillaries for the measurements.

The structure were solved via direct methods using the programme SHELXS-97.¹²⁸ Refinement was carried out by the full matrix least squares method employing the programme SHELXL-97.¹²⁹ All non-hydrogen atoms are refined anisotropically, hydrogen atoms were introduced in proper positions with coupled isotropic factors using the riding model. Absorption corrections were performed numerically using the programme HABITUS.¹³⁰ The programme DIAMOND 2.1e¹³¹ was used for structure drawing.

Crystallographic parameters:

$$\text{GOF} = \{ \sum w (|F_o|^2 - |F_c|^2)^2 / (n - m) \}^{1/2} \quad \text{where } n = \text{number of data and } m = \text{number of variables}$$

$$R = (\sum | |F_o| - |F_c| |) / \sum |F_o|$$

$$\text{WR} = \{ \sum [w (|F_o|^2 - |F_c|^2)^2] / \sum [w(F_o^4)] \}^{1/2}$$

9.5.1. (PPh₄)₄[(CN)₄(NO)Re(μ -O)Re(NO)(CN)₄]

Purple plates for X-ray diffraction were obtained by slow diffusion of a solution of (PPh₄)₄[(CN)₄(NO)Re(μ -O)Re(NO)(CN)₄] in acetonitrile layered with diethylether.

Table 9.5.1.1. Crystallographic data and refinement parameters for (PPh₄)₄[(CN)₄(NO)Re(μ -O)Re(NO)(CN)₄]•4(CH₂Cl₂).

| | |
|-------------------|--|
| empirical formula | C ₁₀₈ H ₈₈ C ₁₈ N ₁₀ O ₃ P ₄ Re ₂ |
| fw | 2353.76 |
| T (K) | 293(2) |
| λ (Å) | 0.71073 |
| crystal system | monoclinic |

| | |
|---|----------------|
| space group | $P2_1/n$ |
| Z | 2 |
| a (Å) | 14.015(3) |
| b (Å) | 26.429(4) |
| c (Å) | 14.472(3) |
| α (deg) | 90 |
| β (deg) | 106.31(1) |
| γ (deg) | 90 |
| V (Å ³) | 5144.8(17) |
| ρ_{calcd} (g cm ⁻³) | 1.519 |
| μ (mm ⁻¹) | 2.68 |
| θ range (deg) | 1.95–26.00 |
| collected data | 10518 |
| unique data/ R_{int} | 10097/0.065 |
| no. of data $> 4\sigma$ | 5803 |
| no. of parameters | 610 |
| GOF ^a | 0.785 |
| $R1, wR2$ ($I > 4\sigma$) ^b | 0.0506, 0.1094 |
| resd dens (e/Å ³) | 1.955/–1.114 |

9.5.2. [(terpy)Ru(Q)Cl](ClO₄)

Purple needles for X-ray diffraction were obtained by slow diffusion of a solution of [(terpy)Ru(Q)Cl](ClO₄) in acetonitrile layered with diethylether.

Table 9.5.2.1. Crystallographic data and refinement parameters for [(terpy)Ru(Q)Cl](ClO₄).

| | |
|-------------------|--|
| empirical formula | C ₃₅ H ₃₆ Cl ₂ N ₄ O ₅ Ru |
| fw | 764.65 |
| T (K) | 100(2) |

| | |
|---|----------------|
| λ (Å) | 0.71073 |
| crystal system | Triclinic |
| space group | $P\bar{1}$ |
| Z | 2 |
| a (Å) | 12.142(1) |
| b (Å) | 12.512(1) |
| c (Å) | 12.967(1) |
| α (deg) | 78.516(3) |
| β (deg) | 86.779(3) |
| γ (deg) | 86.840(3) |
| V (Å ³) | 1925.8(2) |
| ρ_{calcd} (g cm ⁻³) | 1.319 |
| μ (mm ⁻¹) | 0.59 |
| θ range (deg) | 3.36–27.47 |
| collected data | 30755 |
| unique data/ R_{int} | 8691/0.1274 |
| no. of data $> 4\sigma$ | 6535 |
| no. of parameters | 431 |
| GOF ^a | 1.069 |
| $R1, wR2$ ($I > 4\sigma$) ^b | 0.0632, 0.1300 |
| resd dens (e/Å ³) | 0.752/–0.860 |

9.5.3. [(terpy)Ru(Q)(NO₂)](ClO₄)

Blue plates for X-ray diffraction were obtained by slow diffusion of a solution of in [(terpy)Ru(Q)(NO₂)](ClO₄) dichloromethane layered with *n*-hexane.

Table 9.5.3.1. Crystallographic data and refinement parameters for [(terpy)Ru(Q)(NO₂)](ClO₄).

| | |
|---|--------------------------|
| empirical formula | $C_{35}H_{36}ClN_5O_7Ru$ |
| fw | 775.21 |
| T (K) | 293(2) |
| λ (Å) | 0.71073 |
| crystal system | triclinic |
| space group | $P\bar{1}$ |
| Z | 1 |
| a (Å) | 12.5944(2) |
| b (Å) | 13.3586(3) |
| c (Å) | 13.6133(1) |
| α (deg) | 62.008(1) |
| β (deg) | 85.959(1) |
| γ (deg) | 80.139(1) |
| V (Å ³) | 1992.4(7) |
| ρ_{calcd} (g cm ⁻³) | 1.292 |
| μ (mm ⁻¹) | 0.51 |
| θ range (deg) | 3.36–27.47 |
| collected data | 43569 |
| unique data/ R_{int} | 9755/0.1249 |
| no. of data $> 4\sigma$ | 8894 |
| no. of parameters | 434 |
| GOF ^a | 1.037 |
| $R1, wR2$ ($I > 4\sigma$) ^b | 0.0661, 0.1870 |
| resd dens (e/Å ³) | 2.328/–2.566 |

9.5.4. [(terpy)Ru(Q)(NO)](PF₆)₂

Brown plates for X-ray diffraction were obtained by slow diffusion of a solution of [(terpy)Ru(Q)(NO)](PF₆)₂ in acetonitrile layered with diethylether.

Table 9.5.4.1. Crystallographic data and refinement parameters for [(terpy)Ru(Q)(NO)](PF₆)₂.

| | |
|--|---|
| empirical formula | C ₃₅ H ₃₆ F ₁₂ N ₅ O ₂ P ₂ Ru |
| fw | 949.70 |
| <i>T</i> (K) | 100(2) |
| λ (Å) | 0.71073 |
| crystal system | monoclinic |
| space group | <i>P</i> 2 ₁ / <i>c</i> |
| <i>Z</i> | 4 |
| <i>a</i> (Å) | 11.8984(2) |
| <i>b</i> (Å) | 24.8296(3) |
| <i>c</i> (Å) | 14.3286(2) |
| α (deg) | 90 |
| β (deg) | 113.528(1) |
| γ (deg) | 90 |
| <i>V</i> (Å ³) | 3881.2(1) |
| ρ_{calcd} (g cm ⁻³) | 1.625 |
| μ (mm ⁻¹) | 0.584 |
| θ range (deg) | 1.64–28.33 |
| collected data | 66183 |
| unique data/ <i>R</i> _{int} | 3631/0.1363 |
| no. of data > 4 σ | 7112 |
| no. of parameters | 707 |
| GOF ^a | 1.053 |
| <i>R</i> 1, <i>wR</i> 2 (<i>I</i> > 4 σ) ^b | 0.0587, 0.1169 |
| resd dens (e/Å ³) | 0.995/–0.931 |

9.5.5. [(tppz)Ru(Q)Cl](PF₆)

Blue plates for X-ray diffraction were obtained by slow diffusion of a solution of [(tppz)Ru(Q)Cl](PF₆) dichloromethane layered with *n*-hexane.

Table 9.5.5.1. Crystallographic data and refinement parameters for [(tppz)Ru(Q)Cl](PF₆)•(CH₂Cl₂).

| | |
|---|--|
| empirical formula | C ₄₄ H ₄₁ F ₆ ClN ₇ OPRu |
| fw | 965.35 |
| <i>T</i> (K) | 100(2) |
| λ (Å) | 0.71073 |
| crystal system | triclinic |
| space group | <i>P</i> $\bar{1}$ |
| <i>Z</i> | 2 |
| <i>a</i> (Å) | 13.0115(6) |
| <i>b</i> (Å) | 13.1498(6) |
| <i>c</i> (Å) | 13.8235(7) |
| α (deg) | 100.423(3) |
| β (deg) | 99.437(3) |
| γ (deg) | 102.167(3) |
| <i>V</i> (Å ³) | 2223.1(2) |
| ρ_{calcd} (g cm ⁻³) | 1.569 |
| μ (mm ⁻¹) | 0.64 |
| θ range (deg) | 5.78–27.48 |
| collected data | 36674 |
| unique data/ <i>R</i> _{int} | 9994/0.1260 |
| no. of data > 4 σ | 7119 |
| no. of parameters | 595 |
| GOF ^a | 1.044 |

| | |
|--|----------------|
| R1, wR2 ($I > 4\sigma$) ^b | 0.0695, 0.1314 |
| resd dens ($e/\text{\AA}^3$) | 0.774/−0.900 |

9.5.6. [(tppz)Ru(Q)(NO₂)](PF₆)

Blue plates for X-ray diffraction were obtained by slow evaporation of a solution of [(tppz)Ru(Q)(NO₂)](PF₆) in dichloromethane layered with *n*-hexane.

Table 9.5.6.1. Crystallographic data and refinement parameters for [(tppz)Ru(Q)(NO₂)](PF₆)•(CH₂Cl₂).

| | |
|---|--|
| empirical formula | C ₄₄ H ₄₁ F ₆ N ₈ O ₃ PRu |
| fw | 975.91 |
| <i>T</i> (K) | 100(2) |
| λ (Å) | 0.71073 |
| crystal system | Triclinic |
| space group | $P\bar{1}$ |
| <i>Z</i> | 2 |
| <i>a</i> (Å) | 13.0837(4) |
| <i>b</i> (Å) | 13.1182(4) |
| <i>c</i> (Å) | 13.9519(4) |
| α (deg) | 100.058(2) |
| β (deg) | 99.283(2) |
| γ (deg) | 101.247(2) |
| <i>V</i> (Å ³) | 2264.7(1) |
| ρ_{calcd} (g cm ^{−3}) | 1.556 |
| μ (mm ^{−1}) | 0.58 |
| θ range (deg) | 3.03–28.17 |
| collected data | 17990 |
| unique data/ <i>R</i> _{int} | 10884/0.0753 |
| no. of data > 4 σ | 7664 |

| | |
|--|----------------|
| no. of parameters | 606 |
| GOF ^a | 1.028 |
| R1, wR2 (I > 4 σ) ^b | 0.0529, 0.0973 |
| resd dens (e/Å ³) | 1.140/−0.716 |

9.5.7. [(Q)ClRu(μ -tppz)RuCl(Q)](PF₆)₂

Green plates for X-ray diffraction were obtained from acetonitrile solution of [(Q)ClRu(μ -tppz)RuCl(Q)](PF₆)₂ layered with toluene via diffusion method.

Table 9.5.7.1. Crystallographic data and refinement parameters for [(Q)ClRu(μ -tppz)RuCl(Q)](PF₆)₂•(C₇H₈).

| | |
|---|--|
| empirical formula | C ₇₈ H ₈₂ Cl ₂ F ₁₂ N ₈ O ₂ P ₂ Ru ₂ |
| fw | 1726.50 |
| <i>T</i> (K) | 100(1) |
| λ (Å) | 0.71073 |
| crystal system | triclinic |
| space group | <i>P</i> $\bar{1}$ |
| <i>Z</i> | 1 |
| <i>a</i> (Å) | 12.660(1) |
| <i>b</i> (Å) | 13.224(1) |
| <i>c</i> (Å) | 12.9492(9) |
| α (deg) | 81.382(5) |
| β (deg) | 62.819(6) |
| γ (deg) | 76.633(5) |
| <i>V</i> (Å ³) | 1873.8(3) |
| ρ_{calcd} (g cm ^{−3}) | 1.530 |
| μ (mm ^{−1}) | 0.600 |
| θ range (deg) | 3.06–21.96 |
| collected data | 8434 |

| | |
|--|----------------|
| unique data/ R_{int} | 4509/0.141 |
| no. of data $> 4\sigma$ | 2700 |
| no. of parameters | 444 |
| GOF ^a | 1.012 |
| R1, wR2 ($I > 4\sigma$) ^b | 0.0656, 0.1161 |
| resd dens ($e/\text{\AA}^3$) | 0.508/−0.732 |

9.5.8. [(*R,R*-QuinoxP)PtCl₂]

Yellow plates for X-ray diffraction were obtained by slow evaporation of a solution of [(*R,R*-QuinoxP)PtCl₂] in dichloromethane layered with *n*-hexane.

Table 9.5.8.1. Crystallographic data and refinement parameters for [(*R,R*-QuinoxP)PtCl₂].

| | |
|---|--|
| empirical formula | C ₁₉ H ₃₀ C ₁₄ N ₂ P ₂ Pt |
| fw | 685.28 |
| T (K) | 100(1) |
| λ (Å) | 0.71073 |
| crystal system | monoclinic |
| space group | $P2_1$ |
| Z | 1 |
| a (Å) | 7.9288(2) |
| b (Å) | 15.1703(4) |
| c (Å) | 10.5200(2) |
| α (deg) | 90 |
| β (deg) | 99.605(2) |
| γ (deg) | 90 |
| V (Å ³) | 1247.63(5) |
| ρ_{calcd} (g cm ^{−3}) | 1.824 |
| μ (mm ^{−1}) | 0.600 |

| | |
|--|----------------|
| θ range (deg) | 3.74–14.00 |
| collected data | 19599 |
| unique data/ R_{int} | 6001/0.136 |
| no. of data $> 4\sigma$ | 5563 |
| no. of parameters | 444 |
| GOF ^a | 1.051 |
| R1, wR2 ($I > 4\sigma$) ^b | 0.0429, 0.1019 |
| resd dens ($e/\text{\AA}^3$) | 2.303/–1.758 |

9.5.9. [(*R,R*-QuinoxP)Re(CO)₃Cl]

Yellow plates for X-ray diffraction were obtained by slow evaporation of a solution of [(*R,R*-QuinoxP)Re(CO)₃Cl] in dichloromethane layered with *n*-hexane at –30 °C.

Table 9.5.9.1. Crystallographic data and refinement parameters for [(*R,R*-QuinoxP)Re(CO)₃Cl].

| | |
|-------------------|---|
| empirical formula | C ₂₁ H ₂₈ Cl ₁ N ₁ O ₃ P ₂ Re |
| fw | 626.05 |
| T (K) | 100(1) |
| λ (Å) | 0.71073 |
| crystal system | monoclinic |
| space group | <i>C</i> 2 |
| Z | 4 |
| a (Å) | 22.692(4) |
| b (Å) | 11.993(2) |
| c (Å) | 10.439(2) |
| α (deg) | 90.00 |
| β (deg) | 104.36(1) |
| γ (deg) | 90.00 |

| | |
|--|----------------|
| V (\AA^3) | 2751.9(8) |
| ρ_{calcd} (g cm^{-3}) | 1.545 |
| μ (mm^{-1}) | 4.65 |
| θ range (deg) | 2.37–27.50 |
| collected data | 3314 |
| unique data/ R_{int} | 3314/0.0354 |
| no. of data $> 4\sigma$ | 3056 |
| no. of parameters | 281 |
| GOF ^a | 0.998 |
| $R1, wR2$ ($I > 4\sigma$) ^b | 0.0278, 0.0668 |
| resd dens ($\text{e}/\text{\AA}^3$) | 1.055/–1.312 |

CHAPTER 10

Summary

In this doctoral thesis structural and electronic properties of transition metal complexes of redox-active non-innocent² ligands such as nitrosyl, 4,6-di-*tert*-butyl-*N*-phenyl-*o*-iminobenzoquinone³³ and 3,5-di-*tert*-butyl-*o*-quinone¹⁰¹ (Figure 10.1) are described. Additionally, the thesis covers the synthesis, mode of binding and electron transfer behaviors of metal complexes of an air-stable chiral diphosphine derived chelating ligand, *R,R*-QuinoxP³⁷ (Figure 10.9).

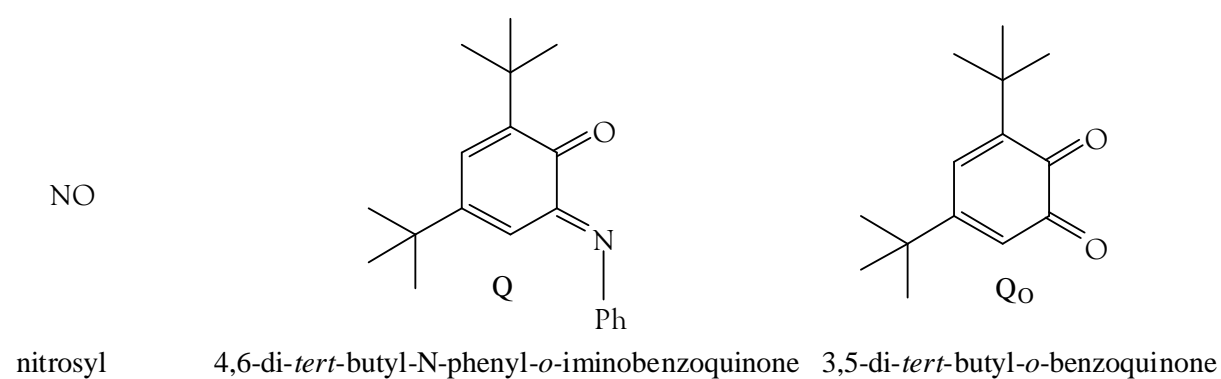


Figure 10.1. Molecular formulae of the non-innocent ligands used in the thesis work.

In the first part of my thesis the synthetic aspects, the structural, spectroscopic and electronic properties of new transition metal (Ru and Re) nitrosyl complexes are described. The actual form of coordinated NO^m ($m = +/0/-$) is established based on the experimental results supported by calculations.

In Chapter 2, different oxidation states of $[\text{Ru}(\text{OEP})(\text{NO})(\text{X})]^{n+}$ (Figure 10.2) ($n = +2, +1, 0, -1$, OEP = octaethylporphyrin dianion) with varying axial sixth ligands X (H_2O , pyridine, 4-cyanopyridine, 4-dimethylaminopyridine) are studied spectroscopically and the electronic structures of the complexes have been rationalized through DFT calculations. Spectroelectrochemical investigations reveal that the first oxidation ($\text{X} = \text{H}_2\text{O}$) occurs on the porphyrin ring, as evident from the appearance of a diagnostic porphyrin radical anion vibrational band² (1530 cm^{-1}), from a small positive shift of 20 cm^{-1} for NO-stretching frequency, and from the EPR signal at $g_{\text{iso}} \approx 2.00$. Predominantly NO-centered reduction process has been established, evident from the large decrease ($\approx 300 \text{ cm}^{-1}$) in $\nu(\text{NO})$

stretching frequency in IR-spectroelectrochemistry and from the well resolved nitrogen hyperfine coupling due to one ^{14}N nucleus in EPR spectroscopy (Figure 10.2). DFT calculations also support the interpretation of the experimental results, HOMO (X = H_2O or pyridines) is dominated by the porphyrin π system, while the LUMO has about 50% π^* (NO) character (Figure 10.2).

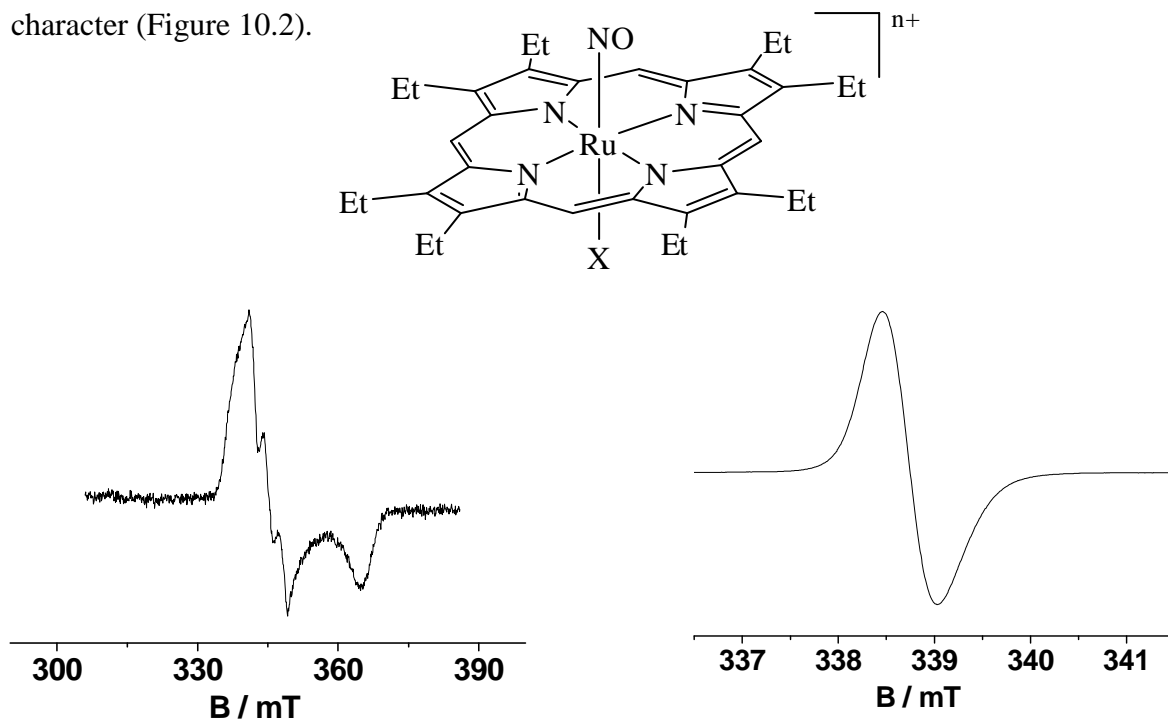


Figure 10.2. Molecular formula of $[(\text{OEP})\text{Ru}(\text{NO})(\text{X})]^{n+}$ where X = H_2O ($n = 1, 2, 3$) or pyridine, 4-cyanopyridine or 4-N,N-dimethylaminopyridine ($n = 1, 0$) (top), EPR spectra of electrochemical generated $[(\text{OEP})\text{Ru}(\text{NO})(\text{py})]^0$ at 110 K in $\text{CH}_2\text{Cl}_2/0.1 \text{ M } n\text{-Bu}_4\text{ClO}_4$ (left) and electrochemically generated $[(\text{OEP})\text{Ru}(\text{NO})(\text{H}_2\text{O})]^{2+}$ at 295 K in $\text{CH}_2\text{Cl}_2/0.1 \text{ M } n\text{-Bu}_4\text{ClO}_4$ (right).

Chapter 3 describes the complex $(\text{PPh}_4)_4[(\text{CN})_4(\text{NO})\text{Re}(\mu\text{-O})\text{Re}(\text{NO})(\text{CN})_4]$ (Figure 10.3), an oxo-bridged rhenium dinitrosyl complex with cyanide as a co-ligand. The complex has been structurally and spectroscopically characterized. Crystal structure analysis confirms the linear coordination of the nitrosyl groups and of the linear mode of $\text{Re}\text{-O}\text{-Re}$ unit. The complex exhibits two sharp $\nu(\text{NO})$ bands at 1710 and 1670 cm^{-1} and two sharp $\nu(\text{CN})$ bands at 2118 and 2129 cm^{-1} in CH_3CN . An oxidation state assignment of $[(\text{CN})_4(\text{NO}^+)\text{Re}^{\text{II}}(\mu\text{-O})\text{Re}^{\text{II}}(\text{NO}^+)(\text{CN})_4]^{4-}$ can be made based on the obtained structural data which are comparable with values previously reported.³ Cyclic voltammetry exhibits one irreversible reduction and one reversible oxidation followed by an irreversible oxidation process.

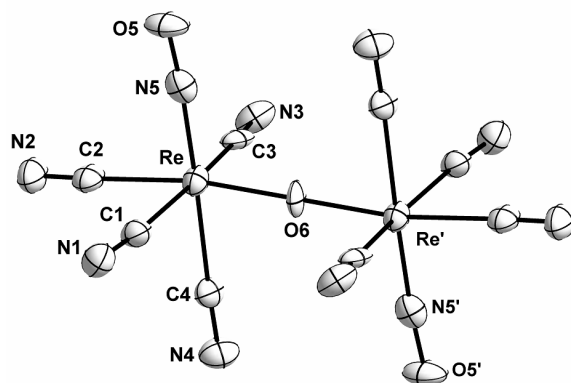


Figure 10.3. Crystal structure of the anionic part of $(\text{PPh}_4)_4[(\text{CN})_4(\text{NO})\text{Re}(\mu\text{-O})\text{Re}(\text{NO})(\text{CN})_4] \cdot 4(\text{CH}_2\text{Cl}_2)$.

In the second part of this thesis several complexes with 1,2-dioxolene⁷ type non-innocent ligands (Q or Q₀) or sometimes combining two non-innocent ligands Q and NO in one system are described.

Chapter 4 describes four ruthenium *o*-iminoquinone complexes with the objective of establishing the metal-ligand valence state distribution. The complexes are isolated in the monocationic form and have also been characterized crystallographically.

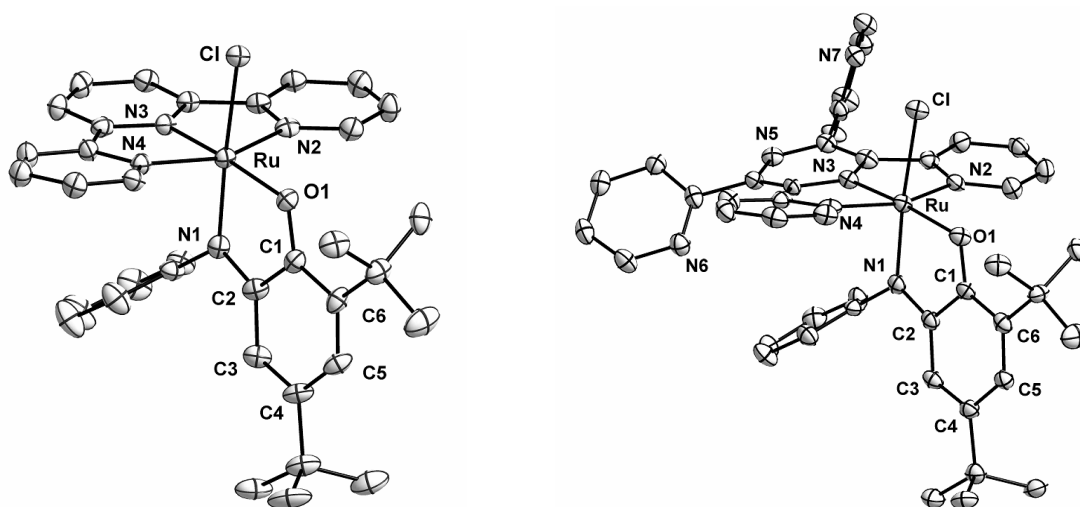


Figure 10.4. Crystal structures of the cationic part of $[(\text{terpy})\text{Ru}(\text{Q})\text{Cl}](\text{ClO}_4)$ (left) and $[(\text{tppz})\text{Ru}(\text{Q})(\text{NO}_2)](\text{PF}_6) \cdot (\text{CH}_2\text{Cl}_2)$ (right) (terpy = 2,2':6'2''-terpyridine and tppz = 2,3,5,6-tetrakis(2-pyridyl)pyrazine).

The C1–O1, C2–N1 bond lengths and the C–C intra-ring distances suggest that Q binds to the metal center in the iminosemiquinonato (Q^{•-}) oxidation state, resulting in an $[\text{Ru}^{\text{III}}(\text{Q}^{\bullet-})]$ electronic formulation in all four cases. The terpy complexes $[(\text{terpy})\text{Ru}(\text{Q})\text{Cl}](\text{ClO}_4)$ and

[(terpy)Ru(Q)(NO₂)](ClO₄) show two reductions and one oxidation; terpy-centered reduction process cannot be observed within the solvent potential limit. However, the tppz complexes [(tppz)Ru(Q)Cl](PF₆) and [(tppz)Ru(Q)(NO₂)](PF₆) show four and three reductions respectively and one oxidation in both cases. The X-band EPR experiment at room temperature of one-electron reduced species give spectra with $g_{\text{iso}} \approx 2.00$, typical values for semiquinone radical complexes; indicating preferential metal-centered reductions leaving the unpaired spin mainly on Q_N^{•-} in [Ru^{II}(Q_N^{•-})]. However, the g anisotropy values as determined from X band EPR at 110 K and high-field EPR data as well as the metal hyperfine data suggest a non-negligible participation of the metal at the singly occupied MO (SOMO). Oxidation of [(tppz)Ru(Q_N)Cl]⁺ results in the appearance of a rhombic EPR signal as is typical for distorted ruthenium(III).

Chapter 5 deals with two paramagnetic complexes [Ru(NO)(Q)(terpy)](PF₆)₂ (Figure 10.5) and [Ru(NO)(Q)(tppz)](PF₆)₂ combining three redox sensitive components such as Ru^{II}/Ru^{III}, NO^m and (Q)ⁿ. The co-ligands terpy and tppz are redox invariant in the present cases. The most stable positional isomer of [Ru(NO)(Q)(terpy)](PF₆)₂ with NO *trans* to the O donor atom of Q was isolated and characterized by single crystal X-ray analysis (Figure 10.6). In conjunction with the experimental Ru–N–O angle and the metrical parameters in the quinonoid ligand especially the C1–O1 distance and with $\nu(\text{NO})$, the EPR studies at 9.5 and 285 GHz reveal a narrow radical-type signal, suggesting [Ru^{II}(NO⁺)(Q^{•-})(terpy)]²⁺ as the most valid oxidation state formulation. DFT calculations confirm the same assignment (Figure 10.5) but suggest about 15% NO character of the SOMO, in agreement with the EPR hyperfine features.

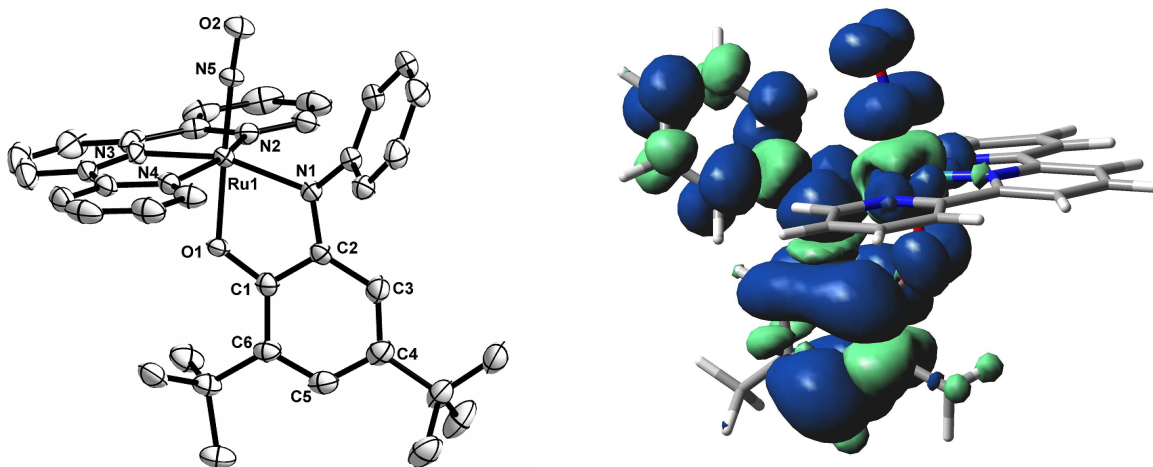


Figure 10.5. Molecular structure of the dication of [Ru(NO)(Q)(terpy)](PF₆)₂ in the crystal (left) and representation of the spin density plot of [Ru(NO)(Q)(terpy)]²⁺ (right).

Similar oxidation state formulation $[\text{Ru}^{\text{II}}(\text{NO}^+)(\text{Q}^{\bullet-})(\text{tppz})]^{2+}$ can be assigned based on the experimental value of $\nu(\text{NO})$ and a radical type EPR signal at 9.5 GHz. Reduction of both complexes and oxidation of the terpy complex cause moderate $\nu(\text{NO})$ shifts to lower and higher frequencies, respectively. This result suggests that neither the NO ligand nor the metal are involved to a major extent in the oxidative or reductive electron transfer process but that the iminoquinone ligand is the main redox component in these systems.

Chapter 6 describes the structural, electrochemical and spectroscopic properties of $[\text{Cl}(\text{Q})\text{Ru}(\mu\text{-tppz})\text{Ru}(\text{Q})\text{Cl}]^n$. The complex $[\text{Cl}(\text{Q})\text{Ru}(\mu\text{-tppz})\text{Ru}(\text{Q})\text{Cl}](\text{PF}_6)_2$, containing five component redox system $[(\text{Q}_\text{N})^n\text{-Ru}^m\text{-}(\mu\text{-tppz}^x)\text{-Ru}^{m'}\text{-}(\text{Q}_\text{N})n']$, has been structurally characterized as *anti* isomer (Figure 10.6), the only configuration obtained.

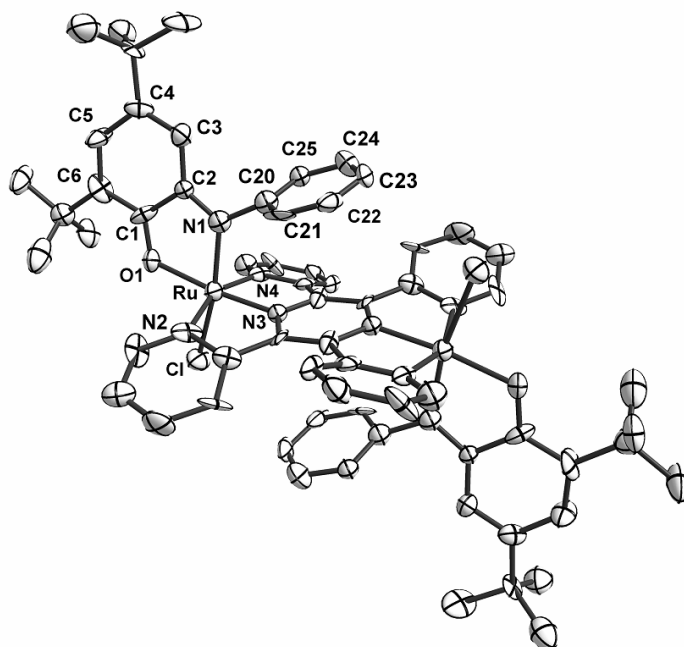


Figure 10.6. Molecular structure of $[(\text{Q})\text{ClRu}(\mu\text{-tppz})\text{RuCl}(\text{Q})]^{2+}$ in the crystal of $[(\text{Q})\text{ClRu}(\mu\text{-tppz})\text{RuCl}(\text{Q})](\text{PF}_6)_2 \cdot (\text{C}_7\text{H}_8)$.

The combined structural and spectroscopic results allow the oxidation state assignment as $[(\text{Q}^{\bullet-})\text{-Ru}^{\text{III}}\text{-}(\mu\text{-tppz}^0)\text{-Ru}^{\text{III}}\text{-}(\text{Q}^{\bullet-})]$. One-electron oxidation of $[\text{Cl}(\text{Q}^{\bullet-})\text{Ru}^{\text{III}}(\mu\text{-tppz}^0)\text{Ru}^{\text{III}}(\text{Q}^{\bullet-})\text{Cl}]^{2+}$ results in the appearance of a rhombic EPR signal (Figure 10.7) as is typical for distorted ruthenium (III). The emergence (on first oxidation) and subsequent disappearance (on second oxidation) of an intense near-infrared band at 1853 nm strongly suggests a mixed-valent configuration with a low-energy IVCT transition and a sizeable comproportionation constant $10^{6.1}$. The narrow IVCT band at 1853 nm and much smaller experimentally derived $\Delta\nu_{1/2}$ value (1357 cm^{-1}) than the value derived from the Hush equation

(3530 cm^{-1}), suggest a delocalized Class III ($\text{Ru}^{2.5}\text{Ru}^{2.5}$) system. DFT calculated spin density in $[\text{Cl}(\text{Q})\text{Ru}(\mu\text{-tppz})\text{Ru}(\text{Q})\text{Cl}]^{3+}$ is mainly localized on the metal centers, with some contribution from Cl and slightly negative spin density on the tppz bridged ligand. The EPR and UV-Vis-NIR results imply that the first two successive reduction steps of $[\text{Cl}(\text{Q}^{\bullet-})\text{Ru}^{\text{III}}(\mu\text{-tppz})\text{Ru}^{\text{III}}(\text{Q}^{\bullet-})\text{Cl}]^{2+}$ occur successively on two Ru(III) center. DFT calculations confirm involvement of orbitals having large contribution from the Q ligands. On the third reduction a characteristic typical absorption feature at 960 nm tppz $^{\bullet-}$ and EPR signal at $g_{\text{iso}} = 1.9987$ without detectable metal hyperfine confirm tppz centered reduction, resulting a three-spin situation $\text{Q}^{\bullet-} // \text{tppz}^{\bullet-} // \text{Q}^{\bullet-}$ with antiparallel spin-spin interaction of the semiquinone ligands ($\uparrow\uparrow\downarrow$). The fourth reduction is also believed to occur at the tppz bridge because the absorption intensity emerging at about 1200 nm has similarly been observed for other diruthenium complexes of tppz $^{\bullet-}$.

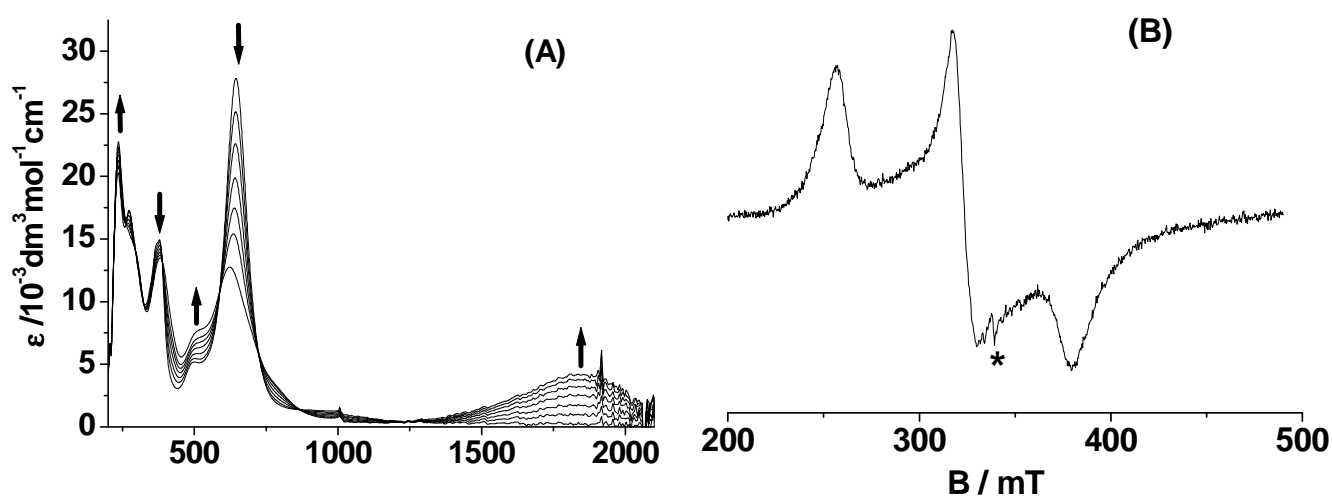
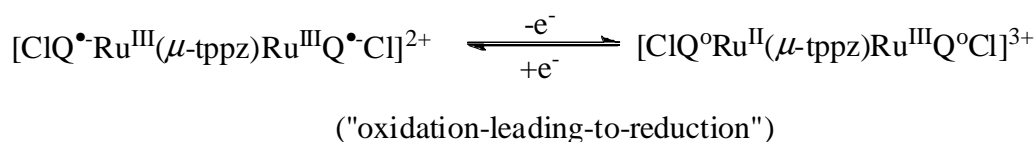


Figure 10.7. UV/Vis/NIR-spectroelectrochemical response of system $[\text{Cl}(\text{Q})\text{Ru}(\mu\text{-tppz})\text{Ru}(\text{Q})\text{Cl}]^{2+}$ on oxidation in $\text{CH}_3\text{CN}/0.1 \text{ M Bu}_4\text{NPF}_6$ (A) and EPR spectrum of electrogenerated $[\text{Cl}(\text{Q})\text{Ru}(\mu\text{-tppz})\text{Ru}(\text{Q})\text{Cl}]^{3+}$ (B, 110 K) (*: cavity signal).

Chapter 7 describes a detail spectroelectrochemical (UV-Vis-NIR and EPR) and theoretical studies of the redox series $[\text{Ru}(\text{Q})_3]^n$, $[\text{Os}(\text{Q})_3]^n$ and $[\text{Ru}(\text{Q}_N)_3]^n$ (Figure 10.8) ($n = +2$ to -2).

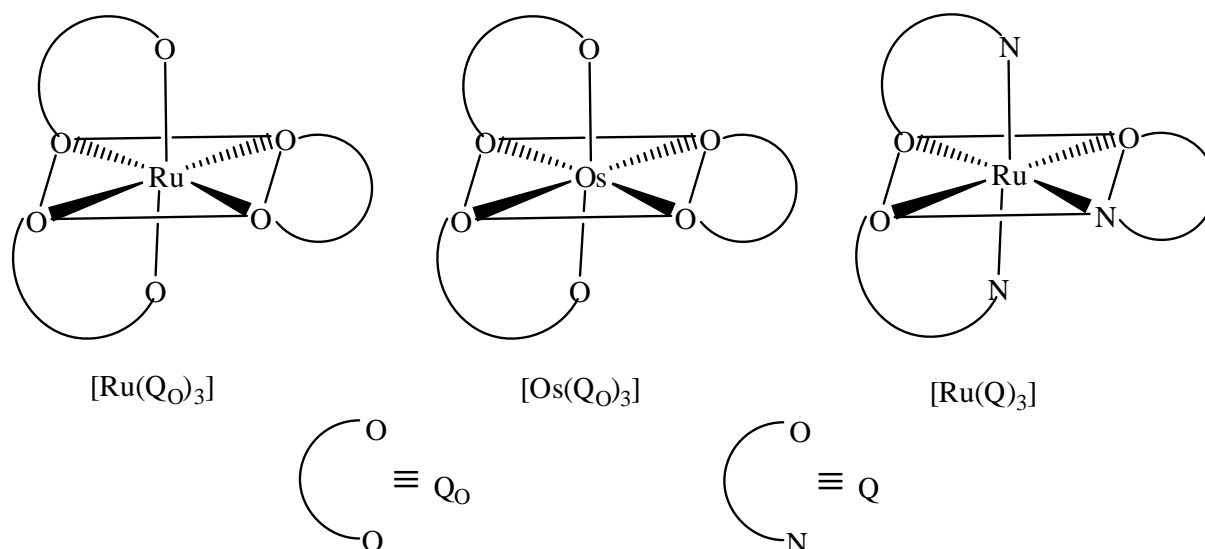


Figure 10.8. Molecular formula of the complexes $[\text{Ru}(\text{QO})_3]$, $[\text{Os}(\text{QO})_3]$ and $[\text{Ru}(\text{Q})_3]$.

The $[\text{Ru}(\text{QO})_3]^0$ and $[\text{Os}(\text{QO})_3]^0$ complexes were reported¹⁰¹ earlier by Pierpont et. al. and the redox states of (QO) in the complexes have been formulated as semiquinonato ($\text{QO}^{\bullet-}$) and catecolate (QO^{2-}), respectively. Based on this assignment the newly synthesized complex $[\text{Ru}(\text{Q})_3]^0$ can also be attributed to antiferromagnetically coupled tris-iminosemiquinonato $[\text{Ru}^{\text{III}}(\text{Q}_\text{N}^{\bullet-})_3]$ system. Consequently the compound $[\text{Ru}^{\text{III}}(\text{Q}^{\bullet-})_3]^0$ is EPR-silent and shows unshifted $^1\text{H-NMR}$ lines. For all three complexes the successive oxidation processes primarily take place from the ligand based orbitals with marginal contribution from the metal ion as evident from the EPR studies and that has been further supported by DFT results. On the other hand EPR results suggest that the reduction process in all three cases $[\text{Ru}(\text{QO})_3]^-$, $[\text{Os}(\text{QO})_3]^-$ and $[\text{Ru}(\text{Q})_3]^-$ is a mixed situation, which has been further supported by the DFT calculations with 27%, 37% and 25% metal contributions in the respective LUMOs.

The last chapter (Chapter 8) deals with the synthesis of two metal complexes $[(\text{QuinoxP})\text{Pt}(\text{Cl})_2]$ and $[(\text{QuinoxP})\text{Re}(\text{CO})_3\text{Cl}]$ (Figure 10.9) which are synthesized by reacting two standard metal precursors $\text{Pt}(\text{dmsO})_2\text{Cl}_2$ and $\text{Re}(\text{CO})_5\text{Cl}$ respectively with the *R,R*-QuinoxP⁹. The crystal structures of the complexes have established that the ligand *R,R*-QuinoxP coordinates to the metal ions through the P donor atoms instead of the quinoxaline heterocycle. Electron acceptance by the quinoxaline heterocycle is responsible not only for the improved stability of the ligand towards air but also facilitates rather facile reduction of the complexes to the persistent radical anions $[(\text{QuinoxP})\text{PtCl}_2]^{\bullet-}$ and $[(\text{QuinoxP})\text{Re}(\text{CO})_3\text{Cl}]^{\bullet-}$.

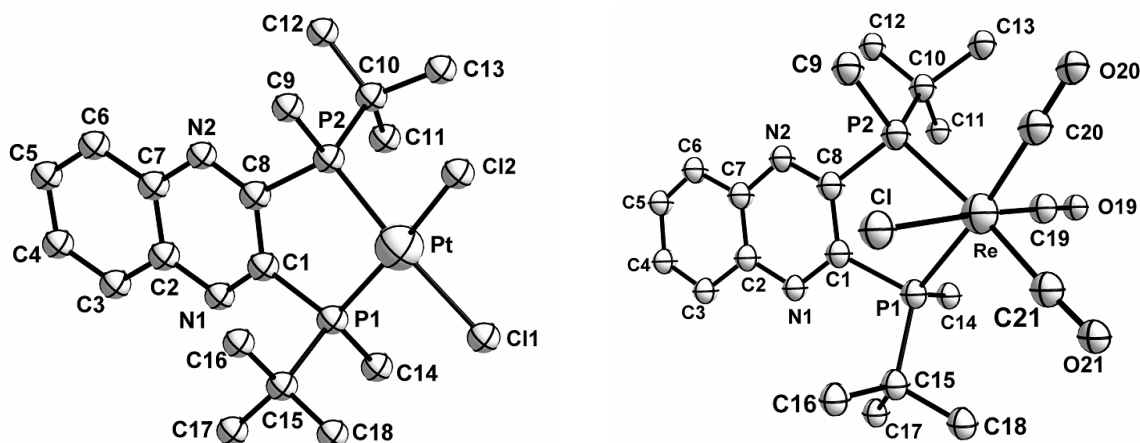


Figure 10.9. Molecular structure of $[(\text{QuinoxP})\text{Pt}(\text{Cl})_2]$ (left) and $[(\text{QuinoxP})\text{Re}(\text{CO})_3\text{Cl}]$ (right) in the crystal.

The EPR spectra of $[(\text{QuinoxP})\text{Pt}(\text{Cl})_2]^{-}$ and $[(\text{QuinoxP})\text{Re}(\text{CO})_3\text{Cl}]^{-}$ show g values close to that of the ligand radical anion ($g = 2.0030$), confirming the marginal contribution of the metals to the singly occupied molecular orbital (SOMO). This result is supported by the lack of detectable g anisotropy at X-band frequency (9.5 GHz). While $[(\text{QuinoxP})\text{Re}(\text{CO})_3\text{Cl}]^{-}$ did not show sufficient EPR resolution for hyperfine structure analysis, except for significantly higher spectral width due to $^{185,187}\text{Re}$ splitting at the order of 5 G, the radical $[(\text{QuinoxP})\text{Pt}(\text{Cl})_2]^{-}$ exhibits (Figure 10.10) a sizable ^{195}Pt hyperfine coupling of 24 G, the typically large ^{14}N ($I = 1$) coupling parameter of quinoxalines (5.7 G) as well as smaller ^1H and ^{31}P splittings. The value of 24 G for ^{195}Pt is certainly much smaller than what would be expected for mononuclear platinum (I) complexes.⁵

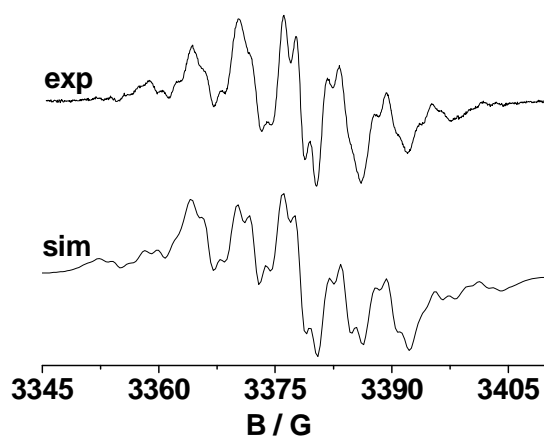


Figure 10.10. EPR spectrum of electrochemically generated $[(\text{QuinoxP})\text{Pt}(\text{Cl})_2]^{-}$ at 298 K in $\text{CH}_2\text{Cl}_2/$ 0.1 M Bu_4NPF_6 (top) with simulation (bottom).

KAPITEL 11

Zusammenfassung

In dieser Arbeit werden die strukturellen sowie elektronischen Eigenschaften von Übergangsmetallkomplexen mit redoxaktiven Liganden wie Nitrosyl, 4,6-Di-*tert*-butyl-*N*-phenyl-*o*-iminobenzochinon und 3,5-Di-*tert*-butyl-*o*-benzochinon (Abbildung. 11.1) vorgestellt. Zusätzlich werden in dieser Arbeit die Synthese, die Bindungsverhältnisse und das Elektronentransferverhalten von Übergangsmetallkomplexen mit dem luftstabilen chiralen chelatisierenden Diphosphinliganden *R,R*-QuinoxP¹ (Abbildung 11.9) beschrieben.

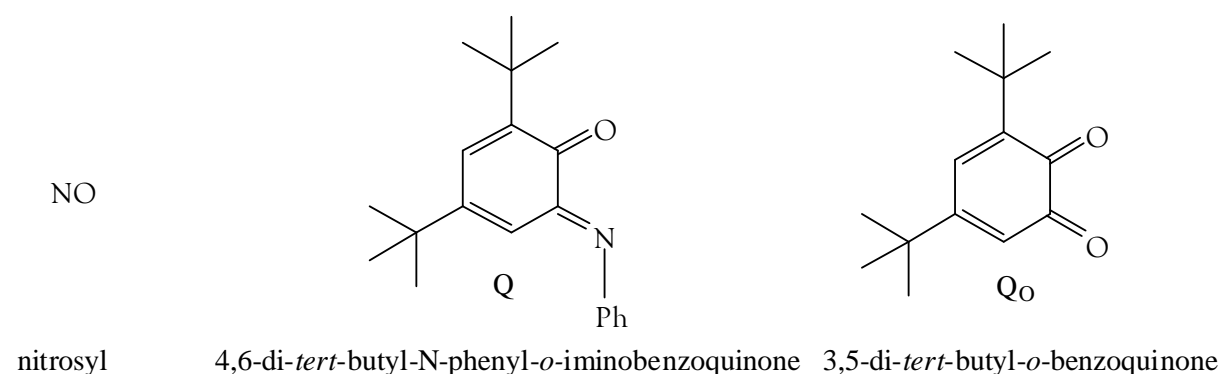


Abbildung 11.1. Molekülstrukturen der in dieser Arbeit verwendeten nicht-unschuldigen Liganden.

Im ersten Teil dieser Arbeit werden die synthetischen Aspekte, die Strukturen, spektroskopische- und elektronische Eigenschaften neuer Nitrosylkomplexe mit den Übergangsmetallen Ru und Re beschrieben. Die tatsächliche Form des koordinierten NO^{*m*} (*m* = +/0/-) wurde durch experimentelle Ergebnisse und von quantenchemischen Rechnungen unterstützt.

Im zweiten Kapitel werden die verschiedenen Oxidationsstufen des [Ru(OEP)(NO)(X)]^{*n*+} (Abbildung. 11.2) (*n* = +2, +1, 0, -1, OEP = Octethylporphyrindianion) mit verschiedenen axialen Liganden X (H₂O, Pyridin, 4-Cyanopyridin, 4-Dimethylaminopyridin) spektroskopisch untersucht. Die elektronische Struktur der Komplexe wurde zufriedenstellend durch DFT Rechnungen geklärt. Spektroelektrochemische Untersuchungen zeigen, dass die erste Oxidation (X = H₂O) am Porphyrinring stattfindet, was durch das Erscheinen der diagnostischen Porphyrin-Radikalanionen-Streckschwingungsbande⁴⁶ (1531 cm⁻¹), einer kleinen positiven Verschiebung der NO-Schwingung um 20 cm⁻¹ erkennbar ist und durch das ESR-Signal bei *g*_{iso} ≈ 2.00 bestätigt

wird. Die erste Reduktion hingegen findet NO-zentriert statt, dies wird vor allem durch eine große Änderung ($\approx 300 \text{ cm}^{-1}$) der $\nu(\text{NO})$ Streckschwingung in der IR-Spektroelektrochemie und von dem gut aufgelöstem ESR-Spektrum, in dem die Stickstoffhyperfeinkopplung des ^{14}N -Kerns (Abbildung. 11.2) zu erkennen ist, bewiesen. DFT-Rechnungen unterstützen die Interpretation der experimentellen Ergebnisse, das HOMO (X = H_2O oder Pyridin) wird dominiert durch das Porphyrin- π -System, obwohl das LUMO einen ca. 50%-igen $\pi^*(\text{NO})$ Charakter aufweist.

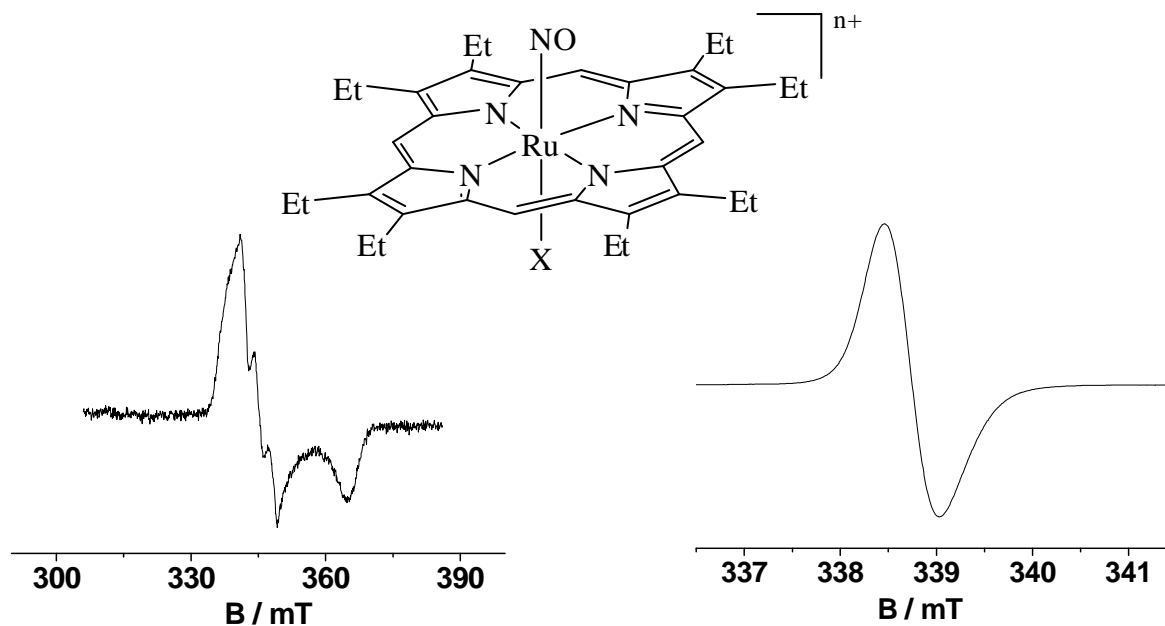


Abbildung 11.2. Molekülstruktur des $[(\text{OEP})\text{Ru}(\text{NO})(\text{X})]^{n+}$ wobei X = H_2O ($n = 1, 2, 3$) oder Pyridin, 4-Cyanopyridin oder 4-*N,N*-Dimethylaminopyridin ($n = 1, 0$) (oben), ESR-Spektrum des bei 110 K in $\text{CH}_2\text{Cl}_2/0.1 \text{ M } n\text{-Bu}_4\text{ClO}_4$ elektrochemisch erzeugten $[(\text{OEP})\text{Ru}(\text{NO})(\text{py})]^0$ (links) und des bei 295 K in $\text{CH}_2\text{Cl}_2/0.1 \text{ M } n\text{-Bu}_4\text{ClO}_4$ elektrochemisch erzeugten $[(\text{OEP})\text{Ru}(\text{NO})(\text{H}_2\text{O})]^{2+}$ (rechts).

In Kapitel 3 wird der Komplex $(\text{PPh}_4)_4[(\text{CN})_4(\text{NO})\text{Re}(\mu\text{-O})\text{Re}(\text{NO})(\text{CN})_4]$ (Abbildung 11.3), eine sauerstoffverbrückte Rheniumdinitrosylverbindung mit Cyanid als Co-Ligand, beschrieben. Der Komplex ist strukturell und spektroskopisch charakterisiert. Molekülstrukturanalyse bestätigen die lineare Anordnung der Nitrosylgruppen sowie der Re-O-Re Einheit. Die Verbindung weist zwei scharfe $\nu(\text{NO})$ Banden bei 1710 cm^{-1} und 1670 cm^{-1} und zwei deutliche $\nu(\text{CN})$ Banden bei 2118 und 2129 cm^{-1} in Acetonitril auf. Die Zuordnung der Oxidationsstufen des $[(\text{CN})_4(\text{NO}^+)\text{Re}^{\text{II}}(\mu\text{-O})\text{Re}^{\text{II}}(\text{NO}^+)(\text{CN})_4]^{4-}$ kann basierend auf der erhaltenen Molekülstruktur sowie der Literatur⁵⁵ gemacht werden. Cyclovoltammetrie weist eine irreversible Reduktion und eine reversible Oxidation gefolgt von einem irreversiblen Prozess auf.

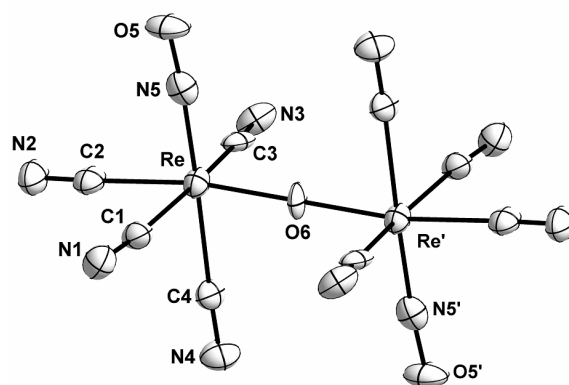


Abbildung 11.3 Molekülstruktur des anionischen Teils von $(\text{PPh}_4)_4[(\text{CN})_4(\text{NO})\text{Re}(\mu\text{-O})\text{Re}(\text{NO})(\text{CN})_4] \cdot 4(\text{CH}_2\text{Cl}_2)$.

Im zweiten Teil dieser Arbeit werden verschiedene Komplexe mit 1,2-Dioxolen-artigen^{2,3} „non-innocent“ Liganden (Q bzw. Q_0) oder die Kombination zweier nicht unschuldiger Liganden Q_N und NO in einem System, beschrieben.

In Kapitel 4 werden vier Ruthenium *o*-Iminochinonkomplexe und die tatsächliche Verteilung der Ladung zwischen Metall und Ligand, diskutiert. Die Verbindungen wurden in der monokationischen Form isoliert und ebenfalls kristallographisch analysiert.

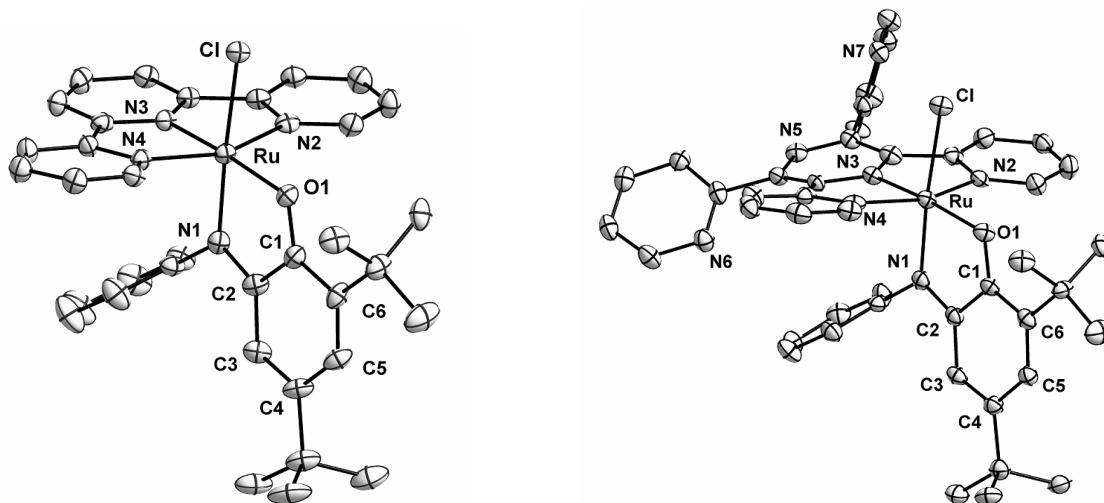


Abbildung 11.4. Molekülstruktur des $[(\text{terpy})\text{Ru}(\text{Q})\text{Cl}](\text{ClO}_4)$ (links) and $[(\text{tppz})\text{Ru}(\text{Q})(\text{NO}_2)](\text{PF}_6) \cdot (\text{CH}_2\text{Cl}_2)$ (rechts) (terpy = 2,2':6'2''-Terpyridin und tppz = 2,3,5,6 Tetrakis(2-pyridyl)pyrazin).

Die C1–O1, C2–N1 Bindungslängen sowie die C–C Abstände im Ring legen die Vermutung nahe, dass Q an das Metallzentrum in der Iminosemichinonform ($\text{Q}^{\cdot-}$) gebunden ist. Somit ergibt sich für alle Verbindungen die Formulierung $[\text{Ru}^{\text{III}}(\text{Q}^{\cdot-})]$. Die Terpyridinkomplexe

$[(\text{terpy})\text{Ru}(\text{Q})\text{Cl}](\text{ClO}_4)$ und $[(\text{terpy})\text{Ru}(\text{Q})(\text{NO}_2)](\text{ClO}_4)$ zeigen jeweils zwei Reduktionen und eine Oxidation; Der terpyridin-zentrierte Reduktionsprozess wurde nicht beobachtet werden da er außerhalb des Lösungsmittelfensters liegt. Die tppz-Komplexe $[(\text{tppz})\text{Ru}(\text{Q})\text{Cl}](\text{PF}_6)$ und $[(\text{tppz})\text{Ru}(\text{Q})(\text{NO}_2)](\text{PF}_6)$ zeigen vier beziehungsweise drei Reduktionen und jeweils eine Oxidation. Die X-Band ESR-Spektroskopie bei Raumtemperatur der Ein-Elektron-Reduzierten-Spezies weist ein $g_{\text{iso}} \approx 2.00$ auf, ein typischer Wert für Semichinonradikalkomplexe. Dies zeigt das die Reduktion vorwiegend metallzentriert verläuft und das ungepaarte Elektron hauptsächlich auf dem $\text{Q}^{\cdot-}$ in $[\text{Ru}^{\text{II}}(\text{Q}^{\cdot-})]$ verbleibt. Die anisotropen g-Werte die aus der X-Band- und Hochfeld-ESR-Spektroskopie bei 110 K erhalten wurden legen, genau wie die Metallhyperfeindaten dar, dass eine nicht geringer Anteil des Metalls am einfach besetzten MO (SOMO) beteiligt ist. Oxidation des $[(\text{tppz})\text{Ru}(\text{Q})\text{Cl}]^+$ führt zu einem rhombisches ESR-Signal welches typisch für verzerrtes Ruthenium(III) ist.

Kapitel 5 beinhaltet die zwei paramagnetischen Komplexe $[\text{Ru}(\text{NO})(\text{Q})(\text{terpy})](\text{PF}_6)_2$ (Abbildung 11.5) und $[\text{Ru}(\text{NO})(\text{Q})(\text{tppz})](\text{PF}_6)_2$ bei denen drei redoxaktive Komponenten, $\text{Ru}^{\text{II}}/\text{Ru}^{\text{III}}$, NO^{m} und $(\text{Q})^{\text{n}}$ verknüpft sind. Die Co-Liganden terpy und tppz sind in diesem Falle nicht redoxaktiv.

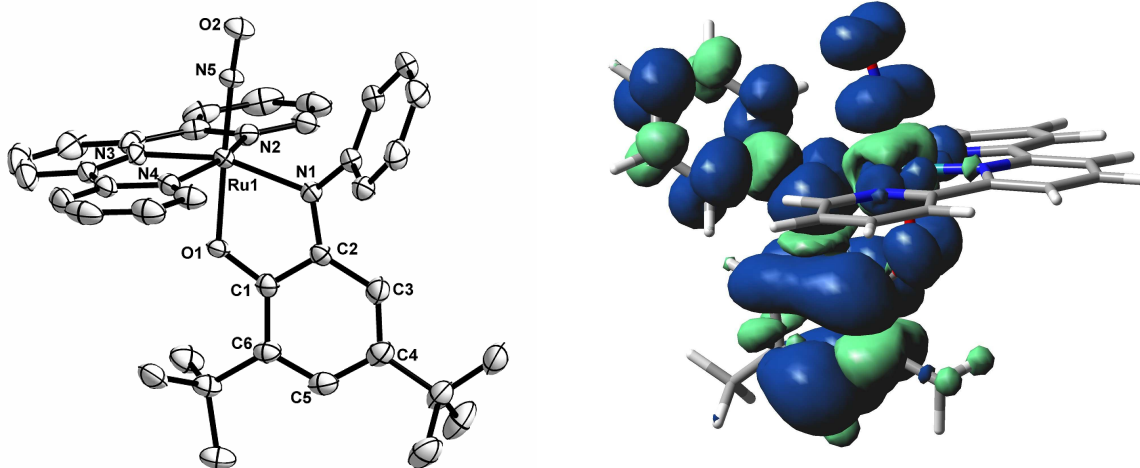


Abbildung 11.5. Molekülstruktur des $[\text{Ru}(\text{NO})(\text{Q})(\text{terpy})](\text{PF}_6)_2$ (links) und Spindichte des $[\text{Ru}(\text{NO})(\text{Q})(\text{terpy})]^{2+}$ (rechts).

Das stabilste Isomer des $[\text{Ru}(\text{NO})(\text{Q})(\text{terpy})](\text{PF}_6)_2$ mit NO *trans* zum Sauerstoffdonor von Q wurde isoliert und strukturell charakterisiert (Abbildung 11.6). In Verbindung mit dem experimentellen $\text{Ru}-\text{N}-\text{O}$ Winkel, den Bindungsabständen im Chinonliganden vor allem der $\text{C1}-\text{O1}$ Abstand, mit $\nu(\text{NO})$ und den ESR-Messungen bei 9.5 und 285 GHz die ein schmales radikalisches Signal zeigen, kann $[\text{Ru}^{\text{II}}(\text{NO}^+)(\text{Q}^{\cdot-})(\text{terpy})]^{2+}$ als gültige Formulierung

angenommen werden. DFT-Rechnungen bekräftigen diese Aussage (Abbildung 11.5) legen aber nahe, dass das SOMO in Übereinstimmung mit der ESR-Hyperfeinaufspaltung, zu 15 % NO Charakter aufweist. Für $[\text{Ru}^{\text{II}}(\text{NO}^+)(\text{Q}^{\bullet-})(\text{tppz})]^{2+}$ kann dieselbe Oxidationsstufenformulierung, basierend auf den experimentellen Daten der NO-Streckschwingung und den ESR-Daten bei 9.5 GHz, formuliert werden. Reduktion beider Komplexe und die Oxidation des terpy-Komplexes führen zu moderaten Veränderungen bei den NO-Streckschwingungen zu niedrigeren, beziehungsweise höheren Frequenzen. Dies legt nahe, dass die Elektronentransferprozesse zum Großteil auf dem Semichinonliganden zentriert sind. Somit ist weder das NO noch das Metall an der Oxidation bzw. Reduktion stark beteiligt.

In Kapitel sechs werden die Struktur, Elektrochemie und die spektroskopischen Eigenschaften des $[\text{Cl}(\text{Q})\text{Ru}(\mu\text{-tppz})\text{Ru}(\text{Q})\text{Cl}]^n$ beschrieben. Die Verbindung $[\text{Cl}(\text{Q})\text{Ru}(\mu\text{-tppz})\text{Ru}(\text{Q})\text{-Cl}](\text{PF}_6)_2$ beinhaltet fünf Redoxsysteme $[(\text{Q})^n\text{-Ru}^m\text{-}(\mu\text{-tppz}^x)\text{-Ru}^{m'}\text{-}(\text{Q})^{n'}]$ und kann über die Einkristallanalyse als *anti* Isomer (Abbildung 11.6) identifiziert werden.

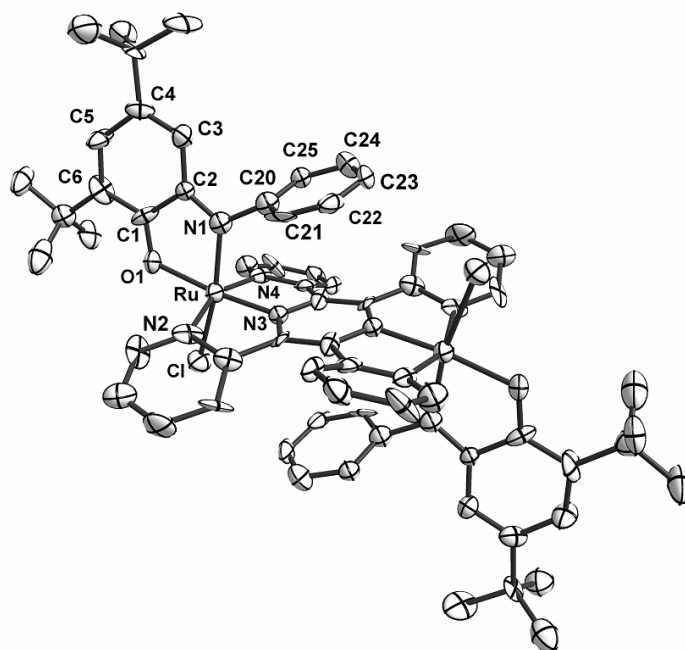


Abbildung 11.6. Molekülstruktur des $[(\text{Q})\text{ClRu}(\mu\text{-tppz})\text{RuCl}(\text{Q})]^{2+}$ im Kristall von $[(\text{Q})\text{ClRu}(\mu\text{-tppz})\text{RuCl}(\text{Q})](\text{PF}_6)_2 \cdot (\text{C}_7\text{H}_8)$.

Durch die spektroskopischen und strukturellen Ergebnisse kann die Verbindung als $[(\text{Q}^{\bullet-})\text{-Ru}^{\text{III}}\text{-}(\mu\text{-tppz}^0)\text{-Ru}^{\text{III}}\text{-}(\text{Q}^{\bullet-})]$ formuliert werden. Ein-Elektronenoxidation des $[\text{Cl}(\text{Q}^{\bullet-})\text{Ru}^{\text{III}}(\mu\text{-tppz}^0)\text{Ru}^{\text{III}}(\text{Q}^{\bullet-})\text{Cl}]^{2+}$ führt zu einem rhombischen ESR-Signal, welches typisch für verzerrtes Ruthenium(III) ist. Das Erscheinen (während der ersten Oxidation) und anschließendes Verschwinden (nach der zweiten Oxidation) einer starken NIR-Bande bei 1850 nm deutet auf

einen gemischtvalenten Zustand mit einem energetisch tief liegenden IVCT Übergang hin. Die Komproportionierungskonstante von $10^{6.1}$ ist beträchtlich. Der eng begrenzte IVCT bei 1850 nm hat einen sehr viel kleineren $\Delta v_{1/2}$ -Wert (1357 cm^{-1}) als nach der Hush-Formel (3530 cm^{-1}) zu erwarten war. Dies weist auf ein delokalisiertes System der Klasse III ($\text{Ru}^{2.5}\text{Ru}^{2.5}$) hin. Ebenso ergeben die DFT-Rechnungen, dass die Spindichte von $[\text{Cl}(\text{Q})\text{Ru}(\mu\text{-tppz})\text{Ru}(\text{Q})\text{Cl}]^{3+}$ hauptsächlich auf den Metallzentren, mit einem kleinem Chloridbeitrag und einer negativen Spindichte auf dem tppz Brückenliganden, liegt. Die ESR und UV-Vis-NIR Ergebnisse legen nahe, dass die ersten zwei Reduktionen des $[\text{Cl}(\text{Q}^{\bullet-})\text{Ru}^{\text{III}}(\mu\text{-tppz})\text{Ru}^{\text{III}}(\text{Q}^{\bullet-})\text{Cl}]^{2+}$ an den beiden Ru(III)zentren stattfinden. DFT-Rechnungen bestätigen, dass die Q Liganden einen großen Beitrag am Orbital besitzen. Die dritte Reduktion weist ein für $\text{tppz}^{\bullet-}$ typisches Absorptionsmaximum bei 960 nm und ein ESR-Signal bei $g_{\text{iso}} = 1.9987$, ohne sichtbare Metallhyperfeinwechselwirkungen auf. Daraus resultiert ein Drei-Spin-System $\text{Q}^{\bullet-}/\text{tppz}^{\bullet-}/\text{O}^{\bullet-}$ mit antiparallelen Spin-Spin-Wechselwirkungen zwischen den Semichinonliganden ($\uparrow\uparrow\downarrow$). Die vierte Reduktion findet wahrscheinlich ebenfalls am tppz statt. Sie zeigt bei 1200 nm eine starke Bande, genau wie sie für andere zweikernige Rutheniumkomplexe mit $\text{tppz}^{\bullet-}$ schon beobachtet wurde.

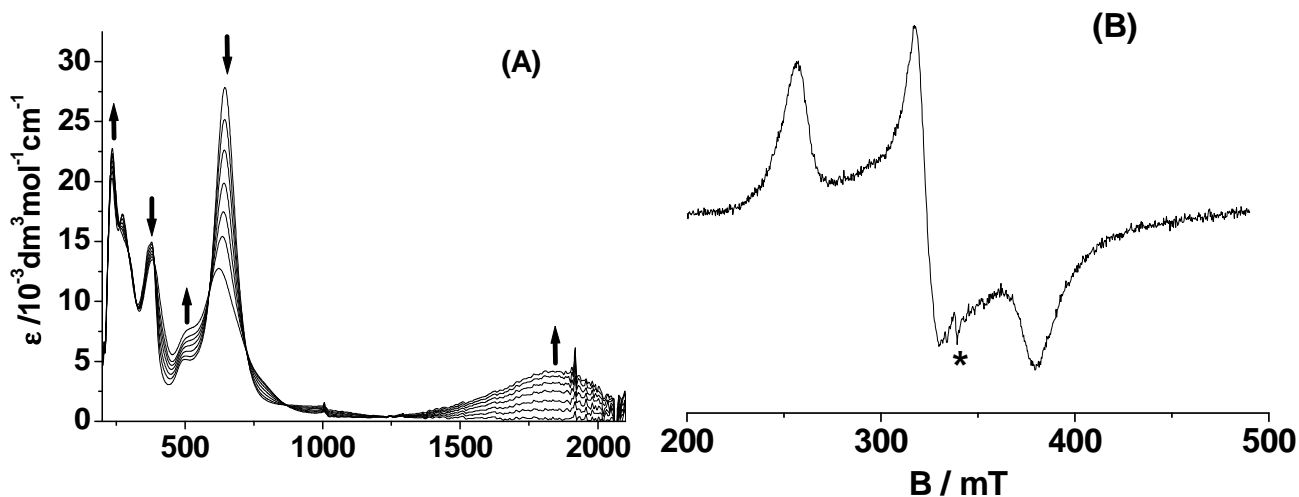
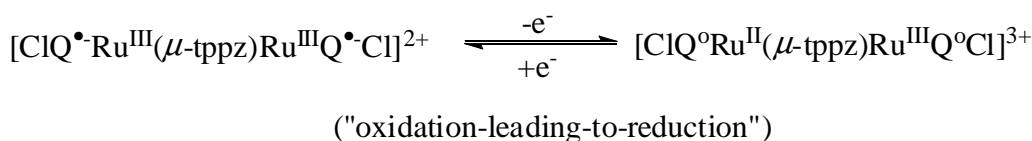


Abbildung 11.7 UV/Vis/NIR-Spektroelektrochemie der ersten Oxidation in $\text{CH}_3\text{CN} / 0.1 \text{ M}$ Bu_4NPF_6 des $[\text{Cl}(\text{Q})\text{Ru}(\mu\text{-tppz})\text{Ru}(\text{Q})\text{Cl}]^{2+}$ (A) und das ESR-Spektrum aus generiertem $[\text{Cl}(\text{Q})\text{Ru}(\mu\text{-tppz})\text{Ru}(\text{Q})\text{Cl}]^{3+}$ (B, 110 K) (*: cavity signal).

Kapitel 7 beschreibt im Detail die Spektroelektrochemie (UV-Vis-NIR und ESR) und theoretische Rechnungen der Redoxprodukte der Reihe $[\text{Ru}(\text{Q}_0)_3]^n$, $[\text{Os}(\text{Q}_0)_3]^n$ und $[\text{Ru}(\text{Q})_3]^n$ (Abbildung 11.8) ($n = +2$ bis -2).

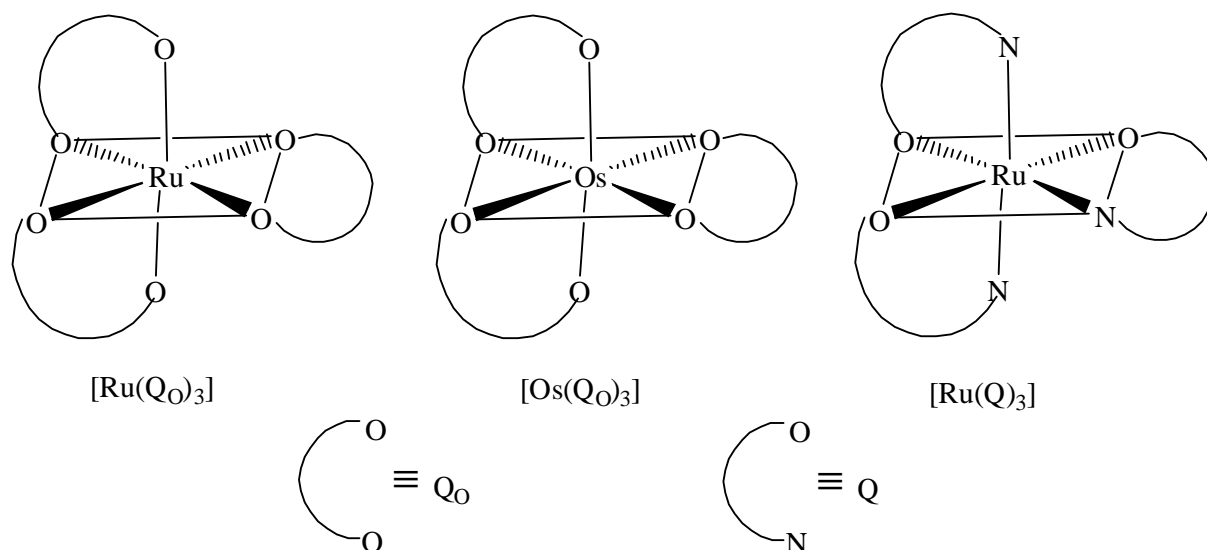


Abbildung 11.8. Molekülstruktur der Komplexe $[\text{Ru}(\text{Q}_0)_3]$, $[\text{Os}(\text{Q}_0)_3]$ and $[\text{Ru}(\text{Q})_3]$.

Über die Verbindungen $[\text{Ru}(\text{Q}_0)_3]^0$ und $[\text{Os}(\text{Q}_0)_3]^0$ wurde schön früher von Pierpont¹⁰¹ et al. berichtet. Die Oxidationstufe des Liganden (Q_0) wurde als Semichinon (Q_0^{\bullet}) beziehungsweise als Catechol (Q_0^{2-}) formuliert. Darauf basierend kann der neu dargestellte Komplex $[\text{Ru}(\text{Q})_3]^0$ als antiferromagnetisch gekoppelte Trisiminosemichinonato $[\text{Ru}^{\text{III}}(\text{Q}^{\bullet})_3]$ Verbindung aufgefasst werden. Der Komplex zeigt kein ESR-Signal und weist $^1\text{H-NMR}$ -Signale an den erwarteten Positionen. Für alle drei Komplexe finden die aufeinanderfolgenden Oxidationen hauptsächlich in den Ligandenorbitalen statt und der Beitrag des Metallions ist, durch die ESR-Messungen gestützt und von den DFT-Rechnungen bestätigt, sehr gering. Die ESR-Messungen der Reduktionen, gestützt durch DFT-Rechnungen, zeigen in allen drei Fällen $[\text{Ru}(\text{Q}_0)_3]^-$, $[\text{Os}(\text{Q}_0)_3]^-$ und $[\text{Ru}(\text{Q})_3]^-$ eine gemischte Situation. Die DFT-Rechnungen lassen den Schluss zu, dass 27%, 37% und 25% Metallanteile in den betrachteten SOMOs vorhanden sein müssen.

Das letzte Kapitel (Kapitel 8) beinhaltet die Darstellung zweier Metallkomplexe $[(\text{QuinoxP})\text{PtCl}_2]$ und $[(\text{QuinoxP})\text{Re}(\text{CO})_3\text{Cl}]$ (Abbildung 11.9). Beide Verbindungen werden durch die Reaktion zweier Standard-Precursoren $\text{Pt}(\text{dmsO})_2\text{Cl}_2$ beziehungsweise $\text{Re}(\text{CO})_5\text{Cl}$ und mit dem *R,R*-QuinoxP erhalten. Die Molekülstruktur der Verbindung zeigt, dass der Ligand *R,R*-QuinoxP über die Phosphordonoratome und nicht durch das Chinoxalin koordiniert. Elektronenaufnahme durch den Chinoxalinring ist nicht nur für die hohe Stabilität

gegenüber Luft verantwortlich, sondern vereinfacht auch die Reduktion der Komplexe zu den persistenten Radikalanionen $[(\text{QuinoxP})\text{PtCl}_2]^{*-}$ und $[(\text{QuinoxP})\text{Re}(\text{CO})_3\text{Cl}]^{*-}$.

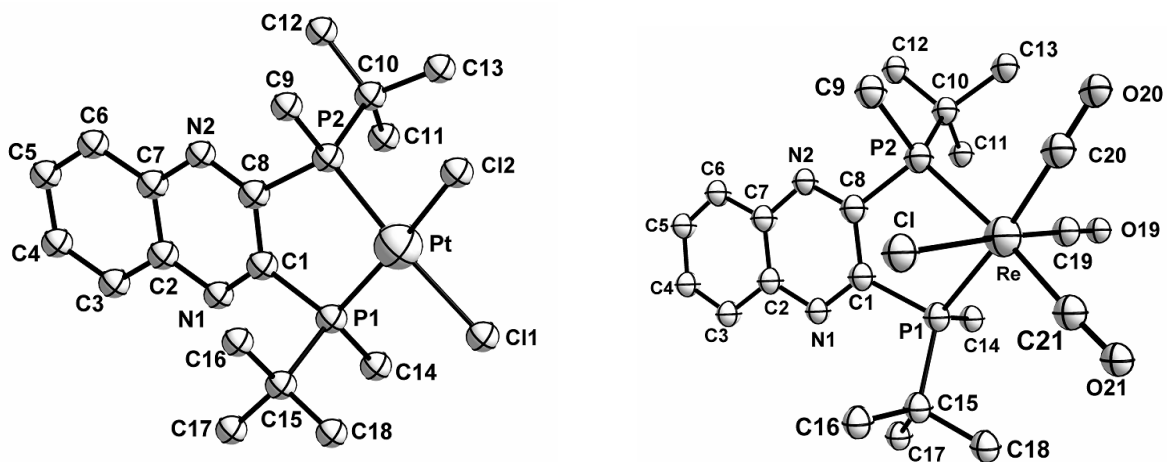


Abbildung 11.9. Molekülstrukturen $[(\text{QuinoxP})\text{PtCl}_2]$ (links) und $[(\text{QuinoxP})\text{Re}(\text{CO})_3\text{Cl}]$ (rechts).

Das ESR-Spektrum von $[(\text{QuinoxP})\text{PtCl}_2]^{*-}$ und $[(\text{QuinoxP})\text{Re}(\text{CO})_3\text{Cl}]^{*-}$ weist g -Werte nahe dem des Ligandenradikalions ($g = 2.0030$), mit geringen Metallanteilen im einfach besetztem Molekülorbital (SOMO), auf. Dies wird auch durch das Fehlen jeglicher g -Anisotropie bei X-Bandfrequenzen (9.5 GHz) bestätigt. Das $[(\text{QuinoxP})\text{Re}(\text{CO})_3\text{Cl}]^{*-}$ weist keine hinreichende Hyperfeinaufspaltung im ESR-Spektrum, außer die Signifikanten $^{185,187}\text{Re}$ Aufspaltungen von 5 G, auf. Das Radikal $[(\text{QuinoxP})\text{PtCl}_2]^{*-}$ besitzt (Abbildung 11.10) eine größere ^{195}Pt Hyperfeinaufspaltung von 24 G, die typischen großen ^{14}N ($I = 1$) Kopplungskonstanten des Chinoxalins (5.7 G) sowie die kleineren ^1H und ^{31}P Aufspaltungen. Die 24 G Aufspaltung für ^{195}Pt ist sehr viel kleiner als die für einkernige Pt(I) Komplexe⁵ erwartet wird.

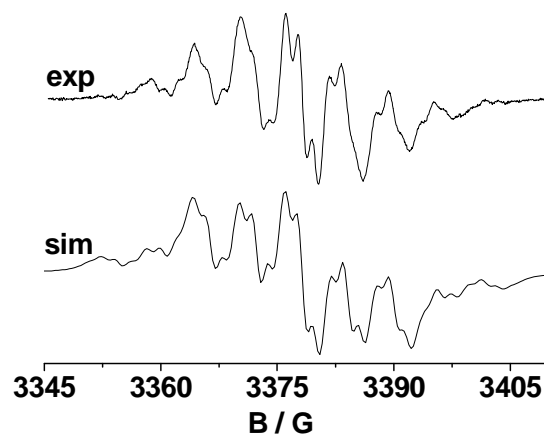


Abbildung 11.10. ESR-Spektrum des elektrochemisch bei 298 K in $\text{CH}_2\text{Cl}_2/0.1 \text{ M Bu}_4\text{NPF}_6$ erzeugten $[(\text{QuinoxP})\text{Pt}(\text{Cl})_2]^{*-}$ (oben); Simulation (unten).

APPENDIX

BIBLIOGRAPHY

1. Jørgensen, C. K. *Coord. Chem. Rev.* **1966**, *1*, 164.
2. Ward, M. D.; McCleverty, J. A. *J. Chem. Soc., Dalton Trans.* **2002**, 275.
3. McCleverty, J. A. *Chem. Rev.* **2004**, *104*, 403.
4. Enemark, J. H.; Feltham, R. D. *Coord. Chem. Rev.* **1974**, *13*, 339.
5. (a) Singh, P.; Fiedler, J.; Zális, S.; Duboc, C.; Niemeyer, M.; Lissner, F.; Schleid, Th.; Kaim, W. *Inorg. Chem.* **2007**, *46*, 9254. (b) Singh, P.; Sarkar, B.; Sieger, M.; Niemeyer, M.; Fiedler, J.; Zalis, S.; Kaim, W. *Inorg. Chem.* **2006**, *45*, 4602. (d) Sieger, M.; Sarkar, B.; Zalis, S.; Fiedler, J.; Escola, N.; Doctorovich, F.; Olabe, J. A.; Kaim, W. *Dalton Trans.* **2004**, 1797.
6. (a) Schrauzer, G. N.; V. Mayweg, V. *J. Am. Chem. Soc.* **1962**, *84*, 3221. (b) Davison, A.; N. Edelstein, N.; R. H. Holm, R. H.; Maki, A. H. *J. Am. Chem. Soc.* **1963**, *85*, 2029. (c) Davison, A.; Edelstein, N.; Holm, R.H.; Maki, A. H. *Inorg. Chem.* **1963**, *2*, 1227.
7. Pierpont, C. G.; Buchanan, R. M. *Coord. Chem. Rev.* **1981**, *38*, 45.
8. Pierpont, C.G. *Coord. Chem. Rev.* **2001**, *216*, 99.
9. Lever, A. B. P.; Masui, H.; Metcalfe, R. A.; Stufkens, D. J.; Dodsworth E. S.; Auburn, P. R. *Coord. Chem. Rev.* **1993**, *125*, 317.
10. (a) Murad, F. *Angew. Chem. Int. Ed.* **1999**, *28*, 1856. (b) Ribiero, J. M. C.; Hazzard, J.M. H.; Nussenzveig, R. H.; Champagne, D. E.; Walker, F. A. *Science* **1993**, *260*, 539.
11. (a) Alderton, W. K.; Cooper, C. E.; Knowles, R. G. *Biochem. J.* **2001**, *357*, 593. (b) Averill, B. A. *Chem. Rev.*, **1996**, *96*, 2951. (c) Tocheva, E. I.; Rosell, F. I.; Mauk, A. G.; Murphy, M. E. P. *Science* **2004**, *304*, 867. (d) Aboeella, N. W.; Reynolds, A. M.; Tolman, W. B. *Science* **2004**, *304*, 836. (e) Ignarro, L. J.; Degnan, J. N.; Baricos, W. H.; Kadowitz, P. J.; Wolin, M. S. *Biochim. Biophys. Acta* **1982**, *718*, 49.
12. (a) Wyllie, G. R. A.; Schulz, C. E.; Scheidt, W. R. *Inorg. Chem.* **2003**, *42*, 5722. (b) Praneeth, V. K. K.; Na'`ther, C.; Peters, G.; Lehnert, N. *Inorg. Chem.* **2006**, *45*, 2795.
13. (a) Praneeth, V. K. K.; Haupt, E.; Lehnert, N. *Inorg. Biochem.* **2005**, *99*, 940. (b) Paulat, F.; Lehnert, N. *Inorg. Chem.* **2007**, *46*, 1547.
14. Miranda, K. M.; Bu, X.; Lorkovi, I.; Ford, P. C. *Inorg. Chem.* **1997**, *36*, 4838. (d) Bohle, D. S.; Hung, C. H.; Smith, B. D. *Inorg. Chem.* **1998**, *37*, 5798.
15. Antipas, A.; Buchler, J. W.; Gouterman, M.; Smith, P. D. *J. Am. Chem. Soc.* **1978**, *100*, 3015.

16. (a) Wyllie, G. R. A.; Scheidt, W. R. *Chem. Rev.* **2002**, *102*, 1067. (b) Bezerra, C. W. B.; da Silva, S. C.; Gambardella, M. T. P.; Santos, R. H. A.; Plicas, L. M. A.; Tfouni, E.; Franco, D. W. *Inorg. Chem.* **1999**, *38*, 5660.
17. (a) Kadish, K. M.; Adamian, V. A.; Van Caemelbecke, E.; Tan, Z.; Tagliatesta, P.; Bianco, P.; Boschi, T.; Yi, G.-B.; Khan, M. A.; Richter-Addo, G. B. *Inorg. Chem.* **1996**, *35*, 1343. (b) Kadish, K. M. *Prog. Inorg. Chem.* **1986**, *34*, 435.
18. Carter, C. M.; Lee, J.; Hixson, C. A.; Powell, D. R.; Wheeler, R. A.; Shaw, M. J.; Richter-Addo, G. B. *Dalton Trans.* **2006**, 1338.
19. Brown, G. M.; Hopf, F. R.; Ferguson, J. A.; Meyer, T. J.; Whitten, D. G. *J. Am. Chem. Soc.* **1973**, *95*, 5939.
20. Pierpont, C. G.; Lange, C. W. *Progr. Inorg. Chem.* **1994**, *41*, 331.
21. (a) Rall, J.; Wanner, M.; Albrecht, M.; Hornung, F. M.; Kaim, W. *Chem. Eur. J.* **1999**, *5*, 2802. (b) Kasack, V.; Kaim, W.; Binder, H.; Jordanov, J.; Roth, E. *Inorg. Chem.* **1995**, *34*, 1924.
22. Kaim, W. *Dalton Trans.* **2003**, 761.
23. (a) Ernst, S.; Hänel, P.; Jordanov, J.; Kaim, W.; Kasack, V.; Roth, E. *J. Am. Chem. Soc.* **1989**, *111*, 1733. (b) Schwederski, B.; Kasack, V.; Kaim, W.; Roth, E.; Jordanov, J. *Angew. Chem.* **1990**, *102*, 74; *Angew. Chem. Int. Ed. Engl.* **1990**, *29*, 78.
24. (a) Patra, S.; Sarkar, B.; Mobin, S. M.; Kaim, W.; Lahiri, G. K. *Inorg. Chem.* **2003**, *42*, 6469. (b) Ghumaan, S.; Sarkar, B.; Patra, S.; van Slageren, J.; Fiedler, J.; Kaim, W.; Lahiri, G. K. *Inorg. Chem.* **2005**, *44*, 3210.
25. Kaim, W.; Ernst, S.; Kasack, V. *J. Am. Chem. Soc.* **1990**, *112*, 173.
26. Ye, S.; Sarkar, B.; Duboc, C.; Fiedler, J.; Kaim, W. *Inorg. Chem.* **2005**, *44*, 2843.
27. Remenyi, C.; Kaupp, M. *J. Am. Chem. Soc.* **2005**, *127*, 11399.
28. (a) Maji, S.; Sarkar, B.; Mobin, S. M.; Fiedler, J.; Urbanos, F. A.; Jimenez-Aparicio, R.; Kaim, W.; Lahiri, G. K. *Inorg. Chem.* **2008**, *47*, 5204. (b) Bill, E.; Bothe, E.; Chaudhuri, P.; Chlopek, K.; Herbian, D.; Kokatam, S.; Ray, K.; Weyhermüller, T.; Neese, F.; Wieghardt, K. *Chem. Eur. J.* **2005**, *11*, 204.
29. Kobayashi, K.; Ohtsu, H.; Wada, T.; Kato T.; Tanaka, K. *J. Am. Chem. Soc.* **2003**, *125*, 6729.
30. Miyazato, Y.; Wada, T.; Muckerman, J. T.; Fujita, E.; Tanaka, K. *Angew. Chem.* **2007**, *119*, 5830; *Angew. Chem. Int. Ed.* **2007**, *46*, 5728.

31. Muckerman, J. T.; Polyansky, D. E.; Wada, T.; Tanaka, K.; Fujita, E. *Inorg. Chem.* **2008**, *47*, 1787.
32. Poddel'sky, A. I.; Cherkasov, V. K.; Abakumov, G. A. *Coord. Chem. Rev.* **2009**, *253*, 291.
33. Chaudhuri, P.; Verani, C. N.; Bill, E.; Bothe, E.; Weyhermüller, T.; Wieghardt, K. *J. Am. Chem. Soc.* **2001**, *123*, 2213.
34. Verani, C. N.; Gallert, S.; Bill, E.; Weyhermüller, T.; Wieghardt, K.; Chaudhuri, P. *Chem. Commun.* **1999**, 1747.
35. Kokatam, S.; Weyhermüller, Th., Bothe, E.; Chaudhuri, P., Wieghardt, K. *Inorg. Chem.* **2005**, *44*, 3709.
36. Imamoto, T.; Watanabe, J.; Wada, Y.; Masuda, H.; Yamada, H.; Tsuruta, H.; Matsukawa, S.; Yamaguchi, K. *J. Am. Chem. Soc.* **1998**, *120*, 1635–1636.
37. Imamoto, T.; Sugita, K.; Yoshida, K. *J. Am. Chem. Soc.* **2005**, *127*, 11934.
38. Imamoto, T.; Kumada, A.; Yoshida, K. *Chem. Lett.* **2007**, *36*, 500.
39. Henning, J. C. M. *J. Chem. Phys.* **1966**, *44*, 2139.
40. (a) Kaim, W. *Chem. Ber.* **1982**, *115*, 910. (b) Kaim, W. *Angew. Chem.* **1983**, *95*, 201; *Angew. Chem., Int. Ed. Engl.* **1983**, *22*, 171. (c) Kaim, W.; Kohlmann, S.; Lees, A. L.; Zulu, M. M. *Z. Anorg. Allg. Chem.* **1989**, *575*, 97.
41. (a) Ford, P. C.; Lorkovic, I. M. *Chem. Rev.* **2002**, *102*, 993. (b) Praneeth, V. K. K.; Neese, F.; Lehnert, N. *Inorg. Chem.* **2005**, *44*, 2570. (c) Richter-Addo, G. B.; Wheeler, R. A.; Hiixson, C. A.; Chen, L.; Khan, M. A.; Ellison, M. A.; Schulz, C. E.; Scheidt, W. R. *J. Am. Chem. Soc.* **2001**, *123*, 6314.
42. (a) Ford, P. C.; Laverman, L. E. *Coord. Chem. Rev.* **2005**, *249*, 391. (b) Miranda, K. M.; Bu, X.; Lorković, I.; Ford, P. C. *Inorg. Chem.* **1997**, *36*, 4838. (c) Bohle, D. S.; Hung, C. H.; Smith, B. D. *Inorg. Chem.* **1998**, *37*, 5798.
43. Antipas, A.; Buchler, J. W.; Gouterman, M.; Smith, P. D. *J. Am. Chem. Soc.* **1978**, *100*, 3015.
44. (a) Wyllie, G. R. A.; Scheidt, W. R. *Chem. Rev.* **2002**, *102*, 1067. (b) Tfouni, E.; Krieger, M.; McGarvey, B. R.; Franco, D. W. *Coord. Chem. Rev.* **2003**, *236*, 57.
45. Yi, G.; Khan, M. A.; Richter-Addo, G. B. *Inorg. Chem.* **1996**, *35*, 3453.

46. One-electron σ oxidized porphyrins are often referred to as "radical cations" because they often contain coordinated divalent metals. However, the ligands themselves are then oxidized from their normal dinegative forms, Por^{2-} , to radical anions, $\text{Por}^{\bullet-}$.
47. Shimomura, E. T.; Phillippi, M. A.; Goff, H. M.; Scholz, W. F.; Reed, C. A. *J. Am. Chem. Soc.* **1981**, *103*, 6778.
48. Kaim, W.; Schwederski, B. *Bioinorganic Chemistry: Inorganic Elements in the Chemistry of Life: An Introduction and Guide*; Wiley: Chichester, U.K. 1994.
49. (a) Kadish, K. M.; Mu, X. *Pure Appl. Chem.* **1990**, *62*, 1051. (b) Mu, X. H.; Kadish, K. M. *Langmuir* **1990**, *6*, 51. Fujita, E.; Chang, C. K.; Fajer, J. *J. Am. Chem. Soc.* **1985**, *107*, 7665. (c) Rillema, D. P.; Nagle, J. K.; Barringer, L.F.; Meyer, T. J. *J. Am. Chem. Soc.* **1981**, *103*, 56.
50. Fuhrhop, J. H.; Kadish, K. M. Davis, D. G. *J. Am. Chem. Soc.* **1973**, *95*, 5140.
51. Olabe, J. A. *Dalton Trans.* **2008**, 3633.
52. (a) Rao, D. N. R.; Cederbaum, A. I. *Arch. Biochem. Biophys.* **1995**, *321*, 363. (b) *Nitric Oxide* **1997**, *1*, and following volumes.
53. Caulton, K.G. *Coord. Chem. Rev.* **1975**, *14*, 317.
54. Chadwick, B.M.; Sharpe, A.G. *Adv. Inorg. Chem. Radiochem.* **1971**, *8*, 83.
55. RoyChowdhury, S.; Dinda, S.; Chakraborty, S.; Simonnet, C.; Mukharjee, A. K.; Okamoto, K.; Bhattacharya, R. *Inorg. Chem. Commun.* **2005**, *8*, 61.
56. Machura, B. *Coord. Chem. Rev.* **2005**, *249*, 2277.
57. Weaver, T. R.; Meyer, T. J.; Adeyemi, S. A.; Brown, G. M.; Eckberg, R. P.; Hatfield, W. E.; Johnson, E. C.; Murray, R.W.; Untereker, D. *J. Am. Chem. Soc.* **1975**, *97*, 3039.
58. Mercati, G; Morazzoni, F; Cariati, F; Giusto, D. *Inorg. Chim. Acta.* **1978**, *29*, 165.
59. Baraldo, L.M.; Forlano, P.; Pise, A.R.; Slep, L.D.; Olabe, J.A. *Coord. Chem. Rev.* **2001**, *219–221*, 881.
60. (a) Ebadi, M.; Lever, A. B. P. *Inorg. Chem.* **1999**, *38*, 467. (b) Masui; H.; Lever, A. B. P.; Auburn, P. *Inorg. Chem.* **1991**, *30*, 2402. (c) Auburn, P. R.; Dodsworth, E. S.; Haga, M.; Liu, W.; Nevin, W. A.; Lever, A. B. P. *Inorg. Chem.* **1991**, *30*, 3502.
61. Bhattacharya, S.; Gupta, P.; Basuli, F., Pierpont, C. G. *Inorg. Chem.* **2002**, *41*, 5810.
62. Kasack, V.; Kaim, W.; Binder, H.; Jordanov, J.; Roth, E. *Inorg. Chem.* **1995**, *34*, 1924.

63. (a) Chanda, N; Laye, R. H; Chakraborty, S; Paul, R. L; Jeffery, J. C; Ward M. D and Lahiri, G. K, *J. Chem. Soc., Dalton Trans.*, **2002**, 3496. (b) J. P. Collin, P. Laine, J. P. Launay, J. P. Sauvage and A. Sour, *J. Chem. Soc., Chem. Commun.*, **1993**, 434. (c) C. R. Arana and H. D. Abruna, *Inorg. Chem.*, **1993**, 32, 194;
64. Patra, S.; Sarkar, B.; Mobin, S. M.; Kaim, W.; Lahiri, G. K. *Inorg. Chem.* **2003**, 42, 6469.
65. Kaim, W. *Coord. Chem. Rev.* **1987**, 76, 187.
66. Krejcik, M.; Danek, M.; Hartl, F. *J. Electroanal. Chem.* **1991**, 317, 179
67. (a) Creutz, C. *Prog. Inorg. Chem.* **1983**, 30, 1. (b) Kaim, W.; Lahiri, G. K. *Angew. Chem.* **2007**, 119, 1808; *Angew. Chem. Int. Ed.* **2007**, 46, 1778. (c) Richardson, D. E.; Taube, H. *Coord. Chem. Rev.* **1984**, 60, 107. (e) Demadis, K. D.; Hartshorn, D. C. Meyer, T. J. *Chem. Rev.* **2001**, 101, 2655.
68. Ye, S.; Sarkar, B.; Lissner, F.; Schleid, Th.; van Slageren, J.; Fiedler, J.; Kaim, W. *Angew. Chem.* **2005**, 117, 2140; *Angew. Chem. Int. Ed.* **2005**, 44, 2103.
69. Kaim, W. *Top. Curr. Chem.* **1994**, 169, 231.
70. Constable, E. C.; Cargill Thompson, A. M. W.; Tocher, D. A.; Daniels, M. A. M. *New. J. Chem.* **1992**, 16, 855.
71. Schubert, U. S.; Hofmeier, H.; Newkome, G. R. *Modern Terpyridine Chemistry*; Wiley-VCH: Weinheim, **2006**.
72. Wang, P. G.; Cai, T. B.; Taniguchi, N. *Nitric Oxide Donors*; Wiley-VCH: Weinheim, 2005.
73. Maji, S.; Patra, S.; Chakraborty, S.; Janardanan, D.; Mobin, S. M.; Sunoj, R. B.; Lahiri, G. K. *Eur. J. Inorg. Chem.* **2007**, 314.
74. Isomeric complexes $[\text{RuCl}(\text{Q})(\text{terpy})]^n$ are being investigated by Fujita, E.; Muckerman, J. T.
75. Videla, M.; Jacinto, J. S.; Baggio, R.; Garland, M. T.; Singh, P.; Kaim, W.; Slep, L. D.; Olabe, J.A. *Inorg. Chem.* **2006**, 45, 8608.

76. Sarkar, B.; Frantz, S.; Roy, S.; Sieger, M.; Duboc, C.; Denninger, D.; Kümmerer, H.-J.; Kaim, W. *J. Mol. Struct.* **2008**, *890*, 133.
77. Hartshorn, C. M.; Daire, N.; Tondreau, V.; Loeb, B.; Meyer, T. J.; White, P. S. *Inorg. Chem.* **1999**, *38*, 3200.
78. (a) Salsman, J. C.; Kubiak, C. P., Ito, T. *J. Am. Chem. Soc.* **2005**, *127*, 2382. (b) Londergan, C. H.; Salsman, J. C.; Lear, B. J.; Kubiak, C. P. *Chem. Phys.* **2006**, *324*, 57.
79. (a) Braun-Sand, S. B.; Wiest, O. *J. Phys. Chem. B* **2003**, *107*, 9624. (b) Braun-Sand, S. B.; Wiest, O. *J. Phys. Chem. A* **2003**, *107*, 285. (c) Wang, Y.; Lieberman, M. *IEEE Trans. Nanotech.* **2004**, *3*, 368.
80. (a) Heyduk, A. F.; Nocera, D. G. *Science* **2001**, *293*, 1639. (b) Esswein, A. J.; Veige, A. S.; Piccoli, P. M. B.; Schultz, A. J.; Nocera, D. G. *Organometallics* **2008**, *27*, 1073.
81. (a) Hush, N. S. *Prog. Inorg. Chem.* **1967**, *8*, 391. (b) Hush, N. S. *Coord. Chem. Rev.* **1985**, *64*, 135. (c) Creutz, C.; Newton, M. D.; Sutin, N. *J. Photochem. Photobiol. A* **1994**, *82*, 47.
82. (a) Petrov, V.; Hupp, J. T.; Mottley, C.; Mann, L. C. *J. Am. Chem. Soc.* **1994**, *116*, 2171. (b) Oh, D. H.; Sano, M.; Boxer, S. G. *J. Am. Chem. Soc.* **1991**, *113*, 6880.
83. (a) Kaim, W.; Klein, A.; Glöckle, M. *Acc. Chem. Res.* **2000**, *33*, 755. (b) Kaim, W.; Sarkar, B. *Coord. Chem. Rev.* **2007**, *251*, 584.
84. Fabre, M.; Bonvoisin, J. *J. Am. Chem. Soc.* **2007**, *129*, 1434.
85. Baumann, F.; Kaim, W.; Denninger, G.; Kümmerer, H. J.; Fiedler, J. *Organometallics* **2005**, *24*, 1966.
86. Singh, P.; Sieger, M.; Fiedler, J.; Su, C.-Y.; Kaim, W. *Dalton Trans.* **2008**, 868.
87. (a) Chanda, N.; Sarkar, B.; Fiedler, J.; Kaim, W.; Lahiri, G. K. *Inorg. Chem.* **2004**, *43*, 5128. (b) Ghumaan, S.; Sarkar, B.; Chanda, N.; Sieger, M.; Fiedler, J.; Kaim, W.; Lahiri, G. K. *Inorg. Chem.* **2006**, *45*, 7955. (c) Koley, M.; Sarkar, B.; Ghumaan, S.; Bulak, E.; Fiedler, J.; Kaim, W.; Lahiri, G. K. *Inorg. Chem.* **2007**, *46*, 3736.
88. Rocha, R. C.; Rein, F. M.; Jude, H.; Shreve, A. P.; Concepcion, J. J., Meyer, T. J. *Angew. Chem.* **2008**, *120*, 513; *Angew. Chem. Int. Ed.* **2008**, *47*, 503.

89. (a) Fantacci, S.; De Angelis, F.; Wang, J.; Bernhard, S.; Selloni, A. *J. Am. Chem. Soc.* **2004**, *126*, 9715. (b) Flores-Torres, S.; Hutchison, G. R.; Soltzberg, L. J.; Abruña, H. D. *J. Am. Chem. Soc.* **2006**, *126*, 1513.
90. Poppe, J.; Moscherosch, M.; Kaim, W. *Inorg. Chem.* **1993**, *32*, 2640.
91. Patra, S.; Sarkar, B.; Mobin, S. M.; Kaim, W.; Lahiri, G. K. *Inorg. Chem.* **2003**, *42*, 6469.
92. Stegmann, H. B.; Ulmschneider, K. B.; Hieke, K.; Scheffler, K. *J. Organomet. Chem.* **1976**, *118*, 259.
93. Creutz, C.; Chou, M. H. *Inorg. Chem.* **1987**, *26*, 2995.
94. Miller, J. S.; Min, K. S. *Angew. Chem.* **2008**, *Angew. Chem. Int. Ed.* **2008**, *48*, 262.
95. (a) Evangelio, E.; Ruiz.-Molina, D. *Eur. J. Inorg. Chem.* **2005**, 2957. (b) (b) Sato, O.; Cui, A.; Matsuda, R.; Tao, J.; Hayami, S. *Acc. Chem. Res.* **2007**, *40*, 361. (c) Dei, A.; Gatteschi, D.; Sangregorio, C.; Sorace, L. *Acc. Chem. Res.* **2004**, *37*, 827.
96. Samanta, S.; Singh, P.; Fiedler, J.; Zalis, S.; Kaim, W.; Goswami, S. *Inorg. Chem.* **2008**, *47*, 1625.
97. (a) Moscherosch, M.; Waldhör, E.; Binder, H.; Kaim, W.; Fiedler, J. *Inorg. Chem.* **1995**, *34*, 4326. (b) Záliš, S.; Kaim, W.; Sarkar, B.; Duboc, C. *Chem. Monthly*, in print.
98. (a) Salsman, J. C.; Ronco, S.; Londergan, C. H.; Kubiak, C. P. *Inorg. Chem.* **2006**, *45*, 547. (b) Adams, H.; Costa, P. J.; Newell, M.; Vickers, S. J.; Ward, M. D.; Félix, V.; Thomas, J. A. *Inorg. Chem.* **2008**, *47*, 11633.
99. (a) Nelsen, S. F. *Chem. Eur. J.* **2000**, *6*, 581. (b) Lambert, C.; Nöll, G.; Schelter, J. *Nature Mat.* **2002**, *1*, 69.
100. Zalis, S.; Kaim, W. *Main Group Chem.* **2007**, *6*, 267.
101. Bhattacharya, S.; Boone, S. R.; Fox, G. A.; Pierpont, C. G. *J. Am. Chem. Soc.* **1990**, *112*, 1088.
102. Pierpont, C. G. *Coord. Chem. Rev.* **2001**, *219-221*, 415.

103. (a) Chakraborty, S.; Laye, R. H.; Paul, R. L.; Gonnade, R. G.; Puranik, V.G.; Ward, M. D.; Lahiri, G. K. *J. Chem. Soc., Dalton Trans.*, **2002**, 1172. (b) Ghumaan, S.; Mukherjee, S.; Kar, S.; Roy, D.; Mobin, S. M.; Sunoj, R. B.; Lahiri, G. K. *Eur. J. Inorg. Chem.* **2006**, 4426.
104. (a) Metcalfe, R. A.; Vasconcellos, L. C. G.; Mirza, H.; Franco, D. W.; Lever, A. B. P. *J. Chem. Soc., Dalton Trans.* **1999**, 2653. (b) Auburn, P. R.; Lever, A. B. P. *Inorg. Chem.* **1990**, 29, 2551.
105. Frantz, S.; Fiedler, J.; Hartenbach, I.; Schleid, Th.; Kaim, W. *J. Organomet. Chem.* **2004**, 689 3031.
106. Knödler, A.; Wanner, M.; Fiedler, J.; Kaim, W. *Dalton Trans.* **2002** 3079.
107. Henning, J. C. M. *J. Chem. Phys.* **1966**, 44 2139.
108. (a) Kaim, W.; Bock, H. *J. Am. Chem. Soc.* **1978**, 100, 6504. (b) Kaim, W.; Bock, H. *Chem. Ber.* **1981**, 114 1576.
109. (a) Gross-Lannert, R.; Kaim, W.; Lechner, U.; Roth, E.; Vogler, C. *Z. Anorg. Allg. Chem.* **1989**, 579, 47. (b) Giordan, J. C.; Moore, J. H.; Tossell, J. A.; Kaim, W. *J. Am. Chem. Soc.* **1985**, 107 5600.
110. (a) Bensmann, W.; Fenske, D. *Angew. Chem.* 1979, 91, 754; *Angew. Chem., Int. Ed. Engl.* **1979**, 18, 677. (b) Fenske, D.; Stock, P. *Angew. Chem.* **1982**, 94, 393; *Angew. Chem., Int. Ed. Engl.* **1982**, 21, 356.
111. Weil, J. A.; Bolton, J. R. *Electron Paramagnetic Resonance*, 2nd ed.; Wiley-Interscience: Hoboken, NJ, **2007**.
112. (a) McInnes, E. J. L.; Farley, R. D.; Macgregor, S. A.; Taylor, K. J.; Yellowlees, L. J.; Rowlands, C. C. *J. Chem. Soc., Faraday Trans.* **1998**, 94 2985. (b) McInnes, E. J. L.; Farley, R. D.; Rowlands, C. C.; Welch, A. J.; Rovatti, L.; Yellowlees, L. J. *J. Chem. Soc., Dalton Trans.* **1999**, 4203.
113. Kaim, W.; Dogan, A.; Wanner, M.; Klein, A.; Tiritiris, I.; Schleid, Th.; Stufkens, D. J.; Snoeck, T. L.; McInnes, E. J. L.; Fiedler, J.; Zalis, S. *Inorg. Chem.* **2002**, 41 4139.

114. Braterman, P. S.; Song, J.-L.; Wimmer, F. M.; Wimmer, S.; Kaim, W.; Klein, A.; Peacock, R. D. *Inorg. Chem.* **1992**, *31*, 5084
115. Shida, T. *Electronic Absorption Spectra of Radical Ions*; Elsevier: Amsterdam, 1988; p 176.
116. Gaussian 03, Revision C.02, Frisch, M. J.; Trucks, G.; Schlegel, H. B.; Scuseria, G. E.; Robb, M. A.; Cheeseman, J. R.; Montgomery, J. A., Jr.; Vreven, T.; Kudin, K. N.; Burant, J. C.; Millam, J. M.; Iyengar, S. S.; Tomasi, J.; Barone, V.; Mennucci, B.; Cossi, M.; Scalmani, G.; Rega, N.; Petersson, G. A.; Nakatsuji, H.; Hada, M.; Ehara, M.; Toyota, K.; Fukuda, R.; Hasegawa, J.; Ishida, M.; Nakajima, T.; Honda, Y.; Kitao, O.; Nakai, H.; Klene, M.; Li, X.; Knox, J. E.; Hratchian, H. P.; Cross, J. B.; Bakken, V.; Adamo, C.; Jaramillo, J.; Gomperts, R.; Stratmann, R. E.; Yazyev, O.; Austin, A. J.; Cammi, R.; Pomelli, C.; Ochterski, J. W.; Ayala, P. Y.; Morokuma, K.; Voth, G. A.; Salvador, P.; Dannenberg, J. J.; Zakrzewski, V. G.; Dapprich, S.; Daniels, A. D.; Strain, M. C.; Farkas, O.; Malick, D. K.; Rabuck, A. D.; Raghavachari, K.; Foresman, J. B.; Ortiz, J. V.; Cui, Q.; Baboul, A. G.; Clifford, S.; Cioslowski, J.; Stefanov, B. B.; Liu, G.; Liashenko, A.; Piskorz, P.; Komaromi, I.; Martin, R. L.; Fox, D. J.; Keith, T.; Al-Laham, M. A.; Peng, C. Y.; Nanayakkara, A.; Challacombe, M.; Gill, P. M. W.; Johnson, B.; Chen, W.; Wong, M. W.; Gonzalez, C.; Pople, J. A., Gaussian, Inc., Wallingford CT, 2004.
117. te Velde, G.; Bickelhaupt, F. M.; van Gisbergen, S. J. A.; Fonseca Guerra, C.; Baerends, E. J.; Snijders, J. G.; Ziegler, T.; *J. Comput. Chem.* **2001**, *22*, 931. (c) ADF2006.01, SCM, Theoretical Chemistry, Vrije Universiteit, Amsterdam, The Netherlands, <http://www.scm.com>.
118. (a) Perdew, J. P.; Burke, K.; Ernzerhof, M. *Phys. Rev. Lett.* **1996**, *77*, 3865.
119. (b) Hariharan, P. C.; Pople, J. A., *Theor. Chim. Acta* **1973**, *28*, 213.
120. (c) Andrae, D.; Häussermann, U.; Dolg, M.; Stoll, H.; Preuss, H. *Theor. Chim. Acta* **1990**, *77*, 123.
121. (d) Woon, D. E.; Dunning, T.H., Jr. *J. Chem. Phys.* **1995**, *103*, 4572.
122. (e) Becke, A. D. *Phys. Rev. A* **1988**, *38*, 3098.
123. (f) Perdew, J. P.; Wang, Y. *Phys. Rev. B* **1992**, *45*, 13244.

124. (g) Perdew, J. P. *Phys. Rev. B* **1986**, *33*, 8822.
125. (a) van Lenthe, E.; van der Avoird, A.; Wormer, P. E. S. *J. Chem. Phys.* **1997**, *107*, 2488.
126. (b) van Lenthe, E.; van der Avoird, A.; Wormer, P. E. S. *J. Chem. Phys.* **1998**, *108*, 4783.
127. Cossi, M.; Rega, N.; Scalmani, G.; Barone, V. *J. Comput. Chem.* **2003**, *24*, 669.
128. Sheldrick, G. M.; *Programme SHELXS*: Göttingen, **1997**.
129. Sheldrick, G. M.; *Programme SHELXL*: Göttingen, **1997**.
130. Herrendorf, W.; Bärnighausen, H. *Programme HABITUS*: Giessen, Karlsruhe, **1993**,
Giessen, **1996**;
131. CRYSTAL IMPACT *Programme DAIMOND, Version 2.1e*: Bonn, **2001**.

ABBREVIATIONS

| | |
|----------------------------------|--|
| a | Hyperfine coupling constant |
| a_0 | isotropic hyperfine constant |
| A | ampere |
| abb. | Abbildung |
| av | average |
| b | broad (IR band) |
| B | magnetic field |
| Bu ₄ NPF ₆ | tetrabutylammonium hexafluorophosphate |
| calc. | calculated |
| cm | centimetre |
| Cl | chloro |
| d | doublet / bond length |
| δ | chemical shift |
| dm | decimetre |
| E_{pa} | anodic peak potential |
| E_{pc} | cathodic peak potential |
| ϵ | molar extinction coefficient |
| EPR | electron paramagnetic resonance |
| exp | experimental |
| Fc ^{0/+} | ferrocene / ferrocenium |
| g | gram |
| GHz | gigahertz |
| HOMO | highest occupied molecular orbital |
| Hz | hertz |
| I | nuclear spin |
| IR | infrared |
| irr | irreversible |
| iso | isotropic |
| IVCT | inter valence charge transfer |
| k | rate constant |
| K_c | comproportionation constant |
| L | ligand |
| λ | wavelength |

| | |
|----------------|---|
| LLCT | ligand to ligand charge transfer |
| LMCT | ligand to metal charge transfer |
| LUMO | lowest unoccupied molecular orbital |
| M | molar / metal |
| max | maximum |
| Me | methyl |
| MeOH | methanol |
| MHz | megahertz |
| ml | millilitre |
| MLCT | metal to ligand charge transfer |
| mm | millimeter |
| mmol | millimole |
| MO | molecular orbital |
| mol | mole |
| mT | militesla |
| mV | milivolt |
| ν | wavenumbers |
| NIR | near infrared |
| nm | nanometer |
| NMR | nuclear magnetic resonance |
| NO | nitric oxide |
| NOSs | nitric oxide syntheses |
| ° | degree |
| ° C | degree centigrade |
| <i>o</i> | ortho |
| OEP | octaethylporphyrin |
| OMP | octamethylporphyrin |
| OTTLE cell | optically transparent thin layer electrochemical cell |
| Ox | oxidized |
| Por | porphyrin |
| <i>p</i> | para |
| Ph | phenyl |
| ppm | parts per million |
| Q ₀ | 3,5-di- <i>tert</i> -butyl- <i>o</i> -benzoquinone |

| | |
|----------|--|
| Q | 4,6-di- <i>tert</i> -butyl-N-phenyl- <i>o</i> -iminobenzoquinone |
| QuinoxP | 2,3-bis(<i>tert</i> -butylmethylphosphino)quinoxaline |
| red | reduced |
| RT | room temperature |
| s | strong (IR band) / singlet |
| S | electron spin |
| SCE | standard calomel electrode |
| sh | shoulder |
| sim | simulated |
| SOMO | singly occupied molecular orbital |
| t | triplet |
| T | temperature / Tesla |
| Terpy | 2,2':6,2''-terpyridine |
| THF | tetrahydrofuran |
| Tppz | 2,3,5,6-tetrakis(2-pyridyl)pyrazine |
| UV | ultra violet |
| V | volt |
| vs. | very strong (IR band) |
| vs. | versus |
| vis | visible |
| ω | dihedral angle |
| Z | atomic number |

CURRICULUM VITAE

Contact Information:

Atanu Kumar Das

Institut für Anorganische Chemie, Universität Stuttgart
Pfaffenwaldring 55
70569 Stuttgart, Germany

Email: das@iac.uni-stuttgart.de / atanu_chem@yahoo.com

Tel: 004971168569034(office)

Education:

1992 to 1998: Baita Mahendranath High School, East Midnapore, West Bengal, India

1998 to 2000: Vidyasagar Vidyapith, Midnapore, West Bengal, India

2000 to 2003: *Calcutta University, Kolkata, West Bengal*
Degree obtained: Bachelor of Science in Chemistry

2003 to 2005: *Indian Institute of Technology, Bombay, Maharashtra, India*
Degree obtained: Master of Science in Chemistry

M.Sc Project : Synthesis of 21-thia calix(4) Phyrin with two *meso* sp³ Carbons

Since 2005: Doctoral work at the Institut für Anorganische Chemie, Stuttgart under the guidance of Prof. Dr. Wolfgang Kaim

Position Held:

September 2005 to April 2006:

Wissenschaftliche Hilfskraft at the Institut für Anorganische Chemie der Universität Stuttgart

May 2006 to June 2009:

Wissenschaftliche Angestellte at the Institut für Anorganische Chemie der Universität Stuttgart

List of Publications

1. A Five-Center Redox System: Molecular Coupling of Two Non-Innocent Imino-*o*-benzoquinonato-Ruthenium Functions through a π Acceptor Bridge

Das, A. K.; Sarkar, B.; Fiedler, J.; Zálíš, S.; Hartenbach, I.; Strobel, S.; Lahiri, G. K.; Kaim, W. *J. Am. Chem. Soc.* In print.

2. An Odd-Electron Complex $[\text{Ru}^k(\text{NO}^m)(\text{Q}^n)(\text{terpy})]^{2+}$ with Two Prototypical Non-Innocent Ligands

Das, A. K.; Sarkar, B.; Duboc, C.; Strobel, S.; Fiedler, J.; Zálíš, S.; Lahiri, G. K.; Kaim, W. *Angew. Chem.* **2009**, *121*, 4306; *Angew. Chem. Int. Ed. Engl.* **2009**, *48*, 4242.

3. Structures and Redox Properties of Metal Complexes of the Electron-Deficient Diphosphine Chelate Ligand *R,R*-QuinoxP

Das, A. K.; Bulak, B.; Sarkar, B.; Lissner, F.; Schleid, Th.; Niemeyer, M.; Fiedler, J.; Wolfgang Kaim, W. *Organometallics* **2008**, *27*, 218.

4. Redox Properties of Ruthenium Nitrosyl Porphyrin Complexes with Different Axial Ligation: Structural, Spectroelectrochemical (IR, UV-Visible, and EPR), and Theoretical Studies

Singh, P.; Das, A. K.; Sarkar, B.; Niemeyer, M.; Roncaroli, F.; Olebe, J. A., Fidler, J.; Zálíš, S.; Kaim, W. *Inorg. Chem.* **2008**, *47*, 7106.

5. First Example of Structurally Characterized Mono- and Dinuclear Ruthenium Complexes Derived from Zwitterionic Quinonoid Ligands

Das, H. S.; Das, A. K.; Pattacini, R.; Hübner, R.; Braunstein, P.; Sarkar, B. *Chem. Commun.* In print.

6. Stabilization of $\{\text{RuNO}\}^6$ and $\{\text{RuNO}\}^7$ States in $[\text{Ru}^{\text{II}}(\text{trpy})(\text{bik})(\text{NO})]^{n+}$ {trpy = 2,2':6',2''-Terpyridine, bik = 2,2'-bis(1-methylimidazolyl)ketone}–Formation, Reactivity, and Photorelease of Metal-Bound Nitrosyl

De, Prinaka.; Sarkar, B.; Maji, S.; Das, A. K.; Bulak, E.; Mobin, S. M.; Kaim, W.; Lahiri, G. K. *Eur. J. Inorg. Chem.* **2009**, *18*, 2702.

7. Formation, Reactivity, and Photorelease of Metal Bound Nitrosyl in $[\text{Ru}(\text{trpy})(\text{L})(\text{NO})]^{n+}$
(trpy) 2,2':6',2''-Terpyridine, L) 2-Phenylimidazo[4,5-f]1,10-phenanthroline)

Maji, S.; Sarkar, B.; Patra, M.; **Das, A. K.**; Mobin, S. M.; Kaim, W.; Lahiri, G. K. *Inorg. Chem.* **2008**, *47*, 3218.

8. Valence Structures of the Diastereomeric Complexes *meso*- and *rac*- $[\text{Ru}_2(\text{acac})_4(\square\text{-Q})]^n$ ($n = 2-, -, 0, +, 2+$) with the Multiply Quinonoid Bridging Ligand Q = 1,2,4,5-Tetraimino-3,6-diketocyclohexane

Kumbhakar, D.; Sarkar, B.; Das, A.; **Das, A. K.**; Mobin, S. M.; Fiedler, J.; Kaim W.; Lahiri, G. K. *Dalton. Trans.* In press.